Role of the proton channel HVCN1 in the regulation of neutrophil activation

Dissertation

zur

Erlangung des Doktorgrades (Dr. rer. nat.)

der

Mathematisch-Naturwissenschaftlichen Fakultät

der

Rheinischen Friedrich-Wilhelms-Universität Bonn

vorgelegt von

Nina Offermann

aus

Mönchengladbach

Bonn, Februar 2023

Angefertigt mit Genehmigung der Mathematisch-Naturwissenschaftlichen Fakultät
der Rheinischen Friedrich-Wilhelms-Universität Bonn

Gutachter: Prof. Dr. Joachim L. Schultze
Gutachterin: Prof. Dr. Irmgard Förster

Tag der Promotion: 25.05.2023
Erscheinungsjahr: 2023

Abstract

Excessive neutrophil activation is a feature of many inflammatory diseases. Neutrophils from affected patients are prone to release reactive oxygen species (ROS) and toxic granule proteins or to undergo NETosis, a special form of cell death characterized by the release of extracellular DNA traps (NETs). Indeed, neutrophils have been shown to play a critical role in the development of autoimmune diseases, as NETs provide autoantigens, such as double-stranded DNA in systemic lupus erythematosus (SLE) or myeloperoxidase (MPO) in ANCA-associated vasculitis. Nonetheless, the molecular switches regulating neutrophil effector functions remain to be further characterized.

HVCN1 is the only voltage-gated proton channel in mammals that regulates pH and membrane potential during neutrophil activation. Its function supports the electrogenic activity of the ROS-generating enzyme NADPH oxidase. Therefore, NADPH oxidase-dependent ROS production is significantly impaired in the absence of HVCN1. However, not much is known about how HVCN1 regulates neutrophil downstream functions.

Therefore, in the first part of my thesis, I further investigated the role of HVCN1 in neutrophils. I demonstrated that PMA-stimulated NETosis and MPO release were significantly increased in HVCN1$^{-/-}$ neutrophils. Fittingly, HVCN1$^{-/-}$ neutrophils showed atypical mobilization of calcium, increased histone citrullination, and high mitochondrial ROS caused by calcium-dependent mitochondrial depolarization. Increased NETosis, MPO release, and mitochondria ROS could be rescued by intracellular calcium chelation but not by antioxidants, suggesting that calcium is the primary determinant of increased NETosis susceptibility in HVCN1$^{-/-}$ neutrophils.

I further examined the consequences of HVCN1 deficiency *in vivo*. In agreement with previous reports, young HVCN1$^{-/-}$ mice did not exhibit a pathogenic phenotype, however we detected a mild (auto-) inflammatory phenotype in aged, female HVCN1$^{-/-}$ mice. Likewise, HVCN1$^{-/-}$ mice showed more severe pathology in two models of inflammation. Correspondingly, we found HVCN1 to be downregulated in neutrophils from SLE patients in two separate datasets.

This is the first study to show that HVCN1 deficiency increases the inflammatory capacity of murine neutrophils *in vitro* and *in vivo*, suggesting that downregulation of HVCN1 may have implications for human disease.

Table of Contents

Abstract III
Table of Contents IV
List of Figures VI
List of Abbreviations VII
1 Introduction 1
1.1 The mammalian immune system 1
1.2 Neutrophils 3
1.3 Neutrophil effector functions 7
1.4 Neutrophils in autoimmune diseases 14
1.5 The hydrogen voltage-gated channel 1 15
1.6 Aim of the thesis 22
2 Material 23
2.1 Equipment 23
2.2 Consumables 24
2.3 Chemicals, reagents and enzymes 24
2.4 Solutions and buffers 26
2.5 Kits 26
2.6 Antibodies 26
2.7 Primers 27
2.8 Software 28
2.9 Mice strains 29
3 Methods 30
3.1 Isolation of bone marrow neutrophils 30
3.2 Histology 30
3.3 Measurements of ROS 32
3.4 Measurements of intracellular ions by flow cytometry 33
3.5 Measurements of membrane potential by flow cytometry 34
3.6 Measurements of mitochondrial fitness and damage 35
3.7 Measurements of granule release and pinocytosis 36
3.8 Plate-bound IgG stimulation 37
3.9 Analysis of phagocytosis and intracellular killing 37
3.10 Western Blot 37
3.11 Gene expression analysis 38
3.12 Flow cytometry analysis 39
3.13 Peritonitis model 40

3.14 Model for pulmonary ANCA-associated vasculitis 40
4 Results 42
4.1 HVCN1 expression and function 42
4.2 NETosis 44
4.3 Calcium dynamics 48
4.4 Mitochondrial function 53
4.5 Increased NETosis HVCN1$^{-/-}$ neutrophils is dependent on calcium 59
4.6 Degranulation 60
4.7 Phenotype of HVCN1$^{-/-}$ neutrophils is dependent on NADPH oxidase activation 64
4.8 HVCN1$^{-/-}$ neutrophils show altered responses to alternative stimuli 66
4.9 Phenotype of HVCN1$^{-/-}$ mice in health and disease 68
5 Discussion 74
5.1 Role for HVCN1 in maintaining pH, membrane potential and ROS production 74
5.2 Pathways of enhanced NETosis in HVCN1$^{-/-}$ neutrophils 76
5.3 Mechanisms of calcium mobilization in HVCN1$^{-/-}$ neutrophils 78
5.4 The role of mitochondrial depolarization and ROS in HVCN1$^{-/-}$ neutrophils 81
5.5 Mechanisms of primary granule release in HVCN1$^{-/-}$ neutrophils 82
5.6 Phenotype of HVCN1$^{-/-}$ mice in acute inflammation 85
5.7 Potential drivers for autoimmune disorder in HVCN1$^{-/-}$ mice 89
5.8 Relevance for human disease 90
5.9 Limitations of the study 92
References 93
Appendix 106

List of Figures

Figure 1.1| Components of the innate and adaptive immune system. 2
Figure 1.2| The neutrophil life cycle. 4
Figure 1.3| Activation regulation of the NADPH oxidase. 8
Figure 1.4| Pathways of NETosis. 13
Figure 1.5| The cycle of neutrophil activation in SLE. 14
Figure 1.6| Molecular structure of HVCN1 16
Figure 1.7| Summary of the role of HVCN1 in different immune cells. 19
Figure 1.8| HVCN1 is downregulated on CD16+ cells of SLE patients. 21
Figure 4.1| HVCN1 is highly expressed on neutrophils. 42
Figure 4.2| Bone marrow neutrophils from HVCN1$^{-/-}$ mice show intracellular acidification and reduced extracellular ROS production after stimulation. 43
Figure 4.3| NET formation is increased in HVCN1$^{-/-}$ neutrophils. 44
Figure 4.4| Chromatin decondensation is accelerated in HVCN1$^{-/-}$ neutrophils. 45
Figure 4.5| Histone citrullination is increased in HVCN1$^{-/-}$ neutrophils. 47
Figure 4.6| HVCN1$^{-/-}$ neutrophils show calcium influx from intracellular and extracellular compartments after PMA stimulation. 48
Figure 4.7| Amiloride induces acidification but no calcium influx in wild type neutrophils. 50
Figure 4.8| Membrane depolarization is augmented in HVCN1$^{-/-}$ neutrophils. 51
Figure 4.9| Neutrophils express different intracellular calcium channels. 52
Figure 4.10| MitoSOX cannot be used to measure mitochondrial ROS in neutrophils. 53
Figure 4.11| Intracellular ROS is increase in HVCN1$^{-/-}$ neutrophils after stimulation. 54
Figure 4.12| Dissipation of the ΔΨm in HVCN1$^{-/-}$ neutrophils is caused by calcium release from intracellular stores. 56
Figure 4.13| No differences in mPTP opening between wild type and HVCN1$^{-/-}$ neutrophils. 57
Figure 4.14 Mitochondrial mass and fitness do not differ steady state between wild type and HVCN1$^{-/-}$ neutrophils. 58
Figure 4.15| Increased NET formation in HVCN1$^{-/-}$ neutrophils is dependent on calcium. 59
Figure 4.16| Active release of primary, but not tertiary granules, is enhanced in HVCN1$^{-/-}$ neutrophils in a calcium-dependent manner. 61
Figure 4.17| HVCN1$^{-/-}$ neutrophils form large vacuoles by pinocytosis. 62
Figure 4.18| HVCN1$^{-/-}$ phenotype is dependent on NADPH oxidase expression: analysis of HVCN1/CYBB$^{-/-}$ neutrophils. 65
Figure 4.19| HVCN1$^{-/-}$ neutrophils have a similar response to plate-bound IgG and PMA. 66
Figure 4.20| Phagocytosis and bacterial killing is unchanged in HVCN1$^{-/-}$ neutrophils. 67
Figure 4.21| No major changes in the neutrophil compartment of HVCN1$^{-/-}$ mice. 68
Figure 4.22| Aged HVCN1$^{-/-}$ mice develop mild inflammatory phenotype. 69
Figure 4.23| HVCN1$^{-/-}$ mice show augmented inflammation in a model of zymosan-induced peritonitis. 71
Figure 4.24| Pulmonary ANCA vasculitis pathology appears aggravated in HVCN1$^{-/-}$ mice. 73
Figure 5.1| Potential mechanisms of calcium mobilization from intracellular stores and extracellular space in HVCN1$^{-/-}$ neutrophils. 80
Figure 5.2| Role of HVCN1 in regulating neutrophil activation. 84

List of Abbreviations

ΔΨm	mitochondrial membrane potential
2GBI	2-guanidinobenzimidazole
8-OHdG	8-hydroxyguanosine
aa	amino acid
AATD	alpha-1 antitrypsin deficiency
AAV	ANCA-associated vasculitis
AM	acetoxymethyl ester
ANCA	anti-neutrophil cytoplasmic antibody
APC	antigen-presenting cell
BAL	Bronchoalveolar lavage
BAPTA	1,2-bis(o-aminophenoxy)ethane-*N,N,N′,N′*-tetraacetic acid
BCECF	2',7'-Bis-(2-Carboxyethyl)-5-(and-6)-Carboxyfluorescein
BCR	B cell receptor
BF	Bright field
BSA	bovine serum albumin
C. albicans	*Candida albicans*
C/EBP	CCAAT-enhancer-binding protein
CD	cluster of differentiation
cDNA	complementary DNA
CGD	chronic granulomatous disease
citH3	citrullinated histone 3
CLL	chronic lymphocytic leukemia
CM-H_2DCFDA	2',7'-Dichlordihydrofluorescein-diacetat
CMP	common myeloid progenitor
CRAC	calcium release-activated channels
CYBB	Cytochrome b(558) subunit beta
DAG	diacylglycerol
DAMPs	damage associated molecular patterns
DAPI	4′,6-Diamidin-2-phenylindol
ddH_2O	double-distilled water
DNP	dinitrophenol
dsDNA	double-stranded DNA
E. coli	*Escherichia coli*
ECAR	extracellular acidification rate
EDTA	ethylenediaminetetraacetic acid
ELISA	enzyme-linked immunosorbent assay
ER	endoplasmic reticulum
FACS	fluorescence activated cell sorting
FCCP	carbonyl cyanide-p-trifluoromethoxyphenylhydrazone
fMLP	*N*-Formylmethionyl-leucyl-phenylalanine
G-CSF	granulocyte colony-stimulating factor
GFP	green fluorescent protein
GMP	granulocyte/monocyte progenitor
GPCR	G protein-coupled receptor
GTP	guanosine-5'-triphosphate

H3	histone 3
HRP	horseradish peroxidase
HSC	hematopoietic stem cell
HVCN1	Hydrogen voltage-gated channel 1
i.p.	intraperitoneal
i.t.	intratracheal
IC	immune complex
ICAM	intercellular adhesion molecules
IFN	interferon
Ig	immunoglobulin
IL	interleukin
ILC	innate lymphoid cells
ING-II	ION Natrium Green - 2
IP_3	iositol trisphosphate
ITAMs	immunoreceptor tyrosine-based activation motifs
Itpr	inositol 1,4,5-trisphosphate receptor type
LDG	low-density granulocytes
LPS	lipopolysaccharide
LTB_4	leukotriene B4
MCU	mitochondrial calcium uniporter
MFI	mean fluorescence intensity
MHC	major histocompatibility complex
MICU1	MCU-regulating protein
MMP	matrix metalloproteinase
MPO	Myeloperoxidase
mPTP	mitochondrial permeability transition pore
NAAPD	*N,N′*-diaspartic acid-3,4,9,10-tetracarboxylic diimide
NAC	*N*-acetyl cysteine
NADPH	nicotinamide adenine dinucleotide phosphate
NADPH	nicotinamide adenine dinucleotide phosphate
NAMPs	neurodegeneration-associated patterns
NCX	sodium–calcium exchanger
NE	neutrophil elastase
NET	neutrophil extracellular trap
NFκB	nuclear factor 'kappa-light-chain-enhancer' of activated B-cells
NHE	sodium–proton exchanger
NK	natural killer
NLR	NOD-like receptor
NOD	nucleotide-binding oligomerization domain
OCR	oxygen consumption rate
ORAI1	calcium release-activated calcium channel protein 1
PAD4	peptidyl arginine deiminase 4
PAMPs	pathogen-associated patterns
PBMCs	peripheral blood mononuclear cell
PBS	phosphate-buffered saline

PFA	paraformaldehyde
PI_3K	phosphoinositide 3-kinase
PIP2	phosphatidylinositol 4,5-bisphosphate
PKC	protein kinase C
PLC	phospholipase
pLL	poly-L-lysine
PMA	Phorbol-12-myristat-13-acetat
PR3	proteinase 3
PRR	pattern recognition receptor
qPCR	real-time quantitative PCR
ROS	reactive oxygen species
RPMI	Roswell Park Memorial Institute medium
RT	room temperature
RyR	ryanodine receptor
S. aureus	*Staphylococcus aureus*
SD	standard deviation
SEM	standard error of the mean
SLE	systemic lupus erythematosus
SNARE	soluble NSF attachment receptor
SOCE	store-operated calcium entry
SOD	superoxide dismutase
STIM	stromal interaction molecule
TAN	tumor-associated neutrophils
TCR	T cell receptor
TLR	Toll-like receptor
TMRM	tetramethylrhodamine methylester
TPC	two-pore channel
TPP	triphenyl-phosphonium
TRITC	tetramethylrhodamine
TRP	transient receptor potential
VAMP	vesicle-associated membrane protein
V_m	membrane potential
VSD	voltage-sensing domain

1 Introduction

1.1 The mammalian immune system

The immune system is a complex network of organs, cells and proteins that protect the body from infectious pathogens as well as from endogenous threats such as tumor cells. Pathogens can be broadly divided into four classes, namely viruses, bacteria, fungi and parasites. All of these can kill or damage host tissue either by directly infecting and lysing cells or by producing toxins[1].

A first layer of protection against exogenous threats is provided by anatomical barriers, which in mammals are the skin or the epithelial layer of the lungs and intestines[2–4]. These physical barriers are further supported by a chemical defense through secretion of antimicrobial agents or mild acidosis. Additionally, these barrier organs are often colonized by commensal microorganisms, the microbiome. Commensals are generally not harmful, but rather support the host by aiding digestion, providing vitamins and amino acids, or training the immune system. In addition, commensals protect the barrier organs from colonization by pathogens[5].

Once a pathogen has overcome these barriers, it encounters a variety of different immune cells called white blood cells or leukocytes. Most of these cells arise from pluripotent hematopoietic stem cells in the bone marrow, where they also differentiate and mature. The exception are tissue-resident macrophages, which originate from the embryonic yolk sac or fetal liver and colonize tissues before birth. Mature immune cells enter the bloodstream, reside in peripheral tissues and circulate back into the blood via lymphatic vessels. The first line of cellular defense is the innate immune system (Fig. 1.1, left), which includes macrophages, dendritic cells, granulocytes, mast cells, and natural killer (NK) cells[1]. Among these cells, neutrophil granulocytes, in short neutrophils, are the first cells at the site of infection and are critical for rapid containment of pathogenic invaders[6]. All innate immune cells express a set of innate recognition receptors, also called pattern recognition receptors (PRRs), that enable them to recognize specific molecular patterns associated with foreign threats or tissue damage. Accordingly, these motifs are referred to as pathogen-, danger-, and neurodegeneration-associated patterns (PAMPs, DAMPs, and NAMPs)[7]. Immune cells activated via PRRs can ingest whole pathogens or directly destroy them through the release of antimicrobial peptides, lytic enzymes or reactive oxygen species (ROS)[8]. Furthermore, activated cells release chemokines and cytokines that propagate the immune response by attracting and activating additional immune cells[1]. Another key element of the innate immune response is the complement system[9]. It includes over 30 different plasma proteins, that circulate through the body in their inactive form and get activated through proteolytic cleavage in the presence of pathogens. Different proteins of the complement system can act as chemoattractants, opsonize pathogens for phagocytosis or directly induce lysis of pathogens by forming a membrane pore.

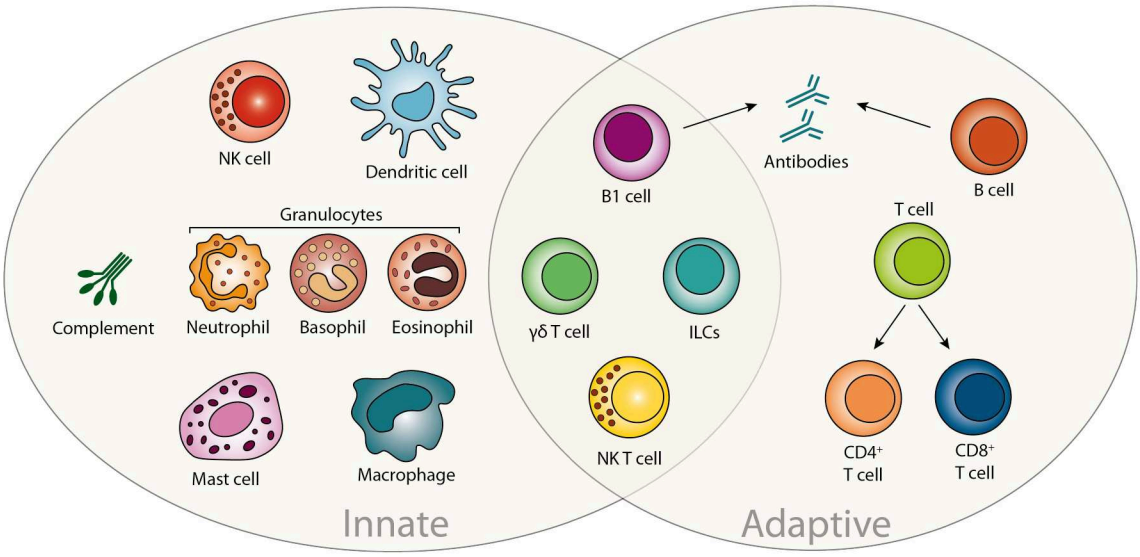

Figure 1.1| Components of the innate and adaptive immune system.
Cells of the innate immune system (left) are able to rapidly respond to invading pathogens by sensing distinct molecular patterns. Their effector functions enable them to kill pathogens through phagocytosis and release of toxic agents. Furthermore, the proteins of the complement system are activated in the presence of pathogens and mediate chemotaxis, opsonization or lysis of pathogens. Cells of the adaptive immune system (right) have a slower but highly specific response as they can recognize pathogens via uniquely recombined receptors. Activated B cells produce antibodies that can opsonize and neutralize pathogens. Some immune cell types cannot be clearly assigned to either the innate or the adaptive immune system, as they exhibit both innate and adaptive characteristics. These include B1 cells, γδ T cells, innate lymphoid cells (ILCs) and natural killer T cells (NK T cells). Modified from Dranoff (2004)[10].

Compared to the innate immune system, the adaptive immune system reacts more slowly but highly specifically to infectious agents (Fig 1.1, right). The two most important cell types of the adaptive immune system are B lymphocytes and T lymphocytes, shortly called B cells and T cells. Both express highly variable antigen receptors that enable them to recognize a very specific molecular structure. Each lymphocyte carries a unique receptor variant that results from somatic recombination of the variable region of the respective antigen receptor gene[11,12]. The B cell receptor (BCR) is composed of a membrane immunoglobulin (Ig) linked to an intracellular signaling domain and it directly recognizes specific moieties of naïve antigens, called epitopes. Upon stimulation of the BCR, naïve B cells proliferate and differentiate into plasma cells, which secrete soluble immunoglobulins also called antibodies[13]. Although T cell receptors (TCRs) are related to BCRs, they cannot recognize antigens on their own, but respond only to antigen-derived peptides presented by other cells on so-called major histocompatibility complex (MHC) molecules. Peptides of degraded antigens can originate from intracellular pathogens or from pathogens taken up by other immune cells such as macrophages, dendritic cells or B cells[14]. These cells are therefore also referred to as antigen-presenting cells (APCs). Stimulation of the TCR induces proliferation and differentiation of T cells into effector T cells, which can be broadly divided into three classes: cytotoxic $CD8^+$ T cells, $CD4^+$ helper T cells, and regulatory T cells. $CD8^+$ T cells can kill infected cells and cancer cells, whereas $CD4^+$ support the function of $CD8^+$ T cells and B cells. Regulatory T cells can identify and suppress immune cells directed against host antigens and are therefore critical for maintaining self-tolerance and preventing autoimmune

responses[15]. Activated B and T cells can also differentiate into memory cells that can trigger a more rapid and robust immune response upon a second encounter with the same pathogen[16].
In addition to the classical division into innate and adaptive immune cells, some cell types combining innate and adaptive properties have been identified. Among these cells are B1 cells, γδT cells, NK T cells or innate lymphoid cells (ILCs)[17] (Fig. 1.1, middle).

1.2 Neutrophils

Neutrophils are the most abundant immune cells in human blood. They account for 70 % of all circulating leukocytes in humans and about 20 - 30 % in mice[18]. Because of their high numbers and relatively short half-life, they are constantly produced and released from the bone marrow[19]. When released into the circulation, neutrophils are already equipped with a variety of enzymes and proteins that enable them to rapidly migrate to sites of infection and effectively kill invading pathogens. Their fundamental role in antimicrobial defense is best exemplified by patients with neutropenia, who are susceptible to infection[20]. However, their cytotoxic effect can also damage healthy tissues, as is the case in many inflammatory diseases such as inflammatory bowel disease, rheumatoid arthritis, or acute respiratory distress syndrome[21–23].
Due to their short lifespan and limited potential for protein synthesis, neutrophils have long been described as a homogeneous cell population. However, recent studies suggest that neutrophils are more heterogeneous and their phenotype varies depending on their age or on the physiological or pathological environment, such as infection, injury, cancer, or autoimmunity[24].

1.2.1 Neutrophil development

Granulopoiesis occurs in the hematopoietic strands of the bone marrow (Fig. 1.2). Here, self-renewing hematopoietic stem cells (HSCs) develop into multipotent progenitor cells, which in turn develop into common myeloid progenitor cells (CMPs) and subsequently into granulocyte/monocyte progenitor cells (GMPs). Stimulated by the granulocyte colony-stimulating factor (G-CSF), GMPs differentiate over a continuum of maturation steps from a mitotic pool of granulocyte-committed progenitors (myeloblasts, promyelocytes, myelocytes) to a postmitotic pool (metamyelocytes, ribbon cells) to mature segmented neutrophils[25]. This classification of human granulopoiesis was developed on the basis of morphological features such as nuclear shape and granule content and therefore does not take into account functional properties. More recent studies have used single-cell techniques to assess human granulopoiesis and have succeeded in redefining early, intermediate, and late neutrophil progenitors based on gene and transcription factor signatures[26]. At the same time, Evrard and colleagues[27] were able to detect a similar subset of neutrophil precursors in mouse bone marrow.
G-CSF was identified as the main stimulator of granulopoiesis as mutation or deletion of its receptor, CSF3R, leads to severe neutropenia in humans and mice[28,29]. Under steady state

conditions, G-CSF expression is regulated by the IL-23/IL-17/G-CSF axis[30]. Upon phagocytosis of apoptotic neutrophils, macrophages and dendritic cells produce less IL-23, which in turn leads to reduced IL-17 production by T cells. Since IL-17 positively regulates G-CSF, a suppression of this cytokine results in reduced granulopoiesis. Further factors that drive neutrophil differentiation are IL-6, GM-CSF and IL-3[31–33].

The commitment to the myeloid linage is mainly driven by the action of the transcription factors PU.1 and CCAAT-enhancer-binding protein α (C/EBPα), which is induced by G-CSF[34,35]. Both these transcription factors are also essential for further differentiation of GMPs as different ratios of C/EBPα to PU.1 can induce commitment to either the granulocytic or the monocytic lineage[36]. Terminal differentiation of neutrophils is also regulated through transient expression of C/EBPε and Gfi-1 and steadily increasing expression of C/EBPβ and C/EBPδ towards the fully mature state[19].

The different stages of granulopoiesis are accompanied by the formation of different types of neutrophil granules. The generation of azurophilic (primary) granules starts during the pre-neutrophil stage followed by the generation of specific (secondary) granules at the immature neutrophil stage and finally the generation of gelatinase (tertiary) granules[37].

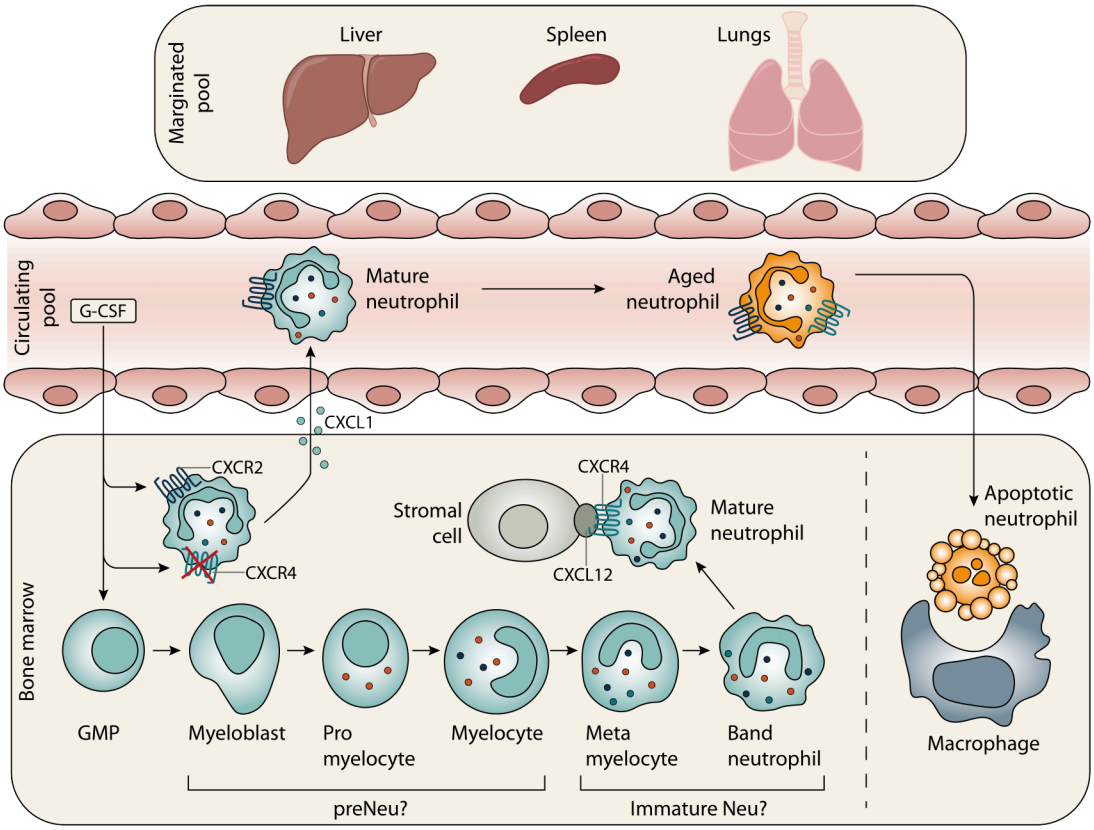

Figure 1.2| The neutrophil life cycle.
Neutrophils develop and mature in the bone marrow. Stimulated by G-CSF, granulocytes/monocyte progenitors develop over a continuum of different maturation states into mature neutrophils. Retention of immature and mature neutrophils is mediated by the interaction of CXCR4 on neutrophils and CXCL12 on bone marrow stromal cells. When neutrophils are mobilized, G-CSF induces downregulation of the homing receptor CXCR4 and upregulation of CXCR2. Sensing chemokines in the blood through CXCR2 induces neutrophil egress from the bone marrow. Neutrophils then circulate through the body and also transition through the intravascular compartment of liver, lungs and spleen. In case neutrophils are not recruited to a site of infection, they age in circulation and are recruited back into the bone marrow, where they are removed by macrophages.

Pathologic conditions which demand enhanced output of neutrophils can trigger emergency granulopoiesis. Here, release of granulopoietic cytokines by other immune cells or direct sensing of pathogens by HSCs induce an enhanced differentiation of neutrophils controlled by the transcription factor C/EBPβ[38].

1.2.2 Neutrophil mobilization and trafficking

The retention and release of neutrophils from the bone marrow is regulated through the chemokine receptors CXCR4 and CXCR2[39] (Fig. 1.2) . Immature neutrophil express high levels of CXCR4 and are thereby retained in the bone marrow through binding to CXCL12, which is expressed on osteoblasts and other stromal cells. Mature neutrophils only express low levels of CXCR4 and upregulate CXCR2. Therefore, G-CSF can induce neutrophil mobilization through the downregulation of CXCL12 on bone marrow stromal cells[40] and production of CXCR2 ligands such as CXCL1, CXCL2, CXCL5, and CXCL8 in the periphery. Furthermore, CXCL12 expression is regulated in a circadian manner through activation of the sympathetic and parasympathetic system. Downregulation of CXCL12 during the day is associated with increased neutrophil mobilization[41,42].

However, not all mature neutrophils egress the bone marrow immediately. Intravital imaging revealed that in mice, neutrophils cluster in CXCL12-expressing niches around the vasculature forming a reservoir[27] whose number of cells is 300-fold higher compared to the number of neutrophils in the blood[43].

Once mobilized into the circulation, neutrophils distribute throughout the body where they either remain in the circulating pool or transition to the marginated pool (Fig. 1.2). The marginated pool refers to all neutrophils which are located within the intravascular compartment of mainly bone marrow, spleen, liver or lung[44–46]. It is still unclear whether the retention of neutrophils in organs is an active process regulated by adhesion molecules or whether they are passively slowed down by mechanical constriction in very small vessels[47]. Of note, adrenalin or physical exercise can lead to recruitment of marginated neutrophils back into the circulation[20].

While circulating, neutrophils are constantly probing the endothelial cell layer for signs of inflammation. In case of injury or inflammation in the underlying tissue, endothelial cells can be activated by PAMPs or cytokines and upregulate adhesion molecules, such as selectins or integrins, on their luminal site[48]. Selectins on the endothelium will slow down and tether L-selectin or P-selectin glycoprotein 1-expressing neutrophils, which start to "roll" along the vessel wall[49]. During rolling, neutrophils are activated by selectin signaling as well as through sensing chemokines bound to endothelial cells. This in turn leads to activation and clustering of β1 integrins (mainly LFA-1 and Mac-1) in neutrophils, which can then bind to ICAMs on the endothelium and mediate arrest[50,51]. After adhering firmly, neutrophils start to spread and crawl along the vessels to find sites that allow transmigration[52]. A complex interaction between

integrins and endothelial junction molecules navigates the neutrophils' paracellular extravasation. In a minority of cases, neutrophils can also pass the endothelium through the transcellular route. Below the endothelial lining, neutrophils must furthermore cross the basement membrane, a protein network mostly consisting of laminin and collagen. This process is not fully understood yet, but it is thought that there are regions less dense in matrix proteins, which allow cells to pass through[53]. Within the tissue, neutrophils then follow a gradient of chemokines and pathogen-derived chemoattractants to find the exact site of inflammation. The highly direct and coordinated migration of many neutrophils and their accumulation at sites of inflammation and injury are termed "neutrophil swarming"[6].

1.2.3 Neutrophil ageing and clearance

In the absence of inflammation, neutrophils remain in the circulation for about 6 – 12 hours. During this period, they undergo several phenotyping changes, a phenomenon called neutrophil ageing[54,55], which is controlled by an intrinsic circadian process via the clock gene *Bmal1*[56]. There are conflicting observations regarding the inflammatory potential of aged neutrophils. One the one hand, diurnal changes in transcription have been shown to cause loss of the ability to migrate to inflammatory sites and promote "programmed disarming" of aged neutrophils, characterized by loss of granule proteins and the ability to undergo NETosis[57]. Conversely, aged neutrophils have been also shown to migrate more rapidly to sites of inflammation, where they exhibit an enhanced phagocytic activity compared to non-aged neutrophils[58].

During the ageing process, neutrophils loose CD62L expression and upregulate CD11b and CXCR4[55]. The latter mediates their homing to the bone marrow where aged neutrophils undergo apoptosis and are cleared by macrophages[59]. Besides the bone marrow, apoptotic neutrophils can also be cleared by tissue-resident macrophages of the liver and the spleen, however this interaction is likely not mediated by CXCR4 expression (Fig. 1.2).

1.2.4 Neutrophil heterogeneity

Since neutrophils were traditionally described as short-lived cells with defined intra- and extracellular markers, reduced RNA content and limited capacity for protein synthesis, they were considered to be a homogenous cell population. In contrast to other immune cells, such as macrophages or lymphocytes, neutrophil diversity has just recently been studied in more detail. Three main factors seem to influence the neutrophilic phenotype and contribute to heterogeneity: (I) maturation state and age, (II) disease and (III) tissue localization.

Neutrophil aging is the primary cause of heterogeneity among neutrophils in the circulation. As described previously, they can be differentiated from mature neutrophils by a specific gene signature and proteomic composition. In addition, as a consequence of emergency granulopoiesis, immature neutrophils may be present in the circulation of patients with acute and chronic inflammatory diseases. They appear to have superior killing ability, suggesting a useful function

in acute bacterial infections[60,61]. On the other hand, increased frequency of hyper reactive immature neutrophils seems to be a pathological feature of acute COVID-19[62] or systemic lupus erythematosus[63] (also see 1.4). High numbers of circulating immature neutrophils are also associated with poor clinical outcome in sepsis because of limited phagocytic abilities but increased production of proinflammatory cytokines[64,65].

Different subsets were also found among tumor-associated neutrophils (TANs). Similar to macrophages, TANs show polarization towards a pro- or anti-tumorigenic phenotype[66]. Neutrophils with anti-tumorigenic function are able to kill tumor cells directly or to support and attract other anti-tumorigenic immune cells[67,68]. Pro-tumorigenic neutrophils were shown to support angiogenesis and invasion by secretion of granular matrix metalloproteinases and serine proteases[69,70]. The dual function of neutrophil granulocytes appears to be dependent on disease stage, as depletion of neutrophil granulocytes in early stages is detrimental to disease progression, whereas depletion in later stages appears to be beneficial[71].

For a long time, it was believed that neutrophils did not reside in healthy tissue. However, recent studies in mice showed that neutrophils actively infiltrate various organs under steady-state conditions[72,73]. Neutrophils also acquired tissue-specific transcriptional programs that were even reflected in differences in open chromatin[73]. There is some evidence that neutrophils also exert tissue-specific functions. In lung and intestine, neutrophils were shown to express genes that support vascular and axonal growth. In addition, a subset of neutrophils with B cell-stimulatory properties has been identified in the human spleen[74]. Whether these homeostatic neutrophil subsets are truly important for proper tissue function remains to be further investigated.

The concept of neutrophil heterogeneity is still relatively new, therefore further research is needed to understand the biological significance of neutrophil subsets and to define the mechanisms that may give rise to different neutrophil programs.

1.3 Neutrophil effector functions

Neutrophils are considered the first line of defense because they can rapidly trap and destroy invading pathogens in a sophisticated manner. To this end, they are equipped with various receptors that recognize bacteria and fungi. For direct sensing of pathogens, neutrophils express different pathogen recognition receptors (PPRs) such as Toll-like receptors (TLRs), nucleotide-binding oligomerization domain-like receptors (NOD-like receptors, NLRs) and C-type lectin receptors. Sensing of pathogens that are opsonized with antibodies or complement proteins is mediated by Fc receptors, complement receptors or integrins[75].

Activation of these receptors either induces phagocytosis of the respective pathogen or causes the release of various toxic molecules and proteins such as reactive oxygen species (ROS), proteases or antimicrobial peptides. As a last resort to scavenge and kill extracellular pathogens, neutrophils

undergo a special form of inflammatory cell death called NETosis (NETs, neutrophil extracellular traps).

1.3.1 ROS production by the NADPH oxidase

The production of ROS plays a central role in the antimicrobial defense of neutrophils. ROS have a direct antimicrobial activity[76,77] but can additionally enhance neutrophil activation by regulation of degranulation, NET formation and cytokine release[78–80]. The majority of ROS in neutrophils is generated by the nicotinamide adenine dinucleotide phosphate (NADPH) oxidase. This multi-subunit enzyme can assemble at the plasma membrane for the generation of extracellular ROS or at the membrane of phagosomes. The importance of ROS for the antimicrobial defense is exemplified by patients suffering from Chronic Granulomatous Disease (CGD), which is caused by mutations in genes that encode different components of the NADPH oxidase. CGD patients suffer from a severe immunodeficiency syndrome which makes them susceptible to recurrent and potentially life-threatening infections, especially in infancy[81,82].

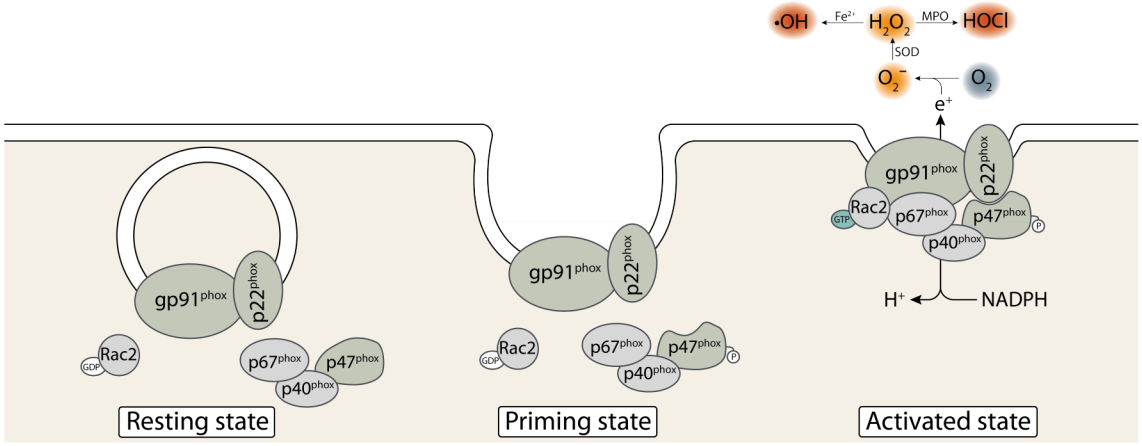

Figure 1.3| Activation regulation of the NADPH oxidase.
In resting neutrophils, the membrane-bound components of the NADPH oxidase are located in intracellular stores and the regulatory components are located in the cytoplasm. Priming of neutrophils leads to transport of gp91^{phox}/p22^{phox} to the plasma membrane. Moreover, the regulatory component p47^{phox} gets phosphorylated. Upon stimulation, the NADPH complex fully assembles and catalyzes the transfer of electrons from NADPH across the membrane onto oxygen, which generate superoxide (O_2^-). Superoxide is very instable and quickly reacts to hydrogen peroxide (H_2O_2) which can be further converted into hypochlorous acid (HOCl) or hydroxly radicals (• OH).

Structurally, the NAPDH oxidase is composed of five subunits: gp91^{phox}, p22^{phox}, p40^{phox}, p47^{phox}, and p67^{phox} (Fig. 1.3). Prior to neutrophil activation, gp91^{phox} and p22^{phox} form a membrane-bound heterodimer also known as flavocytochrome b558 (cytb588). Upon activation, p22^{phox} serves as docking site for the other regulatory subunits, which are located in the cytoplasm during the resting state. gp91^{phox} is the catalytic subunit that facilitates the transfer of electrons from intracellular NADPH across the membrane and onto molecular oxygen to generate superoxide (O_2^-). In addition, the small GTPase Rac2 needs to be recruited in order to allow full activation of the oxidase[83].

The assembly and activation of the NADPH oxidase is tightly regulated through translocation and phosphorylation of the different subunits. Therefore, different stimuli can either induce priming

or direct activation of the oxidase. Priming is signaled through TLRs, cytokine or complement receptors and is characterized by increased expression of $gp91^{phox}$ on the plasma membrane, partial phosphorylation of $p47^{phox}$ or rearrangement of the cytoskeleton facilitating subunit translocation[84]. These changes allow for a faster and more robust ROS production upon stimulation with a second stimulus. Direct activation of the NADPH oxidase can be triggered by the bacterial chemotactic peptide *N*-Formylmethionyl-leucyl-phenylalanine (fMLP), by Fc receptor or integrin signaling[85–87].

Depending on its localization, activation of the NADPH oxidase leads to generation of superoxide in the extracellular space or in phagosomes. Superoxide is a very reactive molecule that rapidly undergoes dismutation to hydrogen peroxide (H_2O_2). H_2O_2 can oxidize ferrous iron generating highly reactive hydroxyl radicals (OH·). Furthermore, the granule protein myeloperoxidase (MPO) can convert H_2O_2 into hypochlorous acid (HOCl)[88]. Both OH· and HOCl are bactericidal by damaging bacterial DNA, proteins and lipids (Fig. 1.3).

1.3.2 Degranulation

Neutrophils harbor four different classes of preformed cytoplasmic granules. Each of them contains a specific set of proteins that can facilitate migration, ROS production or bacterial killing[89]. Depending on the time they are formed during neutrophil maturation, they are called primary, secondary and tertiary granules[37].

Primary, or azurophilic, granules mostly contain antimicrobial peptides such as MPO, neutrophil elastase (NE) or lysozyme[90]. Azurophilic granules can either fuse with the plasma membrane, releasing their content into the extracellular space or fuse with phagosomes to kill engulfed pathogens[91]. Secondary and tertiary granules are also called specific or gelatinase granules, respectively. They share similar content, but can be distinguished based on the presence of lactoferrin and lipocalin in specific granules and the presence of matrix metalloproteinase 9 (MMP-9) in gelatinase granules[89]. The fourth class is called secretory vesicles, and is formed at a very late stage of neutrophil maturation through endocytosis. Therefore, they contain many membrane proteins including cytokine receptors, NADPH oxidase subunits and adhesion molecules[92].

Influx of calcium is required to induce degranulation, and release of each granule type requires different intracellular calcium levels[93]. Therefore, release of different granule types is dependent on the strength of stimulation. Secretory vesicles are already mobilized in response to weak stimulation which leads to exposure of adhesion molecules and chemokine receptors and can be considered as a priming step. Degranulation of specific and gelatinase granules requires stronger stimuli. Finally, degranulation of azurophilic granules requires very strong stimulation by direct activation via integrins or Fc receptors or a biphasic stimulation with a priming and an inducing stimulus.

The exact molecular mechanism underlying the differential degranulation is not fully understood. Possible factors could be the engagement of different members of the Src kinase family or the involvement of different SNAP receptors (SNAREs) and vesicle associated membrane proteins (VAMPs) that facilitate the docking and fusion of the granules with the membrane[85,94].

Many soluble granule proteins not only have a bactericidal effect, but also support neutrophil function and activity. Granule serine proteases, for instance, help degrading extracellular matrix components, in order to facilitate neutrophil migration. Furthermore, they can cleave cytokines to induce their degradation or, conversely, cleave immature cytokines to activate them[95]. Some granule proteins may also regulate neutrophil survival or clearance. While membrane-bound proteinase 3 (PR3) can serve as a "don't eat me" signal[96], lactoferrin can stimulate macrophages to phagocytose apoptotic neutrophils and produce IL-10 to facilitate the resolution of inflammation[97]. Last but not least, granule proteins play a crucial role during formation of NETs (see 1.3.4).

1.3.3 Phagocytosis

Neutrophils are professional phagocytes, therefore they can ingest larger particles (> 0.5 μm) such as apoptotic cells, foreign substances or microorganisms. Phagocytosis of bacteria or fungi is initiated through binding of an opsonized pathogen to Fc or complement receptors but can also be initialed through binding to PRRs. However, most studies focused on the mechanisms of Fc receptor-mediated phagocytosis.

The binding of the antibody-opsonized pathogen to Fc receptors elicit the formation of a membrane raft enriched in other Fc receptors, special phospholipids and kinases, required for efficient phagocytosis[98]. Phosphorylation of immunoreceptor tyrosine-based activation motifs (ITAMs) by Src kinases induces downstream signaling through Syk and PI3K/PLCγ[99]. Finally, different Rho GTPases are activated and induce actin polymerization which is required for the formation of membrane protrusions around the pathogen[100]. Eventually, these protrusions fuse at the distal end and detach from the plasma membrane to form the closed phagosome. In comparison to other professional phagocytes like macrophages, phagosome formation in neutrophils is a very fast process and happens within 30 seconds after sensing the pathogen[101].

Once the phagosome has formed around the pathogen, it undergoes a maturation process. In neutrophils, this process differs a lot from the phagosomal maturation process in other cells. Phagosomal maturation in macrophages is driven by sequential fusion of the phagosome with endosomes and lysosomes which leads to a gradual acidification and enrichment of hydrolases[102]. In neutrophils, however, this process is mediated by fusion with granules, which leads to the accumulation of antimicrobial components. The NADPH oxidase also localizes to the phagosome and facilitates intraphagosomal ROS production[100]. Despite the fusion with acidic granules, the pH in neutrophil phagosomes remains transiently neutral due to high proton consumption during the

dismutation of superoxide to H_2O_2. Furthermore, activation of the NADPH oxidase seems to inhibit the recruitment of the vacuolar H^+-ATPase[103]. The neutral pH in neutrophil phagosomes is thought to be important for sustaining the enzymatic activity of proteases such as cathepsin G or NE, which have an optimum around pH 8[104]. After the intraphagosomal oxidative burst has receded, the neutrophil phagosome acidifies and eventually fuses with lysosomes for final degradation.

1.3.4 Neutrophil Extracellular Traps

In 2004, Brinkmann et al.[105] were the first to report that neutrophils are capable of releasing decondensed chromatin fibers coated with granule proteins, a feature that they termed neutrophil extracellular traps (NETs). These extracellular structures can immobilize and kill pathogens, and are therefore an important part of the neutrophil immune response. In a follow-up study, NETosis was defined as the lytic cell death pathway leading to the formation of NETs[79]. Besides that, neutrophils also exhibit a rapid form of NET release which does not require death of the neutrophil, and is therefore called "vital" NETosis[106].

NET formation was shown to be induced by various different pathogens, immune complexes, biochemical stimuli, or bacterial toxins[107]. The underlying molecular and cellular dynamics can be broadly classified into a NADPH oxidase-dependent pathway and a NADPH oxidase-independent pathway. While the pathways are fairly well defined when activated with phorbol esters or bacterial toxins, it appears that different microbes can trigger either one of the two pathways or a combination of both[108]. Much research has been done to characterize the mechanisms underlying NET formation, but there are still many open questions and controversies surrounding this process.

1.3.4.1 Phases of NETosis

NETosis can be induced by various triggers, however, which signals trigger NETosis instead of phagocytosis or degranulation is still largely unknown. One possible determinant could be the size of the pathogen. Larger pathogens cannot be phagocytosed and ROS production occurs at the plasma membrane, resulting in prolonged NFκB signaling[109]. Small pathogens, on the other hand, can be taken up, causing enzymes important for the induction of chromatin decondensation to be sequestered in the phagosome, instead of migrating to the nucleus[110]. However, also small pathogens were shown to induce NET formation, hence size cannot be the only determinant. Some studies also report the spontaneous formation of NETs *ex vivo* which seems to be dependent on length of cultivation[111], serum conditions[112] or pH[113]. Spontaneous NETosis is also enhanced in diseases associated low-density granulocytes (LDGs) in comparison with high-density granulocytes from the same donor[114].

After activation *in vitro*, neutrophils adhere firmly and begin to spread. When NETosis is initiated, the cytoskeleton is disassembled within the first hour after stimulation, resulting again in

rounding of the cell[115,116]. Actin filament disassembly was proposed to be important for nuclear translocation of NE and to later allow the release of decondensed DNA into the extracellular space[116,117]. Microtubules are also disassembled, however, this does not appear to be critical because pharmaceutical inhibition or stabilization of microtubules has no effect on NETosis[115]. At the same time, the nucleus begins to lose its characteristic lobular shape as the lamin B receptor is lost and heterochromatin detaches[118].

Subsequently, decondensation of chromatin begins, which - depending on the underlying mechanism - is mediated by various enzymes either through histone modifications or direct histone cleavage. In order for chromatin to be released into the cytosol, the nuclear envelope must be disintegrated. Lamins are filament proteins that support the integrity of the nuclear envelope[118]. During NETosis, lamins can either be cleaved directly[119] or can be phosphorylated[120] and subsequently disassembled, leading to nuclear envelope instability. In addition, even before rupture, the nuclear envelope can be permeabilized by gasdermin D. This pore-forming protein can be cleaved by NE and thereby activated[121]. Gasdermin D pores in the nuclear membrane would then allow further proteases to access chromatin. Finally, nuclear rupture is thought to be a passive event caused by entropic pressure generated by the "swelling" of decondensed chromatin[115].

Gasdermin D is also thought to form pores in the plasma membrane leading, to gradual permeabilization of the neutrophil[116]. The plasma membrane is further weakened by degradation of the cortical actin cytoskeleton and eventually ruptures under the force caused by chromatin swelling[115].

1.3.4.2 NADPH oxidase-dependent pathway

Early publications on NETosis already describe the importance of NADPH oxidase-generated ROS for NETosis. Fuchs et al.[79] showed that inhibition of the oxidase significantly decreased NET formation induced by phorbol-12-myristat-13-acetat (PMA) and *S.aureus*. Accordingly, neutrophils from CGD patients were unable to undergo NETosis in the same setting. Addition of H_2O_2, however, induced NET formation in both healthy and CGD neutrophils. One mechanism through which ROS can induce NETosis is their potential to promote dissociation of the azurosome (Fig. 1.4, left). This protein complex resides on the membrane of primary granules of resting neutrophils and consists of MPO, NE, PR3, azurocidin, cathepsin G, defensin-1, eosinophil cationic protein, lysozyme, and lactoferrin. In the presence of H_2O_2, the azurosome disassembles and MPO mediates the release of proteases, especially NE, into the cytosol[117]. NE can then cleave actin, a process known to be important for subsequent swelling of chromatin. NE translocates further into the nucleus where it cleaves histones, leading to decondensation of the chromatin. At later stages, MPO also translocates into the nucleus, and its binding to chromatin further enhances decondensation independently of its peroxidase function[122]. In addition, excessive DNA damage

by ROS and subsequent DNA repair mechanism also appear to promote decondensation on the chromatin[123].

The NADPH oxidase-dependent signaling pathway can be triggered, for example, by phorbol esters, lipopolysaccharide, *C. albicans*, or *S. aureus*.

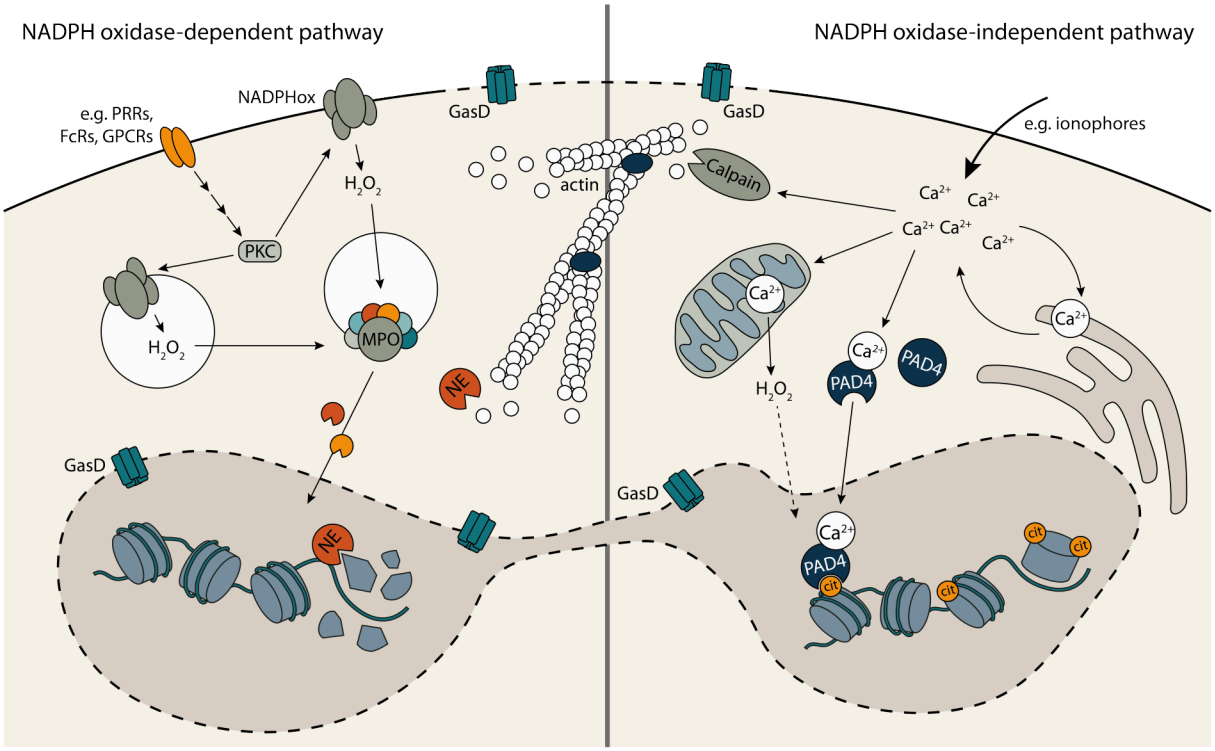

Figure 1.4| Pathways of NETosis.
The ROS-dependent NETosis pathway (left) can be triggered through various receptors expressed by neutrophils. They all converge to activation of the protein kinase C, which can also be directly activated by PMA. PKC strongly activates the NADPH oxidase, which produces ROS. It is hypothesized that ROS induces the disassembly of the azurosome in primary granules whereupon neutrophil elastase is release into the cytosol. NE can degrade the actin cytoskeleton and can localize into the nucleus where it degrades histones. Degradation of histones leads to decondensation of the chromatin. In contrast, the ROS-independent NETosis pathway is induced by influx of calcium. Following, the calcium-activated enzymes calpain and PAD4 mediate actin degradation or chromatin decondensation, respectively. Furthermore, calcium leads to ROS generation in mitochondria which presumably also supports chromatin decondensation. Gasdermin D can form pores in the nuclear and plasma membrane, a mechanism needed for entry of enzymes into the nucleus as well as permeabilization preceding final bursting of the cell.

1.3.4.3 NADPH oxidase-independent pathway

More recent publications demonstrated that some molecules and pathogens can induce NET formation independently of ROS production and subsequent recruitment of NE and MPO to the nucleus. A key feature of this NADPH oxidase-independent pathway of NETosis is a great influx of calcium into the cytoplasm (Fig. 1.4, right). These high levels of calcium induce the activation of the peptidyl arginine deiminase 4 (PAD4), which subsequently translocates to the nucleus and mediates citrullination of histones, mainly histone 3 (H3)[124,125]. As PAD4 converts the positively charged arginine in histones to a neutral citrulline residue, the ionic bond between the histones and the DNA is disrupted and the chromatin decondenses. This process is faster in comparison to chromatin decondensation induced by NE[126]. High levels of calcium were also shown to activate

the cytoplasmic protease calpain, which synergizes with PAD4 in facilitating chromatin decondensation and additionally degrades the actin cytoskeleton[119,127].

Although this pathway does not seem to require ROS production by the NADPH oxidase, it appears that mitochondrial ROS production is needed[128].

The NADPH oxidase-independent signaling pathway can be triggered, for example, by calcium ionophores such as ionomycin, lipopolysaccharide, soluble immune complexes, or monosodium urate crystals[126,129,130].

1.4 Neutrophils in autoimmune diseases

The various effector functions of neutrophils enable them to effectively kill pathogens. However, if these functions are not tightly regulated, they can often cause damage to host tissues. Uncontrolled neutrophil activation has been found in many serious pathologies ranging from acute inflammation to chronic inflammatory and autoimmune diseases. The role of neutrophils in autoimmunity is of particular interest, because neutrophils not only promote inflammation but also contribute to its etiology by providing autoantigens.

Systemic lupus erythematosus (SLE) is a chronic systemic autoimmune disease that affects nearly all organs, but especially joints, skin, brain, kidneys and blood vessels. It is characterized by dysregulation of both innate and adaptive immune cells[131], leading to the production of antinuclear antibodies, i.e., autoantibodies directed against self-DNA or ribonucleoproteins[132]. The nuclear autoantigens are provided by apoptotic cells or NETotic neutrophils, which are not fully cleared by macrophages[133,134]. Autoantibodies and their antigens form immune complexes (ICs), which either directly activate neutrophils or are taken up by dendritic cells. In dendritic cells, ICs stimulate TLR9 signaling and lead to the production of IFNα[135], which then primes neutrophils for NETosis in response to autoantibodies and ICs. Thus, a hallmark of SLE is the vicious cycle of autoantigen release, IFN production and neutrophil activation[136] (Fig. 1.5). Recently, it was

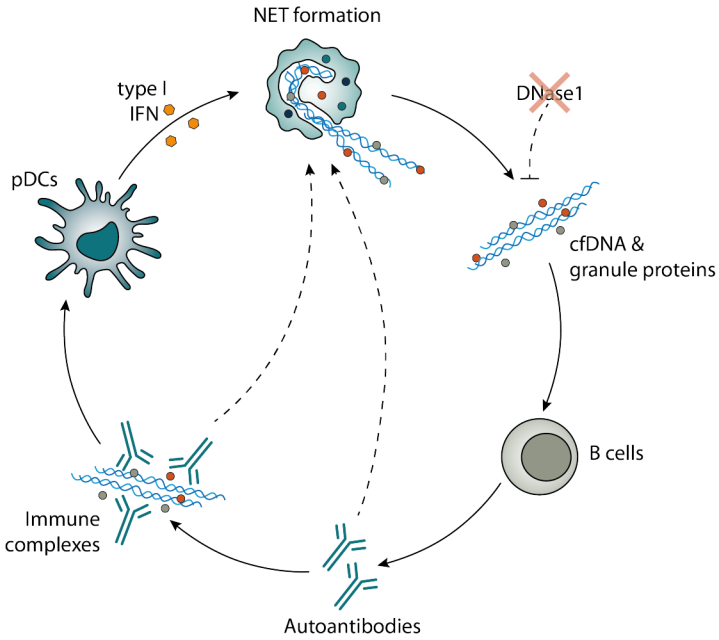

Figure 1.5| The cycle of neutrophil activation in SLE.
SLE patients show a decrease in DNase activity leading to the accumulation of NETs which can stimulate autoreactive B cells to produce autoantibodies against DNA and granule proteins. Autoantibodies and NETs can form immune complexes that damage host tissue, e.g. the kidneys. In addition, immune complexes can stimulate plasmacytoid dendritic cells (pDCs) to produce type I interferons. These cytokines are known to prime neutrophils for NETosis creating an inflammatory feedforward cycle. Modified from Apel *et al.* (2018)[136]

demonstrated that NETosis induced by ICs is supported by mitochondrial ROS production. Moreover, IC-induced NETs were enriched in oxidized mitochondrial DNA, which triggered a strong interferon response in peripheral blood mononuclear cells (PBMCs)[137]. Also characteristic of SLE is the presence of low-density granulocytes (LDGs). This subset of neutrophils is phenotypically immature and has a higher inflammatory capacity. They contribute to disease progression by releasing more inflammatory cytokines and are prone to spontaneous NETosis[114]. Therefore, the frequency of LDGs correlates positively with disease activity and is associated with an interferon-induced gene signature[138,139].

Another autoimmune disease associated with increased neutrophil activation is anti-neutrophil cytoplasmic antibody (ANCA)-associated vasculitis (AAV)[140]. Although the primary cause of the disease is still unclear, the presence of autoantibodies to the neutrophil granule proteins PR3 and MPO appears to be the central mechanism of the pathology. Neutrophils activated by ANCAs generate ROS and degranulate[141]. Moreover, primed neutrophils also undergo NETosis upon ANCA stimulation[142]. Similar to SLE, AAV patients have high numbers of LDGs that spontaneously form NETs containing MPO and PR3, providing additional autoantigens[143,144]. And indeed, vascular injury appears to be a direct consequence of increased neutrophil cell death and NET formation[145]. Elevated LDG levels are also associated with high disease activity and lower response to treatment[143].

1.5 The hydrogen voltage-gated channel 1

Since their identification in snail neurons in 1982[146], proton channels have been studied extensively in a variety of cell types. However, it was not until 2006 that two groups succeeded in cloning the genes for voltage-gated hydrogen channel 1 (HVCN1) in humans and mice[147,148], allowing more sophisticated studies of its molecular properties, regulation and function in different cell types. Research was further facilitated through the development of a HVCN1 knockout mouse line, providing a valuable alternative to pharmacological inhibition of the channel[149]. So far, no proton currents have been detected in any cell type isolated from HVCN1 knockout mice, indicating that HVCN1 is the only proton channel in mice.

Since its cloning, HVCN1 has been subject of an increasing number of studies. Many have focused on the exact biochemical mechanism that enables it to selectively conduct protons in a voltage and pH-dependent manner. Moreover, a number of studies have analyzed on role of HVCN1 in different cell types such as immune cells, spermatozoa, lung epithelial cells or more recently also neurons[150–152].

1.5.1 Molecular structure and properties of HVCN1

The human *HVCN1* gene is located on chromosome 12 and encodes a 273 amino acid (aa)-long protein[153]. To date, only one other isoform (253 aa) has been identified, which arises by

translation from an alternative start codon[154]. This isoform, which exhibits enhanced gating properties, has only been documented in B cells so far[154]. In mice, *Hvcn1* is localized to chromosome 5 and encodes a 269 aa-long protein that is 78% identical to its human analog[155].

HVCN1 possesses four helical transmembrane domains (S1 - S4, Fig. 1.6). Structurally, HVCN1 shares many similarities with the voltage-sensitive domain (VSD) of other ion channels, but lacks the pore-forming domains S5 and S6[147,148]. The literature on structure-function relationship indicates that HVCN1 transports protons through a hydrogen-bonded chain mechanism rather than through an aqueous pore[156]. The N-terminus appears to have regulatory functions for channel opening and harbors a phosphorylation site, Thr^{29}, that allows enhanced gating upon phosphorylation[157] (Fig. 1.6). In enhanced gating mode, HVCN1 opens at more negative voltages and closes more slowly. Furthermore, it can conduct larger proton currents. Hence, enhanced gating is characterized by prolonged and increased proton efflux. HVCN1 is a homodimer and dimerization is mediated by interactions of the coiled-coil regions at the C-termini of two HVCN1 monomers[158]. Truncation of the C-terminus results in monomeric HVCN1, which exhibits increased gating speed, but reduced voltage sensitivity[159].

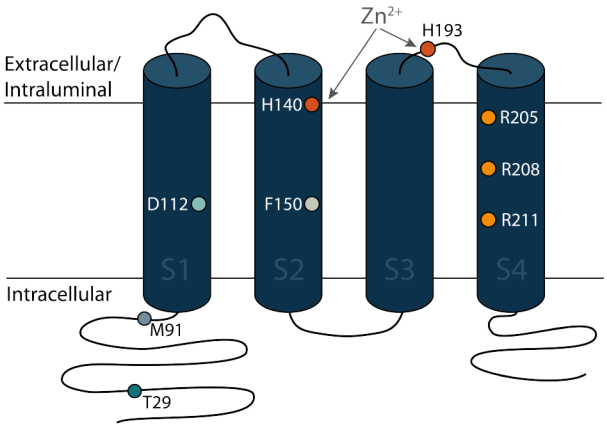

Figure 1.6| Molecular structure of HVCN1.
HVCN1 has four helical transmembrane domains (S1 – S4). Three arginine residues (Arg^{205}, Arg^{208}, Arg^{211}) in the S4 domain are mediating voltage dependence. A salt-bridge formed between Asp^{112} and Arg^{208} is crucial for proton selectivity. The N-terminus harbors a phosphorylation site at Thr^{29}, which is important for inducing the enhanced gating mode. Furthermore, the only functionally relevant, naturally occurring mutation is found at position 91 (M91T). HVCN1 can be inhibited by Zn^{2+}, which binds to the extracellular histidines His^{140} and His^{193}. Moreover, a new class of HVCN1 inhibitors were shown to bind from the intracellular site around Phe^{150}.

HVCN1 is a perfectly selective proton channel. To date, there are no reports of any other ion being transported by HVCN1. This property is of great importance, since physiological proton concentrations are one million-fold lower (40 – 70 nM) compared to concentrations of other ions. Thus, if the channel were more permeable to other ions, they would simply displace proton transport[156]. Proton selectivity was shown to be achieved by a "salt-bridge" between Asp^{112} and Arg^{208} in the S1 and S4 domain, respectively[160] (Fig. 1.6).

HVCN1 opens upon membrane depolarization, but its opening probability depends strongly on the pH difference between intracellular and extracellular space (ΔpH). In practice, this means that under physiological conditions, HVCN1 would open at a membrane potential (V_m) of + 8 mV. If the intracellular pH decreases by one unit, the proton conductance voltage shifts by − 40 mV[161], so that HVCN1 opens at $V_m = -32$ mV. This implies that HVCN1 mediates only the efflux of protons under physiological conditions. Voltage-dependent gating is likely mediated by three arginine residues in S4[162] (Fig. 1.6), as previously found in sodium and

potassium channels. However, it is still unclear which parts of the protein are responsible for the pH sensitivity.

HVCN1 can be inhibited by zinc ions (Zn^{2+}). Zn^{2+} can bind to the outer histidine residues (His^{140} and His^{193}, Fig. 1.6) at the interface between the two HVCN1 monomers, thereby slowing channel opening and shifting the voltage dependence more positively[159]. However, Zn^{2+} inhibits many other biological processes and is therefore not suitable for *in vivo* inhibition of HVCN1. Hence, the search for more selective HVCN1 inhibitors is necessary. One potential lead compound is the aromatic guanosine derivative 2-guanidinobenzimidazole (2GBI)[163]. It was shown to block HVCN1 intracellularly through interaction with a phenylalanine residue in the S2 domain (Phe^{150}, Fig 1.6)[164]. Information about the interaction of 2GBI and HVCN1 now allows for further development of more potent inhibitors[165]. Recently, another novel inhibitor of HVCN1, YHV98-4, was identified in a virtual screening approach. This inhibitor has already been tested in *in vivo* applications, where it was shown to be beneficial in alleviating peripheral neuroinflammation.

1.5.2 Role of HVCN1 during NADPH oxidase activation

Even before the identification of HVCN1, the cooperation of proton channels with the NADPH oxidase during the oxidative burst in phagocytes was the subject of many studies[166–168].

The NADPH oxidase catalyzes the transfer of two electrons from NADPH across the membrane onto molecular oxygen. During the reaction, $NADP^+$ and H^+ remain in the cytosol, which leads to acidification and depolarization of the membrane. In addition, reconstitution of NADPH from $NADP^+$ by the pentose phosphate pathway also generates one more proton[83]. Prolonged membrane depolarization and acidification both may have severe effects on ion homeostasis, cell metabolism or signaling events. Hence, proton extrusion upon NADPH oxidase activation is crucial to maintain cellular functions. Furthermore, both depolarization and acidification directly inhibit NADPH oxidase activity[169,170], with consequences for the bacterial killing capacity of phagocytes[171].

A major advantage of proton extrusion through HVCN1 is that it not only prevents acidification but also depolarization. In comparison to other electroneutral exchanger such as the sodium-hydrogen antiporter (NHE), the efflux of protons through HVCN1 is an electrogenic transport and is therefore charge compensating. In addition, activation of immune cells through protein kinase C (PKC) signaling also induces phosphorylation of HVCN1 which leads to increased proton flux in the enhanced gating mode[154].

1.5.3 Role of HVCN1 in neutrophils

ROS production. Activated neutrophils exhibit a strong production of NADPH oxidase-dependent ROS. Therefore, HVCN1 is crucial for preventing membrane depolarization and acidification to sustain ROS production. It was shown that inhibition or genetic deletion of HVCN1 in neutrophils led to a prolonged decrease of the intracellular pH and increased membrane depolarization[172,173].

As a result, neutrophils produced significantly less ROS, which impacted their capacity to kill bacteria *in vitro*. *In vivo*, however, HVCN1-deficient mice were able to eliminate several different pathogens as efficient as their wild type counterparts[171,174]. Interestingly, a recent study showed that, in contrast to strong stimuli, low-dose chemotactic agents led to increased ROS production in HVCN1-deficient neutrophils. Increased ROS levels induced ERK signaling, enhancing directional migration[175].

Phagosomal pH. HVCN1 is not only located on the plasma membrane of neutrophils, but also in phagosomes. Here, the channel helps to sustain phagosomal ROS production and balance pH, by providing protons that react with NADPH oxidase-generated superoxide to produce H_2O_2. Whereas wild type neutrophils were shown to maintain a neutral pH in their phagosomes, phagosomes in HVCN1-defiecent neutrophils appeared to be either too acidic or too alkaline[176]. This effect is probably due to a different recruitment of the v-ATPase: in phagosomes with residual NADPH oxidase activity, ROS prevented the recruitment of the v-ATPase, hence the phagosome alkalinized. However, in phagosomes where ROS were absent, successful recruitment of the v-ATPase induced acidification. This could have direct effects on the killing of phagocytosed bacteria, since neutrophil proteases require a neutral pH to fully function[104] and could explain why HVCN1-deficient neutrophils show impaired killing *in vitro*.

Degranulation. A study on HVCN1-deficient neutrophils further revealed a role for HVCN1 in degranulation. Okochi et al.[174] reported that HVCN1-deficient neutrophils secreted more primary granule proteins, namely MPO and NE. Pretreatment with the potassium ionophore valinomycin partially rescued increased granule release, which led the authors to conclude that increased membrane depolarization in HVCN1-deficient neutrophils is responsible for augmented granule release. HVCN1-deficient neutrophils displayed more severe lung inflammation after intranasal inoculation with *C. albicans* which might be a direct effect of increased granule release *in vivo*.

Calcium mobilization. Two studies investigated the calcium response in HVCN1-deficient neutrophils. El Chemaly et al.[173] demonstrated that in the absence of HVCN1, the driving force for calcium entry is reduced, due to the accumulation of positively charged protons in the cytoplasm. Defective calcium mobilization resulted in impaired random migration of HVCN1-deficient neutrophils after stimulation with a chemotactic agent. Thus, they proposed that HVCN1 is important to maintain the influx of extracellular and allow normal migration. In contrast, Okochi et al.[175] found no differences in calcium mobilization after stimulation with different concentrations of chemotactic agents. Rather, low doses of stimulants resulted in increased migration of HVCN1-deficient neutrophils, they suggest most likely through enhanced ERK signaling.

1.5.4 Importance of HVCN1 in other immune cells

The role of HVCN1 is best studied in neutrophils, however expression of HVCN1 was reported for almost all mammalian immune cells and a number of studies have investigated its function in those cells.

Eosinophils. Eosinophils, just like neutrophils, express high levels of both HVCN1 and NADPH oxidase and they exhibit an even stronger ROS production[177]. They are specialized in fighting extracellular parasites, which is why NADPH oxidase is mainly located at their plasma membrane[178]. Zhu et al.[179] showed that stimulation of HVCN1-deficient eosinophils also resulted in increased acidification and depolarization. At the same time, eosinophils produced less extracellular ROS and showed enhanced cell death. In contrast to neutrophils, loss of HVCN1 did not affect calcium entry and migration of eosinophils.

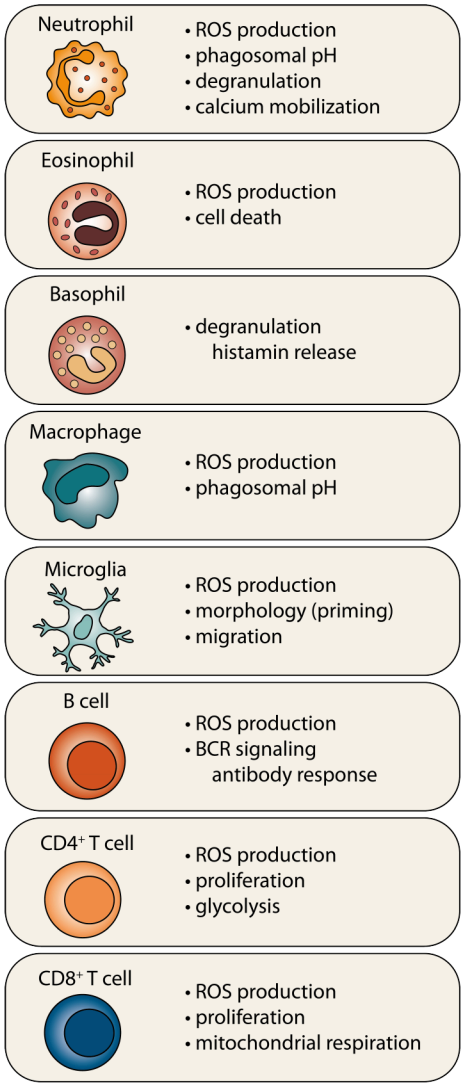

Figure 1.7| Summary of the role of HVCN1 in different immune cells.

Basophils. Although basophils are developmentally closely related to eosinophils, they do not express the NADPH oxidase subunit gp91^{phox}. Unexpectedly, however, it was found that proton currents were enhanced in activated basophils and that inhibition of HVCN1 by Zn^{2+} resulted in proton accumulation[180]. In basophils, HVCN1 seems to regulate histamine responses to IgE; pretreatment of basophils with Zn^{2+} attenuated histamine IgE-dependent histamine release. Exactly how acidification inhibits basophil degranulation remains to be elucidated.

Macrophages. HVCN1 is expressed in macrophages[149], where it facilitates phagosome acidification and phagosomal ROS production[176]. Beyond this, little is known about its function in bone marrow-derived macrophages and monocytes.

Microglia. The role of HVCN1 in microglia cells, the resident macrophages of the brain, has been the subject of more extensive investigation. Microglia can generate ROS via NADPH oxidase in response to infectious stimuli, but also to danger-associated molecular patterns that occur, for example, in neurodegenerative diseases[181]. How HVCN1 regulates microglial ROS production remains somewhat controversial. Wu et al.[182] showed that loss of HVCN1 reduced ROS production by microglia and was therefore beneficial in a model of ischemic stroke. In contrast, Kawai et al.[183] reported increased ROS levels in HVCN1-deficient microglia, however, they confirmed the

beneficial effect of HVCN1 loss *in vivo* in models of ischemia, albeit only in older mice. They proposed that HVCN1 is heterogeneously expressed in the aged brain and that loss of HVCN1 leads to increased oxidative damage, altered microglial morphology, and changes in gene expression only in the cortex[184]. Recent studies have examined the role of HVCN1 in brain and nerve injury. After injury, HVCN1 was significantly upregulated by microglia. In both models, neutralization or loss of HVCN1 ameliorated disease progression, either through increased microglial migration and debris clearance [185] or through decreased ROS and IFNγ production[186].

B cells. HVCN1 was found in many different B cell subsets, with its highest expression in naïve and memory B cells[187]. Activation of B cells also induces ROS production by the NADPH oxidase[188], although ROS levels are very low in comparison to the oxidative burst in phagocytes[150]. Hence, it was proposed that ROS in B cells do not mediate bacterial killing but rather act as signaling modulators by inhibiting ROS-sensitive phosphatases[189]. Indeed, HVCN1-deficient B cells were shown to produce less ROS upon stimulation of the BCR and, as a consequence, phosphatases were insufficiently inhibited, impairing BCR signaling and causing reduced antibody responses *in vivo*. Interestingly, HVCN1 colocalized with the BCR at the plasma membrane and after internalization[187]. Additional research will be required to understand if this proximity is necessary to sustain pH and ROS production locally or if HVCN1 regulates BCR signaling beyond facilitating proton extrusion.

T cells. Naïve T cells express low levels of HVCN1[190]. Activation of T cells leads to upregulation of HVCN1 to counteract intracellular acidification[191]. So far, two studies have investigated the role of HVCN1 in T cell function and they come to conflicting conclusions. Okochi et al.[190] showed that HVCN1-deficient mice have higher numbers of activated $CD4^+$ and $CD8^+$ T cells, both in the resting state and after viral infection. Given that T cells also express NADPH oxidase[192], they also assessed ROS levels in activated T cells and found that production was impaired in HVCN1-deficient T cells. In contrast, Coe et al.[191] recently demonstrated that intracellular acidification due to loss of HVCN1 impairs T cell survival and functionality, leading to reduced host versus graft disease in models of T cell-dependent skin transplantation. Interestingly, HVCN1 deficiency affected $CD4^+$ and $CD8^+$ T cells differently, likely due to differential metabolic adaptation. Both T cell subsets isolated from HVCN1-deficient mice exhibited proliferation defects and decreased cytokine production. However, whereas the impairment of $CD4^+$ T cells could be attributed to decreased glycolysis, $CD8^+$ T cells tended to show defects in mitochondrial respiration. Of note, ROS production was normal in $CD4^+$ cells and increased in $CD8^+$ T cells, likely due to mitochondrial dysfunction.

1.5.5 HVCN1 in disease

So far, there are no reports of HVCN1 deficiency associated with human disease. This corresponds with the observation that young HVCN1 knock out mice do not show a pathological phenotype.

There are seven relevant single nucleotide polymorphisms in the HVCN1 gene, only two of which have a frequency greater than 1%[153]. The M91T polymorphism was previously described in a study investigating the function of HVCN1 in lung epithelial cells. Functional analysis suggested that this mutation would decrease HVCN1 activity due to decreased pH sensitivity[193]. However, there is no clinical evidence to support this hypothesis yet.

Interestingly, HVCN1 plays an important role in several types of cancer[154,194–196]. Cancer cells mainly use glycolysis instead of oxidative phosphorylation for energy production, a metabolic switch referred to as the Warburg effect[197]. Because glycolysis leads to acidification, cancer cells rely on efficient proton extrusion pathways, of which HVCN1 is one. Breast and colon cancer cell lines express large amounts of HVCN1 to regulate their cytoplasmic pH[194,195]. In cancer patients, HVCN1 expression positively correlates with tumor size, tumor classification, or clinical stage. In addition, high HVCN1 levels are associated with shorter survival[195,198]. Knockdown or inhibition of HVCN1 *in vitro* has been shown to decrease cancer cell survival and invasion[194,196,199]. In addition to high expression levels, some cancer cells express a truncated isoform of HVCN1 called $HVCN1_S$. This isoform has previously been found in chronic lymphocytic leukemia (CLL) cells and in two tumorigenic human breast cell lines[154,199]. $HVCN1_S$ arises by translation at an alternative start codon and is subject to enhanced phosphorylation at Thr^{29} and therefore shows enhanced gating. CLL cells expressing this isoform have been shown to exhibit stronger B cell signaling and increased proliferation and migration[154]. Due to its beneficial role in tumor growth, HVCN1 has become a promising target for cancer therapy.

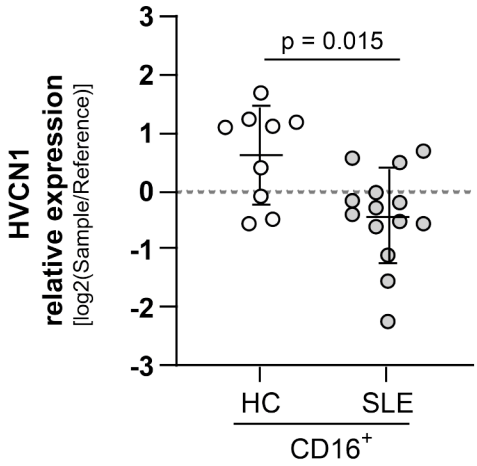

Figure 1.8| HVCN1 is downregulated on CD16+ cells of SLE patients.
Gene array data provided by Ken Smith and Paul Lyons.

However, because HVCN1 plays an important role in the regulation of various immune cells, the side effects of systemic inhibition of HVCN1 will have to be thoroughly investigated. Although there have been no reports of pathological loss-of-function mutations in HVCN1, recent data suggest an association between low HVCN1 expression and the development of autoimmune diseases. Unpublished data from Ken Smith and Paul Lyons' group at the University of Cambridge show a decrease in HVCN1 expression on neutrophils from patients with SLE (Fig. 1.8). These data are supported by a study of leukocytes from Crohn's disease patients, which found that low HVCN1 levels are significantly associated with active disease stage[200]. The fact that aged mice with HVCN1 deficiency were reported to develop a mild autoimmune phenotype by the Okamura group[190] suggests that a decrease in HVCN1 expression not only correlates with autoimmunity but may also be involved in its development.

1.6 Aim of the thesis

Neutrophils are the most abundant cells in human blood and play an important role in the defense against pathogens. A reduction in neutrophil numbers can have devastating effects on the outcome of infections. Neutrophils can kill pathogens through various effector mechanisms, including phagocytosis, generation of ROS, and release of antimicrobial proteins. In addition, they are capable of undergoing a specific inflammatory form of cell death called NETosis, characterized by the release of decondensed chromatin decorated with antimicrobial enzymes that efficiently capture and kill extracellular pathogens. In their role as effective killers, neutrophils can severely damage host tissues under septic and aseptic inflammatory conditions. Neutrophils also play a special role in certain autoimmune diseases by providing autoantigens, such as DNA in systemic lupus erythematosus and granule proteins in anti-neutrophil cytoplasmic antibody (ANCA) - associated vasculitis. Therefore, it is of great importance to understand the regulation of neutrophil effector functions in health and disease.

The hydrogen voltage-gated channel 1 (HVCN1) is highly expressed in neutrophils and functions to limit cell depolarization and acidification during activation of the ROS-generating enzyme NADPH oxidase. In this role, it also supports ROS production, since activation of NADPH oxidase is dependent on membrane potential. Therefore, HVCN1-deficient neutrophils were shown to exhibit significantly lower levels of ROS. Besides their antimicrobial function, ROS are also signaling molecules that were shown to regulate immune cell function. In neutrophils, ROS play an important role in the formation of NETs. Therefore, the aim of this work was to investigate the role of HVCN1 in regulating neutrophil function, with a particular focus on NET formation.

Furthermore, I sought to understand how loss of HVCN1 would influence neutrophil activation *in vivo*. As aged HVCN1-deficient mice were shown to develop a mild autoimmune disorder and neutrophil granulocytes from SLE patients were found to have lower levels of HVCN1, I further sought to understand the relation between HVCN1 downregulation and the development and progression of autoimmunity.

2 Material

2.1 Equipment

Table 2.1 | Equipment

Equipment	Article / Company
Balances	Precision Balance 2100g, Fisher Scientific Analytical Balance 210g, Fisher Scientific
Beakers	Schott
Bio Imaging System	Stella 3200, Raytest
Cell counter	CASY Cell Counter and Analyzer, OMNI Life Science
Centrifuges	Megafuge 40-R TX-1000, Thermo Scientific Centrifuge 5424 R, Eppendorf Centrifuge 5424, Eppendorf
Flow Cytometer	FACSymphony A5, BD Bioscience FACSCelesta, BD Bioscience
Fluorometer for nucleic acid quantification	Qubit 4 Fluorometer, Invitrogen
Forceps	F.S.T. (Fine Science Tools)
Freezer	Liebherr
Gel electrophoresis chambers	Mini Gel Tank, Invitrogen XCell SureLock Mini-Cell, Invitrogen Owl EasyCast B1 and B2 Mini, Thermo Scientific Biometra Compact L/XL, Analytic Jena
Gel electrophoresis power supplies	Power 300 XL, Fisher Scientific Power Supply Mini 300V Plus, Fisher Scientific
Glass bottles	Schott
Heating blocks	ThermoMixer F1.5, Eppendorf ThermoMixer C, Eppendorf
Ice machine	Manitowoc RF0266A
Incubator	Incu-Line, VWR ICO 240, Memmert
Laminar flow hood	Safe2020 Class II, Thermo Scientific
Measuring cylinders	Schott
Microplate reader	FLUOstar Omega, BMG Labtech
Microscope	ZOE™ Fluorencent Cell Imager, BioRad Primovert, Zeiss LSM700, Zeiss LSM900, Zeiss EpiScope, Zeiss
Microwave	MW 7875, Severin
Motorized pipette controller	FisherBrand
PCR cycler	C1000 Touch Thermal Cycler, BioRad
pH Meter	Accumet AE150, Fisher Scientific
Pipettes	Research plus Single-channel, Eppendorf Multipette E3, Eppendorf Pipetman L Multichannel, Gilson
Plate shaker	Titramax 100, Heidolph Instruments
qPCR cycler	StepOnePlus, Applied Biosystems
Rocker	Compact Digital Rocker, Thermo Scientific Compact Digital Waving Rotator, Thermo Scientific Titramax101, Heidolph
Scalpel and blade	F.S.T. (Fine Science Tools)
Scissors	F.S.T. (Fine Science Tools)
Seahorse Flux Analyzer	Seahorse XFe96 Analyzer, Agilent
Spectrophotometer for DNA, RNA and protein	DS-11 Spectrophotometer, DeNovix
Vortex shaker	Vortex-Genie 2, Scientific Industries
Waterbath	Type 1013, GFL

2.2 Consumables

Table 2.2 | Consumables

Item	Company
1.2 ml microtubes	Starlab International
CASYcups	OMNI Life Science
Cell strainer nylon, 70 µm	Sarstedt
Clear bottom, black-walled 96-well plates	Greiner bio-one
CombiTips Advanced®	Eppendorf
Conical centrifuge tubes (15 mL/ 50 mL)	Greiner bio-one
Cover slips, 12 mm, No.1	VWR
Culture plates (6-well/ 12-well/ 24-well/ 96- well, flat-bottom)	Cellstar®, Greiner bio-one
Disposable Centric Luer Two-Part Syringe (5 mL) Inject®	Braun
ELISA plates Costar® (96-well, half-area)	Corning
Gloves	Kimtech
Live Cell Imaging Plates, µ-slides ibiTreat	Ibidi
LS columns	Miltenyi Biotec
Microscope slides (Superfrost plus)	Epredia
Needle, Microlance™ 27 G	Becton Dickinson
Omnican™ 20 U Insulin Injection Syringe	Braun
Parafilm®	Bemis®
PCR tubes, Multiply®.µStrip Pro	Sarstedt
Pipette tips	TipOne, Starlab SureOne, Fisher Brand
Plate sealer ELISA, Thermowell ™ Sealing Tape	Corning
Plate sealer qPCR, MicroAmp™ Optical Adhesive Film	Applied Biosystems, Life Technologies™
PVDF membranes, Immobilon®	Millipore®
qPCR plates, MicroAmp® Fast Optical	Applied Biosystems, Life Technologies™
Round-bottom polystyrene tubes (5 mL)	Falcon
Seahorse XFe24 sensor cartridges	Agilent
Seahorse XFe24 V7 PS Cell Culture Microplates	Agilent
SealSafe tubes (1.5 mL/ 2 mL/ 5 mL)	Sarstedt
Serological pipettes (2 mL/5 mL/ 10 mL/ 25 mL/ 50 mL)	Cellstar®, Greiner bio-one
V-bottom 96-well plates	Greiner bio-one
White 96-well plates	Greiner bio-one

2.3 Chemicals, reagents and enzymes

All standard chemicals were purchased from Sigma-Aldrich (Merck) or Carl Roth.

Table 2.3 | Chemical, reagents and enzymes

Item	Company
100 bp DNA ladder	New England Biolabs
5-(N,N-Dimethyl)amiloride hydrochloride	Biomol
Agarose	Biozym
Amplex Red Reagent	Invitrogen
Antimycin A	Sigma-Aldrich
Bafilomycin A1	Sigma-Aldrich
BAPTA-AM (1,2-bis(o-aminophenoxy)ethane-N,N,N′,N′-tetraacetic acid, AM)	Abcam
BCECF-AM (2′,7′-Bis-(Carboxyethyl)-5-(and-6)-Carboxy-fluorescein, AM)	Invitrogen
Bicinchoninic acid	Sigma-Aldrich
Bovine serum albumin	Sigma-Aldrich
Calcein-AM	Biolegend
CASY ton	OMNI Life Science
Catalase (from bovine liver)	Sigma-Aldrich
Cell-Tak	Corning
CM-H_2DCFDA, General Oxidative Stress Indicator	Invitrogen
DAPI	Biotium

DAPI (4',6-Diamidino-2-phenyl-indol –dihydrochloride)	Biotium
$DiBAC_4(3)$ (Bis-(1,3-Dibutylbarbituric Acid)Trimethine Oxonol)	Invitrogen
Diphenyleneiodonium chloride	Sigma-Aldrich
DNase/RNase-free water	Sigma-Aldrich
Donkey serum	Sigma-Aldrich
Double distilled water	Sigma-Aldrich
Dulbecco's Phosphate Buffered Saline w/o Ca^{2+}/Mg^{2+}	Sigma-Aldrich
ECL	Thermo Scientific
Ethylenediaminetetraacetic acid (EDTA), 0.5 M solution	Invitrogen
FACS Clean Solution	Becton Dickinson
FACS Flow	Becton Dickinson
FACS Rinse Solution	Becton Dickinson
Fetal calf serum	PAN
Fixable Viability Dye	Invitrogen
Fluo-4-AM	Invitrogen
Goat serum	Sigma-Aldrich
Hank's Balanced Salt Solution (HBSS), Ca^{2+}/Mg^{2+}-free	Gibco
Hank's Balanced Salt Solution (HBSS), sterile	Gibco
Horseradish peroxidase (Type VI, salt-free)	Sigma-Aldrich
IgG from mouse serum	Sigma Aldrich
Indo-1 AM	Invitrogen
ING-II AM (ION NaTRIUM Green-2, AM)	Interchim
Isoluminol (4-Aminophtalhydrazide)	Sigma-Aldrich
L-glutamine	Gibco
Luminol	AppliChem
MitoSOX Red™ Mitochondrial Superoxide Indicator	Invitrogen
MitoTracker Green	Invitrogen
MitoTracker Red CXRos	Invitrogen
MyTaq Red 2x	Meridian Bioscience
NuPage 4 – 12 % Bis-Tris gel	Invitrogen
NuPage MES SDS Running buffer (20x)	Invitrogen
Oligomycin	Sigma-Aldrich
Phorbol 12-myristate 13-acetate (PMA)	Sigma-Aldrich
Phosphatase Inhibitor Cocktail 2	Sigma-Aldrich
Phosphatase Inhibitor Cocktail 3	Sigma-Aldrich
Poly-L-lysine	Sigma-Aldrich
Prolong Gold Antifade Mountant	Invitrogen
Protease Inhibitor, cOmplete™ Protease Inhibitor Cocktail	Roche
Proteinase K	Roche
Pyruvate	Gibco
Red blood cell lysis buffer	eBioscience
RIPA buffer	Sigma-Aldrich
Rotenone	Sigma-Aldrich
RPMI 1640, #R8758	Sigma-Aldrich
Superoxide dismutase (SOD)	Sigma-Aldrich
SYBR DNA Gel Stain	Invitrogen
SYBR Green Master Mix	BioRad
TAE buffer (10x)	Invitrogen
TMB substrate	BD
TRITC-dextran (10,000 MW, anionic, fixable)	Invitrogen
TritonX-100	Sigma-Aldrich
Tween-20	Sigma-Aldrich
UltraComp beads	eBioscience
VAS2870	Sigma-Aldrich
XF base medium	Agilent
XF calibrant	Agilent
Zymosan A from *Saccharomyces cerevisiae*	Sigma-Aldrich

2.4 Solutions and buffers

Table 2.4 | Solutions and buffers

Solution/buffer	Content
50 mM potassium phosphate buffer, pH 7	0.0268 M K_2HPO_4 0.0232 M KH_2PO_4
Biopsy lysis buffer	100 mM TRIS-HCl, pH 8.5 5 mM EDTA, pH 8 0.2% SDS 200 mM NaCl 1:100 Proteinase K
Borate buffer	0.2M H_3B0_3 0.02M $Na_2B_4O_7$ x 10 H_2O
ELISA stopping solution	1M H_3PO_4
ELISA wash buffer	0.05% Tween in PBS
Histology blocking buffer	2.5% BSA in PBS + 0.5% Triton X-100
Histology staining buffer	2.5% BSA in PBS + 0.1% Triton X-100
MACS buffer	0.5% FBS + 2 mM EDTA in PBS
Western Blot Transfer buffer	25 mM TRIZMA base 192 mM Glycin pH 8
Western Blot wash buffer	TRIS-buffered saline (20 mM TRIS, 150 mM NaCl) + 0.1% Tween-20

2.5 Kits

Table 2.5 | Kits

Kit	Company
Mouse Myeloperoxidase DuoSet ELISA	R&D Systems
Mouse Total MMP-9 DuoSet ELISA	R&D Systems
High-Capacity cDNA Reverse Transcription Kit	Applied Biosystems
Neutrophil Isolation Kit, mouse	Miltenyi Biotec
RNeasy Micro Kit	Qiagen
Mouse IFNα SimpleStep ELISA Kit	Abcam
Qubit dsDNA HS-Assay Kit	Invitrogen

2.6 Antibodies

2.6.1 Antibodies for flow cytometry

Table 2.6 | Antibodies for flow cytometry

Antigen	Conjugate	Clone	Company
B220	APC-Cy7	RA3-6B2	Biolegend
B220	PE-Cy7	RA3-6B2	Biolegend
CD115	PE-Cy7	AFS98	Biolegend
CD11b	PE	M1/70	Biolegend
CD11b	BUV395	M1/70	BD
CD11c	BV605	N418	Biolegend
CD16/32	AF647	93	Biolegend
CD19	PE-Cy5	eBio1D3	eBioscience
CD19	APC-Cy7	6D5	Biolegend
CD3	BUV737	145-2C11	BD
CD3	APC	17A2	Biolegend
CD34	FITC	HM34	Biolegend
CD3e	PE-Cy7	145-2C11	Biolegend
CD45	BV711	30-F11	Biolegend

CD63	APC	NVG-2	Biolegend
CD90.2	PE-Cy7	30-H12	Biolegend
cKit	BV711	2B8	Biolegend
cKit	PE-Cy7	2B8	Biolegend
CXCR2	AF647	SA044G4	Biolegend
CXCR4	V450	2B11	BD
gdTCR	PE	GL3	Biolegend
Gr1	APC-Cy7	RB6-8C5	Biolegend
Ly6B2	AF700	7/4	Novus Biologicals
Ly6C	eF450	HK1.4	eBioscience
Ly6C	PerCp-Cy5.5	HK1.4	eBioscience
Ly6G	BUV563	1A8	BD
Ly6G	APC-Cy7	1A8	Biolegend
Ly6G	PE-Dazzle594	1A8	Biolegend
MHCII	BV421	M5/114.15.2	Biolegend
NK1.1	PE-Cy7	PK136	Biolegend
NK1.1	APC-Cy7	PK136	Biolegend
Sca1	PE-Cy7	D7	Biolegend
Sca1	BV421	D7	Biolegend
SiglecF	PE	E50-2440	BD
Ter119	APC-Cy7	TER-119	Biolegend

2.6.2 Antibodies for histology

Table 2.7 | Antibodies for histology

Antigen	Isotpye	Clone	Conjugate	Company
8-OHdG	Goat	polyclonal	unconjugated	Enzo Life Science
Goat IgG (H + L)	Donkey	polyclonal	AlexaFluor™ 594	Invitrogen
Histone H3 (citrulline R2 + R8 + R17)	Rabbit IgG	polyclonal	unconjugated	Abcam
HVCN1	Rabbit IgG	polyclonal	unconjugated	Alomone Labs
Lamin B1 – Nuclear envelop marker	Rabbit IgG	polyclonal	unconjugated	Abcam
Myeloperoxidase	Goat IgG	polyclonal	unconjugated	R&D Systems
Neutrophil elastase	Rabbit IgG	polyclonal	unconjugated	Abcam
Rabbit IgG (H + L)	Goat	polyclonal	AlexaFluor™ 488	Invitrogen
Rabbit IgG (H + L)	Donkey	polyclonal	AlexaFluor™ 488	Invitrogen
Rabbit IgG (H + L)	Donkey	polyclonal	AlexaFluor™ 594	Invitrogen

2.7 Primers

2.7.1 Genotyping PCR primers

All primers were supplied from Sigma.

Table 2.8 | PCR primers

Target		Sequence (5' to 3')
HVCN1	For	AATAGACCGTTGTAAACCACCTG
	WT Rev	AAGGCTGATGATCTGAGGTTC
	KO Rev	AGTATCGGCCTCAGGAAGATCG
HVCN1 (floxed construct)	For	AAGAGAAACAGACTGGGTGGCTAGG
	tt-Rev	GATCAAATTCCAGACTTCCCTGGGC
	Rev	CCTAAGCCTGTCTCAGCATCTAGGC
CYBB	For	AAG AGA AAC TCC TCT GCT GTG AA
	WT Rev	CGC ACT GGA ACC CCT GAG AAA GG
	KO Rev	GTT CTA ATT CCA TCA GAA GCT TAT CG
Ly6G-Cre	For	GGTTTTATCTGTGCAGCCC
	Rev	GAGGTCCAAGAGACTTTCTGG
MRP8-Cre	Cre For	GCG GTC TGG CAG TAA AAA CTA TC
	Cre Rev	GTG AAA CAG CAT TGC TGT CAC TT

	Control For	CTA GGC CAC AGA ATT GAA AGA TCT
	Control Rev	GTA GGT GGA AAT TCT AGC ATC ATC C
LysM-Cre	For	CTT GGG CTG CCA GAA TTT CTC
	WT Rev	TTA CAG TCF FCC AFF CTG AC
	Cre Rev	CCC AGA AAT GCC AGA TTA CG

2.7.2 RT-qPCR primers

All primers were supplied from Sigma.

Table 2.9 | Gene expression assays

Target		Sequence (5' to 3')
Hvcn1	For	ATG ACT TCC CAT GAC CCA AAG G
	Rev	TCG TCC CCA ACC ACC GTA A
Ire1α	For	GCC GAA GTT CAG ATG GAA TC
	Rev	ATC AGC AAA GGCCGATGA
Bi-1	For	TCCCACATAACTCCCTCGACA
	Rev	GTGTGTGACCACATGGACATAG
Upc-2	For	GTGGTGGTCGGAGATACCAGA
	Rev	GGGCAACATTGGGAGAAGTCC
Xbp1	For	GAATGGACACGCTGGATCCT
	Rev	GAGTGGAGTAAGGCTGGTGGC
Spliced Xbp1	For	GAGTCCGCAGCAGGTG
	Rev	TCCCATGGACTCTGACAC
Cacna1f	For	TCTGCACATAGTGCTCAATTCC
	Rev	AAGTTCGTGATGCCACCGTT
Tpcn1	For	GATGTGCCGCTCATCCTGAC
	Rev	TGTGGCTGCCCCCATTTTT
Tpcn2	For	CACGACTGATGAACACACTGA
	Rev	CCAGGAGGCACGATGACAC
Ryr1	For	CAGTTTTTGCGGACGGATGAT
	Rev	CACCGGCCTCCACAGTATTG
Ryr2	For	ATGGCTTTAAGGCACAGCG
	Rev	TCCTTGAATGCCAGCTCAGA
Ryr3	For	AGGTGGAGGCATTGGTGATG
	Rev	CCATGAGGGGTCGTGTCAAAG
Itpr1	For	GGGTCCTGCTCCACTTGAC
	Rev	CCACATCTTGGCTAGTAACCAG
Itpr2	For	CCTCTACATTGGGGACATCGT
	Rev	GGCACACCTTGAACAGGCA
Psen1	For	ATACCTGCACCTTTGTCCTACT
	Rev	GCTCAGGGTTGTCAAGTCTCT
Selenok	For	CTGGGGAATAGCAGAATTCGTG
	Rev	TTCTTCGTGGAGGGTTTCCTG
Gapdh	For	CTCCACTCACGGCAAATTCCA
	Rev	GATGACAAGCTTATTCTCG

2.8 Software

Table 2.10 | Software

Software	Company
7900HT Fast Real-Time PCR Program	Applied Biosystems
Adobe Illustrator 2022	Adobe
Adobe InDesign 2022	Adobe
Adobe Photoshop 2022	Adobe
FACS Diva	BD
Fiji (ImageJ)	Open source scientific analysis program
FlowJo 10.7	BD
FLUOstar Software	BMG Labtech

GraphPad Prism 9	GraphPad
Mendeley	Elsevier
Microsoft Office 2011	Microsoft
Seahorse XFp Analyzer Software	Agilent
XStella V1	Raytest
Zen blue	Zeiss

2.9 Mice strains

All strains are on a C57BL/6 background.

Table 2.11 | Mice strains

Mouse line	Strain name	Reference
HVCN1 KO	Hvcn1$^{Gt(RRN293)Byg}$	Okochi *et al.*[149], Ramsey *et al.*[171]
CYBB KO	B6.129S-Cybb^{tm1Din}	Pollock *et al.*[201]
HVCN1 floxed	Hvcn1$^{tm1a(KOMP)Wtsi}$	Skarnes *et al.*[202]
Ly6G-Cre	Ly6g$^{tm2621(cre)Arte}$	Hasenberg *et al.*[203]
MRP8-Cre	Tg(S100A8-cre,-EGFP)1Ilw	Passegue *et al.*[204]
LysM-Cre	B6.129P2-Lyz2$^{tm1(cre)Ifo/J}$	Clausen *et al.*[205]

3 Methods

3.1 Isolation of bone marrow neutrophils

Mature neutrophils were isolated from the bone marrow. For this purpose, mice were killed by carbon dioxide euthanasia and the hind legs were dissected from the hip joint. Tibia and femur were separated at the knee joint, and muscles and residual tissue was removed from the bones. The epiphyses were cut off and the bone marrow was flushed with cold MACS buffer onto a 70 µm cell strainer using a 27G cannula and a 5 ml syringe. The cell suspension was centrifuged at 300 x g for 7 minutes at 4 °C. Subsequently, the pellet was resuspended in 5 ml red blood cell lysis buffer and incubated for 7 minutes at room temperature. Reaction was stopped by adding 20 ml PBS. Cells were counted with an automated cell counter. Neutrophils were isolated using the Neutrophil Isolation Kit from Miltenyi Biotec and isolation was performed according to the manufacturer's protocol. Briefly, for magnetic labeling, 5 x 10^7 bone marrow cells were resuspended in 200 µl MACS buffer and incubated with 50 µl Neutrophil Biotin-Antibody Cocktail for 10 minutes at 4 °C. Cells were washed by adding 10 ml MACS buffer and centrifugation at 300 x g for 10 minutes. Subsequently cells were resuspended in 400 µl MACS buffer and incubated with 100 µl Anti-Biotin MicroBeads for 15 minutes at 4 °C. Cells were again washed as described above and resuspended in 500 µl. For magnetic separation, LS columns were placed in a MACS separator and rinsed with 3 ml MACS buffer. Suspension of magnetically labeled bone marrow cells was transferred onto the columns and columns were washed three times with 3 ml MACS buffer. Flow-through was collected, representing the enriched neutrophils. Neutrophils were counted and collected by centrifugation.

3.2 Histology

3.2.1 Cell culture for histological analysis

Cell culture for immunocytochemistry was performed on poly-L-lysine (pLL) coated coverslips. Coverslips were coated with 5 µg/mL pLL/ddH_2O for 1 hour at 37 °C or at 4 °C overnight. Subsequently, they were washed three times with PBS and transferred into a fresh 24-well culture plate. Neutrophils were resuspended in RPMI 1640 supplemented with 0.5 % FBS to a concentration of 1 x 10^6 cells/ml. 50 µl cell suspension was applied on each coverslip, containing 50,000 cells respectively. Neutrophils were allowed to adhere for 20 minutes at room temperature before addition of 460 µl culture media. In case of pretreatment, 5 µl of 100x concentration substances were added to cells. Afterwards, 50 µl 10x concentrated PMA was added to a final concentration of 100 nM. After desired stimulation times, cells were fixed by the addition of 550 µl 4% PFA and incubated for 15 minutes at room temperature. Coverslips were washed twice with PBS and stored in PBS at 4° C until further use.

3.2.2 Immunofluorescence staining of cultured cells

Immunofluorescence staining of cultures cells on coverslips was performed in a humidified chamber on a parafilm base. First, coverslips were blocked, cells facing up, with 100 µl blocking buffer (2.5 % BSA + 0.5 % Trition-X100 in PBS) with 5 % serum for 1 hour at room temperature. Then, 50 µl of primary antibody in staining solution (2.5 % BSA + 0.1 % Trition-X100) was added as a drop onto the parafilm and coverslips were flipped onto the drop with cells facing down and incubated at 4° C overnight. For washing with PBS, coverslips were again flipped so cells were facing up. Secondary antibodies were diluted 1:500 in PBS and coverslips were again flipped onto the drops and incubated for 2 hours at room temperature. Afterwards, one wash was performed as previously described and coverslips were incubated with 100 µl 1 µg/ml 4',6-Diamidino-2-phenylindol (DAPI) for 5 minutes. After three washes with PBS, coverslips were quickly dipped into ddH_2O to remove salts and dried at room temperature before mounting with ProLong™ Gold Antifade Mountant.

Laser scanning confocal imaging was performed with the Zeiss LSM700 or Zeiss LSM900 microscope and images were edited with the Zen 3.1 (blue edition) software.

3.2.3 Analysis of nuclear decondensation and NETosis

This analysis was performed with the help of Manuel Schölling and Dr. Miguel Fernandes from the Image and Data Analysis Facility (DZNE, Bonn).

For the analysis of the nuclear decondensation preceding NET release, cells on coverslips were stained with DAPI according to the above mentioned protocol (3.2.2). Three confocal images per sample and condition were acquired using the 20x objective of the Zeiss LSM900 microscope. Images were exported as 8-bit TIF-files using the Zen 3.1 (blue edition) software. Subsequently, single nuclei were identified and morphological features were analyzed using the Cell Profiler Software, see appendix for analyzed features. Cell Profiler data was loaded into the Cell Profiler Analyst software and phase classes were defined and at least 100 nuclei per class were manually classified for training the software.

3.2.4 Quantification methods for microscopy images

For quantification of NETosis, manual counting of number of NETotic events per total number of nuclei was performed.

Quantification of histone citrullination was performed using FIJI. Briefly, threshold for single channel images, in this case DAPI and citH3, was set manually using the command *Image > Adjust > Threshold* to obtain binary images. Counting of objects in binary images was performed using the command *Analyze > Analyze particles* (excluding objects on the edges, including holes in objects). Object size was entered in pixel unit adjusted to size and resolution of the image.

Quantification of 8-OHdG was performed on maximum intensity projection images using FIJI. In brief, single channel images were duplicated using the command *Image > Duplicate*. Threshold

for the duplicated image was set manually using command *Image > Adjust > Threshold* to obtain a binary image. Next measurement options were set under *Analyze > Set measurements* to display *integrated density* redirected to the original image. Measurement of selected parameters for single objects was then performed using the command *Analyze > Analyze particles* (excluding objects on the edges, including holes in objects). Object size was entered in pixel unit adjusted to size and resolution of the image.

3.2.5 Live cell imaging

For live cell imaging, neutrophils were resuspended in $HBSS^{+Ca/Mg}$ supplemented with 0.5 % FBS to a concentration of 5 x 10^5 cells/ml. Subsequently, 200 µl cell suspension was seeded into each well of an 8-well IBIDI µ-slide chambered coverslips and cells were rested for 20 minutes at room temperature. In case of pretreatment, inhibitors were added 11x concentrated in a volume of 20 µl and cells were incubated for indicated times. After mounting the chambered coverslip onto the microscope stage, a 11x or 12x concentrated PMA solution was added in a volume of 20 µl. Brightfield images were acquired each minute for a total of 30 to 45 minutes using an ZEISS Axio Observer (Zeiss).

3.3 Measurements of ROS

3.3.1 AmplexRed assay

Neutrophils were resuspended to a concentration of 1.25 x 10^6 cells/ml in phenol red-free RPMI with 0.5 % FBS. 450 µl cell suspension per well was seeded into a 24-well plate and cells were rested for 30 minutes at 37 °C. Subsequently, 50 µl of a 11x PMA solution were added to reach a final concentration of 100 nM and cells were stimulated for 30 minutes at 37 °C. For balancing volumes 50 µl RMPI was added to unstimulated wells. In the meantime, AmplexRed mix was prepared by setting up 100 µM AmplexRed reagent and 0.2 U/ml horseradish peroxidase (HRP) in PBS. Additionally, a no-enzyme control was prepared by setting up the mix without HRP. Then, 50 µl AmplexRed mix and 50 µl cell supernatant were mixed in a black-walled 96-well plate and incubated for 15 minutes at room temperature kept away from light. AmplexRed fluorescence was measured using a microplate reader, ex530nm/em590nm.

3.3.2 Luminol-amplified luminescence assay

Neutrophils were resuspended to a concentration of 1 x 10^6 cells/ml in $HBSS^{+Ca/Mg}$ with 0.5 % FBS and 170 µl cell suspension per well was seeded into a 96-well plate with white walls and bottom. While cells were rested for 30 minutes at 37 °C, luminol and isoluminol mixes were prepared and laid into a v-bottom 96-well plate (see table 3.1). To begin the reaction, 64.5 µl luminol mix were added to the neutrophil cell suspension using a multichannel pipettor. Chemiluminescence was measured every 5 minutes for a period of 2 hours using a microplate reader at 37 °C. As it is not

cell permeant, the signal of isoluminol is representative for extracellular ROS. In contrast, luminol can enter the cell and can – in combination with superoxide dismutase (SOD) and catalase, which degrade extracellular ROS – be used for determination of intracellular ROS.

In case of pretreatment, inhibitors were already added as 100x concentrated solutions (in regard to the final volume of 234.5 µl) to cells during the 30-minute resting time. All conditions were run in duplicates.

Table 3.1 - Master mix for Luminol assay

Luminol mix	Isoluminol mix	Volume per well
Luminol (100 mM in DMSO)	Isoluminol (100 mM in DMSO)	5 µl
Borate buffer	Borate buffer	45 µl
HRP (500 U/m in PBS)	HRP (500 U/mL in PBS)	10 µl
Catalase (100 mg/ml in potassium phosphate buffer)	Potassium phosphate buffer	2.4 µl
SOD (6045 U/ml in ddH_2O)	ddH_2O	2 µl
	Total	64.5 µl

3.3.3 Intracellular and mitochondrial ROS by flow cytometry

For measurements of intracellular (CM-H_2DCFDA) and mitochondrial ROS (MitoSOX™ Red), neutrophils were resuspended in $HBSS^{+Ca/Mg}$ at a density of 8 - 10 x 10^6 cells/ml. Subsequently, 500 µl cell suspension was mixed with 500 µl of a 2x concentrated probe solution. Final concentration of CM-H_2DCFDA and MitoSOX was 2.5 µM, loading was performed for 20 minutes at RT. After loading, cells were washed twice and resuspended in $HBSS^{+Ca/Mg}$ with 0.5 % FBS at a density of 2 Mio/ml. For stimulation, 500 µl cell suspension, i.e. 1 Mio neutrophils, were transferred into a fresh 5 ml round bottom tube. 5 µl of a 100x PMA solution were added to reach a final concentration of 100 nM. After 30 minutes of stimulation at 37° C, cells were put on ice and immediately analyzed by flow cytometry (FACSymphony A5, BD Bioscience). Analysis was performed using FlowJo V10.

For microscopy-based analysis of intracellular ROS production, 5 x 10^5 DCFDA-loaded neutrophils in $HBSS^{+Ca/Mg}$ were seeded and stimulated for 30 minutes at 37°C. For fluorescence quantification, neutrophils were imaged with the BioRad ZOE fluorescent cell imager and fluorescence intensity per cell was analyzed with FIJI.

3.4 Measurements of intracellular ions by flow cytometry

For measurements of intracellular calcium, sodium or protons, neutrophils were resuspended in $HBSS^{+Ca/Mg}$ at a density of 8 - 10 x 10^6 cells/ml. Subsequently, 500 µl cell suspension was mixed with 500 µl of a 2x concentrated probe solution. For final probe concentration, loading time and temperature see table 3.2. After loading, cells were washed twice and resuspended in $HBSS^{+Ca/Mg}$ with 0.5% FBS at a density of 1 Mio/ml. In case of measurements in calcium-free medium, cells were already washed with calcium-free HBSS and resuspended in $HBSS^{-Ca/Mg}$ with 0.5% FBS and 2 mM EDTA. For flow cytometry, 900 µl cell suspension was transferred into a 5 ml round bottom

tube. After acquisition of baseline fluorescence levels for 2 minutes, 100 µl 10x PMA solution was added to reach a final concentration of 100 nM. In case of pretreatment, 9 µl 100x concentrated inhibitors were added at different time points before recording.
Samples were acquired using a FACSymphony A5 (BD Bioscience) and analysis was performed using FlowJo V10. After gating on single neutrophils the median fluorescence intensity per second was extracted using the kinetics tool.

Table 3.2 - Loading conditions for intracellular ion-sensitive probes

Ion	Dye	Final concentration	Loading time	Loading temperature
Calcium	Fluo-4-AM	2 µM	30 min	37 °C
Sodium	ING-II, AM	2.5 µM	60 min	RT
Proton	BCECF-AM	1.25 µM	30 min	RT

3.5 Measurements of membrane potential by flow cytometry

3.5.1 Membrane potential

For measurements of the membrane potential, neutrophils were resuspended in $HBSS^{+Ca/Mg}$ with 0.5% FBS at a density of 1 x 10^6 cells/ml. For flow cytometry analysis, 900 µl cell suspension was transferred into a 5 ml round bottom tube and $DiBAC_4(3)$ was added at a final concentration of 50 nM. After 10 minutes of equilibration with $DiBAC_4(3)$, acquisition was started and baseline fluorescence levels were recorded for 2 minutes. Then 100 µl 10x PMA solution was added to reach a final concentration of 100 nM. In some cases, 9 µl 2 mM di-methyl amiloride (final concentration 20 µM) was added 10 minutes before recording.
Samples were acquired using a FACSCelesta (BD Bioscience) and analysis was performed using FlowJo. After gating on single neutrophils the median fluorescence intensity per second was extracted using the kinetics tool.

3.5.2 Mitochondrial transmembrane potential

For measurements of the mitochondrial membrane potential, neutrophils were resuspended in $HBSS^{+Ca/Mg}$ at a density of 8 - 10 x 10^6 cells/ml. Subsequently, 500 µl cell suspension was mixed with 500 µl of a 100 nM TMRM solution (final concentration 50 nM) and cells were incubated for 30 minutes at 37 °C. After loading, cells were washed twice and resuspended in $HBSS^{+Ca/Mg}$ with 0.5% FBS at a density of 1 Mio/ml. In case of measurements in calcium-free medium, cells were already washed with calcium-free HBSS and resuspended in $HBSS^{-Ca/Mg}$ with 0.5% FBS and 2 mM EDTA. For flow cytometry analysis, 900 µl cell suspension was transferred into a 5 ml round bottom tube. After acquisition of baseline fluorescence levels for 2 minutes, 100 µl 10x PMA solution was added to reach a final concentration of 100 nM. In case of pretreatment, 9 µl of a 1 mM BAPTA-AM (final concentration 10 µM) were added at 30 minutes before recording.

Samples were acquired using a FACSymphony A5 (BD Bioscience) and Analysis was performed using FlowJo. After gating on single neutrophils the median fluorescence intensity per second was extracted using the kinetics tool.

3.6 Measurements of mitochondrial fitness and damage

3.6.1 Quantification of mitochondrial mass

For quantification of mitochondrial mass, neutrophils were resuspended in $HBSS^{+Ca/Mg}$ at a density of 5 x 10^6 cells/ml. Subsequently, 500 µl cell suspension was mixed with 500 µl of a 100 nM MitoTracker™ Green FM or MitoTracker™ Red CMXRos solution (final concentration 50 nM) and cells were incubated for 30 minutes at 37 °C. After loading, cells were washed twice and resuspended in $HBSS^{+Ca/Mg}$ with 0.5% FBS at a density of 1 Mio/ml. Subsequently, MitoTracker Green signal was measured by flow cytometry. For microscopy, MitoTracker Red-loaded cells were seeded onto pLL-coated coverslips and allowed to adhere for 20 minutes at room temperature. Finally, cells were fix with 4% PFA and counterstained with DAPI.

3.6.2 mPTP opening assay

For assessment of mPTP opening, neutrophils were resuspended in $HBSS^{+Ca/Mg}$ at a density of 5 x 10^6 cells/ml. Calcein AM was added to 1 ml of cell suspension to a final concentration of 50 nM and incubated for 20 minutes at 37° C. After loading, cells were washed once and resuspended in $HBSS^{+Ca/Mg}$ with 0.5% FBS at a density of 2 Mio/ml. 1 Mio cells per conditions were transferred into fresh 5 ml round bottom tubes and rested for 15 minutes at 37 °C. Intracellular calcein was quenched by adding 400 µM $CoCl_2$ and incubation for another 15 minutes at 37 °C. Thereafter, neutrophils were stimulated for 30 minutes with either 100 nM PMA or 2 µM ionomycin, or left untreated. After stimulation, tubes were transferred on ice and DAPI was added to exclude dead cells. Calcein median fluorescence measured by flow cytometry using a FACSCelesta (BD Bioscience). This experiment was performed together with Lena Luisa Suhl (master student).

3.6.3 Seahorse XF Cell Mito Stress Test

Extracellular flux analysis to test for mitochondrial fitness was performed using the Agilent Seahorse XFe24 analyzer and the Cell Mito Stress Test kit. Calibrated XFe24 cell culture plates were coated with 1.12 µg/ml Cell-Tak for 20 minutes at room temperature to secure cell adhesion. Neutrophils were resuspended to 5 x 10^6/ml in assay medium (XF base medium supplemented with 1 mM pyruvate, 2 mM L-glutamine and 10 mM glucose) and 100 µl cell suspension was seeded into the XFe24 culture plates. Wells with medium only served for background correction. Cells were quickly spun onto plate bottom and incubated for 25 minutes at 37 °C. Afterwards, wells were filled with additional 400 µl of assay medium, followed by another 15 minutes of incubation. Ports of the sensor cartridge were loaded with 10x inhibitors according to kit

instructions (Port A: 10 µM oligomycin, Port B: 10 µM FCCP, Port C: 5 µM rotenone/antimycin A) and cartridge was inserted into the analyzer for calibration. Finally, the culture plate with neutrophils was inserted into the analyzer and assay was run according to manufacturer's instructions adding the inhibitors at indicated times. During the assay, oxygen consumption rate (OCR) and the extracellular acidification rate (ECAR) were determined. This experiment was performed together with Lukas Faber (master student).

3.7 Measurements of granule release and pinocytosis

3.7.1 Enzyme-linked immunosorbent assay for the measurement of granule protein release

To determine the release of granule proteins, neutrophils were resuspended in RPMI supplemented with 0.5% FBS at a density of 1 x 10^6/ml. Then, 2.5 x 10^5 neutrophils were seeded into a 24-well plate. In case of pretreatment, 25 µl of 11x concentration substances were added to cells. For stimulation, 25 µl of a 11x or 12x PMA solution were added to reach a final concentration of 100 nM PMA. Supernatants were harvested at different time points after stimulation, spun down at 13,000 rpm for 5 minutes and transferred into fresh tubes. Enzyme-linked immunosorbent assays (ELISAs) were performed according to manufacturer's instructions in half-area 96-well plates.

3.7.2 CD63 surface expression

To measure exocytosis of primary granules, surface expression of CD63 was measured by flow cytometry. To this end, neutrophils were resuspended in $HBSS^{+Ca/Mg}$ with 0.5% FBS to a density of 1.25 x 10^6/ml. For stimulation, 500 µl cell suspension was transferred into 5 ml round bottom tubes and stimulated with 100 nM PMA for 60, 30, 15, 7.5 and 0 minutes at 37 °C. After one wash, cells were fix in 500 µl 4% PFA for 10 minutes at RT. After washing off the PFA, cells were stained with anti-CD63-PE (1:100) and Fc receptor blocking solution (1:200), for 25 minutes at 4 °C. Then, cells were again washed twice and immediately analyzed by flow cytometry. Samples were acquired using a FACSymphony A5 (BD Bioscience) and Analysis was performed using FlowJo.

3.7.3 Analysis of fluid-phase pinocytosis

To measure fluid-phase pinocytosis, uptake of fluorescently labelled dextran was measured by flow cytometry. To this end, neutrophils were resuspended in $HBSS^{+Ca/Mg}$ with 0.5% FBS to a density of 1.25 x 10^6/ml. For stimulation, 500 µl cell suspension was transferred into 5 ml round-bottom tubes and stimulated with 100 nM PMA and 100 µg/ml TRITC-dextran for 60, 30, 15, 7.5 and 0 minutes at 37 °C. After one wash, cells were fix in 500 µl 4% PFA for 10 minutes at RT. After washing off the PFA, cells were resuspended in HBSS and immediately analyzed by flow cytometry or transferred into a IBIDI-dish for microscopy. Samples were acquired using a FACSymphony A5

(BD Bioscience) and Analysis was performed using FlowJo. Microscopy images were acquired using a LSM700 (Zeiss).

3.8 Plate-bound IgG stimulation

For stimulation with plate-bound IgG, 96-well plates were coated with 40 µl of 1 mg/ml mouse IgG in PBS at 4 °C overnight. Coverslips were coated by placing them on a drop of 1 mg/ml mouse IgG in PBS. The next day, wells and coverslips were washed three times with PBS. For analysis of ROS production, neutrophils were seeded according to protocol in 3.3.2. For analysis of granule protein release, 1 x 10^5 neutrophils in 100 µl RPMI supplemented with 0.5% FBS were seeded per well and stimulated for 1 hour at 37°C and further processed as described in 3.7.1. For histology, cells were seeded onto IgG-coated coverslips and further processed as described in 3.2.1.

3.9 Analysis of phagocytosis and intracellular killing

This experiment was performed in collaboration with Natascha Ellen Stumpf and Prof. Dr. Christian Kurts (Institute of Molecular Medicine and Experimental Immunology, Medical Faculty, University of Bonn).

To assess phagocytic activity, neutrophils were resuspended in RPMI with 10 % FBS to a density of 1 x 10^6/ml. Then, 1 x 10^5 cells seeded into a 96-well plate and 2.5 x 10^6 heat-killed GFP-expressing *E. coli* were added. After incubation for 30, 60 or 180 minutes at 37 °C, cells were washed and fixed with 4% PFA for 30 minutes at room temperature. Phagocytic uptake of *E. coli* was analyzed by counting of GFP-positive cells by flow cytometry using a BD FACS Canto (BD Bioscience).

To measure intracellular killing of phagocytosed *E. coli*, neutrophils were resuspended in RPMI with 10% FBS to a density of 1 x 10^6/ml. Then, 1 x 10^5 cells seeded into a 96-well plate and 2 x 10^5 *E. coli* were added. After incubation 180 minutes at 37 °C, 50 µg/ml gentamicin was added for 1 h at 37° C to kill all remaining extracellular bacteria. Cells were washed three times with PBS and resuspended in culture medium again. After another 180 minutes of incubation, cells were permeabilized using 0.1% saponin to release intracellular bacteria. Subsequently, a dilution series of the suspension was plated onto LB-agar plates and cultured overnight at 37 °C before counting the colony-forming units.

3.10 Western Blot

3.10.1 Sample preparation for protein analysis

For the preparation of protein lysates, 2 – 4 x 10^6 neutrophils were lysed in 100 µl RIPA buffer. Unstimulated neutrophils were centrifuged and the pellet was directly resuspended in lysis buffer. In case of previous stimulation, neutrophils were seeded into 6-well plates and cultures

for indicated times. After incubation, cells were washed with ice-cold PBS and lysis was performed directly inside the culture dish.

3.10.2 Protein quantification

The bicinchoninic acid assay (BCA assay) was performed to quantify protein concentration. For the working reagent, 4% copper(II)-sulfate solution (w/v) was diluted 1:50 in bicinchoninic acid. For the linear response curve, BSA standards (0 – 1 mg/ml; 0.2 mg/ml steps) were prepared in ddH_2O. Samples were diluted 1:5 in ddH_2O. Finally, 10 µl of standard or diluted sample were mix with 200 µl working reagent in a 96-well plate, incubated for 30 minutes at 37 °C and absorbance at 562 nm was measured on a plate reader.

3.10.3 Protein separation and transfer

30 – 40 µg protein lysate were mixed with 5x WB sample buffer and samples were denatured for 10 minutes at 97 °C. Samples were loaded on 4 – 12% or 10% Bis-Tris gels and electrophoresis was performed in MES or MOPS SDS running buffer at 120 V for 60 – 90 minutes. Proteins were blotted onto 0.45 µm PVDF membranes with Towbin transfer buffer (25mM Tris, 190mM glycine, 10% methanol) in a wet-tank system overnight at 30 V in the cold room.

3.10.4 Protein detection

Membranes were blocked with 5 % skimmed milk in TBS-T for 1 hour at RT. Subsequently, membranes were incubated with primary antibodies diluted in blocking buffer overnight at 4 °C. The next day, membranes were washed with TBS-T three times for 10 minutes. Incubation with HRP-conjugated secondary antibodies was performed for 2 hours at room temperature. After washing three times with TBS-T, antigens were identified by chemiluminescent visualization.

3.11 Gene expression analysis

3.11.1 Sample preparation for gene expression analysis

RNA isolation was performed with the RNeasy Micro Kit. 2 x 10^6 neutrophils were lysed in 350 µl lysis buffer. In case of previous stimulation, neutrophils were resuspended to a concentration of 2 x 10^6/mL and 1 mL cell suspension was seeded into each well of a 12-well plate. For stimulation, 100 µl of a 11x PMA solution were added to reach a final concentration of 100 nM PMA. After stimulation, supernatants were removed and cells were washed carefully with PBS. 350 µl lysis buffer were added to each well and cells were lysed for 5 minutes. If RNA was not isolated directly, lysates were stored at -80 °C until further use.

3.11.2 RNA isolation and cDNA synthesis

RNA isolation was performed using the RNeasy Mini Kit according to manufacturer's instructions. Finally, RNA was eluted in 30 µl RNase-free water and concentration was determined.

cDNA synthesis was performed using the High Capacity cDNA Reverse Transcription Kit according to manufacturer's instruction. Generally, 100 – 200 ng RNA were reversely transcribed in a total volume of 20 µl and reaction was performed in a thermal cycler with following temperature program: 25 °C/10 min – 37 °C/120 min – 85 °C/5 min – 4 °C/∞.

3.11.3 Semi-quantitative real-time PCR

cDNA was diluted five-fold in ddH_2O. In each well of a MicroAmp™ 96-well plate, 10 µl SYBRGreen PCR Master Mix, 1 µl forward and reverse primer (10 µM), 6 µl ddH_2O and 2 µl diluted cDNA were combined. Each sample was analyzed in duplicates. Amplification and detection was performed running the 7900HT Fast Real-Time PCR Program on a StepOne Plus Real-Time PCR system.
Expression analysis of calcium channels was performed together with Caterina Gagliardi.

3.12 Flow cytometry analysis

3.12.1 Cell isolation

The cells for flow cytometry analysis were isolated from bone marrow, spleen and blood. After dissection, hind legs and spleen were kept in PBS on ice until cell isolation. Bone marrow cells were isolated as described in 3.1. For the isolation of splenocytes, 4 - 5 small cuts were incised on one side of the spleen. Cells were separated by passing the spleen tissue through a 70 µm cell strainer using a 5 mL syringe plunger. Subsequently strainer was washed with 15 mL PBS. After spinning down the cells at 300 x g for 7 minutes, splenocytes or bone marrow cells were resuspended in 5 ml red blood cell lysis buffer and incubated for 7 minutes at room temperature. Lysis reaction was stopped by adding 20 mL PBS. After cell counting, cells were resuspended in FACS buffer to a concentration of 25 x 10^6/ml.
Blood was collected by cardiac puncture using EDTA-coated 1 ml syringes and was directly transferred into EDTA-coated 1.5 ml tubes on ice. Coating of syringes and tubes was performed with 0.5 M EDTA overnight at room temperature. In order to retrieve plasma, tubes with blood were spun at 1500 rpm for 10 minutes at 4 °C. Plasma was transferred into fresh tubes again centrifuged at 5000 rpm/5 minutes and 13,000 rpm/3 minutes to clear form cell debris and was finally stored at -80 °C until further use. Blood cells were resuspended in 10 ml PBS and were centrifuged at 300 x g for 7 minutes. Cells were then resuspended in 10 ml red blood cell lysis buffer and incubated for 10 minutes at room temperature. Lysis reaction was stopped by adding 40 mL PBS. After another centrifugation step, all blood cells were resuspended in 200 µl FACS buffer for further processing.

3.12.2 Staining procedure

200 µl cell suspension per sample were transferred into a 96-well v-bottom plate. Cells were centrifuged at 300 x g for 5 minutes and resuspended in 50 µl staining mix. For antibodies and

dilutions see Table 2.6.1. After incubation for 25 minutes at 4 °C, cells were washed twice with ice-cold FACS buffer and finally resuspended in 200 µl FACS buffer for acquisition.
In case of intracellular antigens, cells were fixed in 2% PFA for 15 minutes at room temperature and subsequently washed once with PBS and twice with 0.1% saponin in PBS (saponin/PBS). Primary antibody was diluted in 100 µl saponin/PBS and incubation was performed on an orbital shaker at 450 rpm at 4 °C overnight. The next day, cells were washed three times with saponin/PBS and secondary antibody was diluted 1:500 in 100 µl saponin/PBS and incubated on an orbital shaker at 450 rpm for 2 hours at room temperature. Subsequently, cells were washed twice with saponin/PBS and once with PBS.
All samples were analyzed within 2 hours after the staining on a BD FACSymphony™ A5 Cell Analyzer.
Panels and gating strategies are included in the appendix.

3.13 Peritonitis model

To induce inflammation in the abdominal cavity, mice were intraperitonelly injected with 1 mg Zymosan diluted in 300 µl PBS. Mice were sacrificed at different time points after injection (6 or 24 hours) by CO_2 euthanasia. After drawing blood by cardiac puncture (see 3.12.1), the abdominal skin was carefully opened and 5 ml of ice-old PBS with 2 mM EDTA were injected into the abdominal cavity using a 25G cannula. Gentle massaging was applied to the peritoneum in order to detach cells. Then, peritoneal fluid was slowly retrieved with the syringe. Lavage supernatant and cells were separated by centrifugation. Supernatant was stored at -20 °C for quantification of cell-free DNA (cfDNA) and MPO. Peritoneal cells were analyzed by flow cytometry or frozen at -80 °C for molecular analysis.

3.14 Model for pulmonary ANCA-associated vasculitis

This experiment was performed in collaboration with Nina Kessler and Prof. Dr. Natalio Garbi (Institute of Molecular Medicine and Experimental Immunology, Medical Faculty, University of Bonn).
To induce pulmonary vasculitis, mice were anesthetized with isoflurane and intubated using a rodent laryngoscope. 50 µl PBS containing 10 µg fMLP and 10 µg LPS was applied intratracheally (i.t.) while mice were being ventilated with isoflurane/O2 at a volume of 250 µl/beat and 250 beats/minute (Holland et al. 2017) using a mechanical ventilator (Harvard Apparatus). Following mice were injected i.p. with 1 mg anti-MPO (clones 6D1 and 6G4, 1:1/produced by BioXcell) in 200 µl PBS. Control groups only received the i.t. treatment. Three days after induction, mice were euthanized with ketamine/xylazin. After drawing blood by cardiac puncture (see 3.12.1), bronchoalveolar lavage was performed by intubating the trachea through a small incision using a 20-gauge catheter. Bronchoalveolar lavage (BAL) was collected by flushing lungs three times with

1 ml PBS/2 mM EDTA. Through the catheter, lungs were filled with 1 ml 4% PFA, dissected out and fixed in 4% PFA overnight before paraffin-embedding.

Analysis of pulmonary hemorrhages was performed by quantification of hemoglobin in the BAL. To this end 75 µl BAL was diluted serially and its optical density was measured at 400 and 600 nm. Values in the linear range below saturation ($OD_{400-600} = 1.5$) were selected and corrected for the dilution factor.

Lavage supernatant and cells were separated by centrifugation. Supernatant was stored at -20 °C for quantification of cfDNA and MPO. Peritoneal cells were analyzed by flow cytometry or frozen at -80 °C for molecular analysis.

4.1 HVCN1 expression and function

4.1.1 HVCN1 is highly expressed in neutrophils

It has already been shown that HVCN1 is expressed in different immune cells, both human and mouse[150]. To analyze HVCN1 expression levels in mice, leukocytes from blood were analyzed by flow cytometry. B cells and granulocytes exhibited the highest HVCN1 expression levels (Fig. 4.1 A). Neutrophils in particular showed very high expression. When comparing HVCN1 levels in neutrophils from different organs, no significant difference was found between mature neutrophils ($CXCR2^+$) from bone marrow, spleen and blood (Fig. 4.1 B). Since only an insufficient number of neutrophils could be isolated from mouse blood, neutrophils from bone marrow were used for the following *in vitro* experiments.

Furthermore, immunofluorescence analysis of HVCN1 in naïve bone marrow neutrophils revealed that it is expressed both at the plasma membrane and in intracellular compartments (Fig. 1C). In addition, HVCN1 was minimally colocalized with myeloperoxidase (MPO), however appeared to be distributed in different intracellular compartments.

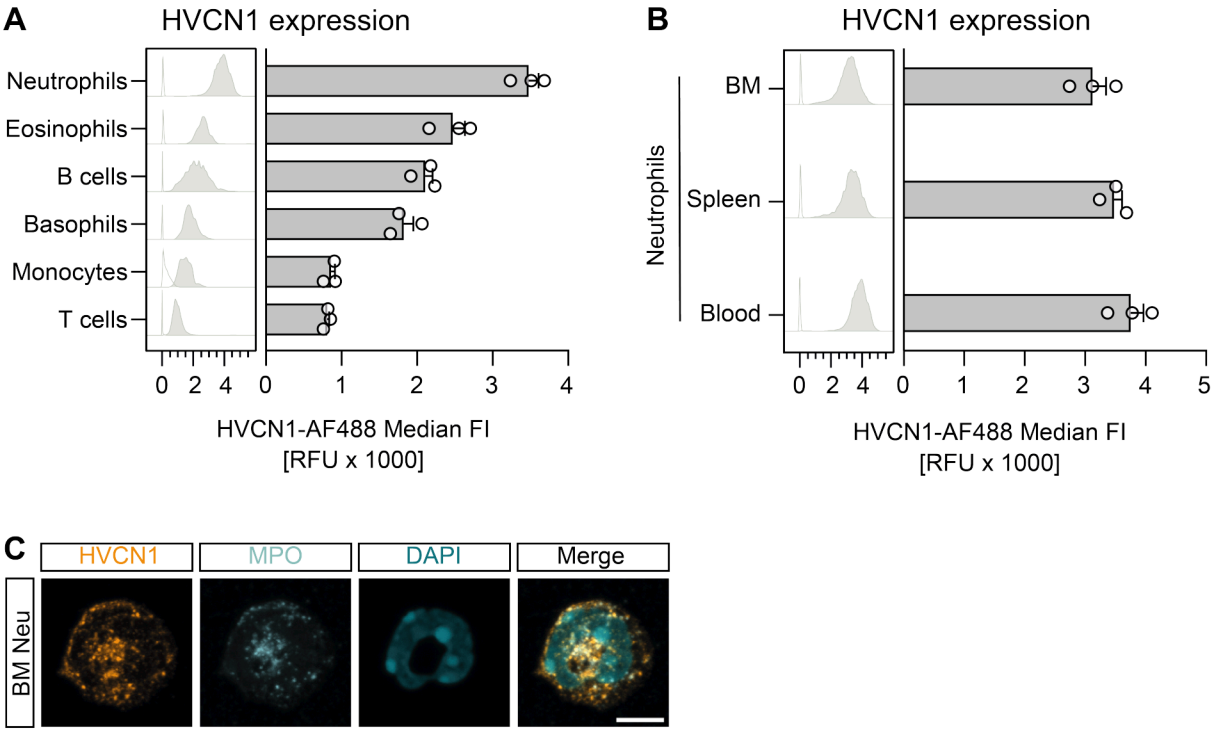

Figure 4.1| HVCN1 is highly expressed on neutrophils.
A| Flow cytometry analysis of HVCN1 expression in different immune cells in the murine blood. Histograms include fluorescence intensities (FI) of secondary antibody control (empty histograms) and cells stained for HVCN1 (filled histograms). Expression is depicted as Median FI – Median FI of secondary antibody control. Columns represent mean ± SEM (n = 3). B| Flow cytometry analysis of HVCN1 expression on neutrophils derived from bone marrow (BM), spleen or blood. Histograms include FI of secondary antibody control (empty histograms) and cells stained for HVCN1 (filled histograms). Expression is depicted as Median FI – Median FI of secondary antibody control. Columns represent mean ± SEM (n = 3). C| Microscopic analysis of HVCN1 expression in bone marrow neutrophils (BM Neu) including staining for MPO and DAPI.
Scale bar ≙ 5 µm.

4.1.2 HVCN1 facilitates proton extrusion and supports ROS production

In the present thesis, HVCN1-deficient mice (HVCN1$^{-/-}$) and bone marrow neutrophils were used to investigate the effects of loss of HVCN1 on neutrophil activation (Fig. 4.2 A). Deletion of HVCN1 in neutrophils was validated by western blot and flow cytometry analysis (Fig. 4.2 B, 4.2 C). To induce cell activation, and in particular ROS production by the NADPH oxidase, neutrophils were stimulated with phorbol-12-myristate-13-acetate (PMA), a potent activator of protein kinase C.

To further validate the deletion of HVCN1, intracellular pH of neutrophils was determined after stimulation with PMA using the pH-sensitive probe BCECF-AM (Fig. 4.2 D). PMA led to intracellular acidification in wild type and HVCN1$^{-/-}$ neutrophils. Interestingly, HVCN1$^{-/-}$ neutrophils failed to restore pH balance, while wild type neutrophils were able to return to basal pH 15 minutes after PMA stimulation. This confirmed that HVCN1$^{-/-}$ neutrophils have a defect in proton extrusion. Furthermore, it was already shown that extracellular ROS production is impaired in HVCN1$^{-/-}$ in various immune cells[150]. Fittingly, HVCN1$^{-/-}$ neutrophils showed reduced levels of extracellular ROS production after stimulation with PMA (Fig. 4.2 E).

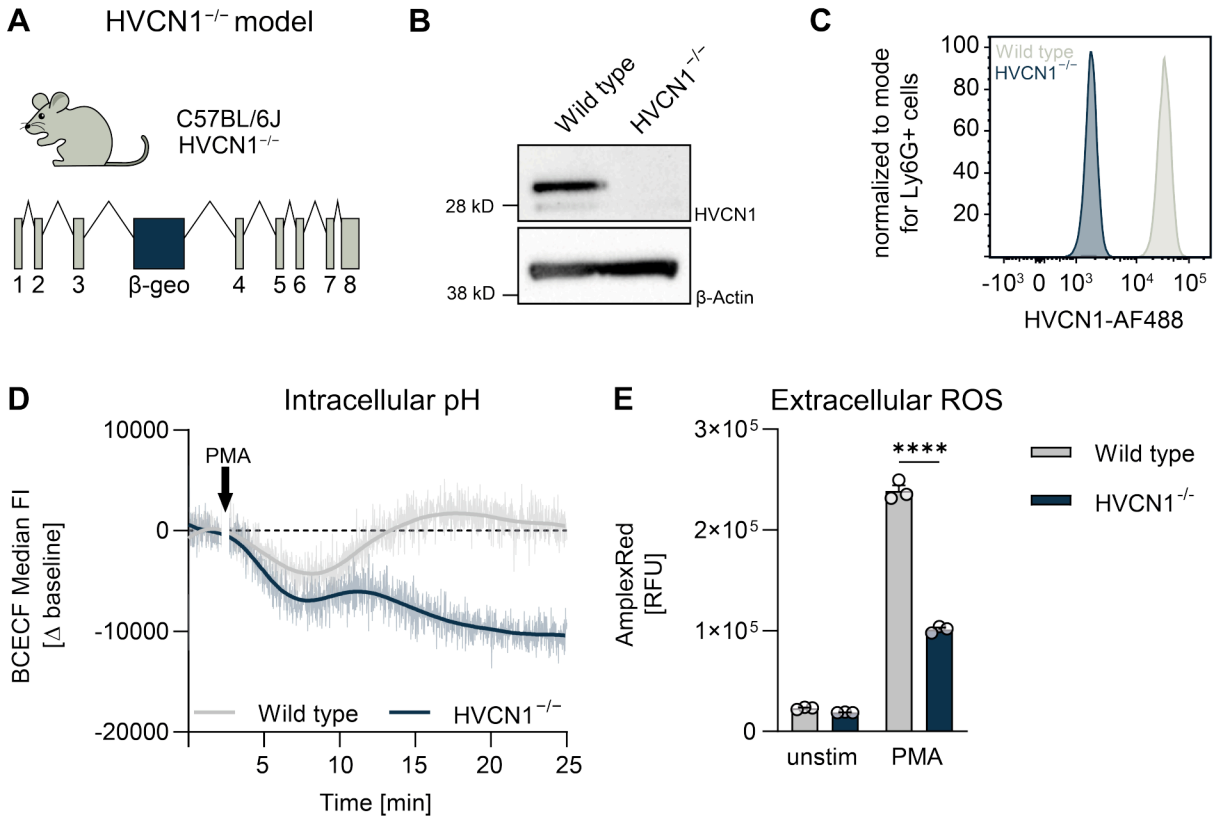

Figure 4.2| Bone marrow neutrophils from HVCN1$^{-/-}$ mice show intracellular acidification and reduced extracellular ROS production after stimulation.

A| Schematic representation of the HVCN1 KO locus generated using a genetrap vector that disrupts the HVCN1 locus by the insertion of a long, β-geo-containing cassette into the 3rd intron. B| Validation of HVCN1 deletion in neutrophils by western blot. C| Validation of HVCN1 deletion in neutrophils by flow cytometry. D| Analysis of intracellular pH in neutrophils loaded with 1.25 µM of the pH-sensitive dye BCECF-AM. Changes in pH after stimulation with 100 nM PMA were measured by flow cytometry and analyzed with the FlowJo Kinetics Tool extracting the median fluorescence intensity (MFI) per second. Data depicted as mean (faint line) with LOWESS curve fit (opaque line) (n = 3). E| Extracellular ROS levels in supernatants of neutrophils after treatment with 100 nM PMA were measured using AmplexRed reagent. Columns represent mean ± SEM (n = 3). Statistical significance was tested by one-way ANOVA with Bonferroni´s post-hoc test for multiple comparisons (****p≤0.0001).

4.2 NETosis

ROS were shown to be pivotal for the generation of neutrophil extracellular traps (NETs)[79]. This specialized form of inflammatory cell death (NETosis) is characterized by chromatin decondensation, cell lysis and ultimately ejection of loose chromatin strands decorated with toxic neutrophil granule proteins, such as MPO and neutrophil elastase (NE)[105]. Although the exact mechanisms of how ROS contribute to NETosis are not fully understood, neutrophils lacking a functional NADPH oxidase, like in Chronic Granulomatous Disease (CGD), are unable to undergo NETosis after PMA stimulation[79]. Since HVCN1$^{-/-}$ neutrophils exhibited reduced levels of ROS, it was hypothesized that they would also display diminished formation of NETs.

4.2.1 NET formation is increased in HVCN1$^{-/-}$ neutrophils

To analyze NET formation, wild type and HVCN1$^{-/-}$ neutrophils were stimulated with PMA for 4 hours. Cells were fixed and NET formation was visualized by staining for DNA (DAPI) and MPO (Fig. 3A). Both wild type and HVCN1$^{-/-}$ neutrophils showed formation of NETs upon stimulation with PMA. Interestingly, however, visual examination of microscopic images indicated that HVCN1$^{-/-}$ neutrophils release more NETs (Fig. 4.3 A). Quantification of NETotic nuclei revealed that only 5 % of wild type neutrophils but 19.5 % of HVCN1$^{-/-}$ neutrophils formed NETs 4 hours after stimulation (Fig. 4.3 B).

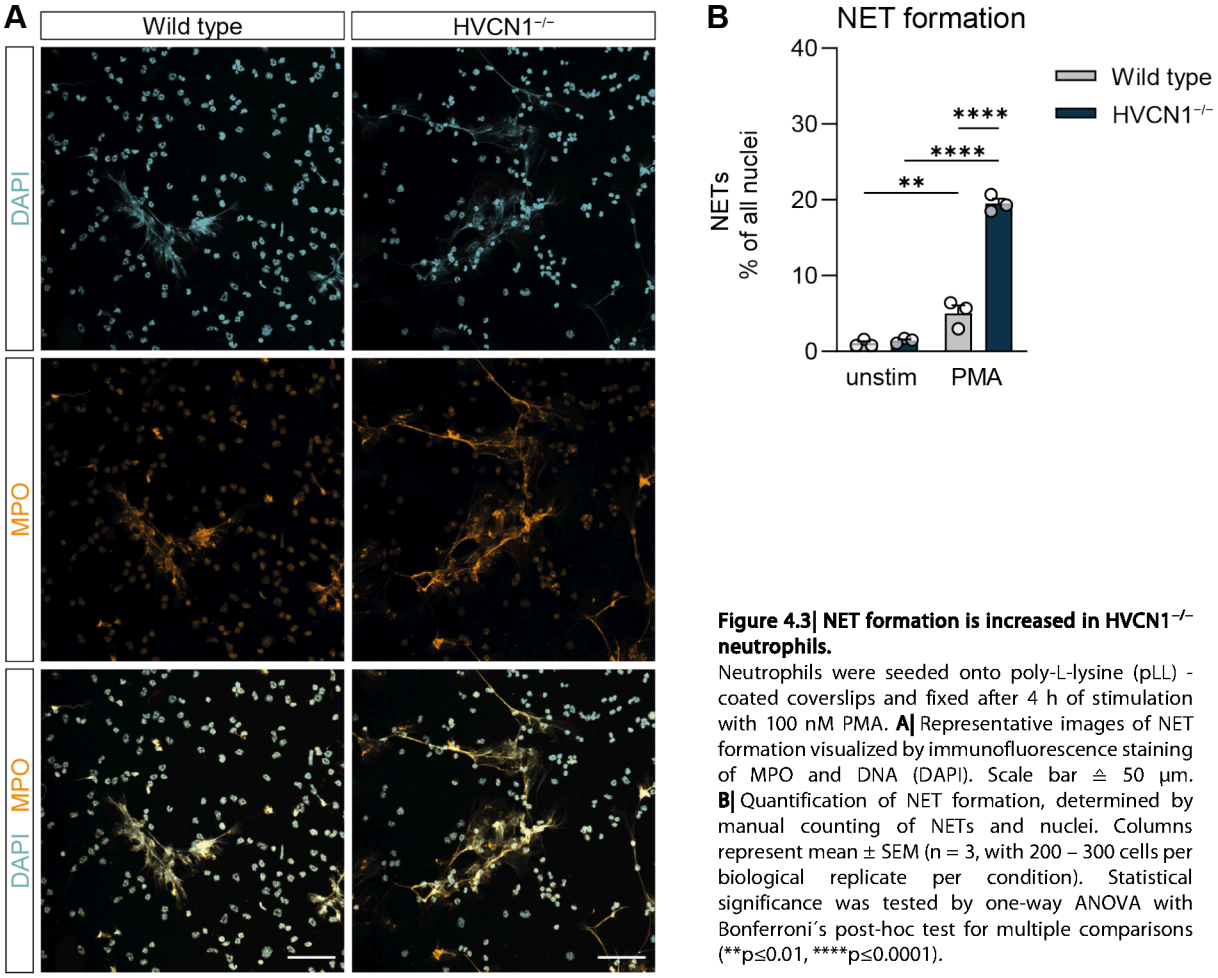

Figure 4.3| NET formation is increased in HVCN1$^{-/-}$ neutrophils.
Neutrophils were seeded onto poly-L-lysine (pLL) - coated coverslips and fixed after 4 h of stimulation with 100 nM PMA. **A|** Representative images of NET formation visualized by immunofluorescence staining of MPO and DNA (DAPI). Scale bar ≙ 50 µm. **B|** Quantification of NET formation, determined by manual counting of NETs and nuclei. Columns represent mean ± SEM (n = 3, with 200 – 300 cells per biological replicate per condition). Statistical significance was tested by one-way ANOVA with Bonferroni´s post-hoc test for multiple comparisons (**p≤0.01, ****p≤0.0001).

4.2.2 Chromatin decondensation is accelerated in HVCN1$^{-/-}$ neutrophils

The changes in nuclear morphology and decondensation of chromatin preceding NET formation are tightly regulated. Neuberg *et al.*[115] described that NETosis can be divided into three distinct phases according to chromatin status. In order to compare chromatin dynamics between wild type and HVCN1$^{-/-}$ neutrophils, cells were stimulated for 1 hour and 4 hours. Nuclei were stained

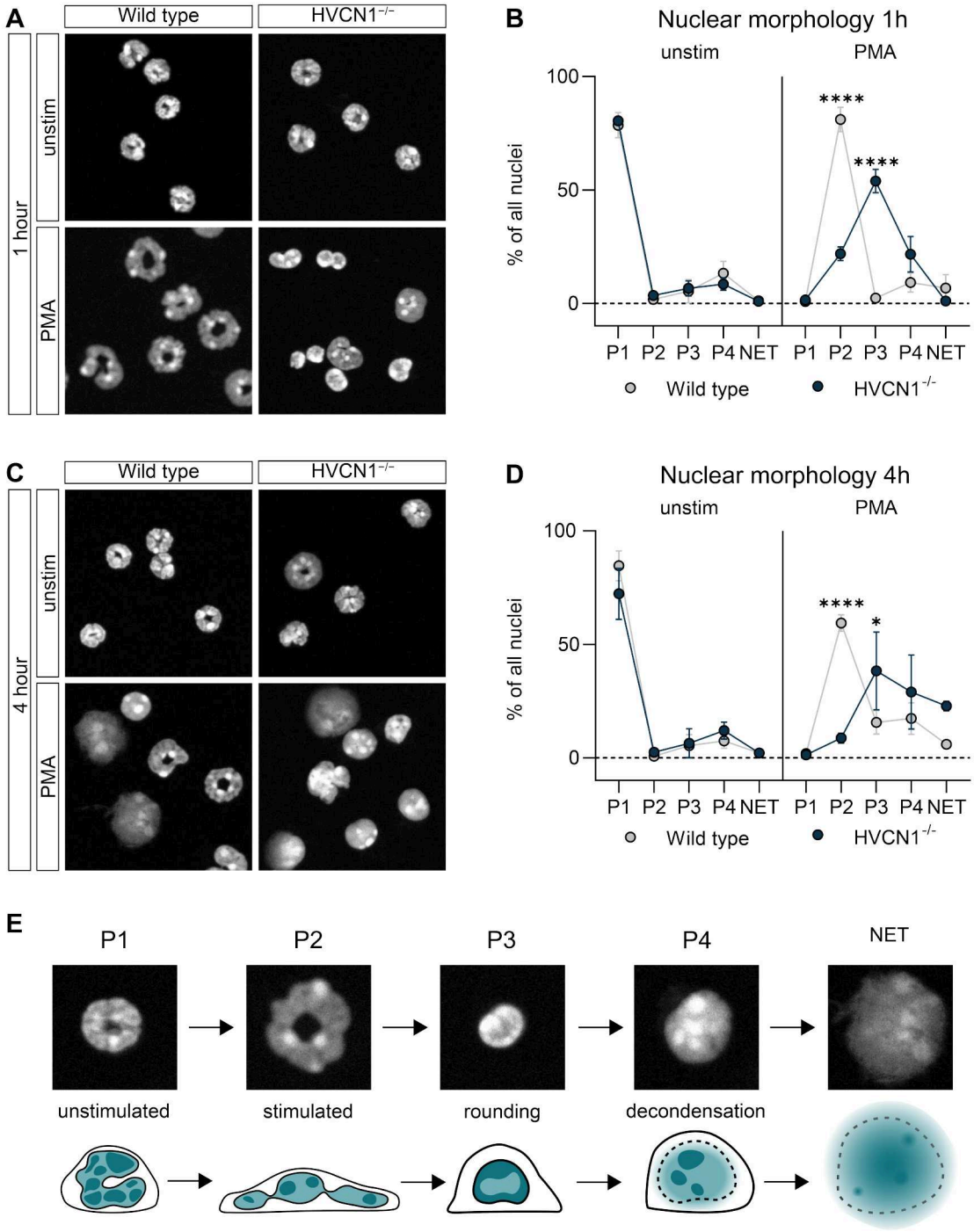

Figure 4.4| Chromatin decondensation is accelerated in HVCN1$^{-/-}$ neutrophils.
Neutrophils were stimulated for 1 h or 4 h with 100 nM PMA and DAPI staining was performed to visualize the chromatin. A| Images of nuclear morphology after 1 h of stimulation. B| Percentage of nuclei at different morphological stages of NETosis at 1 h of PMA stimulation. Nuclei identification and morphology parameter measurements were performed using CellProfiler™ and classification of phases (see E) was performed with the CellProfiler Analyst™ supervised machine learning. Dots represent mean ± SEM system (n = 3, with ~300 cells/replicate and condition). C| Images of nuclear morphology after 4 h of stimulation. D| Percentage of nuclei at different morphological stages of NETosis at 4 h of PMA stimulation. Dots represent mean ± SEM (n = 3, with ~ 300 cells/ replicate per condition). Statistical significance was tested by three-way ANOVA with Tukey's post-hoc test for multiple comparisons (*p≤0.05, ***p≤0.0001).

with DAPI, imaged and analyzed using the CellProfiler Software (Fig. 4.4 A and 4.4 C). For each nucleus, morphological features such as area shape, granularity, texture and intensity were determined. Subsequently, nuclei were classified using the supervised machine learning software CellProfiler Analyst applying a modified five-phase model of the distinct phases of chromatin status for murine neutrophils. The five phases were defined as 'P1 - unstimulated', 'P2 – lobulated', 'P3 – rounded', 'P4 – decondensed' and 'P5 – NET' (see scheme in Fig. 4.4 E).

As can be seen in Figs. 4.4 B and 4.4 D no significant differences could be detected between unstimulated wild type and HVCN1$^{-/-}$ neutrophils at 1 or 4 hours after stimulation. Here, more than 70% of all nuclei kept an unstimulated morphology, while some nuclei acquired features of P3 or P4, which most probably is an artifact due to misclassification. Following PMA stimulation, striking differences were observed between the nuclear morphology of wild type and HVCN1$^{-/-}$ neutrophils. One hour after stimulation (Fig. 4.4 B), around 80 % of all wild type neutrophils reached P2 while only very few displayed features of P3, P4 or NET-like morphology. In contrast, only 20% of the HVCN1$^{-/-}$ neutrophils remained in P2, while the majority of cell were detected in P3 and P4. This already indicated that changes in chromatin status were accelerated in HVCN1$^{-/-}$ neutrophils. 4 hours after stimulation (Fig. 4.4 D), 50% of all wild type neutrophils still showed P1 morphological features. The rest of the cells progressed to later stages of NETosis with around 20% in both P3 and P4, and 6% forming NETs. Only about 10% of all HVCN1$^{-/-}$ neutrophils remained in P1. Most nuclei showed features of P3, or already progressed to the late stages of NETosis. This further support the assumption that NETosis is accelerated in HVCN1$^{-/-}$ neutrophils.

4.2.3 HVCN1$^{-/-}$ neutrophils show increased histone citrullination

Previous findings raised the question of how HVCN1$^{-/-}$ neutrophils undergo increased NETosis despite producing less ROS. Besides the NADPH-dependent NETosis pathway, several studies describe a form of ROS-independent NETosis characterized by calcium-induced histone citrullination[206]. To check for histone citrullination, wild type and HVCN1$^{-/-}$ neutrophils were stimulated with PMA for 4 hours and subsequently stained for citrullinated histone 3 (citH3, Fig. 4.5 A). Quantification of citH3 revealed that histone citrullination was increased 7.5-fold in HVCN1$^{-/-}$ neutrophils compared to wild type controls (Fig. 4.5 B). While only 2% of all nuclei in wild type neutrophils showed citrullination, 15% of all nuclei in HVCN1$^{-/-}$ neutrophils were positive for citH3.

In summary, these experiments show that HVCN1$^{-/-}$ neutrophils exhibit accelerated NETotic changes in chromatin and enhanced histone citrullination leading to increased NET formation 4 hours after stimulation with PMA.

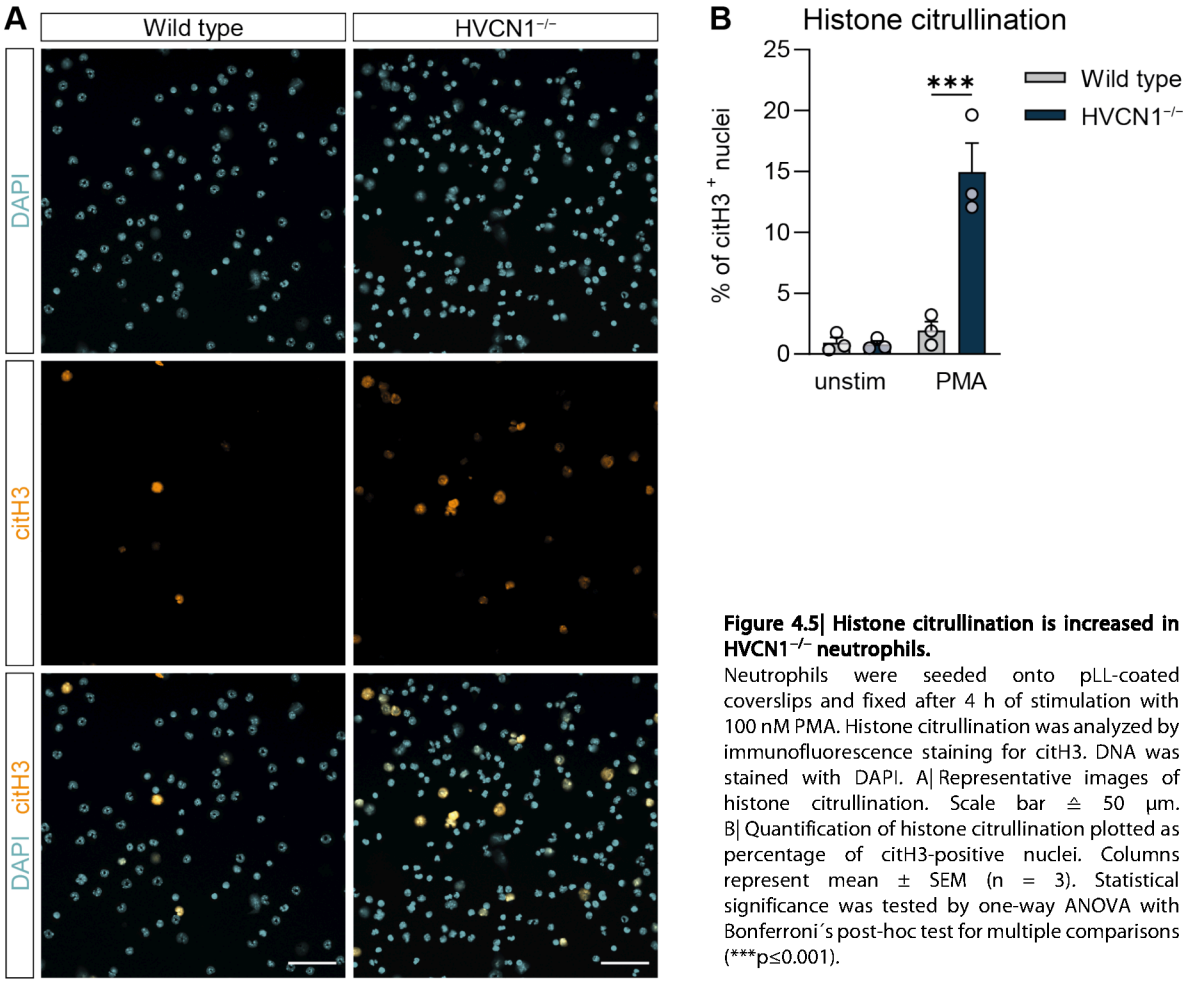

Figure 4.5| Histone citrullination is increased in HVCN1$^{-/-}$ neutrophils.
Neutrophils were seeded onto pLL-coated coverslips and fixed after 4 h of stimulation with 100 nM PMA. Histone citrullination was analyzed by immunofluorescence staining for citH3. DNA was stained with DAPI. A| Representative images of histone citrullination. Scale bar ≙ 50 µm. B| Quantification of histone citrullination plotted as percentage of citH3-positive nuclei. Columns represent mean ± SEM (n = 3). Statistical significance was tested by one-way ANOVA with Bonferroni´s post-hoc test for multiple comparisons (***p≤0.001).

4.3 Calcium dynamics

Histone citrullination is a calcium-regulated process. Citrullination is mediated by peptidyl arginine deiminase 4 (PAD4) and its activation requires calcium increase exceeding the homeostatic levels[126]. Thus, induction of NETosis by calcium ionophores, but not PMA, is associated with high levels of citH3. This raised the question, whether PMA stimulation induces different calcium dynamics in wild type and HVCN1$^{-/-}$ neutrophils.

4.3.1 PMA stimulation induces calcium influx in HVCN1$^{-/-}$ neutrophils

As the calcium-dependent histone citrullination was increased in HVCN1$^{-/-}$ neutrophils (Fig. 4.5), it was important to measure intracellular calcium levels in neutrophils after stimulation with PMA. To this end, neutrophils were loaded with the calcium-sensitive dye Fluo-4-AM and calcium influx kinetics were measured by flow cytometry.

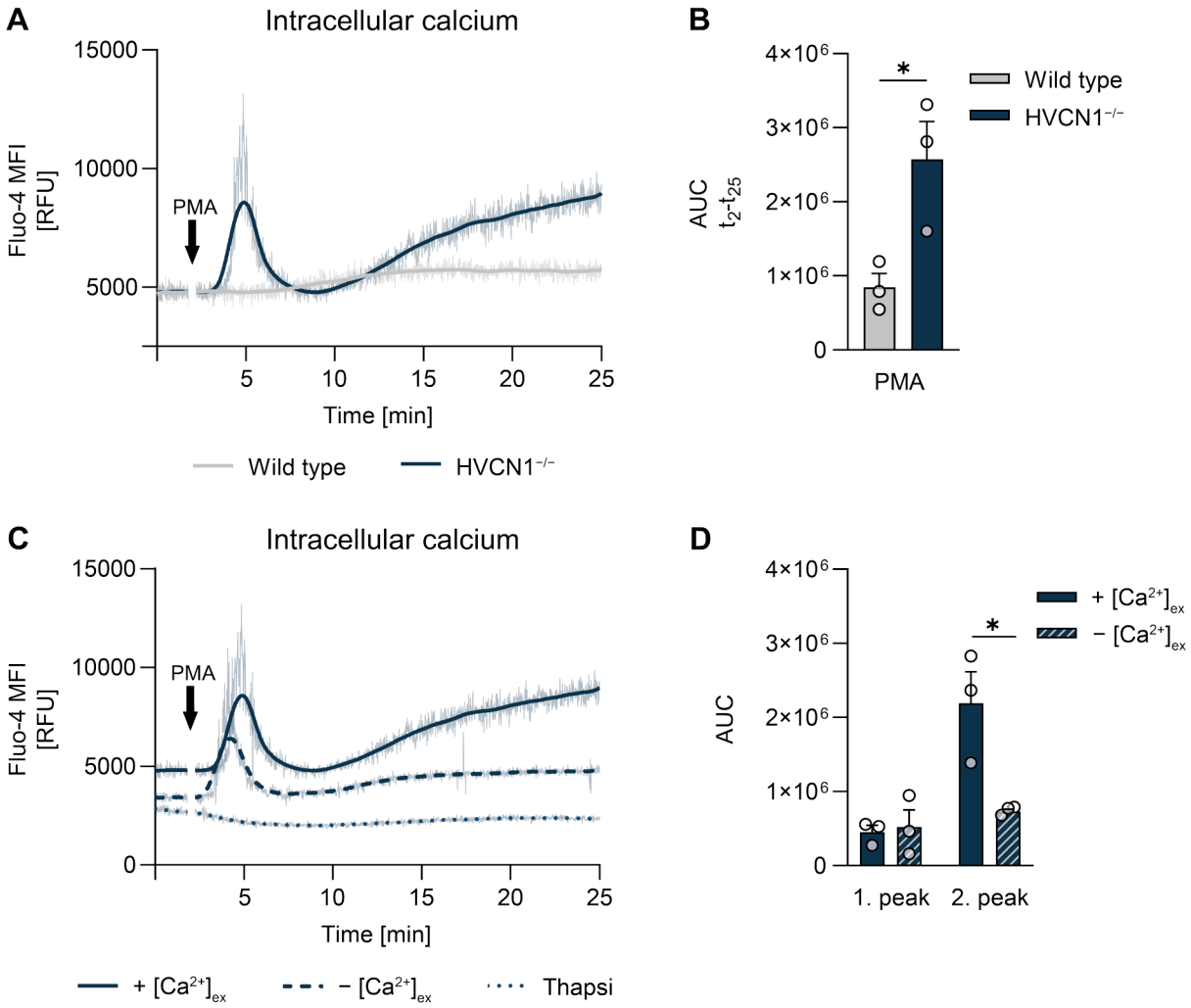

Figure 4.6| HVCN1$^{-/-}$ neutrophils show calcium influx from intracellular and extracellular compartments after PMA stimulation. Neutrophils were loaded with 2 µM Fluo-4-AM for 30 min at 37° C. Intracellular calcium levels were measured by flow cytometry and analyzed with the FlowJo Kinetics Tool extracting the median fluorescence intensity (MFI) per second. A| Calcium flux of neutrophils treated with 100 nM PMA at t = 2 min. Data depicted as mean (faint line) with LOWESS curve fit (opaque line) (n = 3). B| Area under the curve for PMA-induced calcium flux. Columns represent mean ± SEM (n = 3). Statistical significance was tested by unpaired t-test (*p≤0.05). C | Calcium flux of neutrophils treated with 100 nM PMA at t = 2 min in calcium-containing medium (continuous line), calcium-free medium (dashed line) or pretreated with 1 µM Thapsigargin for 20 minutes (dotted line). Data depicted as mean (faint line) with LOWESS curve fit (opaque line) (n = 3). D| Area under the curve for first peak (t = 2 min – t = 8.5 min) and second peak (t = 8.5 min – t = 25 min). Columns represent mean ± SEM (n = 3). Statistical significance was tested by unpaired t-test (*p≤0.05).

Unstimulated wild type and HVCN1$^{-/-}$ neutrophils exhibited equal levels of intracellular calcium (Fig. 4.6 A). After stimulation with PMA, wild type neutrophils did not show an influx of calcium. Interestingly, HVCN1$^{-/-}$ neutrophils exhibited a significant increase in intracellular calcium levels shortly after stimulation. The influx of calcium occurred in two distinct waves. One minute after addition of PMA, a sharp increase in intracellular calcium levels was detected, which peaked at 3 minutes and reached baseline levels at 7 minutes. Subsequently, the second wave of calcium influx started, still rising 23 minutes after stimulation (Fig. 4.6 A).

To identify the sources of calcium influx into HVCN1$^{-/-}$ neutrophils, the same experiment was conducted in calcium-free medium (Fig. 4.6 B). While the first wave of calcium influx could still be detected, the second wave was depleted in calcium-free medium. This indicates that during the first wave, calcium is released from intracellular stores while during the second wave, calcium enters from the extracellular space. In a subsequent experiment, an inhibitor of the sarcoplasmic/endoplasmic reticulum (ER) calcium ATPase called Thapsigargin was used to deplete calcium from the ER. Pretreatment of HVCN1$^{-/-}$ neutrophils with Thapsigargin led to depletion of the first calcium wave, indicating that the calcium in the first wave was indeed derived from the ER (Fig. 4.6 B).

In summary, it could be demonstrated that in HVCN1$^{-/-}$ neutrophils, PMA stimulation induced a release of calcium from the ER, followed by influx of calcium from the extracellular space.

4.3.2 Acidification alone is not sufficient to induce calcium release from the ER

Given the observed calcium mobilization in HVCN1$^{-/-}$ cells, we investigated which early changes in HVCN1$^{-/-}$ neutrophils would induce calcium influx. Since HVCN1 facilitates efflux of protons, a drop in cytosolic pH could be responsible for the release of calcium from the ER.

To test this hypothesis, I induced acidification in wild type neutrophils, in order to assess if this would induce a calcium influx comparable to HVCN1$^{-/-}$ neutrophils. To this end, wild type and HVCN1$^{-/-}$ neutrophils were pretreated for 10 minutes with dimethyl-amiloride, an inhibitor of the sodium-hydrogen exchanger (NHE1). NHE1 catalyzes the electroneutral exchange of intracellular protons and extracellular sodium, and thereby also plays a role in proton extrusion during NADPH oxidase activation (Fig. 4.7 A)[207].

To test the efficacy of amiloride, cells were loaded with the sodium-sensitive dye ING-II-AM and intracellular sodium kinetics were measured by flow cytometry (Fig. 4.7 B). As expected, while PMA stimulation only induced a minor influx of sodium in wild type neutrophils, sodium levels of HVCN1$^{-/-}$ neutrophils were highly elevated, indicating that NHE1 was in part compensating the excessive acidification caused by HVCN1 loss. Pretreatment of neutrophils with amiloride decreased sodium influx in both wild type and HVCN1$^{-/-}$ neutrophils.

In the presence of amiloride, pH measurements with BCECF-AM showed substantial acidification in PMA-stimulated HVCN1$^{-/-}$ neutrophils, highlighting the important compensatory role of NHE1

in these cells (Fig. 4.7 C). Furthermore, pretreatment of wild type neutrophils with amiloride led to an acidification level comparable to HVCN1$^{-/-}$ neutrophils. Hence, amiloride could be used to test if a decrease in pH would be sufficient to induce the release of calcium from the ER.

Surprisingly, however, pretreatment with amiloride failed to induce an influx of calcium in wild type neutrophils (Fig. 4.7 D), disproving the hypothesis of an acidification-induced calcium release from the ER. In contrast, HVCN1$^{-/-}$ neutrophils pretreated with amiloride displayed decreased levels of calcium in the second wave of influx, suggesting this calcium influx is a sodium-dependent mechanism.

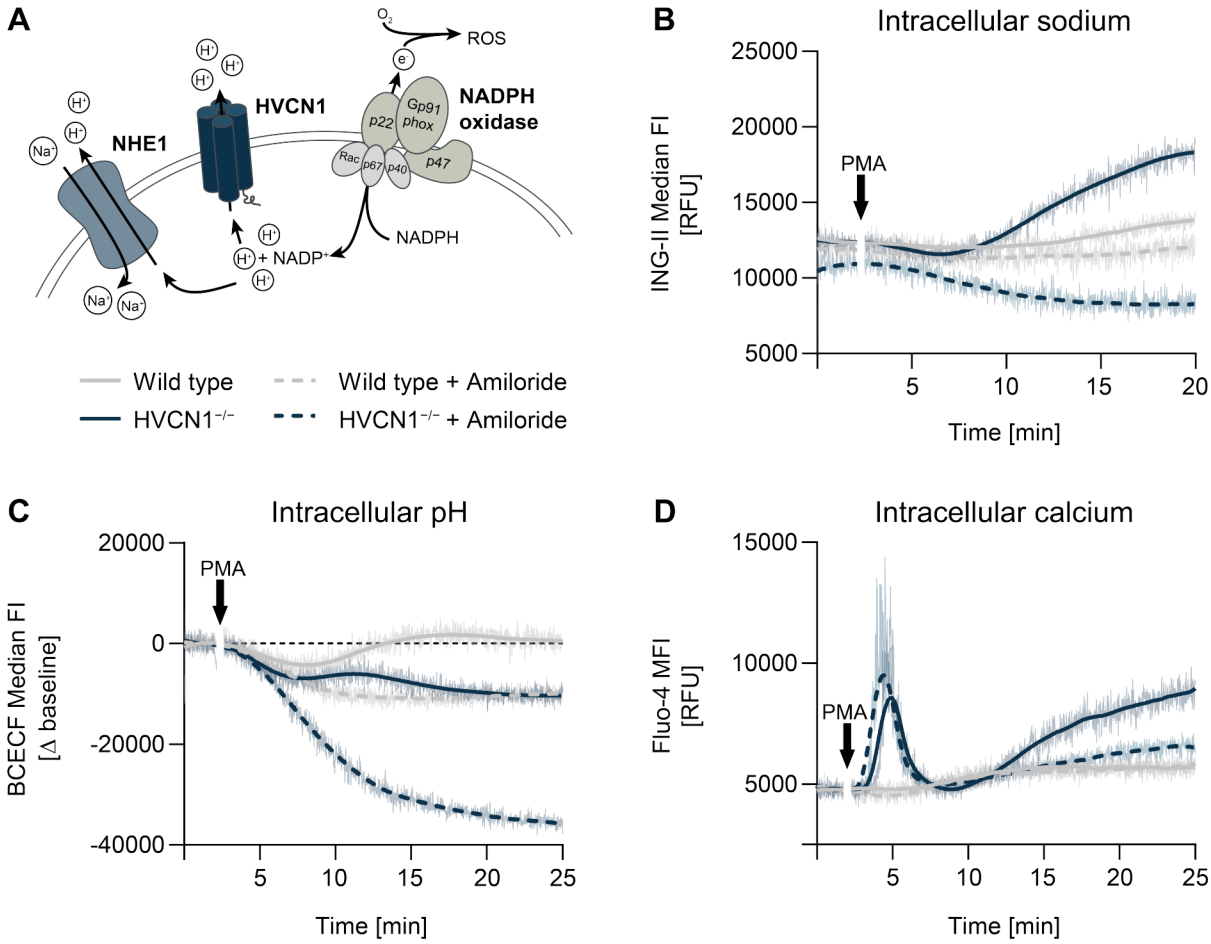

Figure 4.7| Amiloride induces acidification but no calcium influx in wild type neutrophils.
A| Schematic view of proton extrusion after activation of the NADPH oxidase. Intracellular protons produced during ROS production can leave the cell by electrogenic transport through HVCN1 or by electroneutral exchange with sodium through NHE1. B| Intracellular sodium levels. Neutrophils were loaded with 2.5 µM ING-II, AM for 1 h at RT. Sodium levels after stimulation with 100 nM PMA were measured by flow cytometry and analyzed with the FlowJo Kinetics Tool extracting the median fluorescence intensity (MFI) per second. Neutrophils were either pretreated with 20 µM di-methyl amiloride for 10 min (dashed line) or left untreated (continuous line). Data depicted as MFI (faint line) from one representative experiment with LOWESS curve fit (opaque line) (n = 2) C| Intracellular pH. Neutrophils were loaded with 1.25 µM BCECF-AM for 30 min at RT. pH after stimulation with 100 nM PMA was measured by flow cytometry and analyzed with the FlowJo Kinetics Tool extracting the median fluorescence intensity (MFI) per second. Neutrophils were either pretreated with 20 µM di-methyl amiloride for 10 min (dashed line) or left untreated (continuous line). Data depicted as mean (faint line) with LOWESS curve fit (opaque line) (n = 3). D| Intracellular calcium. Neutrophils were loaded with 2 µM Fluo-4-AM for 30 min at 37° C. Calcium levels after treatment with 100 nM PMA were measured by flow cytometry and analyzed with the FlowJo Kinetics Tool extracting the median fluorescence intensity (MFI) per second. Neutrophils were either pretreated with 20 µM di-methyl amiloride for 10 min (dashed line) or left untreated (continuous line). Data depicted as mean (faint line) with LOWESS curve fit (opaque line) (n = 3).

4.3.3 Strong depolarization is induced upon activation of HVCN1$^{-/-}$ neutrophils

Since acidification alone failed to induce calcium influx, another mechanism, presumably during early PMA stimulation, must cause this effect. Besides balancing the pH, the electrogenic efflux of protons through HVCN1 also prevents membrane depolarization. El Chemaly *et al.*[173] already showed that besides the intracellular pH also the membrane potential of HVCN1$^{-/-}$ neutrophils is changed compared to wild type controls. To verify this finding, neutrophils were stimulated with PMA in the presence of $DiBAC_4(3)$, a membrane potential-sensitive fluorescent probe that can enter depolarizing cells.

PMA stimulation induced membrane depolarization in both wild type and HVCN1$^{-/-}$ neutrophils (Fig. 4.8 A). However, depolarization was significantly higher in HVCN1$^{-/-}$ neutrophils. Pretreatment with amiloride, however, did not significantly change the extent of membrane depolarization in wild type or HVCN1$^{-/-}$ neutrophils.

In an attempt to limit depolarization, neutrophils were pretreated with valinomycin. Valinomycin is a potassium ionophore and therefore could counterbalance depolarization by mediating potassium efflux. Simultaneous administration of valinomycin and PMA delayed, but did not completely abolish membrane depolarization in HVCN1$^{-/-}$ neutrophils (Fig. 4.8 B). Upcoming experiments will now test whether valinomycin can also delay calcium influx. This would suggest that intracellular calcium mobilization in HVCN1$^{-/-}$ neutrophils is induced by membrane depolarization.

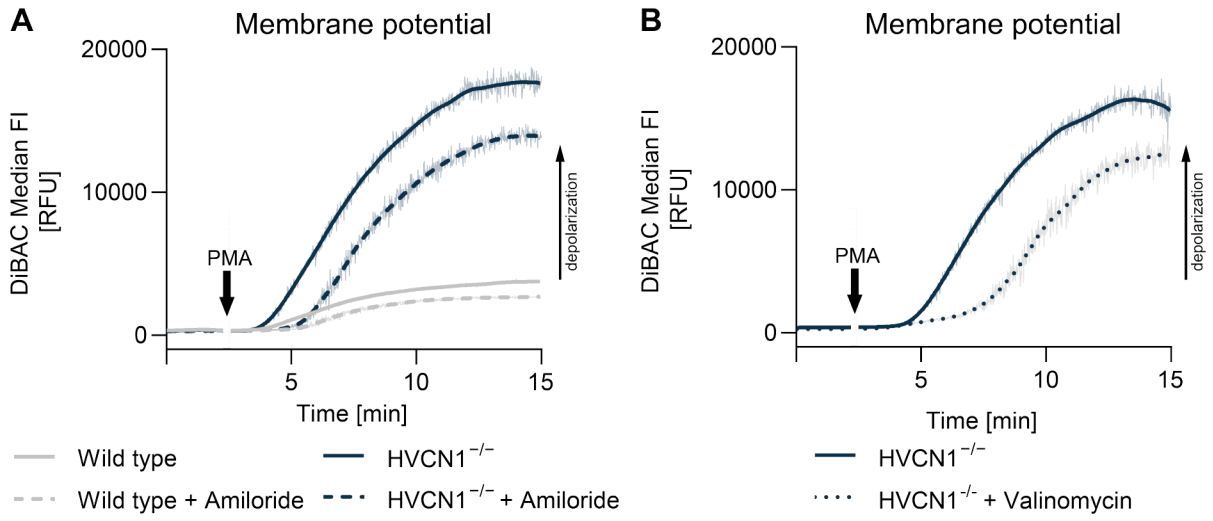

Figure 4.8| Membrane depolarization is augmented in HVCN1$^{-/-}$ neutrophils.
In the presence of 50 nM DiBAC(3)4, neutrophils were stimulated with 100 nM PMA and DiBAC fluorescence was measured by flow cytometry. Data was analyzed with the FlowJo Kinetics Tool extracting the median fluorescence intensity (MFI) per second. Increase in DiBAC fluorescence indicates membrane depolarization. A| Neutrophils were either pretreated with 20 µM di-methyl amiloride for 10 min (dashed line) or left untreated (continuous line). Data depicted as mean (faint line) with LOWESS curve fit (opaque line) (n = 3). B| Neutrophils were simultaneously treated with PMA and 1 µM valinomycin (dotted line) or with PMA only (continuous line). Data depicted as mean (faint line) with LOWESS curve fit (opaque line) (n = 2).

4.3.4 Neutrophils express different calcium channels

To further unravel the mechanism of calcium release from the ER, it is important to understand through which channels calcium is released. Some candidates were selected based on a literature review and proteomic data obtained from mass spectrometry of wild type and HVCN1$^{-/-}$ neutrophils. Expression of candidate genes was validated by qPCR (Fig. 4.9). Expression levels were normalized to the house keeping gene GAPDH. Neutrophils expressed both, *Itpr1* and *Itpr2*, which encode for the two isoforms of the IP3 receptor. Furthermore, neutrophils expressed high levels of *Tpcn1* and *Tpcn2*, which encode for two pore channel 1 and 2 (TPC1 and TPC2). TPCs are located on acidic intracellular organelles and can be activated by the messenger molecules NAADP and PI(3,5)P_2 or through voltage changes across the organelle membrane[208]. While ryanodine receptor 1 seems to be expressed, its other isoforms could not be detected in neutrophils. Lastly, neutrophils did not express classical voltage-gated calcium channels (data not shown).

Overall, the were no differences in expression levels for all channels between wild type and HVCN1$^{-/-}$ neutrophils.

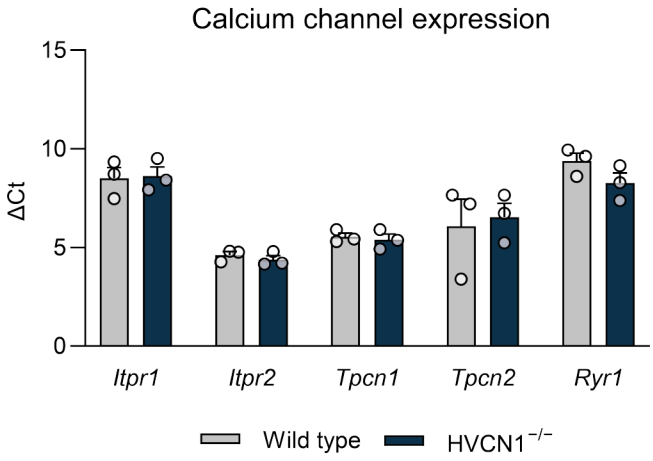

Figure 4.9| Neutrophils express different intracellular calcium channels.
Gene expression in naïve neutrophils was analyzed by qPCR. Genes with distinct melting curves and Ct values < 35 were considered expressed and plotted normalized to the house keeping gene GAPDH. Columns represent mean ± SEM (n = 3).

4.4 Mitochondrial function

PMA stimulation of HVCN1$^{-/-}$ neutrophils induces NET formation possibly through an increased calcium-induced histone citrullination. It was previously shown that NETosis induced by calcium ionophores also features the production of ROS by mitochondria[128]. This raised the question if HVCN1$^{-/-}$ neutrophils also show a similar activation pattern.

4.4.1 Intracellular ROS is increased in HVCN1$^{-/-}$ neutrophils

In order to measure the generation of mitochondrial ROS, neutrophils were loaded with the mitochondrial superoxide indicator MitoSOX and its signal was quantified by flow cytometry after 30 minutes of PMA stimulation (Fig. 4.9 A). The MitoSOX signal was comparable between unstimulated wild type and HVCN1$^{-/-}$ neutrophils. Stimulation with PMA did not induce an increase of mitochondrial superoxide in wild type neutrophils. In contrast, HVCN1$^{-/-}$ neutrophils displayed a 2-fold increase of superoxide 30 minutes after stimulation. However, microscopy analysis revealed that especially in stimulated HVCN1$^{-/-}$ neutrophils, MitoSOX appeared to exit mitochondria and to localize more to the cytoplasm and nucleus (Fig. 4.9 B). Hence, it is likely that the signal measured by flow cytometry is not representative exclusively of mitochondrial ROS. This phenomenon was already reported by other groups and can be explained by the localization mechanism of MitoSOX which is based on the negatively charged mitochondrial matrix[209,210].

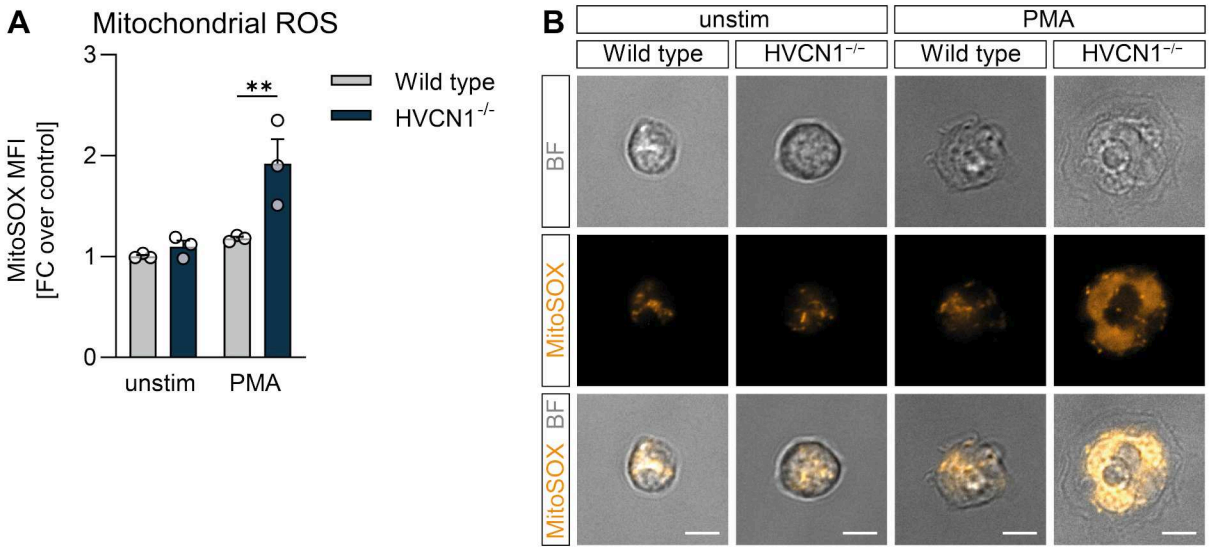

Figure 4.10| MitoSOX cannot be used to measure mitochondrial ROS in neutrophils.
A| Levels of mitochondrial ROS were analyzed in neutrophils which were loaded with 2.5 µM MitoSOX for 20 min at RT and subsequently stimulated with 100 nM PMA for 30 min. MitoSOX median FI was determined by flow cytometry and plotted as fold change over the MFI of unstimulated wild type cells. Columns represent mean ± SEM (n = 3). Statistical significance was tested by one-way ANOVA with Bonferroni´s post-hoc test for multiple comparisons (**p≤0.01). B| Microscopic analysis of MitoSOX localization in unstimulated and PMA-stimulated neutrophils. BF, bright field images. Scale bar ≙ 5 µm.

Since MitoSOX did not yield reliable results, general intracellular ROS production was measured using the ROS-sensitive probe CM-H_2DCFDA. Indeed, intracellular ROS levels of unstimulated wild type and HVCN1$^{-/-}$ neutrophils were comparable, while PMA stimulation induced a significantly higher ROS production in HVCN1$^{-/-}$ neutrophils (Fig. 4.11 A). Of course, these results do not unequivocally show that increased intracellular ROS levels in HVCN1$^{-/-}$ neutrophils are of mitochondrial origin but more experiments could be conducted to exclude other sources of ROS. In line with the elevated intracellular ROS production, PMA treated HVCN1$^{-/-}$ neutrophils also showed increased oxidative damage of nucleic acids, which was measured by histology-based quantification of 8-OHdG, an oxidized form of guanosine (Fig. 4.11 B).

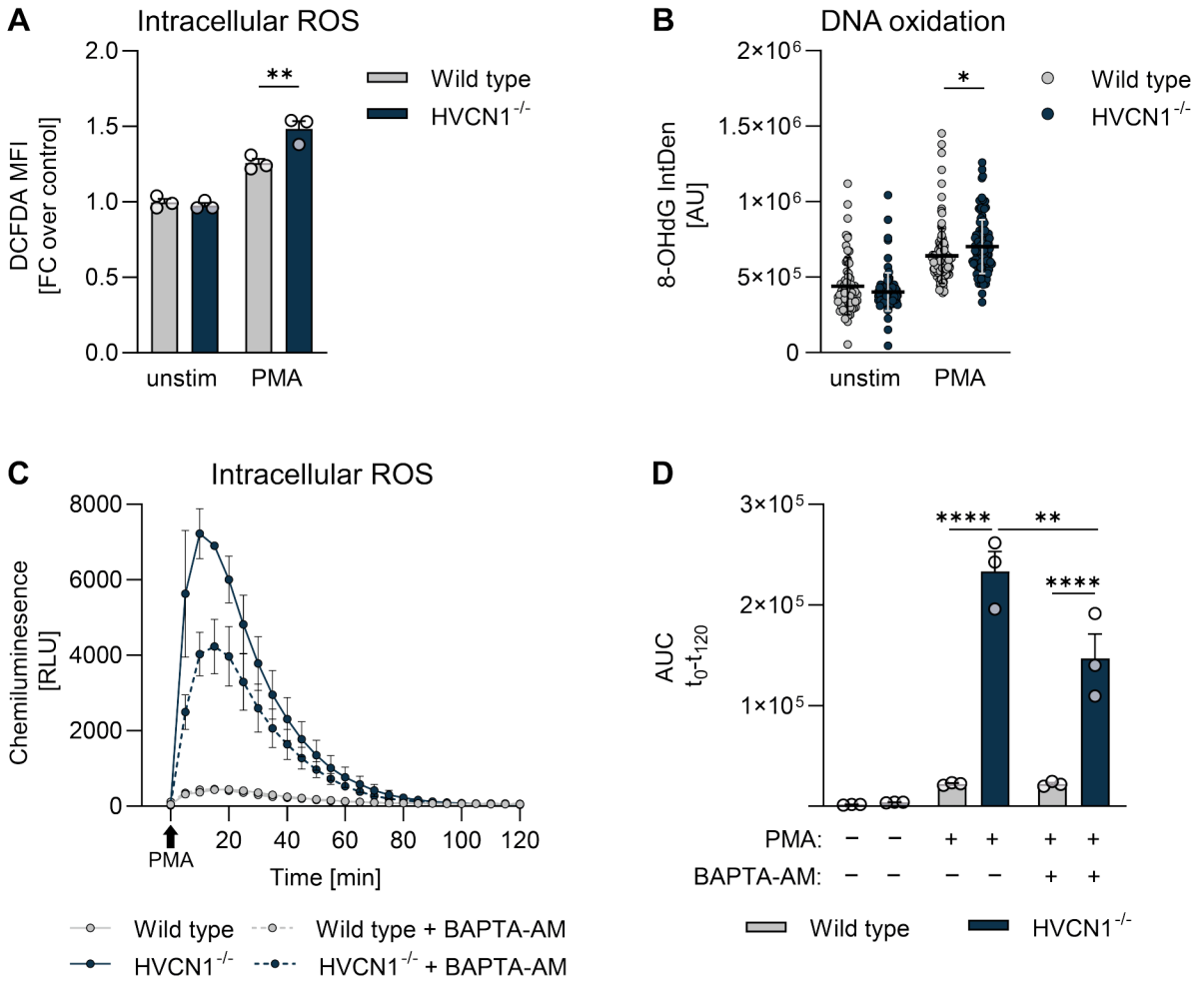

Figure 4.11| Intracellular ROS is increase in HVCN1$^{-/-}$ neutrophils after stimulation.
A| Levels of intracellular ROS were analyzed in neutrophils which were loaded with 2.5 µM CM-H_2DCFDA for 20 min at RT and subsequently stimulated with 100 nM PMA for 30 min. DCFDA median FI was determined by flow cytometry and plotted as fold change over the MFI of unstimulated wild type cells. Columns represent mean ± SEM (n = 3). Statistical significance was tested by one-way ANOVA with Bonferroni´s post-hoc test for multiple comparisons (**p≤0.01). B| DNA oxidation was determined by quantification of 8-OHdG levels in neutrophils stimulated with 100 nM PMA for 3 h. 8-OHdG was detected by immunofluorescence staining of fixed cells. Dots represent single cells with line at mean ± SD (n = 1, with 100 cells per condition). Statistical significance was tested by one-way ANOVA with Bonferroni´s post-hoc test for multiple comparisons (*p≤0.05). C| Intracellular ROS was measured by luminol-amplified luminescence assay. Neutrophils pretreated with 10 µM BAPTA-AM or left untreated for 30 min. Subsequently, luminol mix and 100 nM PMA were added to cells and chemiluminescent signal was measured every 5 min for a total of 2 h. D| Area under the curve for intracellular ROS measurement by luminol-amplified luminescence. Columns represent mean ± SEM (n = 3). Statistical significance was tested by one-way ANOVA with Bonferroni´s post-hoc test for multiple comparisons (**p≤0.01, ****p≤0.0001).

Furthermore, in order to establish whether the increased intracellular ROS production depended on calcium mobilization, neutrophils were pretreated with the intracellular calcium chelator BAPTA-AM and ROS levels were determined by the luminol-amplified luminescence assay. The increased intracellular ROS production by HVCN1$^{-/-}$ neutrophils after PMA stimulation could be confirmed (Fig. 4.11 C and D). The kinetic measurement also revealed that ROS production peaks around 15 to 20 minutes after addition of PMA and is exhausted after 80 minutes (Fig. 4.11 C). While addition of BAPTA-AM did not influence ROS production in wild type neutrophils, it decreased intracellular ROS production in HVCN1$^{-/-}$ neutrophils by ~ 30 % (Fig. 4.11 D). These results indicate that elevated intracellular ROS levels in HVCN1$^{-/-}$ neutrophils are partially dependent on calcium mobilization.

4.4.2 Mitochondrial membrane potential collapses rapidly in HVCN1$^{-/-}$ neutrophils

Little is known about how calcium can influence mitochondria in neutrophils. More extensive studies in cardiac muscle cells for example show that mitochondria can take up large amounts of calcium, however an overload of calcium can lead to dissipation of the mitochondrial transmembrane potential ($\Delta\Psi m$) which is also associated with increased production of ROS[211].

To analyze the mitochondrial transmembrane potential ($\Delta\Psi m$), neutrophils were loaded with tetramethylrhodamine methyl ester (TMRM), a positively charged dye that accumulates in mitochondria with a negative $\Delta\Psi m$. The uncoupling agent FCCP was used as positive control, since it is known to completely depolarize the mitochondrial membrane. Unstimulated wild type and HVCN1$^{-/-}$ neutrophils showed no differences in $\Delta\Psi m$ (Fig. 4.12 A). After 30 minutes of PMA stimulation, wild type neutrophils showed a slight depolarization of the mitochondrial membrane. Strikingly, PMA stimulation induced a complete dissipation of the $\Delta\Psi m$ in HVCN1$^{-/-}$ neutrophils. To test if calcium was responsible for dissipation of the $\Delta\Psi m$, kinetic measurement of TMRM fluorescence were conducted in the absence and presence of BAPTA-AM. Indeed, intracellular chelation of calcium could prevent the rapid depolarization of the mitochondrial membrane in HVCN1$^{-/-}$ neutrophils (Fig. 4.12 B and C). As the $\Delta\Psi m$ of HVCN1$^{-/-}$ neutrophils rapidly drops after addition of PMA, it is likely that calcium released from the ER is quickly taken up by mitochondria. In fact, stimulation of HVCN1$^{-/-}$ neutrophils in calcium-free medium could not rescue $\Delta\Psi m$ dissipation, indicating that transfer of calcium from the ER into mitochondria is responsible for depolarization of mitochondria (Fig. 4.12 D and E).

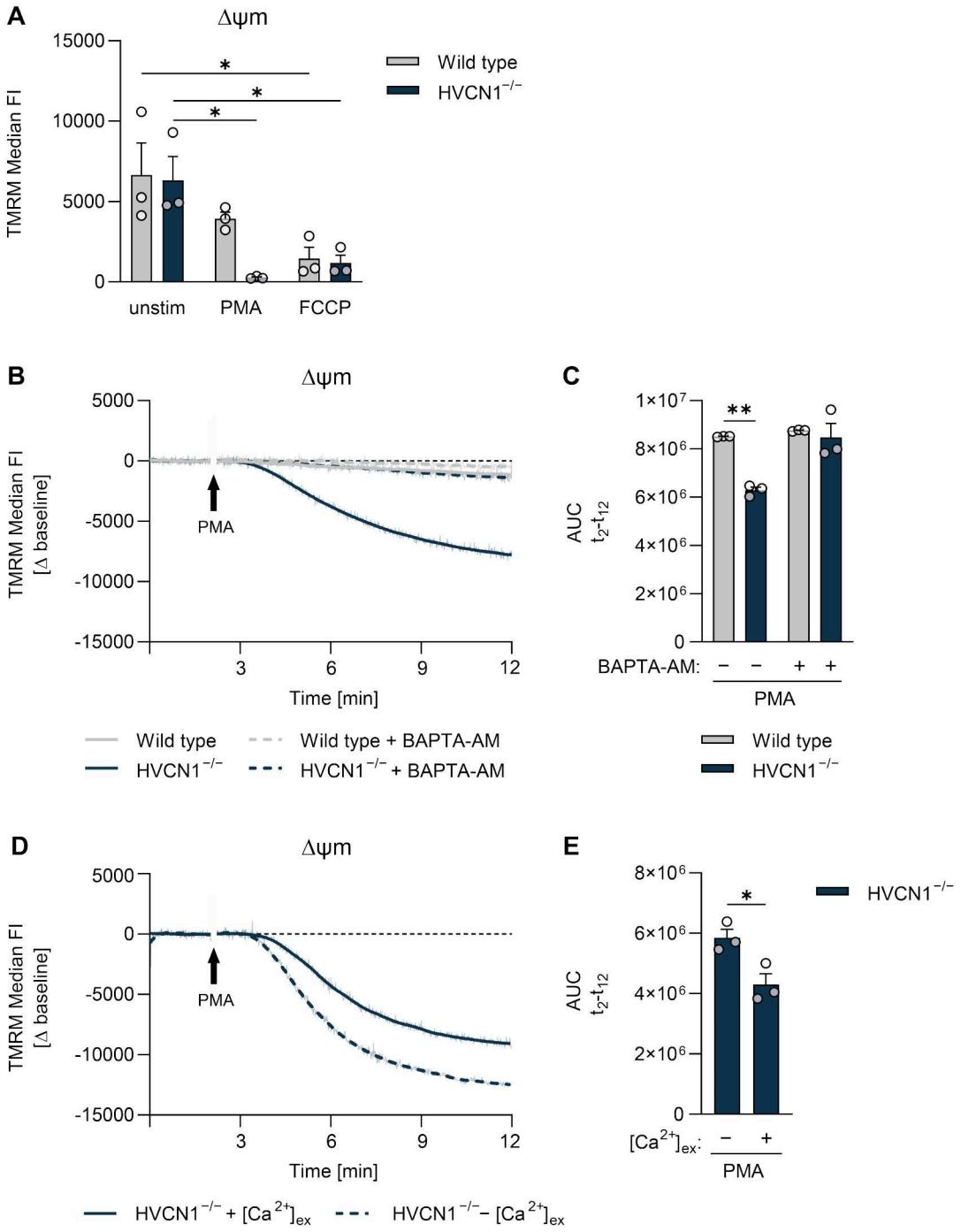

Figure 4.12| Dissipation of the ΔΨm in HVCN1$^{-/-}$ neutrophils is caused by calcium release from intracellular stores.
To measure the mitochondrial ΔΨm, neutrophils were loaded with 50 nM TMRM for 30 min at 37° C. A| TMRM median FI of unstimulated neutrophils and neutrophils stimulated with 100 nM PMA or 1 µM FCCP for 30 min. Columns represent mean ± SEM (n = 3). Statistical significance was tested by one-way ANOVA with Bonferroni´s post-hoc test for multiple comparisons (*p≤0.05). B| Kinetic measurement of ΔΨm depicted as TMRM median FI per second normalized to baseline for neutrophils stimulated with 100 nM PMA. Neutrophils were either pretreated with 10 µM BAPTA-AM for 30 min (dashed line) or left untreated (continuous line). Data depicted as mean (faint line) with LOWESS curve fit (opaque line) (n = 3). C| Area under the curve for ΔΨm from time point of PMA stimulation (t = 2 min). Columns represent mean ± SEM (n = 3). Statistical significance was tested by one-way ANOVA with Bonferroni´s post-hoc test for multiple comparisons (**p≤0.01). D| Kinetic measurement of ΔΨm depicted as TMRM median FI per second normalized to baseline for neutrophils stimulated with 100 nM PMA in calcium-free (dashed line) or calcium-containing medium (continuous line). Data depicted as mean (faint line) with LOWESS curve fit (opaque line) (n = 3). E| Area under the curve for ΔΨm from time point of PMA stimulation (t = 2 min). Columns represent mean ± SEM (n = 3). Statistical significance was tested by one-way ANOVA with Bonferroni´s post-hoc test for multiple comparisons (**p≤0.01).

4.4.3 mPTP opening is not involved in mitochondrial depolarization

Mitochondrial calcium overload is not only associated with increased production of ROS, but was also shown to induce the opening of the mitochondrial permeability transition pore (mPTP). This non-selective pore can transiently open and allows ions and molecules to cross the inner mitochondrial membrane. This, in turn leads to further dissipation of the ΔΨm and eventually to the release of cell death-inducing factors[212]. Recently, Vorobjeva *et al.*[213] demonstrated that the mPTP is associated with calcium ionophore-induced NETosis. Thus, opening of the mPTP could also be involved in NET formation in HVCN1$^{-/-}$ neutrophils upon PMA stimulation.

To test for mPTP opening, neutrophils were subjected to a calcein quenching assay. Neutrophils were loaded with the cell- and mitochondria-permeant dye calcein-AM. Subsequent treatment with cobalt induced quenching of calcein only in the cytoplasm since it cannot cross the inner mitochondrial membrane. Only upon opening of the mPTP, cobalt can enter and quench calcein within the mitochondria. Ionomycin was used as a positive control.

As shown in Fig. 4.13, no difference in calcein fluorescence were detected between unstimulated wild type and HVCN1$^{-/-}$ neutrophils. After treatment with ionomycin, calcein fluorescence was completely absent in both genotypes indicating a permanent and complete opening of the mPTP. However, after PMA stimulation only a minor decrease in fluorescence was observed in both wild type and HVCN1$^{-/-}$ neutrophils, indicating a moderate or only transient opening of the mPTP. This suggests that there is no signification contribution of mPTP opening to NET formation in HVCN1$^{-/-}$ neutrophils.

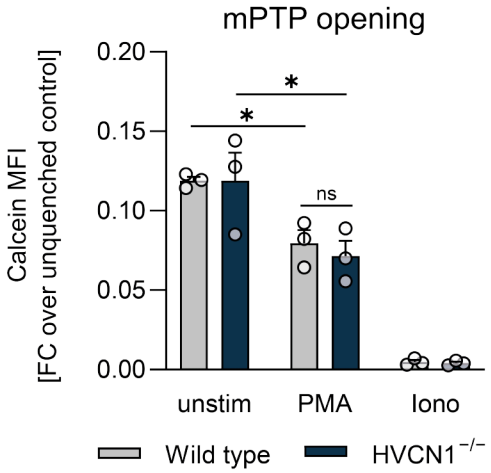

Figure 4.13| No differences in mPTP opening between wild type and HVCN1$^{-/-}$ neutrophils.
Neutrophils were loaded with 100 nM calcein AM for 20 min at 37° C, rested for another 15 min and fluorescence was quenched by adding 400 µM $CoCl_2$. Then cells were left untreated or stimulated with 100 nM PMA or 2 µM ionomycin for 30 min. Calcein fluorescence was assessed by flow cytometry. Data is depicted as fold change over the unquenched control. Columns represent mean ± SEM (n = 3). Statistical significance was tested by one-way ANOVA with Bonferroni´s post-hoc test for multiple comparisons (*p≤0.05).

4.4.4 Loss of HVCN1 does not impair mitochondrial fitness at steady state

To further exclude the possibility that mitochondria in HVCN1$^{-/-}$ neutrophils are already impaired before stimulation with PMA, mitochondria were stained with MitoTracker to analyze mitochondrial mass (Fig. 4.14 A). Microscopic inspection as well as quantification by flow cytometry (Fig. 4.14 B) revealed no differences in MitoTracker signal in either genotype, indicating no differences in mitochondrial mass at steady state.

Furthermore, mitochondrial fitness was examined using the Seahorse XF Cell Mito Stress Test which can measure the oxygen consumption rate. Compared to other immune cells, neutrophils show a relatively low basal respiration, since they only have few mitochondria and mostly rely on glycolysis for energy supply. Indeed, both wild type and HVCN1$^{-/-}$ neutrophils displayed a similarly low basal respiration (t0 – t20). Also the maximal respiration, after addition of the uncoupling agent FCCP, was comparable between wild type and HVCN1$^{-/-}$. These results indicate that mitochondria of HVCN1$^{-/-}$ neutrophils do not seem to have any defects in the absence of PMA stimulation.

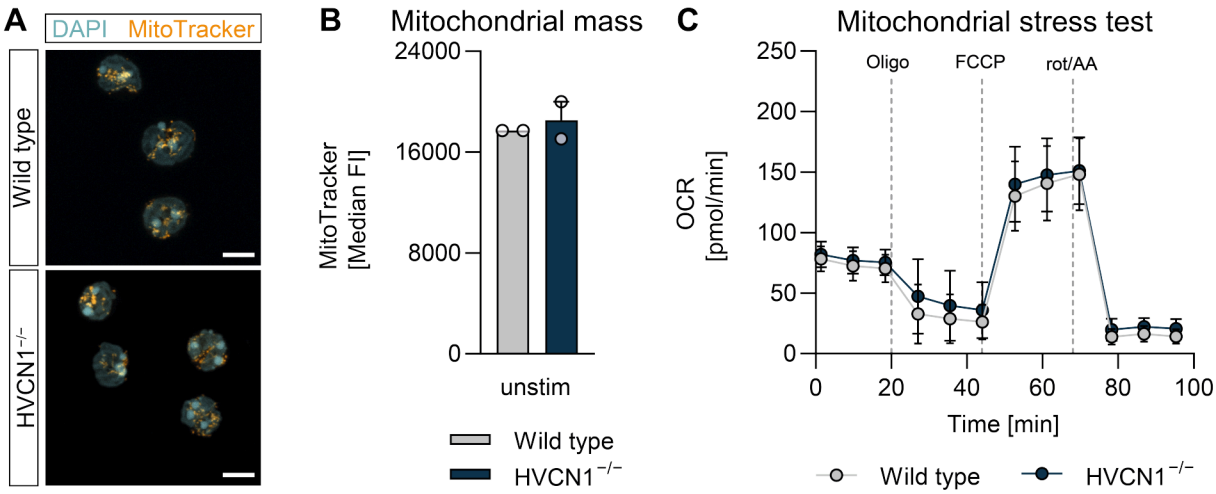

Figure 4.14 Mitochondrial mass and fitness do not differ steady state between wild type and HVCN1$^{-/-}$ neutrophils.
A| For microscopic analysis of mitochondria, neutrophils were loaded with 50 nM MitoTracker Red for 30 min at 37° C and seeded onto coverslips. After fixation, DNA was counterstained with DAPI. Scale bar ≙ 5 µm. **B|** Mitochondrial mass was quantified by flow cytometry in neutrophils loaded with 50 nM MitoTracker Green. Columns represent mean ± SD (n = 2). C| Mitochondrial fitness was assessed using the Agilent Seahorse XF Cell Mito Stress Test Kit. Oxygen consumption rate (OCR) was determined after addition of 1 µM oligomycin, 1 µM FCCP and 0.5 µM antimycin A/ 0.5 µM rotenone.

In summary, we could not find evidence for impaired mitochondria in HVCN1$^{-/-}$ neutrophils in the resting state. After stimulation however, a rapid dissipation of ΔΨm was observed in HVCN1$^{-/-}$ neutrophils. Loss of ΔΨm is probably driven by mitochondrial influx of calcium from the ER, since treatment with BAPTA-AM rescued the dissipation whereas absence of extracellular calcium did not. Mitochondria depolarization then resulted in increased ROS production, leading to greater DNA oxidation.

4.5 Increased NETosis HVCN1$^{-/-}$ neutrophils is dependent on calcium

After identifying substantial differences in the activation of HVCN1$^{-/-}$ neutrophils in response to PMA (i.e., increased calcium levels and production of intracellular ROS), I next investigated if either of the two factors could be responsible for the enhanced NET formation. For this purpose, wild type and HCVN1$^{-/-}$ neutrophils were activated with PMA in the presence of BAPTA-AM or the antioxidant N-acetyl cysteine (NAC). Following 4 hours of PMA stimulation, NET formation and histone citrullination were assessed using immunofluorescence microscopy.

As shown in Fig. 4.15 A and B, pretreatment with BAPTA-AM or NAC only had a minor impact on NET formation in wild type neutrophils, reducing the percentage of NETotic nuclei from 5% to 3% for both conditions. However, in HVCN1$^{-/-}$ neutrophils, pretreatment with BAPTA-AM completely

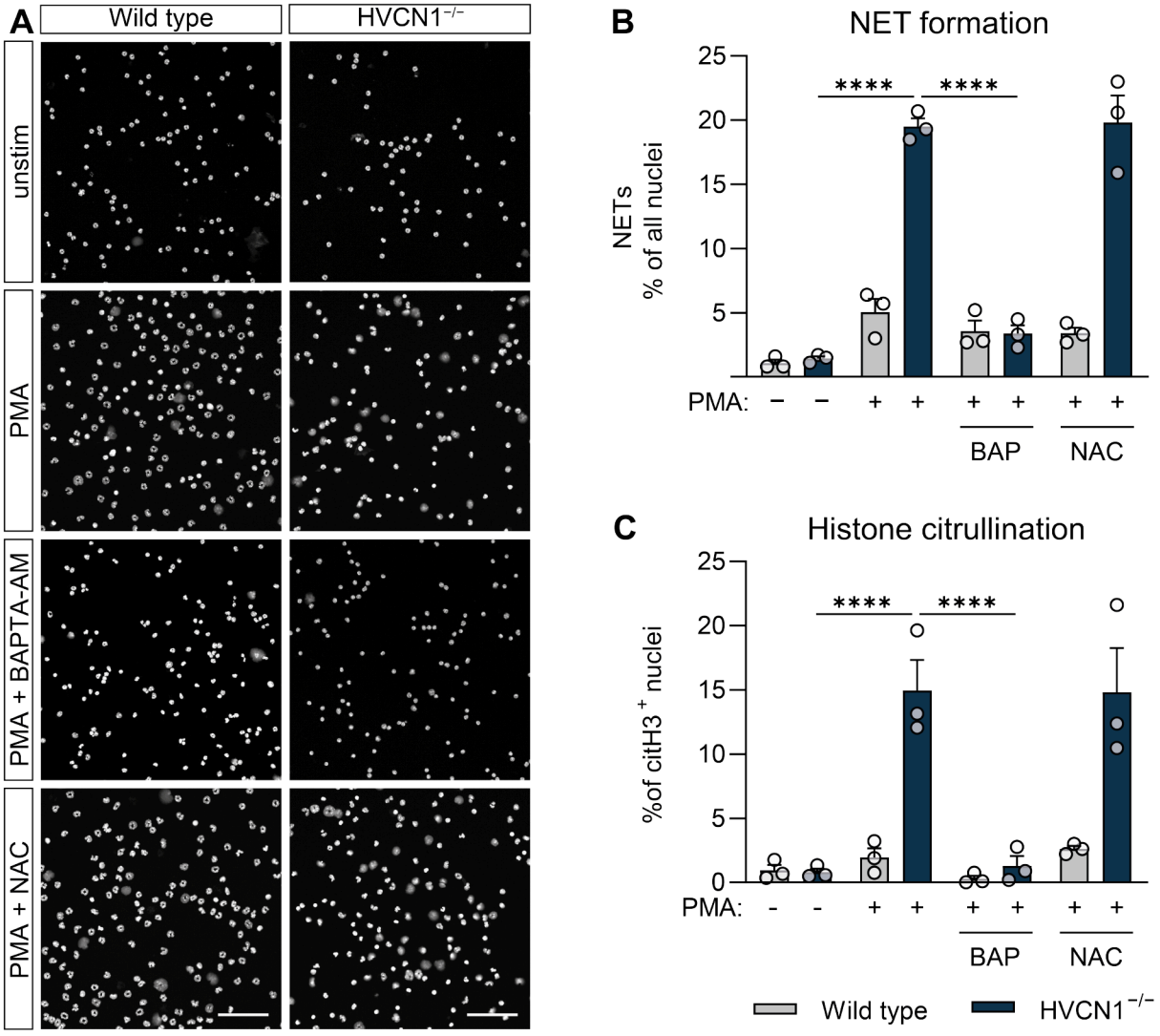

Figure 4.15| Increased NET formation in HVCN1$^{-/-}$ neutrophils is dependent on calcium.
Neutrophils were seeded onto pLL-coated coverslips. Cells were pretreated with 10 µM BAPTA-AM (30 min) or 10 mM NAC (1 h), stimulated with 100 nM PMA and fixed after 4 h. A| Representative images of NET formation visualized by DAPI staining. B| Quantification of NET formation, determined by manual counting of NETs and nuclei (n = 3, with 200 – 300 cells per biological replicate per condition). Columns represent mean ± SEM. Statistical significance was tested by one-way ANOVA with Bonferroni´s post-hoc test for multiple comparisons (****p≤0.0001). C| Histone citrullination was analyzed by immunofluorescence staining for citH3 and quantified as percentage of citH3-positive nuclei (n = 3). Columns represent mean ± SEM. Statistical significance was tested by one-way ANOVA with Bonferroni´s post-hoc test for multiple comparisons (****p≤0.0001).

rescued enhanced NET formation and reduced the percentage of NETotic nuclei to ~ 3%. NAC pretreatment on the other hand had no effect on NET formation in HVCN1$^{-/-}$ neutrophils. Accordingly, pretreatment with BAPTA-AM almost completely inhibited histone citrullination in both wild type and HVCN1$^{-/-}$ whereas NAC had no effect (Fig. 4.15 C).

In conclusion, increased NET formation in PMA-stimulated HVCN1$^{-/-}$ neutrophils was mainly driven by increased calcium levels, since chelation of intracellular calcium completely abolished histone citrullination and significantly reduced NET formation. In contrast, NAC had no effect, suggesting that NET formation in HVCN1$^{-/-}$ neutrophils is independent of ROS production.

4.6 Degranulation

Besides inducing NET formation through histone citrullination, calcium is an important signaling molecule for the release of neutrophil granules. Receptor stimulation-induced granule secretion is tightly regulated through different signaling pathways. However, it was also shown that increase of intracellular calcium alone is sufficient to induce granule release. Interestingly, the calcium concentrations needed for induction of exocytosis differ among the four types of granules, with the highest calcium concentration needed for exocytosis of the MPO-containing primary granules[93].

4.6.1 Primary granule release is increased HVCN1$^{-/-}$ neutrophils

To analyze the release of granule proteins, neutrophils were stimulated with PMA and the concentration of two secreted granule proteins was determined by ELISA. MPO is contained in primary granules while MMP-9 is mainly stored in tertiary granules. To examine calcium and ROS dependency of granule release, neutrophils were pretreated with BAPTA-AM to chelate intracellular calcium, EDTA to deplete extracellular calcium or NAC to block ROS.

Basal levels of MPO release were comparably low in wild type and HVCN1$^{-/-}$ neutrophils (Fig. 4.16 A). After stimulation with PMA, HVCN1$^{-/-}$ neutrophils released significantly more MPO compared to wild type controls. Interestingly, pretreatment of HVCN1$^{-/-}$ neutrophils with BAPTA-AM significantly reduced MPO release, suggesting a role for intracellular calcium. Treatment with EDTA also reduced MPO release, however the reduction in MPO did not reach statistical significance. Surprisingly, treatment with NAC had the opposite effect as it increased the release of MPO. Wild type neutrophils displayed a similar phenotype, although MPO release was generally much lower compared to HVCN1$^{-/-}$ neutrophils.

Of note, the increased release of MPO was not due to elevated levels of MPO stored in HVCN1$^{-/-}$ neutrophils, since MPO concentration in the supernatants of lysed cells was comparable to wild type neutrophils (data not shown).

In contrast, there was no significant increase of MMP-9 release in HVCN1$^{-/-}$ neutrophils compared to wild type controls (Fig. 4.16 B). Unstimulated neutrophils already released large

amounts of MMP-9, which were increased upon stimulation with PMA. Additional treatment with BAPTA-AM or NAC did not influence MMP-9 release. Interestingly, chelation of extracellular calcium with EDTA almost completely abolished MMP-9 release in both wild type and HVCN1$^{-/-}$ neutrophils.

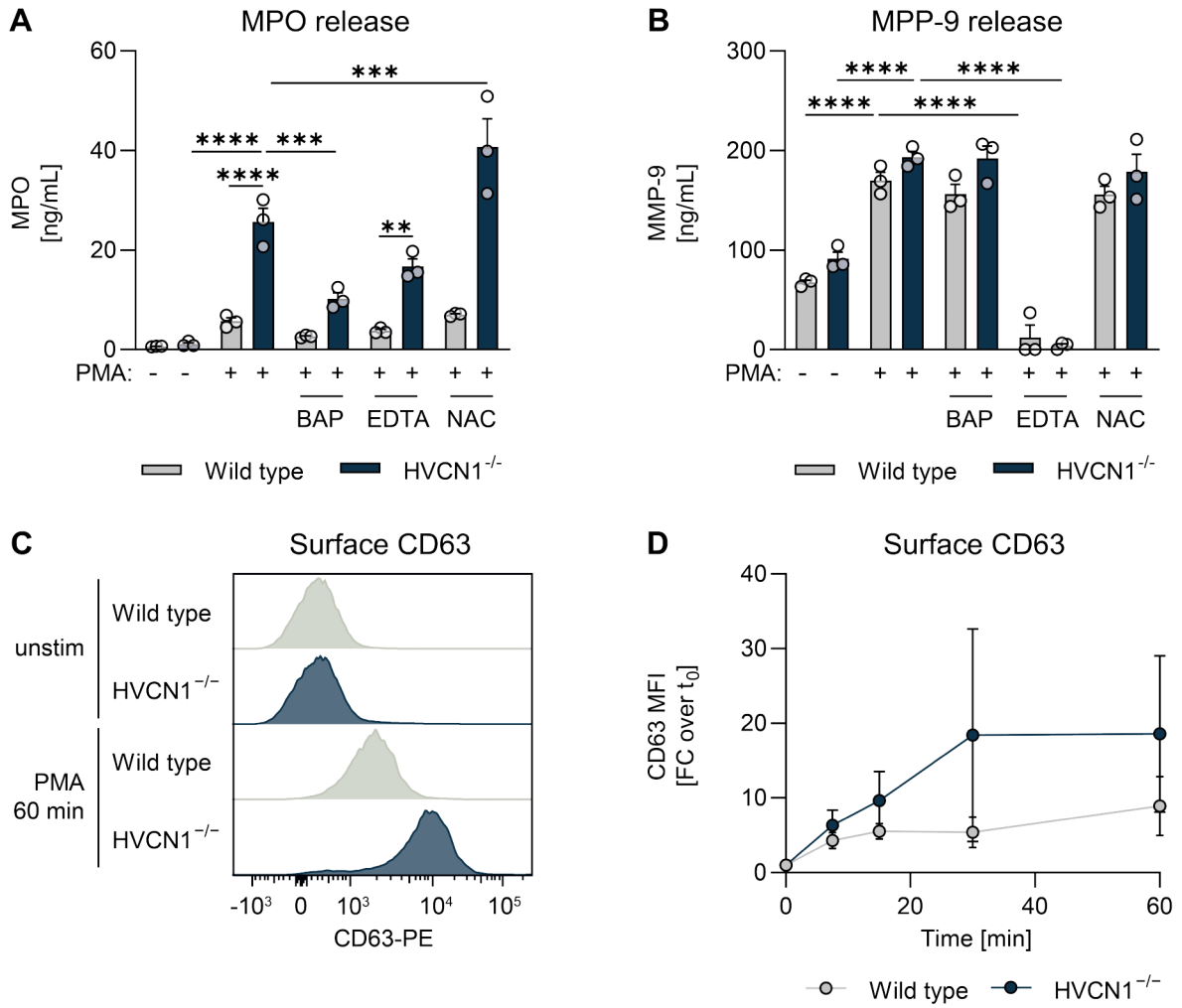

Figure 4.16| Active release of primary, but not tertiary granules, is enhanced in HVCN1$^{-/-}$ neutrophils in a calcium-dependent manner.
A| Primary granule secretion of neutrophils pretreated with 10 µM BAPTA-AM, 2 mM EDTA or 10 mM NAC for 30 min. Supernatants were harvested after 3 h of stimulation with 100 nM PMA. MPO concentration was assessed by ELISA. Columns represent mean ± SEM (n = 3). Statistical significance was tested by one-way ANOVA with Bonferroni´s post-hoc test for multiple comparisons (***p≤0.001, ****p≤0.001). B| Tertiary granule secretion of neutrophils were treated as described in A. MMP-9 concentration was assessed by ELISA Columns represent mean ± SEM (n = 3). Statistical significance was tested by one-way ANOVA with Bonferroni´s post-hoc test for multiple comparisons (****p≤0.001). C| Histogram of surface CD63 expression. Neutrophils were stimulated with 100 nM PMA for 60 min. Fixed cells were stained with anti-CD63 PE and surface expression was assessed by flow cytometry. D| Kinetic of CD63 surface expression. Neutrophils were treated as described in C. Data is depicted as fold change of CD63 median FI at 0 min of stimulation. Data points represent mean ± SD (n = 2).

To confirm that increased MPO release by HVCN1$^{-/-}$ neutrophils is the result of active secretion, exocytosis was measured by quantifying surface exposure of the primary granule marker CD63 early after PMA stimulation. For this purpose, neutrophils were fixed at different time points after stimulation and surface signal of CD63 was measured by flow cytometry. Indeed, HVCN1$^{-/-}$ neutrophils already showed increased surface expression of CD63 as early as 7.5 minutes after stimulation (Fig. 4.16 C and D). Furthermore, 30 and 60 minutes after stimulation, surface levels of CD63 were markedly increased in HVCN1$^{-/-}$ neutrophils compared to wild type controls.

Fittingly, the MPO concentration in the supernatant was already higher in HVCN1$^{-/-}$ neutrophils than in wild-type controls one hour after stimulation, i.e., before NET formation (data not shown).

4.6.2 Increased granule release in HVCN1$^{-/-}$ neutrophils correlates with vacuole formation by fluid-phase pinocytosis

As depicted in Fig. 4.17 A, HVCN1$^{-/-}$ neutrophils formed large intracellular vacuoles shortly after stimulation with PMA. Live cell imaging revealed that the vacuoles started forming approximately 5 minutes after addition of PMA. They continued to grow and appear to fuse intracellularly to form even larger vacuoles which persist over a period of 60 minutes. Vacuole formation was also observed in wild type neutrophils, however they remained relatively small in comparison to HVCN1$^{-/-}$ cells.

It has been previously described that various cell types, including neutrophils, perform pinocytosis to retrieve membrane-bound vesicle components and counteract excessive surface enlargement after exocytosis[214,215]. Therefore, it may be possible that vacuoles found in HVCN1$^{-/-}$ neutrophils are a result of fluid-phase pinocytosis in response to increased release of primary granules. To quantify pinocytic activity, neutrophils were stimulated with PMA in the presence of fluorescently-labelled dextran (TRITC dextran) which can be taken up together with extracellular fluid. Neutrophils were fixed at different time points after stimulation, extensively washed to

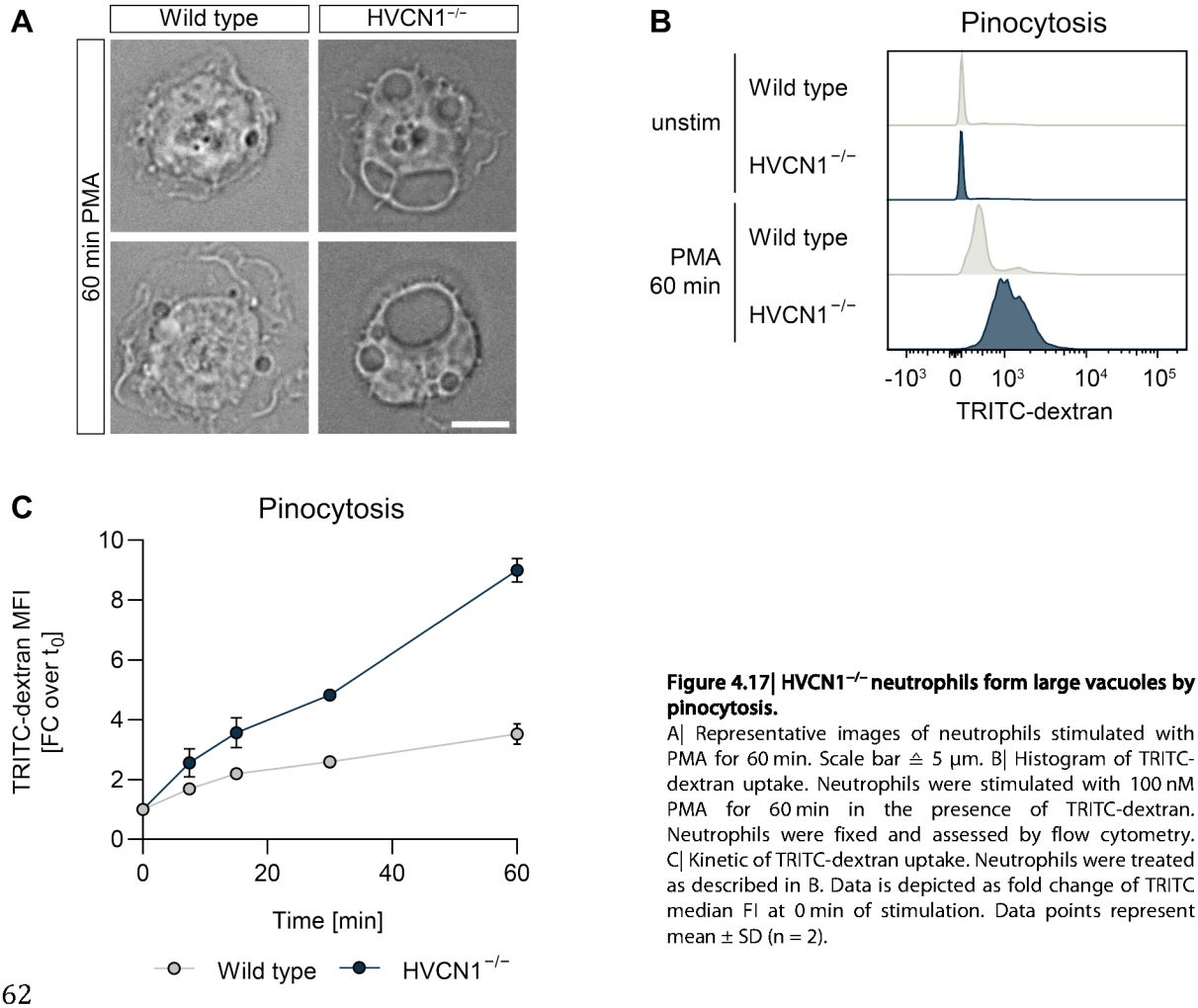

Figure 4.17| HVCN1$^{-/-}$ neutrophils form large vacuoles by pinocytosis.
A| Representative images of neutrophils stimulated with PMA for 60 min. Scale bar ≙ 5 µm. B| Histogram of TRITC-dextran uptake. Neutrophils were stimulated with 100 nM PMA for 60 min in the presence of TRITC-dextran. Neutrophils were fixed and assessed by flow cytometry. C| Kinetic of TRITC-dextran uptake. Neutrophils were treated as described in B. Data is depicted as fold change of TRITC median FI at 0 min of stimulation. Data points represent mean ± SD (n = 2).

remove any surface-bound dextran and analyzed by flow cytometry. Indeed, PMA stimulation induced uptake of TRITC dextran in neutrophils of both genotypes. However, HVCN1$^{-/-}$ neutrophils ingested more dextran, indicating increased pinocytosis (Fig. 4.17 B and C).

In summary, it could be demonstrated that primary granule release (i.e., MPO) but not tertiary granule release (i.e., MMP-9) is enhanced in HVCN1$^{-/-}$ neutrophils compared to wild type controls. This phenomenon is also caused by increased intracellular calcium, since chelation of calcium significantly reduced granule release. Furthermore, HVCN1$^{-/-}$ neutrophils increase fluid-phase pinocytosis, which may be a mechanism for retrieving parts of the granule membrane.

4.7 Phenotype of HVCN1$^{-/-}$ neutrophils is dependent on NADPH oxidase activation

The function of HVCN1 is closely linked to the activation of NAPDH oxidase. And in fact, unstimulated neutrophils do not exhibit proton currents[216]. Nevertheless, the question remained if the activation of the NADPH oxidase and its production of protons is prerequisite for differences between wild type and HVCN1$^{-/-}$ neutrophils; or if HVCN1$^{-/-}$ neutrophils would show any of the previously described features in the absence of the NAPDH oxidase.

There are various inhibitors for the NADPH oxidase, the most commonly used ones are DPI and apocynin. However, all of them display unspecific inhibition of other oxidases, nitric oxide synthases or even G-protein coupled receptors[217]. Hence, genetic deletion of its core subunit gp91^{phox} encoded by the *Cybb* gene is the most specific way to block activation of the NADPH oxidase. In order to obtain HVCN1 and CYBB-double deficient (HVCN1/CYBB$^{-/-}$) neutrophils, HVCN1$^{-/-}$ mice were crossed with CYBB$^{-/-}$ mice and neutrophils were isolated from the bone marrow. Wild type, HVCN1$^{-/-}$, and CYBB$^{-/-}$ neutrophils were used as controls.

First, the intracellular pH was assessed in neutrophils of all four genotypes. PMA-induced acidification observed in HVCN1$^{-/-}$ neutrophils was rescued by the additional deletion of CYBB. In fact, both CYBB$^{-/-}$ and HVCN1/CYBB$^{-/-}$ neutrophils exhibited alkalization of the cytosol upon PMA stimulation (Fig. 4.18 A).

Furthermore, PMA did not induce calcium mobilization in CYBB$^{-/-}$ or HVCN1/CYBB$^{-/-}$ neutrophils (Fig 4.18 B). Hence, also calcium-dependent features of PMA-stimulated HVCN1$^{-/-}$ neutrophils, such as dissipation of the mitochondrial transmembrane potential (Fig. 4.18 C), increased production of intracellular ROS (Fig. 4.18 D) or augmented release of MPO (Fig. 4.18 E), were not observed in CYBB$^{-/-}$ or HVCN1/CYBB$^{-/-}$ neutrophils. Overall, as expected, neutrophils lacking CYBB appeared to be even less responsive compared to wild type neutrophils.

These findings indicate that all of the observed changes in HVCN1$^{-/-}$ neutrophils after stimulation with PMA are downstream of NADPH oxidase activation and that the electrogenic activity of the NADPH oxidase is required to generate the ion imbalance that causes the altered phenotype of HVCN1$^{-/-}$ neutrophils.

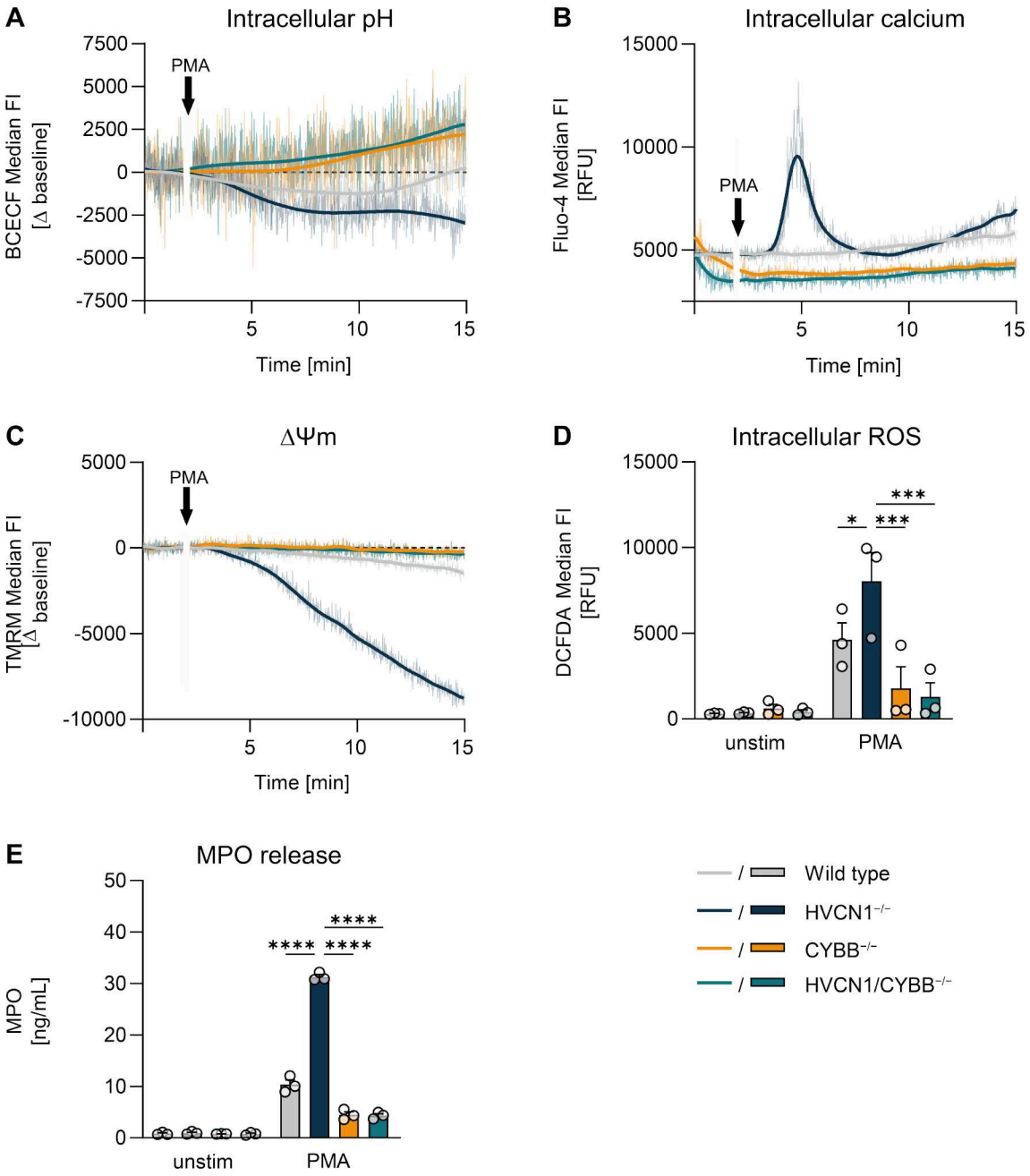

Figure 4.18| HVCN1$^{-/-}$ phenotype is dependent on NADPH oxidase expression: analysis of HVCN1/CYBB$^{-/-}$ neutrophils.
A| Intracellular pH. Neutrophils were loaded with 1.25 µM BCECF-AM for 30 min at RT. After stimulation with 100 nM PMA, BCECF FI was measured by flow cytometry and analyzed with the FlowJo Kinetics Tool extracting the median fluorescence intensity (MFI) per second. Data depicted as mean (faint line) with LOWESS curve fit (opaque line) (n = 3). B| Intracellular calcium. Neutrophils were loaded with 2 µM Fluo-4-AM for 30 min at 37° C. Fluo-4 FI after treatment with 100 nM PMA was measured by flow cytometry and analyzed with the FlowJo Kinetics Tool extracting the median fluorescence intensity (MFI) per second. Data depicted as mean (faint line) with LOWESS curve fit (opaque line) (n = 3). C| ΔΨm. Neutrophils were loaded with 50 nM TMRM for 30 min at 37° C. TMRM FI after stimulation with 100 nM PMA was measured by flow cytometry and analyzed with the FlowJo Kinetics Tool extracting the median fluorescence intensity (MFI) per second which was normalized to baseline. Data depicted as mean (faint line) with LOWESS curve fit (opaque line) (n = 3). D| Intracellular ROS. Neutrophils were loaded with 2.5 µM CM-H_2DCFA for 20 min at RT, stimulated with 100 nM PMA for 30 min at 37° C and subsequently median DCFDA FI was measured by flow cytometry. Columns represent mean ± SEM (n = 3). Statistical significance was tested by one-way ANOVA with Bonferroni´s post-hoc test for multiple comparisons (*p≤0.05, ***p≤0.001). E| Primary granule secretion of neutrophils stimulated with 100 nM PMA for 30 min. MPO concentration was assessed by ELISA. Columns represent mean ± SEM (n = 3). Statistical significance was tested by one-way ANOVA with Bonferroni´s post-hoc test for multiple comparisons (****p≤0.001).

4.8 HVCN1$^{-/-}$ neutrophils show altered responses to alternative stimuli

Although PMA is commonly used to stimulate granulocytes, it is a rather artificial stimulus and elicits a high rate of ROS production by the NADPH oxidase. Consequently, it also leads to very strong acidification and HVCN1 activation. To investigate how loss of HVCN1 would influence neutrophil activation with more physiological stimuli, neutrophils were stimulated with plate-bound IgG or *Escherichia coli* (*E. coli*).

4.8.1 Plate-bound IgG elicits activation similar to PMA in HVCN1$^{-/-}$ neutrophils

Neutrophils express a variety of receptors for IgG antibodies[75]. These Fcγ receptors enable neutrophils to recognize and engulf antibody-opsonized pathogens. However, internalization results in localized ROS production in phagosomes and prevents neutrophils from undergoing NETosis. Conversely, when phagocytosis cannot take place, for example when the target is too big to be phagocytosed, neutrophils undergo NETosis[110]. In order to stimulate Fcγ receptor signaling without inducing phagocytosis, cell culture plates were coated with soluble mouse IgG and various parameters of neutrophil activation were assessed (Fig. 4.19).

Stimulation of neutrophils by plate-bound IgG induced the production of ROS. As for PMA, extracellular ROS production was severely impaired in HVCN1$^{-/-}$ neutrophils after stimulation with IgG (Fig. 4.19 A). In contrast, intracellular ROS levels were higher in HVCN1$^{-/-}$ neutrophils compared with wild type controls (Fig. 4.19 B). Thus, ROS production after stimulation with IgG follows the same pattern as stimulation with PMA (Fig. 4.2 E and Fig. 4.11 A).

Additionally, IgG-induced MPO release was assessed (Fig. 4.19 C). In wild type neutrophils, MPO concentration (~8 ng/ml, Fig. 4.16 A) was comparable to that released after stimulation with PMA. HVCN1$^{-/-}$ neutrophils released less MPO upon stimulation with IgG than upon PMA

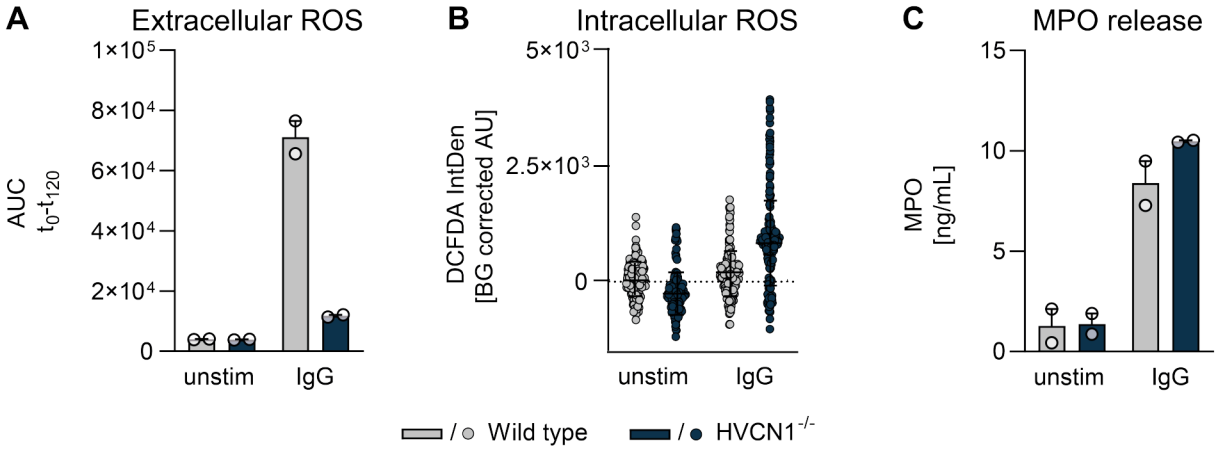

Figure 4.19| HVCN1$^{-/-}$ neutrophils have a similar response to plate-bound IgG and PMA.
For stimulation cell culture plate were coated with 1 mg/ml mouse IgG overnight at 4 °C. A| Intracellular ROS was measured by a luminol-amplified luminescence assay. Cells were seeded on a IgG-coated plate and isoluminol mix was added to cells immediately. Chemiluminescent signal was measured every 5 min for a total of 2 h. Area under the curve for isoluminal signal. Columns represent mean ± SD (n = 2). B| Levels of intracellular ROS were analyzed in neutrophils which were loaded with 2.5 µM CM-H_2DCFDA for 20 min at RT and subsequently stimulated on IgG-coated plates for 30 min. Background-corrected integrated density of DCFDA per cell was determined by microscopy and quantified with FIJI. Dots represent single cells with line at mean ± SD (n = 1, with 200 cells per condition). C| MPO secretion by neutrophils. Supernatants were harvested after 1 h of stimulation with plate-bound IgG. MPO concentration was assessed by ELISA. Columns represent mean ± SD (n = 2).

stimulation (~ 25 ng/ml, Fig. 4.16 A), but still tend to release more MPO compared to wild type neutrophils. However, with these number of biological replicates the difference did not reach statistical significance.

The data suggest that HVCN1 might also be important in regulating ROS production and granule release when stimulated with IgG. Future experiments should address if NETosis is also altered in HVCN1$^{-/-}$ neutrophils after stimulation with plate-bound IgG.

4.8.2 Killing of bacteria is not altered in HVCN1$^{-/-}$ neutrophils

An important function of neutrophils is to engulf and kill pathogens in the phagosome. Several studies have shown that the phagosome of HVCN1$^{-/-}$ neutrophils exhibits aberrant pH regulation[104,176]. To determine whether these changes affect their phagocytic killing capacities, HVCN1$^{-/-}$ neutrophils were incubated with *E. coli*, and uptake and bacterial survival were analyzed.

There was no difference in the uptake of heat-killed GFP-labeled *E. coli* between wild type and HVCN1$^{-/-}$ neutrophils at any of the three different time points (30, 60 and 180 minutes, Fig. 4.20 A). Similarly, bacterial killing after 3 hours of co-incubation did not differ between wild type and HVCN1$^{-/-}$ neutrophils, as the colony-forming units of surviving bacteria were similar between genotypes (Fig. 4.20 B). Interestingly, compared with stimulation with PMA and IgG, there was no difference in MPO secretion between HVCN1$^{-/-}$ neutrophils and wild type controls stimulated with *E. coli*.

These results suggest that HVCN1 is not required for efficient killing of phagocytosed bacteria. It would be interesting to analyze killing capacity of non-phagocytosed bacteria, to investigate whether HVCN1$^{-/-}$ neutrophils have heightened bactericidal potential due to enhanced NET formation.

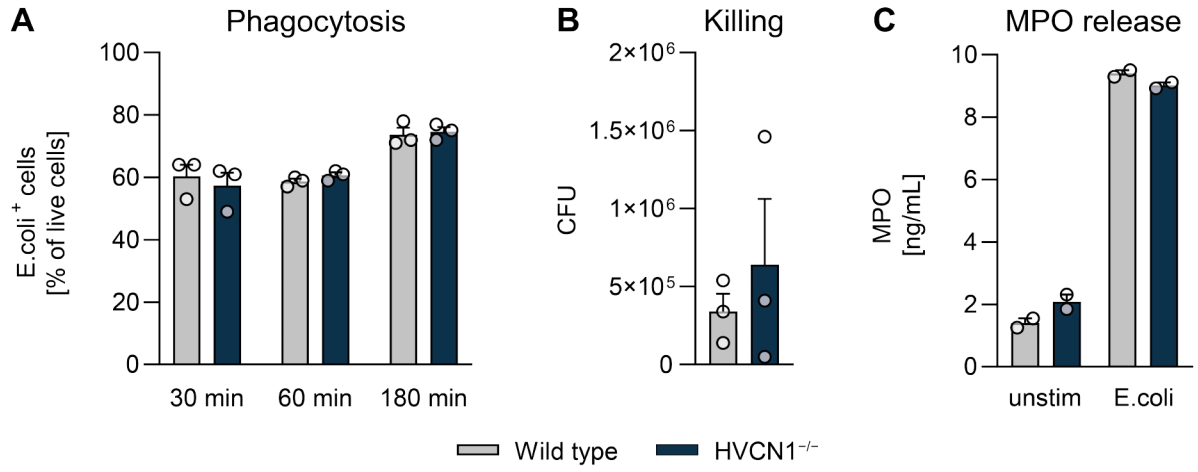

Figure 4.20| Phagocytosis and bacterial killing is unchanged in HVCN1$^{-/-}$ neutrophils.
A| Neutrophils were incubated with heat-killed GFP-labelled *E. coli*. At indicated times, cells were fix and washed. Uptake of fluorescently labelled bacteria was assessed by flow cytometry. Data represent mean of % of bacteria-containing cells ± SEM (n = 3). B| Neutrophils were incubated with *E. coli* for 3 h, remaining extracellular bacteria were killed by gentamicin treatment. Neutrophils were then lysed in saponin, and surviving bacteria were serially diluted and allowed to grow overnight. Bacterial killing is depicted as colony-forming units (CFU) ± SEM (n = 3). C| MPO release was measured in supernatants of neutrophils stimulated with *E. coli* for 3 h.

4.9 Phenotype of HVCN1$^{-/-}$ mice in health and disease

As demonstrated *in vitro*, loss of HVCN1 increases the proinflammatory capacity of neutrophils by enhancing granule release and accelerating NETosis. Hence, it was also important to study how HVCN1 deficiency would influence neutrophil activation *in vivo*. To this end, HVCN1$^{-/-}$ mice were analyzed at steady state and in two different models of inflammation.

4.9.1 HVCN1$^{-/-}$ mice show no pronounced changes in the neutrophil compartment

Unchallenged, young HVCN1$^{-/-}$ mice do not develop an obvious pathological phenotype. To analyze if loss of HVCN1 affects neutrophil development, bone marrow and blood neutrophils of HVCN1$^{-/-}$ and wild type mice were assessed by flow cytometry (Fig. 4.21). Neutrophil progenitors in the bone marrow were analyzed according to markers published by Evrard *et al.*[27]. No differences in the frequencies of GMPs, pre-neutrophils and mature neutrophils could be detected between wild type and HVCN1$^{-/-}$ mice (Fig. 4.21A, B, D). However, the frequency of immature neutrophils was slightly elevated in the bone marrow of HVCN1$^{-/-}$ mice (Fig. 4.21C). Yet, this had no apparent effect on the maturation status of blood neutrophils, since cell frequency and expression levels of CXCR2 and CD11b were not affected by the loss of HVCN1.

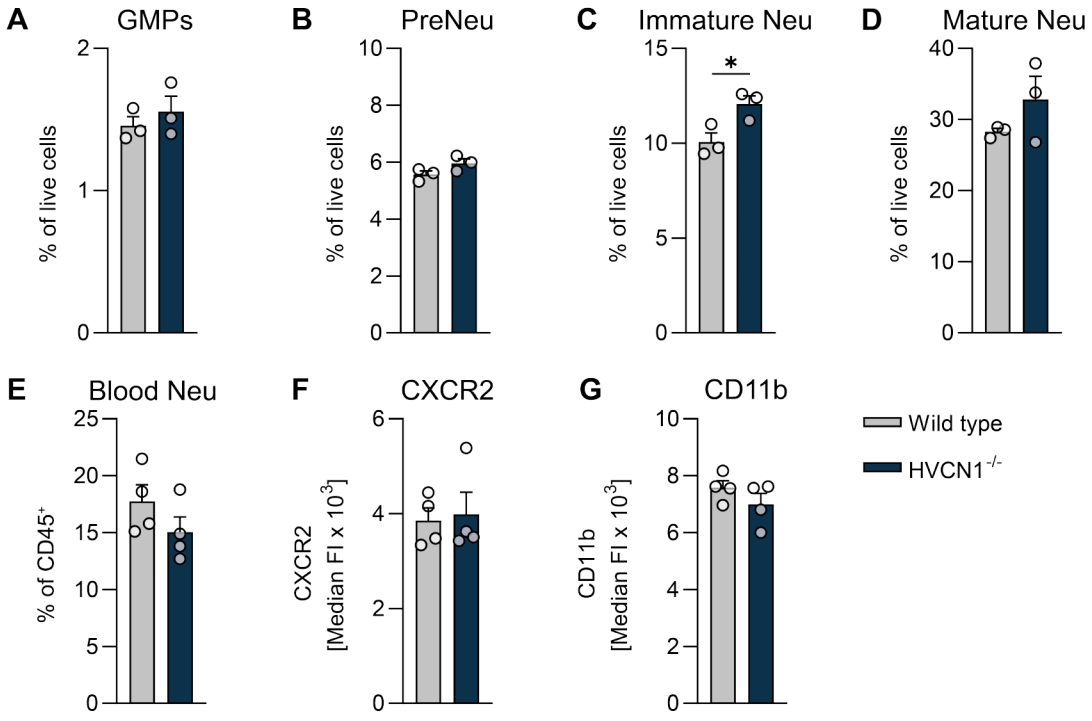

Figure 4.21| No major changes in the neutrophil compartment of HVCN1$^{-/-}$ mice.
Cells were isolated from bone marrow and blood of 3 – 5 month-old wild type and HVCN1$^{-/-}$ mice. A – D| Frequency of neutrophil progenitors and mature neutrophils in the bone marrow was determined by flow cytometry. Frequency depicted as percentage of live cells ± SEM (n = 3). E| Frequency of neutrophils in the peripheral blood was determined by flow cytometry. Frequency depicted as percentage of CD45-positive cells, columns represent mean ± SEM (n = 4). F and G| Levels of maturity markers CXCR2 and CD11b on neutrophils in peripheral blood. Levels depicted as median fluorescence intensity, columns represent mean ± SEM (n = 4). Statistical significance was tested by one-way ANOVA with Bonferroni´s post-hoc test for multiple comparisons *p≤0.05).

4.9.2 Aged HVCN1$^{-/-}$ mice develop a mild inflammatory phenotype

While young HVCN1$^{-/-}$ mice do not display pathology, ~ 70 % of aged (older than 14 month), female HVCN1$^{-/-}$ mice were shown to develop a mild lupus-like autoimmune disorder, characterized by increased splenomegaly, circulating anti-dsDNA antibodies, and nephritis[190]. To further investigate this phenomenon, particularly in regard to neutrophil activation in aged mice, 5- and 20-month-old female wild type and HVCN1$^{-/-}$ mice were studied. As shown in Fig 4.22 A, young HVCN1$^{-/-}$ mice showed a tendency toward increased spleen weight compared to wild type controls. Spleen weight increased with age in both genotypes. However, we could not clearly observe increased spleen weight in aged HVCN1$^{-/-}$ mice compared to wild type controls, as demonstrated by Sasaki *et al.*[190].

In addition, serum IFNα levels were determined, since elevated levels of this cytokine are characteristic of human SLE and lupus mouse models[218]. While IFNα was relatively low in both genotypes and age groups, aged HVCN1$^{-/-}$ mice still had significantly higher IFNα levels compared to age-matched wild type controls.

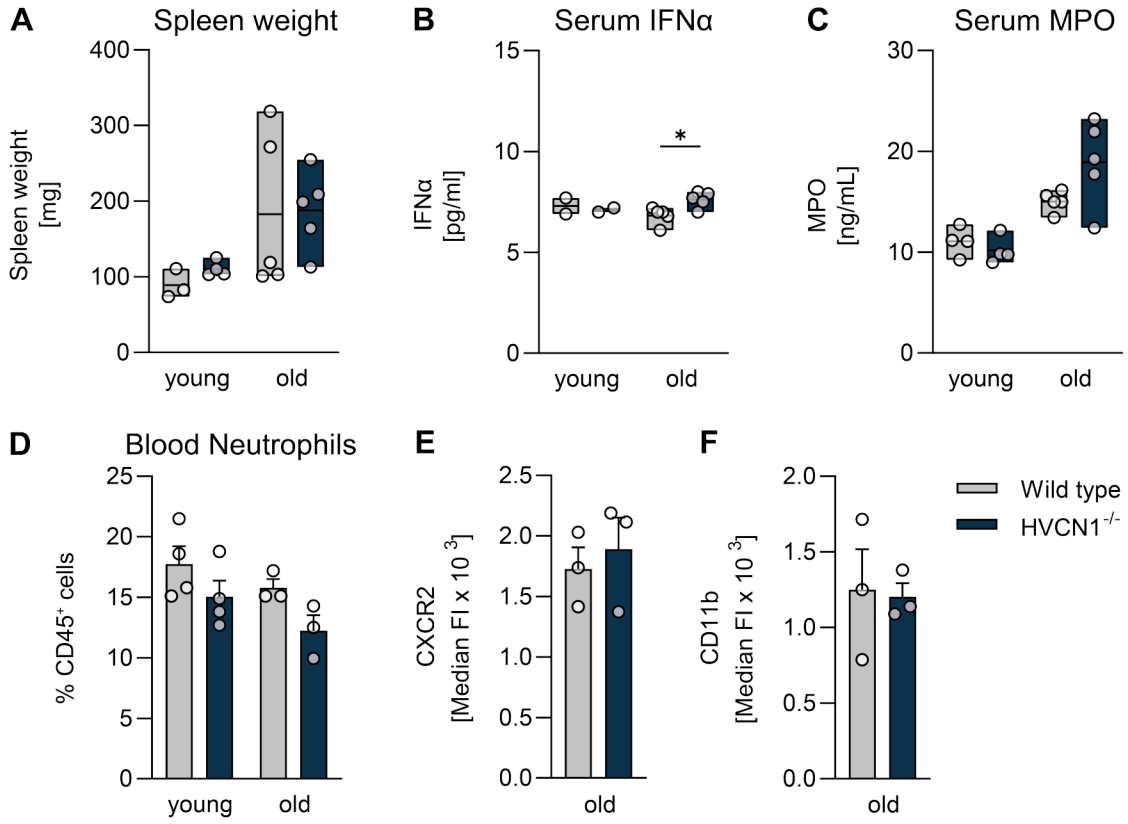

Figure 4.22| Aged HVCN1$^{-/-}$ mice develop mild inflammatory phenotype.
A| Spleen weight of young and old mice. Bars from min to max, with line at mean (5-month n = 3/4 for wild type or HVCN1$^{-/-}$, 20-month n = 5). B| INFα levels in serum measured by ELISA. Bars from min to max, with line at mean (5-month n = 2, 20-month n = 5). Statistical significance was tested by one-way ANOVA with Bonferroni´s post-hoc test for multiple comparisons (*p≤0.05). C| MPO levels in serum measured by ELISA. Bars from min to max, with line at mean (5-month n = 4, 20-month n = 5). D| Frequency of neutrophils in peripheral blood determined by flow cytometry. Frequency depicted as percentage of CD45^{+} cells, columns represent mean ± SEM (5-month n = 4, 20-month n = 3). E| Levels of CXCR2 and F| CD11b on neutrophils in peripheral blood of aged mice. Levels depicted as median fluorescence intensity, columns represent mean ± SEM (n = 3).

Neutrophil activation was assessed by measuring the concentration of MPO in the serum. As depicted in Fig. 4.22 C no significant difference could be observed between young wild type and HVCN1$^{-/-}$ mice. Serum MPO in both, wild type and HVCN1$^{-/-}$ mice increased with age. However, aged HVCN1$^{-/-}$ mice had significantly higher serum MPO compared to young HVCN1$^{-/-}$ mice, indicating a more pronounced release of MPO in the absence of HVCN1. Analysis of blood cell counts revealed that old HVCN1$^{-/-}$ mice showed a trend for reduced neutrophil numbers compared to age-matched wild type controls (Fig. 4.22 D), although this difference did not reach statistical significance. Expression of the maturation and activation markers CXCR2 and CD11b were comparable between neutrophils of aged wild type and HVCN1$^{-/-}$ mice (Fig. 4.22 E and F).

4.9.3 Zymosan-induced peritonitis is aggravated in HVCN1$^{-/-}$ mice

Peritoneal injection of zymosan, a yeast-derived polysaccharide, causes acute peritonitis in mice[219]. To study this inflammatory response, wild type and HVCN1$^{-/-}$ mice were injected with 1 µg zymosan or PBS as control into the peritoneal cavity and were then closely monitored. After 6 or 24 hours, mice were sacrificed and the peritoneal lavage and blood were analyzed for neutrophil-related inflammatory parameters (Fig. 4.23 A).

No differences in disease score based on appearance and behavior were observed between wild type and HVCN1$^{-/-}$ mice at different time points after injection (not shown). As expected, 6 hours after zymosan injection, cells started accumulating the peritoneal cavity (Fig. 4.23 B). No differences in the number of peritoneal cell infiltration were detected at this time point. However, 24 hours after zymosan injection, HVCN1$^{-/-}$ mice showed significantly higher numbers of infiltrating cells (Fig. 4.23 B). Flow cytometry analysis revealed that infiltration of all major immune cell types into the peritoneal cavity was increased in HVCN1$^{-/-}$ mice. Neutrophils accounted for 80% of all infiltrating cells, and their number was twice as high in HVCN1$^{-/-}$ mice compared with wild type controls. (Fig. 4.23 C). Interestingly, MPO levels in HVCN1$^{-/-}$ mice were elevated both in serum and peritoneal lavage, albeit this latter difference did not reach statistical significance likely due to the small number of samples (Fig. 4.23 D and E).

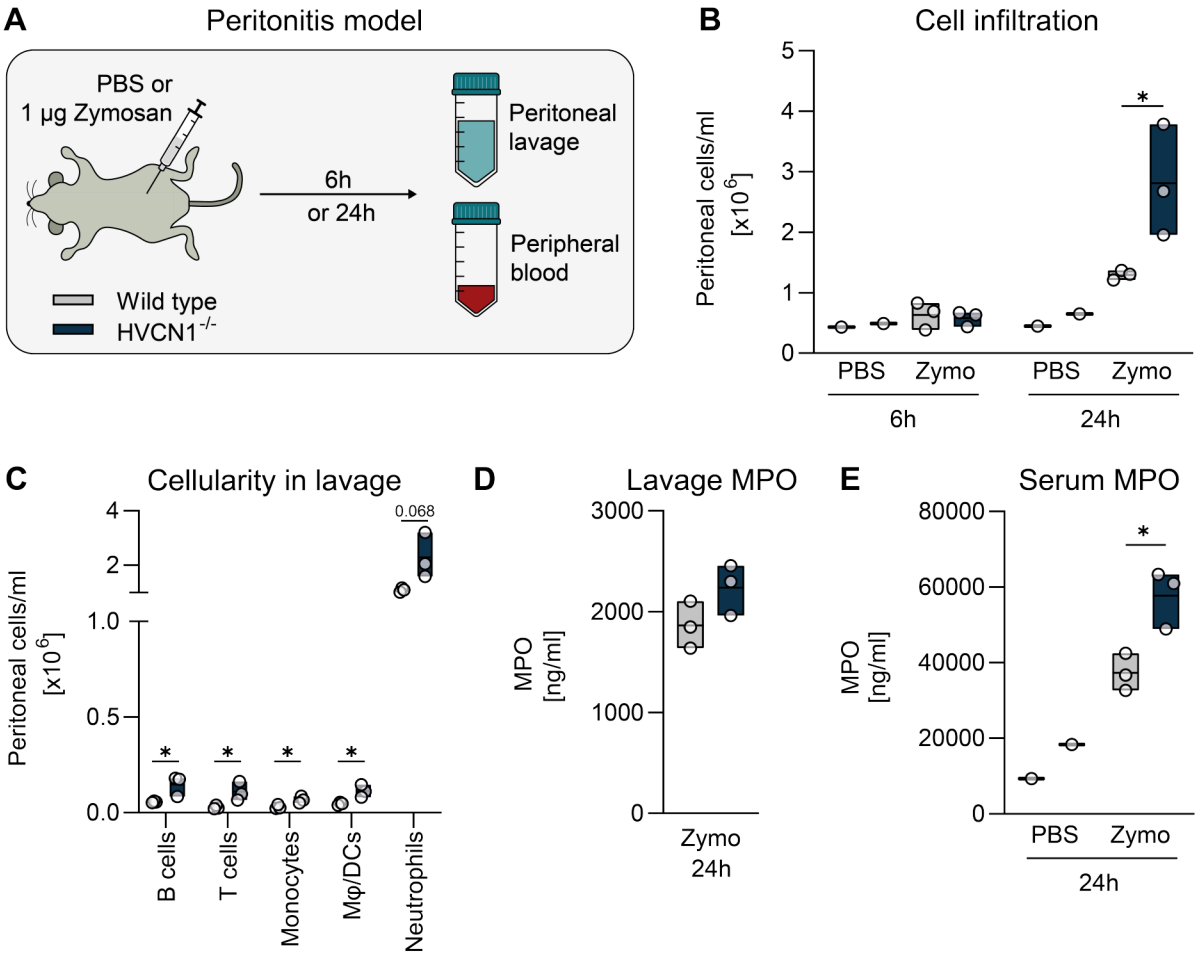

Figure 4.23| HVCN1$^{-/-}$ mice show augmented inflammation in a model of zymosan-induced peritonitis.
A| Experimental procedure of the zymosan-induced peritonitis model. 3 month old male mice were injected i.p. with 1µg zymosan, or PBS as control. After 6 or 24 h, mice were sacrificed and blood and peritoneal lavage was collected. B| Cell counts from peritoneal lavage. Bars min to max, with mean (Control n = 1, Zymosan n = 3). Statistical significance was tested by one-way ANOVA with Bonferroni´s post-hoc test for multiple comparisons (*p≤0.05). C| Cell populations in lavage of mice treated with zymosan for 24 h were analyzed by flow cytometry and depicted as total counts. Bars min to max, with mean (Zymosan n = 3). D| MPO levels in lavage measured by ELISA. Bars min to max, with mean (n = 3). E| MPO levels in serum measured by ELISA. Bars min to max, with mean (Control n = 1, Zymosan n = 3). Statistical significance was tested by student's t-test (*p≤0.05).

4.9.4 HVCN1$^{-/-}$ mice show enhanced pathology in a model for pulmonary ANCA-associated vasculitis

To further investigate neutrophil activation *in vivo*, we chose to test wild type and HVCN1$^{-/-}$ mice in a model of anti-neutrophil cytoplasmic antibody (ANCA)-associated pulmonary vasculitis (AAPV)[220]. In this model, neutrophil recruitment to the lung is induced by intratracheal application of low doses of the bacterial ligands fMLP and LPS. Concurrent systemic application of anti-MPO IgGs then causes severe inflammation and damage of the lung vasculature resembling characteristics of human ANCA-associated small vessel vasculitis (AAPV mice). Control mice only received fMLP/LPS intratracheally. All mice were sacrificed at day 3 after induction, as it represents the peak of disease (Fig. 4.24 A).

Histological analysis of lungs showed severe hemorrhages and infiltration of immune cells in both wild type and HVCN1$^{-/-}$ AAPV mice (Fig. 4.24 B), while lung hemorrhages appeared to be increased in HVCN1$^{-/-}$ mice, indicating more severe vasculature damage (Fig. 4.24. C and D). Interestingly, whereas the total number of leukocytes in the BAL did not differ between genotypes, neutrophil numbers in HVCN1$^{-/-}$ AAPV mice were significantly higher compared to wild type AAPV mice (Fig. 4.24 E and F).

Kessler *et al.*[220] identified DNA sensing by the cGAS/STING pathway as a major hallmark for disease progression. As cGAS[221] is activated by DNA, cell-free DNA (cfDNA) concentrations were measured in the bronchoalveolar lavage. As depicted in Fig. 4.24 G, levels of cfDNA were comparable in both conditions and between genotypes.

In order to further analyze systemic neutrophil activation, I measured MPO levels in the blood (Fig. 4.24 H). Unexpectedly, serum MPO levels seemed to be reduced in AAPV compared to control-treated mice. Also, there were differences in MPO levels between genotypes in either treatment.

Molecular and histological pathology was supported by weight scores, as AAPV mice lost significantly more weight compared to controls (Fig. 4.24 I). Also here, weight loss was more severe in HVCN1$^{-/-}$ mice. Of note, there was no difference in any of the observed parameters between wild type and HVCN1$^{-/-}$ mice receiving only fMLP/LPS.

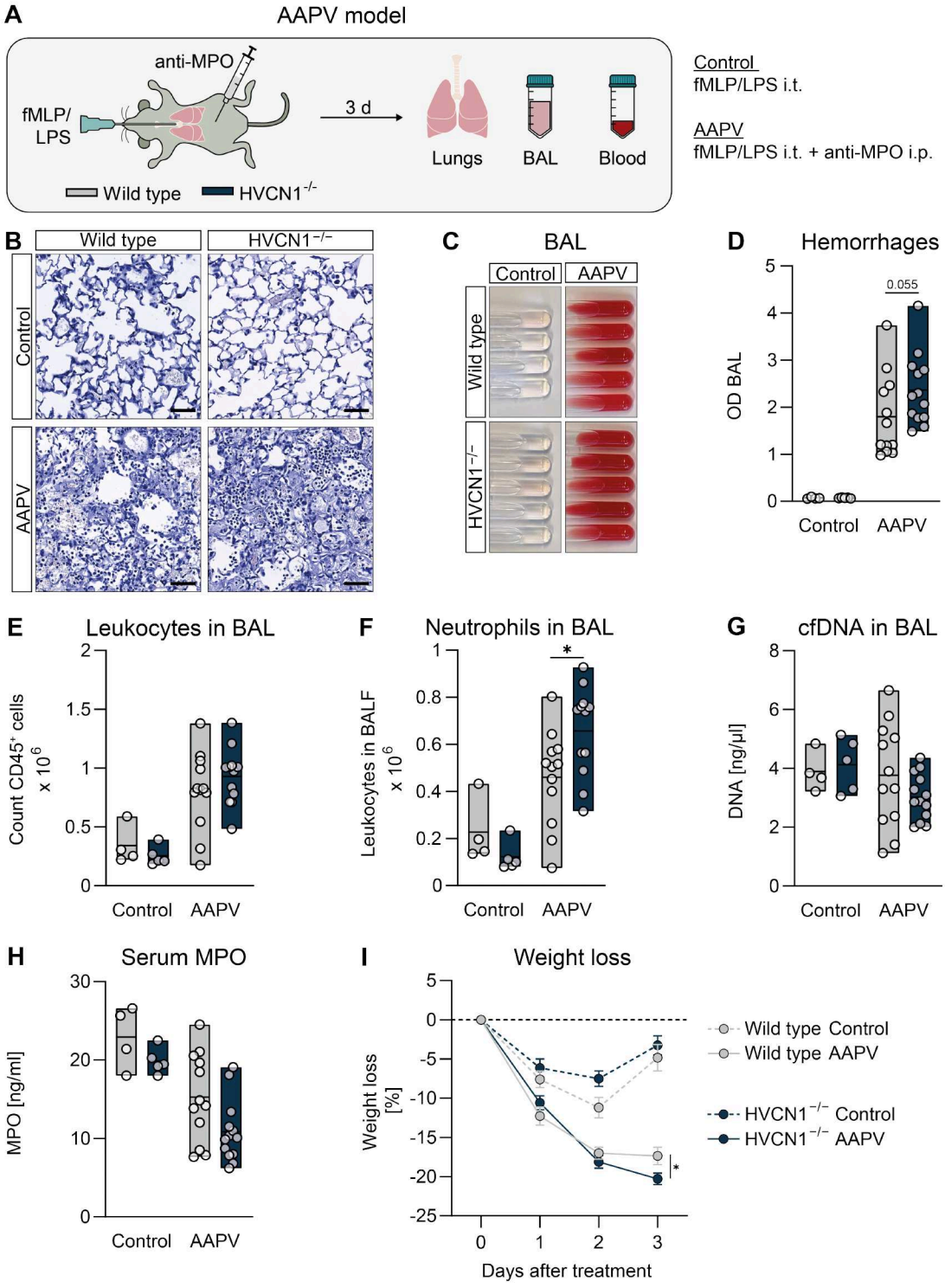

Figure 4.24| Pulmonary ANCA vasculitis pathology appears aggravated in HVCN1$^{-/-}$ mice.
A| For induction of AAPV, mice received 10 µg fMLP/10 µg LPS i.t. and 1 mg anti-MPO i.p. Control mice only received fMLP/LPS. At day 3 after treatment, mice were sacrificed and lungs, BAL and blood were collected. (WT control n = 4, HVCN1$^{-/-}$ control n = 5, WT AAPV n = 12, HVCN1$^{-/-}$ AAPV n = 13) B| H&E staining of lungs. Scale bar ≙ 50 µm. C| Representative images of hemorrhages in BAL. D| Quantification of hemorrhages in BAL. $OD_{400\,nm} - OD_{600\,nm}$. Bars min to max, with line at mean. Statistical significance was tested by one-way ANOVA with Bonferroni´s post-hoc test for multiple comparisons. E| Quantification of leukocytes in BAL determined by flow cytometry. Bars min to max, with line at mean. F| Quantification of neutrophils in BAL determined by flow cytometry. Bars min to max, with line at mean. Statistical significance was tested by one-way ANOVA with Bonferroni´s post-hoc test for multiple comparisons (*p≤0.05). G| cfDNA in BAL was quantified using the Qubit™ dsDNA HS-Assay-Kit. H| MPO levels in serum measured by ELISA. Bars min to max, with line at mean. I| Weight loss curve over 3 days of treatment. Dots represent mean ± SEM. Statistical significance was tested by two-way ANOVA with Bonferroni´s post-hoc test for multiple comparisons (*p≤0.05).

5 Discussion

Neutrophils are key players in the innate immune response and are critical to the initial response to invading pathogens. They are equipped with a variety of effector functions that enable them to kill pathogens and release factors that attract other immune cells. If not tightly regulated, these capabilities can often harm host tissues, as seen in many severe pathologies such as acute or chronic inflammation or autoimmune diseases. Therefore, an important aspect of neutrophil research focuses on the molecular regulation of neutrophil effector functions in health and disease. It has been reported that the proton channel HVCN1 regulates neutrophil activation through its ability to maintain intracellular pH. However, previous studies mainly focused on its role in NADPH oxidase-mediated ROS production and phagocytosis-related functions of neutrophils.

Therefore, in the first part of this study, I investigated the role of HVCN1 in the development of NETs. I demonstrated that loss of HVCN1 leads to an increase in the calcium-activated NETosis pathway, which is associated with increased intracellular ROS production and mitochondrial damage. In addition, HVCN1 was found to regulate primary granule release in a calcium-dependent manner. Hence, we concluded that HVCN1controls neutrophil activation by maintaining ion homeostasis.

In the second part of the study, the effects of HVCN1 deficiency were examined *in vivo*. Whereas young HVCN1$^{-/-}$ mice do not show a pathological phenotype, we and others observed a mild inflammation in old HVCN1$^{-/-}$ females, including elevated levels of neutrophils activation markers in the blood. Likewise, HVCN1$^{-/-}$ mice showed more severe pathology in two models of inflammation involving increased neutrophil infiltration into the inflamed tissue.

Interestingly, reduced HVCN1 expression on neutrophils has also been associated with autoimmune diseases in human patients.

This is the first study to show that HVCN1 deficiency increases the inflammatory capacity of neutrophils *in vitro* and *in vivo*, with potential consequences for human disease. In addition, these results have direct implications for the intended use of HVCN1 as a drug target in cancer and neuroinflammatory diseases.

5.1 Role for HVCN1 in maintaining pH, membrane potential and ROS production

In neutrophils, proton currents were shown to be crucial for balancing the intracellular pH during activation[172]. Applying flow-based kinetic pH measurements, I could show that upon stimulation with PMA, the cytosol of wild type neutrophils acidified quickly, but pH balance was already restored after 15 minutes (Fig. 4.2 D). Acidification of the cytosol was mainly due to activation of the ROS-generating enzyme NADPH oxidase, as neutrophils lacking the core component of the oxidase (CYBB$^{-/-}$) did not exhibit a decrease in pH, but rather alkalinized (Fig. 4.18 A). In accordance with previous publications[172], HVCN1$^{-/-}$ neutrophils were unable to return to neutral

pH after NADPH oxidase-induced acidification indicating that HVCN1 is crucial for successful proton extrusion. HVCN1 is not the only molecule that can mediate proton efflux. Neutrophils also express the sodium-proton exchanger 1 (NHE1)[207], which regulates pH in almost all cell types. NHE1 is expressed on the plasma membrane and uses the sodium gradient as a driving force to export protons while importing sodium in an electroneutral manner. I could demonstrate that inhibition of NHE1 in wild type neutrophils impaired pH rebalancing to a similar extent as loss of HVCN1 (Fig. 4.7 B). This indicates that both, HVCN1 and NHE1 contribute to proton extrusion after NADPH oxidase activation in neutrophils. Interestingly, our data further indicate that in HVCN1$^{-/-}$ neutrophils, NHE1 seems to partially compensate for the loss of the channel. We base this hypothesis on the fact that after stimulation, sodium influx was increased in HVCN1$^{-/-}$ neutrophils. Furthermore, inhibition of NHE1 in HVCN1$^{-/-}$ neutrophils strongly exacerbated acidification.

Besides inducing acidification, proton accumulation also increases the membrane potential. Protons are positively charged ions and therefore rising intracellular proton concentrations lead to membrane depolarization. Accordingly, I could demonstrate that HVCN1 is required to maintain the membrane potential, given that HVCN1$^{-/-}$ cells strongly depolarized upon stimulation (Fig. 4.8 A). It must be noted that pH compensation through NHE1 is not able to prevent depolarization of HVCN1$^{-/-}$ neutrophils as the exchange of proton and sodium is electroneutral. Depolarization of the membrane was shown to slow down the transport of electrons through the NADPH oxidase. At a membrane potential of + 200 mV the activity of the NADPH oxidase is blocked completely. Thus, it was proposed that membrane depolarization due to loss or inhibition of HVCN1 causes reduced ROS generation by the NADPH oxidase[222]. In fact, we and others have shown that extracellular ROS production was significantly decreased in HVCN1$^{-/-}$ neutrophils[171,173]. This mechanism also holds true for other immune cells capable of a respiratory burst, such as eosinophils[179] or macrophages (unpublished data). Besides PMA, which is the most commonly used activator for neutrophils, I could show that ROS production in HVCN1$^{-/-}$ neutrophils is also impaired upon stimulation with zymosan (data not shown) or plate-bound IgG (Fig. 4.19 A).

Since ROS play an important role in antimicrobial defense[223], decreased ROS production in HVCN1$^{-/-}$ neutrophils would directly lead to impaired killing of pathogens. Previous studies have shown that *S. aureus* survival was slightly higher in co-cultures with HVCN1$^{-/-}$ neutrophils compared with wild-type controls[171]. In contrast, I showed that killing of *E. coli* was not impaired in HVCN1$^{-/-}$ neutrophils (Fig. 4.20 B). These differences could be due to the different sensitivity of the pathogens to ROS[223]. However, in general, it appears that HVCN1$^{-/-}$ neutrophils can compensate for the reduced ROS production by other killing mechanisms. For example, it has been

shown by us and others that HVCN1$^{-/-}$ neutrophils release more primary granules (Fig. 4.16 A)[174]. Myeloperoxidase (MPO) stored in these granules can catalyze the reaction of hydrogen peroxide to hypochlorous acid, a very potent bactericidal ROS[224]. Because of this mechanism, HVCN1$^{-/-}$ neutrophils produce more hypochlorous acid[174], albeit generating less superoxide by NADPH oxidase[171]. The role of HVCN1 in granule release is discussed in more detail in chapter 5.5. In addition, several studies have shown that HVCN1$^{-/-}$ mice are able to successfully fight bacterial infections *in vivo*[171,174], suggesting that, again, impaired ROS-mediated killing may be compensated for by other effector functions of neutrophils and other immune cells.

Other consequences of reduced ROS production in HVCN1$^{-/-}$ neutrophils have not been investigated so far. However, ROS are also important signaling molecules that regulate immune cell functions. In HVCN1$^{-/-}$ B cells for example, ROS-mediated inhibition of the tyrosine phosphatase SHP-1 is lost, which leads to reduced B cell receptor signaling, impaired B cell proliferation and antibody response[187]. Hence, I continued to also study other ROS-dependent neutrophil effector functions in HVCN1$^{-/-}$ neutrophils.

5.2 Pathways of enhanced NETosis in HVCN1$^{-/-}$ neutrophils

NETosis is a very important effector function of neutrophils and is highly dependent on ROS. Several studies have shown that inhibition of the NADPH oxidase or treatment with ROS scavengers can reduce or even completely block the formation of NETs triggered by various stimuli[79,108]. This raised the question whether HVCN1$^{-/-}$ neutrophils would also show impaired NET formation due to reduced production of extracellular ROS. Contrary to the hypothesis, I found that four times more HVCN1$^{-/-}$ neutrophils underwent NETosis after stimulation with PMA (Fig. 4.3). Of note, the number of NETs generated by mouse neutrophils is very different compared to human neutrophils. For PMA stimulation, a percentage of 80 – 100 % was reported for human neutrophils, while the percentage for mouse neutrophils ranged from 2 – 20 %[57,225,226].

To analyze NET formation in more detail, I used an image-based analysis of nuclear and chromatin morphology (Fig. 4.4). Analysis revealed that as early as one hour after PMA stimulation, a higher percentage of HVCN1$^{-/-}$ neutrophils exhibited morphological features of NETosis compared to wild type neutrophils. Four hours after stimulation, also wild type neutrophils showed morphological changes of nuclei. At this time, however, an increasing percentage of HVCN1$^{-/-}$ neutrophils already showed the morphological features characteristic of later phases of NET formation. Thus, it appears that, first, chromatin changes occur more rapidly in HVCN1$^{-/-}$ neutrophils than in wild type neutrophils, which also suggests that chromatin decondensation in HVCN1 neutrophils may be driven by different mechanisms. Second, it appears that HVCN1$^{-/-}$ neutrophils are generally more prone to undergo NETosis.

In support of the finding that NETosis is enhanced in HVCN1$^{-/-}$ neutrophils, Zhu et al.[179] reported that HVCN1$^{-/-}$ eosinophils also increasingly undergo an activation-induced lytic form of cell death after stimulation with PMA. Since eosinophils are also capable of generating extracellular DNA traps[227], this lytic form of cell death may follow a similar mechanism as observed in HVCN1$^{-/-}$ neutrophils.

Previously, two molecular pathways of NET formation have been described. The classical pathway depends on ROS production by the NADPH oxidase and can be induced by various stimuli, including PMA. This pathway is blocked by NADPH oxidase inhibitors and is absent in human or mice deficient for the NADPH oxidase[79]. Besides that, a NADPH oxidase-independent pathway of NET formation was identified[108,128], which is mainly triggered by calcium ionophores, such as ionomycin or A23187, but also by Group B Streptococcus[108,228]. Here, high levels of intracellular calcium induce a strong activation of PAD4, which directly citrullinates histones[229]. This, in turn, induces a fast disassembly of DNA-histone complexes and chromatin decondensation. In contrast, major histone citrullination does normally not occur in NETosis following PMA stimulation[108].
Accordingly, I could show that in HVCN1$^{-/-}$ neutrophils, histone citrullination was significantly increased compared to wild type controls. This suggests NET formation in PMA-stimulated HVCN1$^{-/-}$ neutrophils may be triggered by enhanced calcium-mediated PAD4 activation rather than NADPH oxidase-dependent ROS production (Fig. 4.5). There are contradictory reports about the necessity of PAD4 activation for induction of NETosis. While some studies report that inhibition of PAD4 prevents NET release[116,229] others claim that PAD4 activation is a feature of NET formation but not required for it[108,230]. Hence, it would be interesting to further analyze the importance of PAD4 activation and histone citrullination in HVCN1$^{-/-}$ neutrophils, for example through chemical inhibition or usage of PAD4/HVCN1-double deficient mice. Interestingly, Zhou et. al[231] could show that in human neutrophils, PAD4 is able to citrullinate subunits of the NADPH oxidase leading to disassembly of the complex and hence reduced ROS production. Further experiments could investigate whether citrullination of these subunits is an additional factor causing reduced ROS production in HVCN1$^{-/-}$ neutrophils.
In line with the above mentioned findings, I could show that chelation of intracellular calcium with BAPTA-AM led to a significant reduction of NET formation in HVCN1$^{-/-}$ neutrophils comparable to wild type levels (Fig. 4.15 A and B). NET formation in wild type neutrophils was only mildly reduced by BAPTA-AM. Fittingly, in human neutrophils it was shown that chelation of intracellular calcium can reduce NET formation induced by both PMA or calcium ionophores[232,233]. This suggests that PMA-induced NET formation also relies on some calcium-mediated signaling events, but may require smaller changes in calcium levels compared to calcium ionophore-induced NET formation. Since calcium ionophore-induced NET formation involves calcium influx from the

extracellular space[232], it would also be critical to investigate the effects of extracellular calcium depletion on NET formation in wild type and HVCN1$^{-/-}$ deficient neutrophils.

In addition, some studies report the involvement of mitochondrial ROS in calcium-induced NETosis[128], but the necessity of this is still controversial. Of interest, HVCN1$^{-/-}$ neutrophils also showed increased intracellular ROS production (Fig. 4.11 A). However, NET formation could not be reduced in the presence of the antioxidant NAC (Fig. 4.11 B). This suggests that the increased NET formation in HVCN1$^{-/-}$ neutrophils depends exclusively on increased calcium and not on intracellular ROS production (further discussed in chapter 5.4).

5.3 Mechanisms of calcium mobilization in HVCN1$^{-/-}$ neutrophils

In wild type neutrophils, PMA stimulation does not lead to calcium mobilization[232,234]. Accordingly, I did not observe increased calcium levels in wild type neutrophils after PMA stimulation. However, consistent with the fact that histone citrullination requires very high intracellular calcium concentrations[235], I demonstrated that PMA induced calcium mobilization HVCN1$^{-/-}$ neutrophils. Calcium mobilization occurred in two waves: first a release from the ER which was followed by calcium influx from the extracellular space (Fig. 4.6). In contrast to our data, Chemaly et. al[173] demonstrated that calcium influx into HVCN1$^{-/-}$ neutrophils is inhibited due to augmented cell depolarization caused by accumulation of protons which decreases the driving force for calcium entry. The authors show that calcium mobilization upon stimulation with chemotactic agents, as well as calcium influx upon addition of extracellular calcium was decreased in HVCN1$^{-/-}$ neutrophils pretreated with PMA. However, they did not study the direct effect of PMA on calcium mobilization, hence their data cannot directly be compared to our data.

To date, we have not been able to elucidate the exact mechanism leading to calcium release from the ER of PMA-stimulated HVCN1$^{-/-}$ neutrophils. However, the following possible mechanisms can be excluded.

The lack of calcium mobilization in wild type neutrophils treated with the NHE1 inhibitor amiloride indicates that ER calcium release cannot be induced by intracellular acidification alone (Fig. 4.7). Fittingly, also in human neutrophils stimulated with immune complexes, cytoplasmic acidification by inhibition of the NHE1 had no effect on intracellular calcium levels[236].

Moreover, no classical voltage-gated calcium channels have yet been identified in neutrophils, ruling out simple membrane depolarization as a cause of calcium mobilization.

Analysis of calcium channels expressed on cellular organelles suggests two possible scenarios of how calcium could be mobilized from the ER in HVCN1$^{-/-}$ neutrophils (Fig. 5.1 A and B). The classical calcium-dependent signaling pathway in neutrophils is mediated via phospholipase C and inositol trisphosphate (PLC/IP_3). Stimulation of neutrophils via GPCRs, Fc receptors or TLRs eventually results in the activation of PLC, which cleaves phosphatidylinositol 4,5-bisphosphate (PIP_2) to DAG and IP_3, which ultimately leads to release of calcium through IP_3 receptors (IP_3R)

located on the ER[237]. However, PMA stimulation normally only induces activation of PKC which is downstream of ER calcium release. Nonetheless, it was previously shown that for example in mouse embryonic fibroblasts[238] or human intestinal epithelial cells[239] ROS can activate PLC directly, suggesting a potential role for the increased intracellular ROS levels observed in HVCN1$^{-/-}$ neutrophils. Despite this, the observation that treatment with an antioxidant did not reduce NETosis in HVCN1$^{-/-}$ neutrophils indicates that ROS-induced PLC activation does not play a role. Further experiments should aim to analyze if PLC might be activated in HVCN1$^{-/-}$ neutrophils and if ER calcium release could be induced by increased levels of IP_3.

HVCN1 is also expressed intracellularly (Fig. 4.1 C) and possibly also influences pH of acidic intracellular compartments, including neutrophil granules, which are also known to store calcium[240,241]. Two pore channels (TPCs) are non-selective cation channels that are primarily expressed on acidic organelles and can be activated by binding to NAAPD or PIP_2. Interestingly, gating of these channels is further regulated by differences in pH and voltage (intraluminal versus intracellular). Local release of calcium from acidic organelles can convert into global calcium waves by inducing calcium-induced calcium release through IP_3R or ryanodine receptors from the ER a process best described in muscle cells but known to take place in various cell types[242]. We confirmed expression of *Tpcn1* and *Tpcn2* in neutrophils, however not much is known about their role in calcium control in neutrophils. Further experiments therefore should aim to test if these channels are activated during stimulation of HVCN1$^{-/-}$ neutrophils.

While it remains unclear what causes the release of calcium from the ER in HVCN1$^{-/-}$ neutrophils, for the second wave caused by extracellular calcium influx we assume that there are two alternative mechanisms (Fig. 5 C and D). The first, already well described in lymphocytes, is store-operated calcium entry (SOCE). This process is triggered by depletion of calcium from the ER, which is sensed by the stromal interaction molecule (STIM), a calcium-sensitive protein located in the ER membrane. Upon calcium depletion, STIM oligomerizes and activates the calcium release-activated calcium channel (CRAC) protein 1 (ORAI1, the pore subunit of the CRAC channel) in the plasma membrane that facilitates influx of calcium[243]. Until now, there is only little indication that SOCE might regulate NET formation. There is one study showing that emptying of the ER by Thapsigargin alone is enough to induce NETosis[244]. Furthermore, Muñoz-Caro *et al.*[245] showed that inhibition of SOCE reduced parasite-induced NET formation. However, the inhibitor used (2-APB) is also known to have many off-target effects such as an activation of transient receptor potential (TRP) channels. In contrast to the limited information of the role of SOCE in NETosis, many studies could show an important role for STIM1 and STIM2 in phagocytosis, degranulation and ROS production[246]. Usage of a more specific inhibitor of STIM, such as YM 58483, could help to clarify the exact role of SOCE in calcium mobilization in HVCN1$^{-/-}$ neutrophils.

Besides SOCE, influx of extracellular calcium in HVCN1$^{-/-}$ neutrophils could be mediated by the sodium-calcium exchanger 1 (NCX1)[247]. I could show that sodium levels are increasing in HVCN1$^{-/-}$ neutrophils upon PMA stimulation, most likely due to the compensating activity of NHE1, which brings one sodium into the cytoplasm in exchange for a proton; indeed, treatment with the NHE1 inhibitor amiloride blocks sodium influx in HVCN1 $^{-/-}$ neutrophils (Fig. 4.7 B). Interestingly, amiloride also reduced the magnitude of the second calcium wave in HVCN1$^{-/-}$ neutrophils, suggesting that this influx is dependent on a rise in intracellular sodium (Fig. 4.7 D). Fittingly, it could be demonstrated that inhibition of NCX1 only and subsequent calcium accumulation was sufficient to trigger NETosis in human neutrophils[248].Whereas some questions about how loss of HVCN1 induced calcium influx in PMA stimulated neutrophils remain to be answered, my work has clarified some significant steps: calcium is the key mediator of the differences observed in HVCN1$^{-/-}$ neutrophils, namely NETosis, mitochondrial depolarization and granule release. Hence, future experiments need to address (I) what channels are involved in calcium mobilization from the ER, (II) if calcium release from the ER is causing influx of extracellular calcium or not (SOCE vs. NCX1) and (III) if blockade of extracellular calcium is enough to inhibit enhanced NETosis.

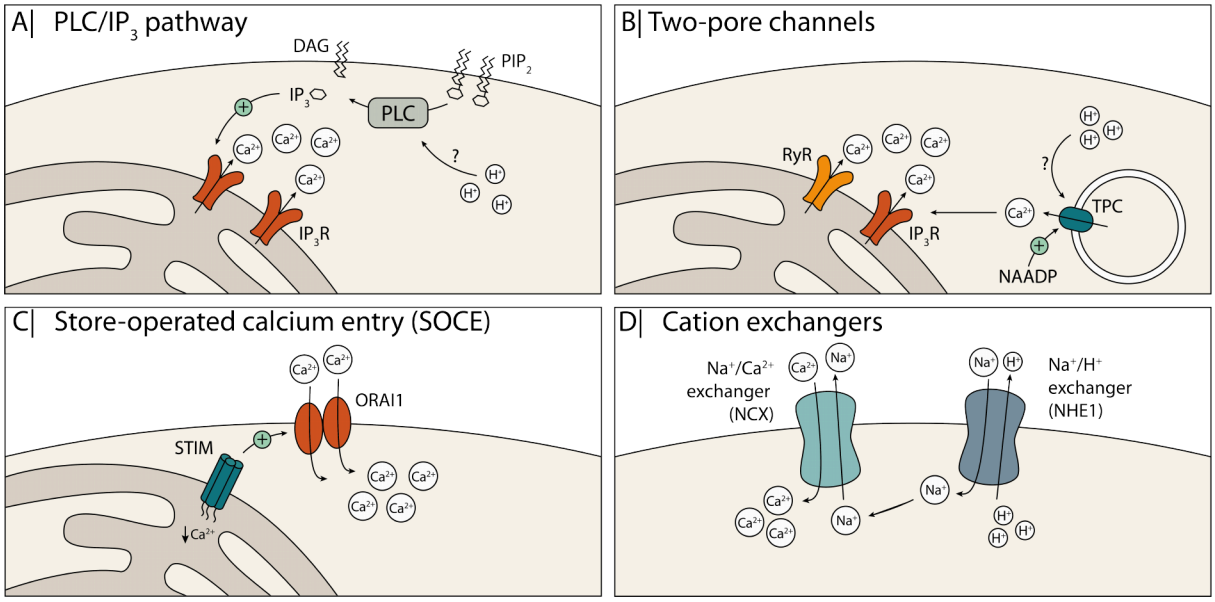

Figure 5.1| Potential mechanisms of calcium mobilization from intracellular stores and extracellular space in HVCN1$^{-/-}$ neutrophils.
A| The PLC/IP$_3$ pathway is a common mechanism of calcium mobilization in neutrophils. Activated PLC will cleave PIP$_2$ to DAG and IP$_3$. Thereafter, IP3 will activate IP3 receptors, which will induce calcium release from the ER. There are no reports yet of how intracellular acidification could activate PLC. B| TPCs are cation channels expressed on acidic organelles. They are activated by binding of their ligand NAAPD, however pH and voltage can influence TPC activity. Local release of calcium can then induce calcium–activated calcium release from the ER.
C| Reduction in calcium concentration in the ER can be sensed by STIM, which then oligomerizes and activated ORAI1 channels on the plasma membrane. Activated ORAI1 allows entry of extracellular calcium into the cytoplasm. This mechanism is called store-operated calcium entry. D| Together with HVCN1, NHE1 facilitates the efflux of protons after activation of the NADPH oxidase. NHE1 exchanges one proton against one sodium, which will result in a rise of intracellular sodium concentration. Sodium can again be exchange with calcium by the NCX which will finally lead to calcium influx from the extracellular space into the cytosol.

5.4 The role of mitochondrial depolarization and ROS in HVCN1$^{-/-}$ neutrophils

Calcium induced NETosis is accompanied by the generation of mitochondrial ROS[128]. Interestingly, I found that the mitochondrial membrane potential of HVCN1$^{-/-}$, but not wild type, neutrophils collapses within a few minutes after PMA stimulation (Fig. 4.12 A). Dissipation of mitochondrial membrane potential was dependent on calcium release from the ER (Fig. 4.12 B and C). Transfer of calcium from the ER into mitochondria happens at close contact microdomains where the calcium concentration is much higher compared to the rest of the cytoplasm, but can be blocked by the calcium chelator BAPTA, as is indeed the case in HVCN1$^{-/-}$ neutrophils[249]. Calcium entry into the inner mitochondrial matrix is mediated by the mitochondrial calcium uniporter (MCU) or the sodium calcium exchanger (NCX). Transfer of calcium between ER and mitochondria was already reported for neutrophils of human, mice and zebrafish and it was shown to be crucial for functional migration[250]. However, under pathological conditions, such as ischemia[251], neurodegeneration[252] or, as I showed, potentially also in NETosis, mitochondria are overloaded with calcium which leads to dissipation of the mitochondrial membrane potential[253]. Overload with calcium is associated with increased mitochondrial ROS production in a variety of cell types[254–256], including neutrophils[257]. Indeed, HVCN1$^{-/-}$ neutrophils also showed higher intracellular ROS levels that could be reduced by calcium chelation (Fig. 4.11). There are conflicting reports on the requirement of mitochondrial ROS in the induction of calcium-dependent NETosis, which might depend on the use of different methods to inhibit ROS production. Calcium ionophore-induced NET formation of human neutrophils was shown to be reduced by the mitochondrially targeting antioxidant SkQ1[213] or by the mitochondrial uncoupler dinitrophenol[128] (DNP). In contrast, calcium-induced NET formation was not inhibited in the presence of the broader antioxidant pyrocatechol[108]. In line with this finding, I also found that NET formation in HVCN1$^{-/-}$ neutrophils was not inhibited by the antioxidant NAC. This suggests that ROS formation might need to be inhibited directly inside mitochondria to prevent NET formation. In this case the use of MitoTEMPO, an antioxidant which accumulates in mitochondria, would have helped to better understand the role of mitochondrial ROS in HVCN1$^{-/-}$ neutrophils. Almost all mitochondria-targeting molecules possess a triphenyl-phosphonium-based modification (TPP^{+}) or are lipophilic cations (e.g. rhodamine) and therefore accumulate in the mitochondrial matrix due to the strongly negative mitochondrial membrane potential[258]. In HVCN1$^{-/-}$ neutrophils, however, the profound loss of the mitochondrial membrane potential leads to release of positively charged molecules from the mitochondria, which we could also observe for the mitochondria-targeted probe MitoSOX (Fig. 4.10.). For this reason, mitochondria-targeted molecules unfortunately cannot be used in our studies.

In accordance with our data, it was reported that neutrophils that are deficient for the MCU-regulating protein MICU1 accumulate higher levels of mitochondrial calcium and show an increased propensity to undergo NETosis upon stimulation with *S. aureus*[257].

Furthermore, Lood *et al.*[137] demonstrated that human neutrophils stimulated with immune complexes contain increased numbers of depolarized, ROS-generating mitochondria, and NETs from these neutrophils were enriched with oxidized mitochondrial DNA, which induced an enhanced inflammatory response in human PBMCs or mouse splenocytes. However, in contrast to our data, they showed that ROS scavenging could reduce NET formation. Interestingly, they further demonstrated that NETs formed by low-density granulocytes (LDGs) of SLE patients are also enriched in mitochondrial DNA.

In summary, it appears that depolarized, ROS-generating mitochondria are a hallmark of calcium-induced NET formation and we observed a similar phenotype in HVCN1$^{-/-}$ neutrophils after PMA stimulation. However, further experiments using for example electron transport chain inhibitors are needed to show that mitochondrial ROS generation is indeed not essential for NET formation in HVCN1$^{-/-}$ neutrophils. Furthermore, it would be interesting to check if NETs from HVCN1$^{-/-}$ neutrophils are also enriched in oxidized mitochondrial DNA. In fact, I could already show that general DNA oxidation was enhanced in HVCN1$^{-/-}$ neutrophils compared to wild type controls (Fig. 4.11 B). This could be a potential inducer of the autoimmune phenotype observed in HVCN1$^{-/-}$ mice (further discussed in 5.7).

5.5 Mechanisms of primary granule release in HVCN1$^{-/-}$ neutrophils

Neutrophil degranulation has an important role for the killing of pathogens, and, more generally, for orchestrating an immune response. There are four classes of neutrophil granules, distinguished by their content. Moreover, each class requires a different strength of stimulation, from mild to strong stimulation the order is secretory vesicles, tertiary, secondary and finally primary granules. Degranulation needs to be tightly regulated, as the granule proteins have cytotoxic properties and can damage the host tissue. In particular, proteins stored in primary granules are extremely cytotoxic and are therefore released only upon very strong neutrophil activation. A critical role can be attributed to the primary granule protein MPO since it accounts for 5 % of the dry weight of human neutrophils[259]. I found that PMA-stimulated HVCN1$^{-/-}$ neutrophils secrete more MPO, whereas secretion of MMP-9, stored in tertiary granules, was not changed compared to wild type neutrophils (Fig. 4.16). This effect was also reported by Sasaki *et al.*[174] who showed that HVCN1$^{-/-}$ neutrophils stimulated with PMA or IgG secrete more MPO and NE, but similar levels of lactoferrin (secondary granules) compared to wild type controls. This means that HVCN1 dampens neutrophil activation by inhibiting the degranulation of primary, but not secondary or tertiary granules.

The regulation of granule secretion has multiple layers including the activation of different kinases, calcium influx and various proteins that mediate membrane fusion[260]. However, the most important factor for degranulation is increase of intracellular calcium concentrations as calcium mobilization alone is sufficient to induce degranulation. Interestingly, degranulation of primary

granules requires the highest levels of calcium[261]. This might explain why higher levels of intracellular calcium observed in HVCN1$^{-/-}$ neutrophils might be enough for the release of primary granules whereas lower calcium levels in wild type neutrophils are not sufficient to induce the release of primary granules. Interestingly, in other immune cells degranulation is also regulated by local calcium release from acidic granules. For example, in human cytotoxic T cells, calcium flux through two pore channels (TPCs, also see 5.3) was described to be essential for exocytosis of cytolytic granules[262]. In the presence of TPC inhibitors, global calcium flux from the ER failed to induce degranulation in T cells. Exocytosis rather required local perigranular calcium domains created by release of granular calcium through TPCs. In contrast, genetic deletion of TPC1 in murine mast cells leads to increased degranulation upon stimulation[263], because in TPC1$^{-/-}$ mast cells, more calcium is stored in the ER as TPC-regulated calcium storage in lysosomes is reduced. Following stimulation, more calcium is released from the ER of TPC1$^{-/-}$ mast cells, resulting in enhanced degranulation. The regulation of degranulation by TPCs was not yet investigated in neutrophils. However, our data suggest that TPC1 and TPC2 are highly expressed in murine neutrophils (Fig. 4.9) and might therefore play a role in the control of degranulation.

Given the central role for calcium in degranulation, it was not surprising to find that chelation of intra- or extracellular calcium reduced MPO secretion in HVCN1$^{-/-}$ neutrophils (Fig. 4.16 A). However, calcium chelation did not completely abolish primary granule release, which suggests that HVCN1 can regulate degranulation via additional factors.

In many cell types, low intravesicular pH was shown to promote exocytosis[264,265]. In neutrophils, alkalinization of granules with the v-ATPase inhibitor bafilomycin results in a significant reduction in primary granule release[266]. Interestingly, activation of v-ATPase is not only critical for acidification of granules, but was also shown to act as a sensor of granule pH[267] and, in addition, serves as an adaptor for proteins that mediate membrane fusion[268,269]. Therefore, the localization of v-ATPase to the granules is a crucial mechanism for triggering degranulation. Interestingly, HVCN1 was shown to regulate v-ATPase recruitment to phagosomes in a ROS-dependent manner[176]. Phagosomes from HVCN1$^{-/-}$ neutrophils exhibit either very high or very low pH, depending on whether or not there is residual activation of NADPH oxidase. Although primary granules are the only ones that show minimal expression of HVCN1 (Fig. 4.1 C), we cannot exclude the possibility that the presence of HVCN1 on their membranes may still affect granule pH or that proton channels play a role in an indirect manner. Therefore, measurements of granule pH and localization studies of v-ATPase are necessary to clarify whether intragranular pH affects the increased degranulation in HVCN1$^{-/-}$ neutrophils.

In line with our findings, Gewirtz *et al.*[236] demonstrated that inhibition of NHE1 and subsequent acidification of human neutrophils led to increased release of primary granules upon FcR stimulation. Interestingly, the authors could not detect an increase in intracellular calcium, but

demonstrated increased degranulation by enhanced activation of phospholipase D. However, the mechanism by which acidification enhances PLD activation still needs to be established.

Summarizing, HVCN1 seems to regulate release of primary neutrophil granules through calcium-dependent and independent mechanisms. Further studies are needed to identify the calcium-independent signals through which HVCN1 can inhibit granule release.

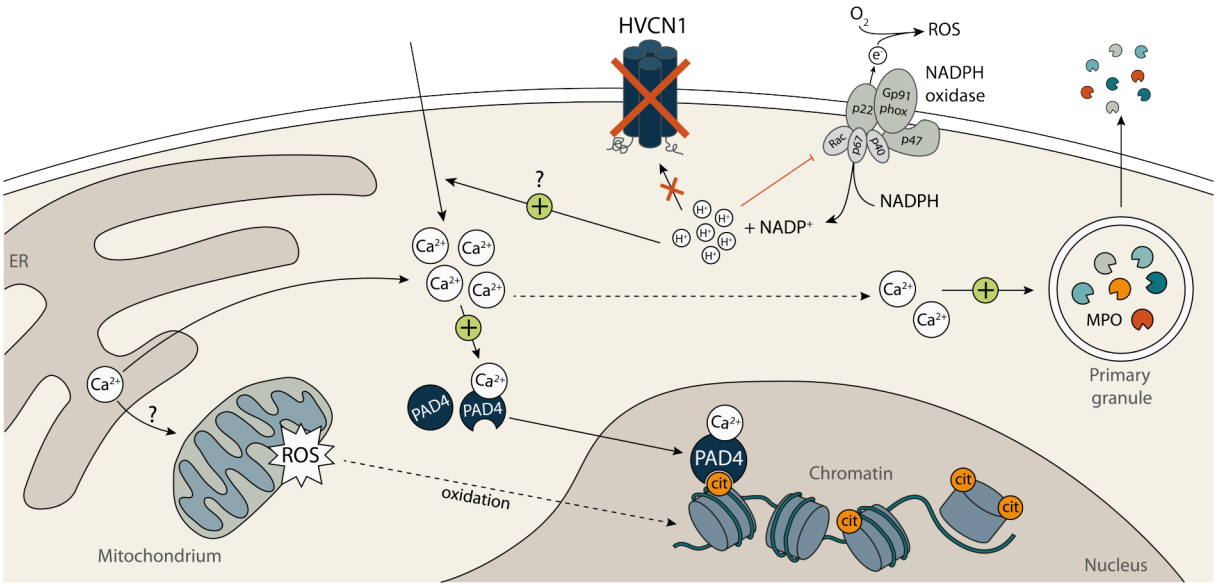

Figure 5.2| Role of HVCN1 in regulating neutrophil activation.
Upon neutrophil activation, the NADPH oxidase assembles at the plasma membrane. It generates extracellular ROS by transferring electrons from NADPH across the membrane. This reaction leaves NADP+ and protons behind in the cytoplasm. HVCN1 is crucial to mediate the efflux of protons and thereby sustains the intracellular pH and the membrane potential. In the absence of HVCN1, protons accumulate which leads to membrane depolarization and thus inhibition of the oxidase. Furthermore, although not yet fully understood (see Fig. 5.1), accumulation of protons also induces a biphasic calcium mobilization: first from the ER, followed by influx from the extracellular space. Calcium from the ER enters into mitochondria which leads to collapse of the mitochondrial membrane potential and ROS production. Calcium influx from the extracellular space is inducing activation of PAD4, which subsequently translocates into the nucleus and citrullinates histone. This modification induces disassembly of nucleosomes which results in chromatin decondensation and finally NET formation. Furthermore, increase intracellular calcium levels induce release of primary neutrophil granules containing MPO and NE.

In addition, we found that HVCN1$^{-/-}$ neutrophils exhibited formation of large vacuoles resulting from increased pinocytosis (Fig. 4.17). Although wild type neutrophils also formed pinocytic vacuoles, these remained much smaller compared to vacuoles in HVCN1$^{-/-}$ neutrophils. It has been described that stimulation with PMA induces pinocytosis in human neutrophils. Concordantly, Botelho *et al.*[214] showed that exocytosis of primary granules is associated with pinocytosis, presumably to recycle membrane components and to prevent excessive expansion of the cell membrane. However, because the underlying mechanisms remain to be elucidated, it is not yet clear whether pinocytosis is dependent on degranulation or whether they are two simultaneous yet independent events that occur upon neutrophil activation. Our data show that increased primary granule release is associated with increased pinocytosis indicating that pinocytosis is in fact dependent on exocytosis.

A striking feature of the pinocytic vacuoles in HVCN1$^{-/-}$ neutrophils is their large size. Growing of vacuoles could result from merging of several pinosomes. Fusion of intracellular vesicles is - similar to exocytosis - mediated by SNARE proteins. As these also require calcium to function,

calcium mobilization in HVCN1$^{-/-}$ neutrophils might be sufficient to induce fusion of pinosomes. Furthermore, Levine *et al.*[104] demonstrated that phagosomes of HVCN1$^{-/-}$ neutrophils displayed abnormal swelling most likely due to changes in osmolality. They hypothesize that potassium ions, which unlike protons are osmotically active, are transported into the phagosome to partially compensate for the loss of charge resulting from activation of NADPH oxidase in the absence of HVCN1. A similar mechanism based on aberrant ion distribution could also cause pinocytic swelling.

In addition, swelling of vacuoles could also be an indication for a degradation defect. In order to mature and finally be degraded, lysosomes need to acidify. It was shown that phagosomes of HVCN1$^{-/-}$ neutrophils fail to properly acidify[176]. Hence, it would be worth investigating whether pinosomes in HVCN1$^{-/-}$ neutrophils also exhibit impaired acidification, which could explain the retention and growth of vacuoles.

5.6 Phenotype of HVCN1$^{-/-}$ mice in acute inflammation

Despite significant differences in neutrophil activation, young HVCN1$^{-/-}$ mice do not exhibit a pathological phenotype. Moreover, they are able to efficiently clear various pathogens *in vivo*[171]. However, HVCN1$^{-/-}$ mice showed enhanced inflammation during pulmonary infection with *C. albicans*[174], which may be related to the increased inflammatory capacity of HVCN1$^{-/-}$ neutrophils that I observed in the response to PMA *in vitro.*

Accordingly, in a model of peritonitis, HVCN1$^{-/-}$ mice showed increased inflammation characterized by enhanced immune cell infiltration into the peritoneal cavity, the majority of which were neutrophils (Fig. 4.23). I could exclude that enhanced neutrophil infiltration into the peritoneum was due to elevated numbers of blood neutrophils before challenge, as naïve wild type and HVCN1$^{-/-}$ mice showed similar blood neutrophil numbers and similar expression levels of maturation markers. However, HVCN1$^{-/-}$ mice exhibit a higher number of immature neutrophils in the bone marrow, which could be additionally recruited under inflammatory conditions (Fig. 21.C). Indeed, zymosan-induced peritonitis leads to an increased number of circulating neutrophils, whereas the neutrophil count in the bone marrow decreases[270]. Moreover, it is known that under inflammatory conditions immature neutrophils can be mobilized from the bone marrow to maximize the neutrophil response[24]. Analysis of maturation markers, such as CXCR2, on circulating and peritoneal neutrophils from wild type and HVCN1$^{-/-}$ mice would help to understand if increased numbers of immature neutrophils contribute to the increase in total neutrophil numbers.

In addition to increased numbers of neutrophils in the circulation, enhanced extravasation could also contribute to increased neutrophil numbers in the peritoneum. There are conflicting reports on the role of HVCN1 in regulating neutrophil migration. El Chemaly *et al.*[173] demonstrated that HVCN1$^{-/-}$ neutrophils exhibit defective undirected migration in response to 10 µM of the

chemotactic agent fMIVIL as a result of impaired calcium entry. In contrast, Okochi *et al.*[175] reported that HVCN1$^{-/-}$ neutrophils showed enhanced undirected as well as directed migration across the membrane of a transwell chamber, particularly at low concentrations of the chemotactic agent fMLP (up to 1 µM). They could further demonstrate that the enhanced migration is due to a cell-intrinsic mechanism that depends on ROS-driven ERK phosphorylation. In addition to intrinsic cellular factors, migration of neutrophils into the peritoneal cavity could also be promoted by increased levels of chemokines or other proteins with chemotactic activity. Neutrophil recruitment is mainly driven by CXCL1 and CXCL2, which are produced by peritoneal macrophages upon pathogen encounter[271]. Recently, it was shown that peritoneal mast cells also produce these two chemokines[272]. Since I used global HVCN1$^{-/-}$ mice for this experiment, it must be considered that all other immune cells are also deficient in HVCN1. There are no studies yet on chemokine production in HVCN1$^{-/-}$ macrophages. However, it has been shown that in the presence of zinc, activated mast cells show increased degranulation[273], and mast cell granules also contain CXCL1[272]. Therefore, it would be interesting to investigate if HVCN1$^{-/-}$ mice have higher levels of chemotactic molecules after zymosan injection and if this could be due to loss of HVCN1 in macrophages or mast cells.

Moreover, HVCN1$^{-/-}$ neutrophils themselves might release increased chemotactic molecules. The characteristic self-amplifying swarming behavior of neutrophils is triggered by the release of leukotriene B4 (LTB_4) and CXCL2 from early recruited neutrophils, leading to further recruitment of neutrophils from the circulation[274]. Because HVCN1$^{-/-}$ neutrophils show increased degranulation, one could speculate that they also release more chemoattractants. Quantification of chemoattractants in supernatants from neutrophils stimulated *in vitro* or in the peritoneal lavage would help to understand if loss of HVCN1 leads to enhanced LTB_4-induced neutrophil swarming.

Furthermore, the loss of HVCN1 impairs phagosomal acidification of macrophages[176], suggesting that these cells might display impaired digestion of apoptotic cells. Interestingly it was shown that impaired efferocytosis of apoptotic neutrophils by macrophages leads to neutrophil accumulation and increased production of inflammatory cytokines in the peritoneal cavity after zymosan injection[275]. Hence, potential impairment of efferocytosis in HVCN1$^{-/-}$ macrophages could contribute to enhanced peritoneal inflammation in HVCN1$^{-/-}$ mice.

Taken together, increased neutrophil numbers in the peritoneal cavity of HVCN1$^{-/-}$ mice could be explained by neutrophil-intrinsic factors, i.e., increased immature neutrophil numbers, augmented migration or release of chemoattractants such as LTB_4, or by changes in other immune cells, i.e., increased release of chemokines or impaired efferocytosis. In order to exclude the contribution of HVCN1 deficiency in other immune cells, it would be necessary to analyze neutrophil-specific HVCN1$^{-/-}$ mice. Until now, we were not able to generate an effective neutrophil-specific deletion of HVCN1 (see 5.8).

Furthermore, I detected higher MPO levels in the peritoneal cavity and serum of HVCN1$^{-/-}$ mice treated with zymosan compared with wild type controls (Fig. 4.23 D & E). Higher MPO levels in the peritoneal cavity correlate with the observed increased neutrophil count. Elevated blood MPO levels could either reflect increased mobilization of neutrophils into the circulation or, in agreement with my data obtained *in vitro*, result from increased degranulation or NETosis of HVCN1$^{-/-}$ neutrophils. Increased MPO levels in the blood could further promote neutrophil infiltration into the peritoneal cavity. It was shown that due to its positive charge, MPO binds to heparan sulfate glycosaminoglycans, which are part of the endothelial glycocalyx. Thereby it creates a positively charged surface that allows binding of negatively charged neutrophils[276]. Furthermore, MPO can bind to CD11b supporting migration[277], activation[278] and prolonged survival[279] of neutrophils.
In addition to MPO, it would be interesting to also analyze NET formation in the peritoneal cavity after injection of zymosan. However, identification and quantification of NETs *in vivo* is very challenging. Measurement of cell-free DNA alone is not sufficient to prove NET formation as DNA is also expelled from necrotic cells. Furthermore, *in vivo* NETs are rapidly degraded by DNases which makes it even more challenging to detect them. According to Yousefi *et al.*[280], the only reliable method to unambiguously show NET formation *in vivo* is by histological analysis. Therefore, quantification of NETs in the peritoneal cavity might not be possible.

To further study the role of HVCN1 in inflammation, we decided to subject wild type and HVCN1$^{-/-}$ mice to a model of anti-neutrophil cytoplasmic antibody (ANCA)-associated pulmonary vasculitis (AAPV)[220]. In contrast to zymosan-induced peritonitis, AAPV reflects an autoimmune disease primarily driven by neutrophils. In this model, administration of fMLP and LPS is intended to mimic a bacterial infection which often causes severe flare-ups in AAPV patients[281]. Intratracheal administration of these two ligands leads to neutrophil recruitment into the pulmonary vasculature and additionally stimulates neutrophils to expose MPO on their surface. This step is crucial for the subsequent activation of neutrophils by anti-MPO antibodies administered intraperitoneally[282] (Fig. 4.24). At day 3 after AAPV induction, we observed a similar lung pathology between wild type and HVCN1$^{-/-}$. However, augmented weight loss and an increase in lung hemorrhages indicated enhanced inflammation in HVCN1$^{-/-}$ mice. In line, the number of neutrophils in the BAL of HVCN1$^{-/-}$ mice was increased compared to wild type controls, despite total leukocyte numbers not being different between genotypes. At this time point of the disease model, it is most likely that cells recovered from the BAL did not actively migrate into the lung tissue, but rather entered passively through damaged vessels. Hence, increased numbers of neutrophils in the BAL could be an indicator for increased vessel permeabilization or could reflect increased numbers of neutrophils mobilized from the bone marrow. Enhanced mobilization could be caused by increased numbers of immature neutrophil

in the bone marrow of HVCN1$^{-/-}$ mice or reflect increased overall inflammation. Of note, number of neutrophils in the lungs of fMLP/LPS treated control mice were similar between wild type and HVCN1$^{-/-}$ at day 3. However, it would be important to analyze neutrophil numbers at earlier time points to exclude that increased recruitment at earlier time points, which we observed in the peritonitis model, is causing augmented inflammation at day 3 of AAPV.

The main cause of vasculature damage in AAV is the activation of neutrophils by ANCAs[283]. These autoantibodies can bind to their antigens exposed on the surface of neutrophils and can additionally bind Fc receptors, which leads to enhanced neutrophil activation[284,285]. The fact that HVCN1$^{-/-}$ neutrophils release more MPO *in vitro* would suggest that the increased inflammation in AAPV may be due to increased exposure of MPO on the surface of neutrophils. However, we did not detect increased levels of MPO in the blood of AAPV mice compared to control mice. This suggests that MPO might be sequestered by the injected anti-MPO antibodies and thus is not suitable for measuring degranulation in this model. To confirm the increased degranulation of HVCN1$^{-/-}$ neutrophils in AAPV, levels of neutrophil elastase or PR3 in the circulation could be determined.

Moreover, primed neutrophils activated by ANCAs were shown to undergo NETosis[142]. Accordingly, AAV patients display higher levels of NET remnants (nucleosome-MPO complexes) in their circulation[144]. Interestingly, in another mouse model for vasculitis, inhibition of PAD was shown to reduce serum levels of ANCAs, which suggests that PAD4-driven NET formation is enhancing autoantibody production by providing autoantigens[286]. In our model, no increase in cell-free DNA could be detected in the BAL of AAPV mice in comparison with control mice. However, because cell-free DNA is not a sufficient indicator of NETosis *in vivo* anyway, we are attempting to quantify histone citrullination in neutrophils by histological examination of lung tissue. Furthermore, stimulation of primed neutrophils with ANCAs *in vitro* could be useful to assess if HVCN1$^{-/-}$ neutrophils also show enhanced NET formation in the AAPV setting.

Applying the same AAPV model, Kessler *et al.*[220] were able to show that disease severity is highly dependent on interferon signaling in monocyte-derived macrophages. As we used global HVCN1$^{-/-}$ mice, also monocytes are deficient for HVCN1. Thus, we cannot rule out that loss of HVCN1 would also influence the activation and interferon production by these cells. Not much is known about how HVCN1$^{-/-}$ macrophages are reacting during inflammation. Studies in related cells, such as microglia[182,186], however suggest that loss of HVCN1 would lead to a less inflammatory phenotype of macrophages. Hence, the phenotype observed in HVCN1$^{-/-}$ mice could be a result of increased neutrophil inflammation on the one side and reduced macrophage activation on the other hand.

Since it was shown that immune cell infiltration and hemorrhages peaked at day 3 after vasculitis induction[220], we chose that time point for our analysis. At this time, the differences in pathology between genotypes, although small, are suggestive of increased and ongoing neutrophil-driven

inflammation in HVCN1$^{-/-}$ mice. Interestingly, day 3 is the first day on which HVCN1$^{-/-}$ mice lost significantly more weight compared to wild type controls. Hence, future experiments should include analysis of disease progression after day 3 which might reveal more pronounced differences between wild type and HVCN1$^{-/-}$ mice, or even impaired resolution of diseases in HVCN1$^{-/-}$ mice, due to prolonged neutrophil activation with enhanced antigen release.

The AAPV model is suitable to study neutrophil-driven inflammation in autoimmunity. However, it does not allow to explore whether neutrophils are involved in the etiology of vasculitis, as autoantibodies are applied exogenously. Therefore, other models for autoimmune diseases are needed to further study how increased degranulation and NET formation by HVCN1$^{-/-}$ neutrophils contribute to autoimmunity.

5.7 Potential drivers for autoimmune disorder in HVCN1$^{-/-}$ mice

With increasing age, HVCN1$^{-/-}$ mice develop mild symptoms of autoimmunity. This phenomenon was first described by Sasaki *et al.*[190]. They reported that in particular female HVCN1$^{-/-}$ mice aged 14 to 16 months showed splenomegaly, the presence of anti-DNA antibodies, and renal damage caused by immune complexes. We found no difference in mean spleen weight between 20 month-old wild-type and HVCN1$^{-/-}$ mice. However, defining splenomegaly as a spleen weight greater than 150 mg, four of five HVCN1$^{-/-}$ mice but only 2 of 5 wild type mice presented splenomegaly (Fig. 4.22 A).

In humans, aging is associated with an increased risk for autoimmunity caused by loss of self-tolerance and increased levels of autoantigens, such as circulating cell-free DNA[287,288]. A hallmark of autoimmunity is the presence of self-reactive T cells. Sasaki *et al.*[190] showed that HVCN1$^{-/-}$ mice had higher levels of activated CD4$^+$ and CD8$^+$ T cells which they hypothesized could cause autoreactivity. In contrast, Coe *et al.*[191] demonstrated that both T cell subsets exhibited proliferation and activation defects in the absence of HVCN1. However, they speculate that HVCN1 may be required only for strong T cell activation. This could lead to preferential survival of autoreactive T cells, which normally have lower antigen affinity. To date, there are no reports on the expression and function of HVCN1 in regulatory T cells (T_{reg}). It could be speculated that, similar to CD4$^+$ and CD8$^+$ T cells, loss of HVCN1 could also affect T_{reg} cell function, leading to loss of self-tolerance.

Beside T cells, autoreactive B cells play a central role in the development of autoimmunity, as they produce autoreactive antibodies[289]. In HVCN1$^{-/-}$ mice, higher levels of anti-DNA antibodies could be detected in the blood[190]. This finding is quite surprising, as HVCN1$^{-/-}$ B cells show an impaired antibody response[187]. Therefore, it is unlikely that loss of HVCN1 in B cells is responsible for the development of autoimmunity.

Furthermore, activated plasmacytoid dendritic cells (pDCs) contribute to autoimmunity, mainly by producing type I interferons as a response to nucleic acid sensing[290]. Although levels of INFα

were low in both young and aged wild type and HVCN1$^{-/-}$ mice, there was a small but significant increase in aged HVCN1$^{-/-}$ mice compared to age-matched wild type controls (Fig. 4.22 B). However, it is unlikely that this is a direct effect of loss of HVCN1 in pDCs since Montes-Cobos *et al.*[291] could show that HVCN1$^{-/-}$ pDCs activated via TLR9 produce significantly less INFα compared to wild type pDCs.

Last but not least, neutrophils also play an important role in autoimmune reactions. In many autoimmune diseases, autoantibodies are directed against neutrophil antigens that are released via NETs. Interestingly, serum MPO levels were elevated in aged HVCN1$^{-/-}$ mice compared with wild type controls, even though numbers of neutrophils in the blood were similar. This suggests that in aged HVCN1$^{-/-}$ mice, neutrophils are more activated and contribute to inflammation. Interestingly, it has been shown for ANCA-associated vasculitides that increased concentrations of neutrophil antigens in plasma can lead to loss of tolerance, suggesting that increased availability of the antigen is sufficient to trigger autoimmune responses[292]. Based on my *in vitro* results, it could be hypothesized that loss of HVCN1 in neutrophils could cause autoimmunity through increased plasma levels of neutrophil antigens released by NETosis. Accordingly, aged HVCN1$^{-/-}$ mice also present with anti-DNA antibodies[190] which could be produced in the response to enhanced NETotic DNA release.

In conclusion, the exact mechanism of how loss of HVCN1 can enhance autoimmunity needs to be further studied. However, my data suggest that loss of HVCN1 in neutrophil in particular may be one of the major factors in this context. The use of a neutrophil or myeloid-specific knockout line would help to further unravel the development of autoimmunity in absence of HVCN1. Furthermore, it would be interesting to challenge aged HVCN1$^{-/-}$ mice, in order to investigate if infection would aggravate autoimmune associated symptoms as this is a common observation in human autoimmune diseases patients.

5.8 Relevance for human disease

I could show that loss of HVCN1 in murine neutrophils leads to increased degranulation and enhanced NET formation. Until now, there are no reports of mutations in HVCN1 that are related to human disease. However, there is evidence that HVCN1 is downregulated on RNA level in neutrophils of patients with SLE (personal communication Ken Smith and Paul Lyons). SLE is a multifactorial disease which is caused by interactions of various genetic and environmental factors[293]. Neutrophils play a central role in SLE, since the release of NETs directly increases the presence of autoantigens and is therefore associated with increased disease severity[294]. Given that different factors (i.e., single-nucleotide polymorphisms, epigenetics, or differences in proteostasis) might result in variable expression of HVCN1, we hypothesize that HVCN1 downregulation in humans might be a contributing factor in autoimmunity, most likely because of its role in regulating NET formation. To test this hypothesis, we are currently investigating

neutrophils of SLE patients and healthy controls for HVCN1 expression, and are also conducting functional assays with neutrophils, in order to test if an inverse correlation between HVCN1 expression and calcium-dependent NETosis exists, similarly to HVCN1$^{-/-}$ murine neutrophils.
In addition, decrease in HVCN1 protein levels can also be a result by proteolytic cleavage. Hawkins *et al.*[295] demonstrated that HVCN1 can be degraded by NE. They showed that in patients with alpha-1 antitrypsin deficiency (AATD), a serine protease inhibitor, neutrophils have lower surface HVCN1 levels, likely due to decreased inhibition of NE. Interestingly, AATD patients suffer from neutrophil-induced emphysematous lung disease. These results also suggest that lower HVCN1 levels in neutrophils are associated with increased inflammation. Along the same lines, we plan to have follow-up testing of SLE patients to evaluate if HVCN1 expression could decrease further in the course of the disease and serve as a marker for disease progression.

Our findings also have implications for the use of HVCN1 as a drug target. As described previously, HVCN1 represents a promising target for the treatment of cancer because HVCN1 expression in tumors correlates positively with tumor size, tumor classification, or clinical stage[296]. In addition, studies in microglia suggest that inhibition of HVCN1 may lead to beneficial outcomes in ischemic stroke or neurodegenerative diseases[153]. However, my data suggest that systemic treatment with HVCN1 inhibitors might have side effects as a result of inhibition of HVCN1 in neutrophils, causing increased NETosis that could cause general neutrophil-driven inflammation, as well as potentially be counterproductive in cancer and also neurodegeneration. Therefore, it is important that any potential effect of HVCN1 inhibition is thoroughly investigated.
Neutrophils were identified as important players in the immune response to tumors. In late-stage cancer, neutrophils acquire pro-tumorigenic features[71]. In this context, NET formation was shown to aid the development of metastasis[297]. Furthermore, increased NET formation was shown to stimulate cancer-associated thrombosis, which is associated with a poorer prognosis in cancer patients[298]. Therefore, increased NET formation in neutrophils in the presence of an HVCN1 inhibitor could promote tumor growth, and hence needs to be carefully evaluated.
Recently, NET formation was also detected in cortical vessels and brain parenchyma of patients with Alzheimer's disease (AD), and NETs were proposed to harm the blood-brain barrier and neurons[299]. Accordingly, neutrophil depletion rescued AD pathology and improved cognitive function in a mouse model of AD[300]. Furthermore, MPO release by neutrophils was shown to contribute to endothelial damage in the brain in the context of AD[301]. Thus, inhibition of HVCN1 in neutrophils in neurodegenerative diseases could also interfere with therapeutic effects.
Nevertheless, the advantages and disadvantages of systemic HVCN1 inhibition must be evaluated individually in each disease context, as different cell types have different degrees of impact on pathology. For example, results from our laboratory indicate that global HVCN1 deficiency has a positive effect on cognitive performance of mice in the APP/PS1 mouse model of Alzheimer's

disease. This, in turn, suggests that the positive effect of inhibiting HVCN1 in microglia outweighs the negative effects of inhibiting HVCN1 in neutrophils.

5.9 Limitations of the study

My results also have potential limitations which are primarily based on the particular properties of neutrophils.

First of all, caution should be taken when comparing mouse and human neutrophils. There are striking differences between the neutrophils of these two species. First of all, the abundance of neutrophils differs greatly; while the frequency of neutrophils in the blood is as high as 70 % in humans, the frequency in mice is much lower at ~20-30 %[18]. Furthermore, compared to murine neutrophils, human neutrophils express higher levels of granule proteins[302] and were shown to be more effective in NET formation[303]. Given that neutrophils are easy to isolate from human blood, they are the preferred material for experiments, and most of the available data are generated with human neutrophils. However, keeping these differences in mind, murine neutrophils are a good model to study the basis of activation, which can be later confirmed with human neutrophils

Secondly, neutrophils are very shorted lived cells and only survive *ex vivo* for a few hours[304]. Furthermore, they are very fragile cells that rapidly undergo cell death under stress conditions. Consequently, genetic manipulations of neutrophils are very challenging, if not impossible. Thus, we were limited to the use of inhibitors which might not cause complete deactivation of their targets or might have unknown off-target effects.

Finally, all *in vivo* experiments were performed in global HVCN1$^{-/-}$ mice. As all major immune cells express HVCN1, we cannot rule out the possibility that the phenotype we observed is not exclusively due to loss of HVCN1 in neutrophils. To overcome this limitation, we attempted to generate a neutrophil-specific HVCN1$^{-/-}$ mouse line, by crossing HVCN1 floxed mice with neutrophil-specific Cre mice. Unfortunately, we have not yet succeeded in obtaining a line with sufficient HVCN1 deletion (see appendix Fig. A2 - 4).

In mature neutrophils from HVCN1-floxed x Ly6G-Cre[203] or HVCN1-floxed x LysM-Cre[205] mice, I was still able to detect high levels of HVCN1. HVCN1 is already expressed in GMPs (data not shown) and is a stable membrane protein. Therefore, expression of the Cre recombinase under the Ly6G or LysM promoter might occur too late in neutrophil development to prevent HVCN1 expression.

The Mrp8-Cre[204] is known to be expressed in neutrophil progenitor cells and was therefore more promising for HVCN1 deletion. However, breeding did not generate any Cre-positive homozygous floxed mice, suggesting genetic linkage of HVCN1 with the Mrp8-Cre transgene. Recently, the Mrp8-Cre transgene was shown to be integrated into chromosome 5, the same chromosome as the mouse HVCN1 gene[305].

References

1. Murphy, K. & Weaver, C. *Janeway's Immunobiology, Ninth Edition*. (2016).
2. Turner, J. R. Intestinal mucosal barrier function in health and disease. *Nat. Rev. Immunol.* **9**, 799–809 (2009).
3. Eyerich, S., Eyerich, K., Traidl-Hoffmann, C. & Biedermann, T. Cutaneous Barriers and Skin Immunity: Differentiating A Connected Network. *Trends Immunol.* **39**, 315–327 (2018).
4. Brune, K., Frank, J., Schwingshackl, A., Finigan, J. & Sidhaye, V. K. Pulmonary epithelial barrier function: some new players and mechanisms. *Am. J. Physiol. Cell. Mol. Physiol.* **308**, L731–L745 (2015).
5. Dekaboruah, E., Suryavanshi, M. V., Chettri, D. & Verma, A. K. Human microbiome: an academic update on human body site specific surveillance and its possible role. *Arch. Microbiol.* **202**, 2147–2167 (2020).
6. Kienle, K. & Lämmermann, T. Neutrophil swarming: an essential process of the neutrophil tissue response. *Immunol. Rev.* **273**, 76–93 (2016).
7. Li, D. & Wu, M. Pattern recognition receptors in health and diseases. *Signal Transduct. Target. Ther.* **6**, 291 (2021).
8. Carrillo, J. L. M., Rodríguez, F. P. C., Coronado, O. G., García, M. A. M. & Cordero, J. F. C. Physiology and Pathology of Innate Immune Response Against Pathogens. in *Physiology and Pathology of Immunology* (InTech, 2017). doi:10.5772/intechopen.70556.
9. Dunkelberger, J. R. & Song, W.-C. Complement and its role in innate and adaptive immune responses. *Cell Res.* **20**, 34–50 (2010).
10. Dranoff, G. Cytokines in cancer pathogenesis and cancer therapy. *Nat. Rev. Cancer* **4**, 11–22 (2004).
11. Chi, X., Li, Y. & Qiu, X. V(D)J recombination, somatic hypermutation and class switch recombination of immunoglobulins: mechanism and regulation. *Immunology* **160**, 233–247 (2020).
12. Krangel, M. S. Mechanics of T cell receptor gene rearrangement. *Curr. Opin. Immunol.* **21**, 133–139 (2009).
13. Oleinika, K., Mauri, C. & Blair, P. A. B Cell Activation and B Cell Tolerance. in *The Autoimmune Diseases* 171–187 (Elsevier, 2020). doi:10.1016/B978-0-12-812102-3.00009-9.
14. Shah, K., Al-Haidari, A., Sun, J. & Kazi, J. U. T cell receptor (TCR) signaling in health and disease. *Signal Transduct. Target. Ther.* **6**, 412 (2021).
15. Appay, V., van Lier, R. A. W., Sallusto, F. & Roederer, M. Phenotype and function of human T lymphocyte subsets: Consensus and issues. *Cytom. Part A* **73A**, 975–983 (2008).
16. Ratajczak, W., Niedźwiedzka-Rystwej, P., Tokarz-Deptuła, B. & Deptuła, W. Immunological memory cells. *Cent. Eur. J. Immunol.* **43**, 194–203 (2018).
17. Lanier, L. L. Shades of grey — the blurring view of innate and adaptive immunity. *Nat. Rev. Immunol.* **13**, 73–74 (2013).
18. Mestas, J. & Hughes, C. C. W. Of Mice and Not Men: Differences between Mouse and Human Immunology. *J. Immunol.* **172**, 2731–2738 (2004).
19. Lawrence, S. M., Corriden, R. & Nizet, V. The Ontogeny of a Neutrophil: Mechanisms of Granulopoiesis and Homeostasis. *Microbiol. Mol. Biol. Rev.* **82**, (2018).
20. Summers, C. *et al.* Neutrophil kinetics in health and disease. *Trends Immunol.* **31**, 318–324 (2010).
21. Wéra, O., Lancellotti, P. & Oury, C. The Dual Role of Neutrophils in Inflammatory Bowel Diseases. *J. Clin. Med.* **5**, 118 (2016).
22. Wright, H. L., Moots, R. J. & Edwards, S. W. The multifactorial role of neutrophils in rheumatoid arthritis. *Nat. Rev. Rheumatol.* **10**, 593–601 (2014).
23. Yang, S.-C., Tsai, Y.-F., Pan, Y.-L. & Hwang, T.-L. Understanding the role of neutrophils in acute respiratory distress syndrome. *Biomed. J.* **44**, 439–446 (2021).
24. Ng, L. G., Ostuni, R. & Hidalgo, A. Heterogeneity of neutrophils. *Nat. Rev. Immunol.* **19**, 255–265 (2019).
25. Dancey, J. T., Deubelbeiss, K. A., Harker, L. A. & Finch, C. A. Neutrophil kinetics in man. *J. Clin.*

Invest. **58**, 705–715 (1976).
26. Velten, L. *et al.* Human haematopoietic stem cell lineage commitment is a continuous process. *Nat. Cell Biol.* **19**, 271–281 (2017).
27. Evrard, M. *et al.* Developmental Analysis of Bone Marrow Neutrophils Reveals Populations Specialized in Expansion, Trafficking, and Effector Functions. *Immunity* **48**, 364-379.e8 (2018).
28. Lieschke, G. J. *et al.* Mice lacking granulocyte colony-stimulating factor have chronic neutropenia, granulocyte and macrophage progenitor cell deficiency, and impaired neutrophil mobilization. *Blood* **84**, 1737–46 (1994).
29. Zeidler, C., Germeshausen, M., Klein, C. & Welte, K. Clinical implications of ELA2 -, HAX1 -, and G-CSF-receptor (CSF3R) mutations in severe congenital neutropenia. *Br. J. Haematol.* **144**, 459–467 (2009).
30. Ishigame, Y. I. H. The IL-23/IL-17 axis in inflammation. *J. Clin. Invest.* **116**, 1218–1222 (2006).
31. Pojda, Z. & Tsuboi, A. In vivo effects of human recombinant interleukin 6 on hemopoietic stem and progenitor cells and circulating blood cells in normal mice. *Exp. Hematol.* **18**, 1034–7 (1990).
32. Metcalf, D. *et al.* Hemopoietic responses in mice injected with purified recombinant murine GM-CSF. *Exp. Hematol.* **15**, 1–9 (1987).
33. Metcalf, D. *et al.* Effects of purified bacterially synthesized murine multi-CSF (IL-3) on hematopoiesis in normal adult mice. *Blood* **68**, 46–57 (1986).
34. Scott, E. W., Simon, M. C., Anastasi, J. & Singh, H. Requirement of Transcription Factor PU.1 in the Development of Multiple Hematopoietic Lineages. *Science (80-.).* **265**, 1573–1577 (1994).
35. Zhang, P. *et al.* Enhancement of Hematopoietic Stem Cell Repopulating Capacity and Self-Renewal in the Absence of the Transcription Factor C/EBPα. *Immunity* **21**, 853–863 (2004).
36. Yeamans, C. *et al.* C/EBPα binds and activates the PU.1 distal enhancer to induce monocyte lineage commitment. *Blood* **110**, 3136–3142 (2007).
37. Cowland, J. B. & Borregaard, N. Granulopoiesis and granules of human neutrophils. *Immunol. Rev.* **273**, 11–28 (2016).
38. Hirai, H. *et al.* C/EBPβ is required for 'emergency' granulopoiesis. *Nat. Immunol.* **7**, 732–739 (2006).
39. Eash, K. J., Greenbaum, A. M., Gopalan, P. K. & Link, D. C. CXCR2 and CXCR4 antagonistically regulate neutrophil trafficking from murine bone marrow. *J. Clin. Invest.* **120**, 2423–2431 (2010).
40. Semerad, C. L. *et al.* G-CSF potently inhibits osteoblast activity and CXCL12 mRNA expression in the bone marrow. *Blood* **106**, 3020–3027 (2005).
41. Méndez-Ferrer, S., Lucas, D., Battista, M. & Frenette, P. S. Haematopoietic stem cell release is regulated by circadian oscillations. *Nature* **452**, 442–447 (2008).
42. García-García, A. *et al.* Dual cholinergic signals regulate daily migration of hematopoietic stem cells and leukocytes. *Blood* **133**, 224–236 (2019).
43. Furze, R. C. & Rankin, S. M. Neutrophil mobilization and clearance in the bone marrow. *Immunology* **125**, 281–288 (2008).
44. Gee, M. H. & Albertine, K. H. Neutrophil-Endothelial Cell Interactions in the Lung. *Annu. Rev. Physiol.* **55**, 227–248 (1993).
45. Peters, A. M., Saverymuttu, S. H., Keshavarzian, A., Bell, R. N. & Lavender, J. P. Splenic pooling of granulocytes. *Clin. Sci.* **68**, 283–289 (1985).
46. Ussov, W. Y., Aktolun, C., Myers, M. J., Jamar, F. & Peters, A. M. Granulocyte margination in bone marrow: comparison with margination in the spleen and liver. *Scand. J. Clin. Lab. Invest.* **55**, 87–96 (1995).
47. De Filippo, K. & Rankin, S. M. The Secretive Life of Neutrophils Revealed by Intravital Microscopy. *Front. Cell Dev. Biol.* **8**, 1–15 (2020).
48. Amulic, B., Cazalet, C., Hayes, G. L., Metzler, K. D. & Zychlinsky, A. Neutrophil Function: From Mechanisms to Disease. *Annu. Rev. Immunol.* **30**, 459–489 (2012).

49. Sperandio, M. *et al.* P-selectin Glycoprotein Ligand-1 Mediates L-Selectin–dependent Leukocyte Rolling in Venules. *J. Exp. Med.* **197**, 1355–1363 (2003).
50. Constantin, G. *et al.* Chemokines trigger immediate beta2 integrin affinity and mobility changes: differential regulation and roles in lymphocyte arrest under flow. *Immunity* **13**, 759–69 (2000).
51. Jung, U., Norman, K. E., Scharffetter-Kochanek, K., Beaudet, A. L. & Ley, K. Transit time of leukocytes rolling through venules controls cytokine-induced inflammatory cell recruitment in vivo. *J. Clin. Invest.* **102**, 1526–1533 (1998).
52. Phillipson, M. *et al.* Intraluminal crawling of neutrophils to emigration sites: a molecularly distinct process from adhesion in the recruitment cascade. *J. Exp. Med.* **203**, 2569–2575 (2006).
53. Ley, K., Laudanna, C., Cybulsky, M. I. & Nourshargh, S. Getting to the site of inflammation: the leukocyte adhesion cascade updated. *Nat. Rev. Immunol.* **7**, 678–689 (2007).
54. Martin, C. *et al.* Chemokines Acting via CXCR2 and CXCR4 Control the Release of Neutrophils from the Bone Marrow and Their Return following Senescence. *Immunity* **19**, 583–593 (2003).
55. Casanova-Acebes, M. *et al.* Rhythmic Modulation of the Hematopoietic Niche through Neutrophil Clearance. *Cell* **153**, 1025–1035 (2013).
56. Adrover, J. M. *et al.* A Neutrophil Timer Coordinates Immune Defense and Vascular Protection. *Immunity* **50**, 390-402.e10 (2019).
57. Adrover, J. M. *et al.* Programmed 'disarming' of the neutrophil proteome reduces the magnitude of inflammation. *Nat. Immunol.* **21**, 135–144 (2020).
58. Uhl, B. *et al.* Aged neutrophils contribute to the first line of defense in the acute inflammatory response. *Blood* **128**, 2327–2337 (2016).
59. Furze, R. C. & Rankin, S. M. The role of the bone marrow in neutrophil clearance under homeostatic conditions in the mouse. *FASEB J.* **22**, 3111–3119 (2008).
60. Leliefeld, P. H. C. *et al.* Differential antibacterial control by neutrophil subsets. *Blood Adv.* **2**, 1344–1355 (2018).
61. Deniset, J. F., Surewaard, B. G., Lee, W.-Y. & Kubes, P. Splenic Ly6Ghigh mature and Ly6Gint immature neutrophils contribute to eradication of S. pneumoniae. *J. Exp. Med.* **214**, 1333–1350 (2017).
62. Rice, C. M. *et al.* Neutrophils in severe COVID-19 are characterized by a hyperactive immature state and maintained CXCR2 expression. *medRxiv* 2022.03.23.22272828 (2022).
63. Tay, S. H., Celhar, T. & Fairhurst, A. Low-Density Neutrophils in Systemic Lupus Erythematosus. *Arthritis Rheumatol.* **72**, 1587–1595 (2020).
64. Drifte, G., Dunn-Siegrist, I., Tissières, P. & Pugin, J. Innate Immune Functions of Immature Neutrophils in Patients With Sepsis and Severe Systemic Inflammatory Response Syndrome*. *Crit. Care Med.* **41**, 820–832 (2013).
65. Meghraoui-Kheddar, A. *et al.* Two New Neutrophil Subsets Define a Discriminating Sepsis Signature. *Am. J. Respir. Crit. Care Med.* **205**, 46–59 (2022).
66. Fridlender, Z. G. *et al.* Polarization of Tumor-Associated Neutrophil Phenotype by TGF-β: "N1" versus "N2" TAN. *Cancer Cell* **16**, 183–194 (2009).
67. Katano, M. & Torisu, M. Neutrophil-Mediated Tumor Cell Destruction in Cancer Ascites. *Cancer* **50**, 62–68 (1982).
68. Fridlender, Z. G. & Albelda, S. M. Tumor-associated neutrophils: friend or foe? *Carcinogenesis* **33**, 949–955 (2012).
69. Tazzyman, S., Lewis, C. E. & Murdoch, C. Neutrophils: key mediators of tumour angiogenesis. *Int. J. Exp. Pathol.* **90**, 222–231 (2009).
70. Wu, Q. Di, Wang, J. H., Condron, C., Bouchier-Hayes, D. & Redmond, H. P. Human neutrophils facilitate tumor cell transendothelial migration. *Am. J. Physiol. Physiol.* **280**, C814–C822 (2001).
71. Mishalian, I. *et al.* Tumor-associated neutrophils (TAN) develop pro-tumorigenic properties during tumor progression. *Cancer Immunol. Immunother.* **62**, 1745–1756 (2013).
72. Becher, B. *et al.* High-dimensional analysis of the murine myeloid cell system. *Nat. Immunol.*

15, 1181–1189 (2014).
73. Ballesteros, I. *et al.* Co-option of Neutrophil Fates by Tissue Environments. *Cell* **183**, 1282-1297.e18 (2020).
74. Puga, I. *et al.* B cell–helper neutrophils stimulate the diversification and production of immunoglobulin in the marginal zone of the spleen. *Nat. Immunol.* **13**, 170–180 (2012).
75. Futosi, K., Fodor, S. & Mócsai, A. Neutrophil cell surface receptors and their intracellular signal transduction pathways. *Int. Immunopharmacol.* **17**, 638–650 (2013).
76. Van Acker, H. & Coenye, T. The Role of Reactive Oxygen Species in Antibiotic-Mediated Killing of Bacteria. *Trends Microbiol.* **25**, 456–466 (2017).
77. Paiva, C. N. & Bozza, M. T. Are Reactive Oxygen Species Always Detrimental to Pathogens? *Antioxid. Redox Signal.* **20**, 1000–1037 (2014).
78. Potera, R. M. *et al.* Neutrophil azurophilic granule exocytosis is primed by TNF-α and partially regulated by NADPH oxidase. *Innate Immun.* **22**, 635–646 (2016).
79. Fuchs, T. A. *et al.* Novel cell death program leads to neutrophil extracellular traps. *J. Cell Biol.* **176**, 231–241 (2007).
80. Naik, E. & Dixit, V. M. Mitochondrial reactive oxygen species drive proinflammatory cytokine production. *J. Exp. Med.* **208**, 417–420 (2011).
81. Baehner, R. L. & Nathan, D. G. Leukocyte Oxidase: Defective Activity in Chronic Granulomatous Disease. *Science (80-.).* **155**, 835–836 (1967).
82. Segal, A., Jones, O. ., Webster, D. & Allison, A. Absence of a newly described cytochrome b from neutrophils of patients with chronic granulomatous disease. *Lancet* **312**, 446–449 (1978).
83. Panday, A., Sahoo, M. K., Osorio, D. & Batra, S. NADPH oxidases: an overview from structure to innate immunity-associated pathologies. *Cell. Mol. Immunol.* **12**, 5–23 (2015).
84. El-Benna, J., Dang, P. M.-C. & Gougerot-Pocidalo, M.-A. Priming of the neutrophil NADPH oxidase activation: role of p47phox phosphorylation and NOX2 mobilization to the plasma membrane. *Semin. Immunopathol.* **30**, 279–289 (2008).
85. Fumagalli, L., Zhang, H., Baruzzi, A., Lowell, C. A. & Berton, G. The Src Family Kinases Hck and Fgr Regulate Neutrophil Responses to N -Formyl-Methionyl-Leucyl-Phenylalanine. *J. Immunol.* **178**, 3874–3885 (2007).
86. García-García, E. & Rosales, C. Signal transduction during Fc receptor-mediated phagocytosis. *J. Leukoc. Biol.* **72**, 1092–108 (2002).
87. Williams, M. A. & Solomkin, J. S. Integrin-mediated signaling in human neutrophil functioning. *J. Leukoc. Biol.* **65**, 725–736 (1999).
88. Rosen, H. & Klebanoff, S. J. Bactericidal activity of a superoxide anion-generating system. A model for the polymorphonuclear leukocyte. *J. Exp. Med.* **149**, 27–39 (1979).
89. Rørvig, S., Østergaard, O., Heegaard, N. H. H. & Borregaard, N. Proteome profiling of human neutrophil granule subsets, secretory vesicles, and cell membrane: correlation with transcriptome profiling of neutrophil precursors. *J. Leukoc. Biol.* **94**, 711–721 (2013).
90. Lominadze, G. *et al.* Proteomic Analysis of Human Neutrophil Granules. *Mol. Cell. Proteomics* **4**, 1503–1521 (2005).
91. Munafó, D. B. *et al.* Rab27a is a key component of the secretory machinery of azurophilic granules in granulocytes. *Biochem. J.* **402**, 229–239 (2007).
92. Uriarte, S. M. *et al.* Comparison of Proteins Expressed on Secretory Vesicle Membranes and Plasma Membranes of Human Neutrophils. *J. Immunol.* **180**, 5575–5581 (2008).
93. Lacy, P. Mechanisms of Degranulation in Neutrophils. *Allergy, Asthma Clin. Immunol.* **2**, 98 (2006).
94. Mollinedo, F. *et al.* Combinatorial SNARE Complexes Modulate the Secretion of Cytoplasmic Granules in Human Neutrophils. *J. Immunol.* **177**, 2831–2841 (2006).
95. Pham, C. T. N. Neutrophil serine proteases fine-tune the inflammatory response. *Int. J. Biochem. Cell Biol.* **40**, 1317–1333 (2008).
96. Kantari, C. *et al.* Proteinase 3, the Wegener autoantigen, is externalized during neutrophil apoptosis: evidence for a functional association with phospholipid scramblase 1 and interference with macrophage phagocytosis. *Blood* **110**, 4086–4095 (2007).
97. Lutaty, A. *et al.* A 17-kDa Fragment of Lactoferrin Associates With the Termination of

Inflammation and Peptides Within Promote Resolution. *Front. Immunol.* **9**, (2018).
98. Mansfield, P. J., Hinkovska-Galcheva, V., Borofsky, M. S., Shayman, J. A. & Boxer, L. A. Phagocytic signaling molecules in lipid rafts of COS-1 cells transfected with FcγRIIA. *Biochem. Biophys. Res. Commun.* **331**, 132–138 (2005).
99. Cooney, D. S., Phee, H., Jacob, A. & Coggeshall, K. M. Signal Transduction by Human-Restricted FcγRIIa Involves Three Distinct Cytoplasmic Kinase Families Leading to Phagocytosis. *J. Immunol.* **167**, 844–854 (2001).
100. Lee, W. L., Harrison, R. E. & Grinstein, S. Phagocytosis by neutrophils. **5**, 1299–1306 (2003).
101. Nordenfelt, P. & Tapper, H. Phagosome dynamics during phagocytosis by neutrophils. *J. Leukoc. Biol.* **90**, 271–284 (2011).
102. Fountain, A., Inpanathan, S., Alves, P., Verdawala, M. B. & Botelho, R. J. Phagosome maturation in macrophages: Eat, digest, adapt, and repeat. *Adv. Biol. Regul.* **82**, 100832 (2021).
103. Jankowski, A., Scott, C. C. & Grinstein, S. Determinants of the phagosomal pH in neutrophils. *J. Biol. Chem.* **277**, 6059–6066 (2002).
104. Levine, A. P., Duchen, M. R., De Villiers, S., Rich, P. R. & Segal, A. W. Alkalinity of neutrophil phagocytic vacuoles is modulated by HVCN1 and has consequences for myeloperoxidase activity. *PLoS One* **10**, 1–20 (2015).
105. Brinkmann, V. *et al.* Neutrophil Extracellular Traps Kill Bacteria. *Science (80-.).* **303**, 1532–1535 (2004).
106. Pilsczek, F. H. *et al.* A Novel Mechanism of Rapid Nuclear Neutrophil Extracellular Trap Formation in Response to Staphylococcus aureus. *J. Immunol.* **185**, 7413–7425 (2010).
107. Branzk, N. & Papayannopoulos, V. Molecular mechanisms regulating NETosis in infection and disease. *Semin. Immunopathol.* **35**, 513–530 (2013).
108. Kenny, E. F. *et al.* Diverse stimuli engage different neutrophil extracellular trap pathways. *Elife* **6**, 1–21 (2017).
109. Tsourouktsoglou, T. *et al.* Reactive Oxygen Species Localization Programs Inflammation to Clear Microbes of Different Size Article Reactive Oxygen Species Localization Programs Inflammation to Clear Microbes of Different Size. *Immunity* **46**, 421–432 (2017).
110. Branzk, N. *et al.* Neutrophils sense microbe size and selectively release neutrophil extracellular traps in response to large pathogens. *Nat. Immunol.* **15**, 1017–1025 (2014).
111. Guo, Y. *et al.* Spontaneous formation of neutrophil extracellular traps is associated with autophagy. *Sci. Rep.* **11**, 24005 (2021).
112. Kamoshida, G. *et al.* Spontaneous formation of neutrophil extracellular traps in serum-free culture conditions. *FEBS Open Bio* **7**, 877–886 (2017).
113. Khan, M. A. *et al.* Regulating NETosis: Increasing pH Promotes NADPH Oxidase-Dependent NETosis. *Front. Med.* **5**, (2018).
114. Denny, M. F. *et al.* A Distinct Subset of Proinflammatory Neutrophils Isolated from Patients with Systemic Lupus Erythematosus Induces Vascular Damage and Synthesizes Type I IFNs. *J. Immunol.* **184**, 3284–3297 (2010).
115. Neubert, E. *et al.* Chromatin swelling drives neutrophil extracellular trap release. *Nat. Commun.* **9**, 3767 (2018).
116. Thiam, H. R. *et al.* NETosis proceeds by cytoskeleton and endomembrane disassembly and PAD4-mediated chromatin decondensation and nuclear envelope rupture. *Proc. Natl. Acad. Sci. U. S. A.* **117**, 7326–7337 (2020).
117. Metzler, K. D., Goosmann, C., Lubojemska, A., Zychlinsky, A. & Papayannopoulos, V. A Myeloperoxidase-Containing Complex Regulates Neutrophil Elastase Release and Actin Dynamics during NETosis. *Cell Rep.* **8**, 883–896 (2014).
118. Manley, H. R., Keightley, M. C. & Lieschke, G. J. The Neutrophil Nucleus: An Important Influence on Neutrophil Migration and Function. *Front. Immunol.* **9**, (2018).
119. Gößwein, S. *et al.* Citrullination Licenses Calpain to Decondense Nuclei in Neutrophil Extracellular Trap Formation. *Front. Immunol.* **10**, (2019).
120. Li, Y. *et al.* Nuclear envelope rupture and NET formation is driven by PKCα-mediated lamin B disassembly. *EMBO Rep.* **21**, (2020).
121. Sollberger, G. *et al.* Gasdermin D plays a vital role in the generation of neutrophil

extracellular traps. *Sci. Immunol.* **3**, (2018).
122. Papayannopoulos, V., Metzler, K. D., Hakkim, A. & Zychlinsky, A. Neutrophil elastase and myeloperoxidase regulate the formation of neutrophil extracellular traps. *J. Cell Biol.* **191**, 677–691 (2010).
123. Azzouz, D., Khan, M. A. & Palaniyar, N. ROS induces NETosis by oxidizing DNA and initiating DNA repair. *Cell Death Discov.* **7**, 113 (2021).
124. Li, P. *et al.* PAD4 is essential for antibacterial innate immunity mediated by neutrophil extracellular traps. *J. Exp. Med.* **207**, 1853–1862 (2010).
125. Wang, Y. *et al.* Histone hypercitrullination mediates chromatin decondensation and neutrophil extracellular trap formation. *J. Cell Biol.* **184**, 205–213 (2009).
126. Rohrbach, A. S., Slade, D. J., Thompson, P. R. & Mowen, K. A. Activation of PAD4 in NET formation. *Front. Immunol.* **3**, 1–10 (2012).
127. de Lourdes Ochoa-González, F. *et al.* Calpain Participates in Cortical Cytoskeleton Modification and DNA Release during Neutrophil Extracellular Trap Formation. *Int. Arch. Allergy Immunol.* **182**, 877–887 (2021).
128. Douda, D. N., Khan, M. A., Grasemann, H. & Palaniyar, N. SK3 channel and mitochondrial ROS mediate NADPH oxidase-independent NETosis induced by calcium influx. *Proc. Natl. Acad. Sci.* **112**, 2817–2822 (2015).
129. Chen, K. *et al.* Endocytosis of soluble immune complexes leads to their clearance by FcγRIIIB but induces neutrophil extracellular traps via FcγRIIA in vivo. *Blood* **120**, 4421–4431 (2012).
130. van der Linden, M., Westerlaken, G. H. A., van der Vlist, M., van Montfrans, J. & Meyaard, L. Differential Signalling and Kinetics of Neutrophil Extracellular Trap Release Revealed by Quantitative Live Imaging. *Sci. Rep.* **7**, 6529 (2017).
131. Tsokos, G. C. Autoimmunity and organ damage in systemic lupus erythematosus. *Nat. Immunol.* **21**, 605–614 (2020).
132. Bruns, A., Bläss, S., Hausdorf, G., Burmester, G. R. & Hiepe, F. Nucleosomes are major T and B cell autoantigens in systemic lupus erythematosus. *Arthritis Rheum.* **43**, 2307–2315 (2000).
133. McHugh, N. J. Systemic lupus erythematosus and dysregulated apoptosis--what is the evidence? *Rheumatology* **41**, 242–245 (2002).
134. Liu, C. L. *et al.* Specific post-translational histone modifications of neutrophil extracellular traps as immunogens and potential targets of lupus autoantibodies. *Arthritis Res. Ther.* **14**, R25 (2012).
135. Lande, R. *et al.* Neutrophils Activate Plasmacytoid Dendritic Cells by Releasing Self-DNA–Peptide Complexes in Systemic Lupus Erythematosus. *Sci. Transl. Med.* **3**, (2011).
136. Apel, F., Zychlinsky, A. & Kenny, E. F. The role of neutrophil extracellular traps in rheumatic diseases. *Nat. Rev. Rheumatol.* **14**, 467–475 (2018).
137. Lood, C. *et al.* Neutrophil extracellular traps enriched in oxidized mitochondrial DNA are interferogenic and contribute to lupus-like disease. *Nat. Med.* **22**, 146–153 (2016).
138. Kegerreis, B. J. *et al.* Genomic Identification of Low-Density Granulocytes and Analysis of Their Role in the Pathogenesis of Systemic Lupus Erythematosus. *J. Immunol.* **202**, 3309–3317 (2019).
139. Rahman, S. *et al.* Low-density granulocytes activate T cells and demonstrate a non-suppressive role in systemic lupus erythematosus. *Ann. Rheum. Dis.* **78**, 957–966 (2019).
140. Brogan, P. & Eleftheriou, D. Vasculitis update: pathogenesis and biomarkers. *Pediatr. Nephrol.* **33**, 187–198 (2018).
141. Falk, R. J., Terrell, R. S., Charles, L. A. & Jennette, J. C. Anti-neutrophil cytoplasmic autoantibodies induce neutrophils to degranulate and produce oxygen radicals in vitro. *Proc. Natl. Acad. Sci.* **87**, 4115–4119 (1990).
142. Kessenbrock, K. *et al.* Netting neutrophils in autoimmune small-vessel vasculitis. *Nat. Med.* **15**, 623–625 (2009).
143. Grayson, P. C. *et al.* Neutrophil-Related Gene Expression and Low-Density Granulocytes Associated With Disease Activity and Response to Treatment in Antineutrophil Cytoplasmic Antibody-Associated Vasculitis. *Arthritis Rheumatol.* **67**, 1922–1932 (2015).

144. Söderberg, D. *et al.* Increased levels of neutrophil extracellular trap remnants in the circulation of patients with small vessel vasculitis, but an inverse correlation to anti-neutrophil cytoplasmic antibodies during remission. *Rheumatology* **54**, 2085–2094 (2015).
145. Schreiber, A. *et al.* Necroptosis controls NET generation and mediates complement activation, endothelial damage, and autoimmune vasculitis. *Proc. Natl. Acad. Sci.* **114**, (2017).
146. Thomas, R. C. & Meech, R. W. Hydrogen ion currents and intracellular pH in depolarized voltage-clamped snail neurones. *Nature* **299**, 826–8 (1982).
147. Sasaki, M., Takagi, M. & Okamura, Y. A Voltage Sensor-Domain Protein Is a Voltage-Gated Proton Channel. *Science (80-.).* **312**, 589–592 (2006).
148. Ramsey, I. S., Moran, M. M., Chong, J. A. & Clapham, D. E. A voltage-gated proton-selective channel lacking the pore domain. *Nature* **440**, 1213–1216 (2006).
149. Okochi, Y., Sasaki, M., Iwasaki, H. & Okamura, Y. Voltage-gated proton channel is expressed on phagosomes. *Biochem. Biophys. Res. Commun.* **382**, 274–279 (2009).
150. Capasso, M. Regulation of immune responses by proton channels. *Immunology* **143**, 131–137 (2014).
151. Fischer, H. Function of proton channels in lung epithelia. *Wiley Interdiscip. Rev. Membr. Transp. Signal.* **1**, 247–258 (2012).
152. Zhang, Q. *et al.* Inhibiting Hv1 channel in peripheral sensory neurons attenuates chronic inflammatory pain and opioid side effects. *Cell Res.* **32**, 461–476 (2022).
153. Seredenina, T., Demaurex, N. & Krause, K.-H. Voltage-Gated Proton Channels as Novel Drug Targets: From NADPH Oxidase Regulation to Sperm Biology. *Antioxid. Redox Signal.* **23**, 490–513 (2015).
154. Hondares, E. *et al.* Enhanced activation of an amino-terminally truncated isoform of the voltage-gated proton channel HVCN1 enriched in malignant B cells. *Proc. Natl. Acad. Sci. U. S. A.* **111**, 18078–18083 (2014).
155. DeCoursey, T. E. Voltage-gated proton channels: Molecular biology, physiology, and pathophysiology of the HV family. *Physiol. Rev.* **93**, 599–652 (2013).
156. Decoursey, T. E. The voltage-gated proton channel: A riddle, wrapped in a mystery, inside an enigma. *Biochemistry* **54**, 3250–3268 (2015).
157. Musset, B. *et al.* Identification of Thr29 as a Critical Phosphorylation Site That Activates the Human Proton Channel Hvcn1 in Leukocytes. *J. Biol. Chem.* **285**, 5117–5121 (2010).
158. Lee, S.-Y., Letts, J. A. & MacKinnon, R. Dimeric subunit stoichiometry of the human voltage-dependent proton channel Hv1. *Proc. Natl. Acad. Sci.* **105**, 7692–7695 (2008).
159. Musset, B. *et al.* Zinc inhibition of monomeric and dimeric proton channels suggests cooperative gating. *J. Physiol.* **588**, 1435–1449 (2010).
160. Kulleperuma, K. *et al.* Construction and validation of a homology model of the human voltage-gated proton channel hHV1. *J. Gen. Physiol.* **141**, 445–465 (2013).
161. Cherny, V. V, Markin, V. S. & DeCoursey, T. E. The voltage-activated hydrogen ion conductance in rat alveolar epithelial cells is determined by the pH gradient. *J. Gen. Physiol.* **105**, 861–896 (1995).
162. Smith, S. M. E. *et al.* Voltage-gated proton channel in a dinoflagellate. *Proc. Natl. Acad. Sci.* **108**, 18162–18167 (2011).
163. Hong, L., Pathak, M. M., Kim, I. H., Ta, D. & Tombola, F. Voltage-Sensing Domain of Voltage-Gated Proton Channel Hv1 Shares Mechanism of Block with Pore Domains. *Neuron* **77**, 274–287 (2013).
164. Hong, L., Kim, I. H. & Tombola, F. Molecular determinants of Hv1 proton channel inhibition by guanidine derivatives. *Proc. Natl. Acad. Sci. U. S. A.* **111**, 9971–9976 (2014).
165. Zhao, C. *et al.* HIFs: New arginine mimic inhibitors of the Hv1 channel with improved VSD–ligand interactions. *J. Gen. Physiol.* **153**, (2021).
166. Henderson, L. M., Chappell, J. B. & Jones, O. T. The superoxide-generating NADPH oxidase of human neutrophils is electrogenic and associated with an H+ channel. *Biochem. J.* **246**, 325–9 (1987).
167. DeCoursey, T. E. & Cherny, V. V. Potential, pH, and arachidonate gate hydrogen ion currents

in human neutrophils. *Biophys. J.* **65**, 1590–1598 (1993).
168. Demaurex, N. *et al.* Proton currents in human granulocytes: regulation by membrane potential and intracellular pH. *J. Physiol.* **466**, 329–44 (1993).
169. DeCoursey, T. E., Morgan, D. & Cherny, V. V. The voltage dependence of NADPH oxidase reveals why phagocytes need proton channels. *Nature* **422**, 531–4 (2003).
170. Morgan, D., Cherny, V. V, Murphy, R., Katz, B. Z. & DeCoursey, T. E. The pH dependence of NADPH oxidase in human eosinophils. *J. Physiol.* **569**, 419–31 (2005).
171. Ramsey, I. S., Ruchti, E., Kaczmarek, J. S. & Clapham, D. E. Hv1 proton channels are required for high-level NADPH oxidase-dependent superoxide production during the phagocyte respiratory burst. *Proc. Natl. Acad. Sci. U. S. A.* **106**, 7642–7647 (2009).
172. Morgan, D. *et al.* Voltage-gated proton channels maintain pH in human neutrophils during phagocytosis. *Proc. Natl. Acad. Sci. U. S. A.* **106**, 18022–18027 (2009).
173. El Chemaly, A. *et al.* VSOP/Hv1 proton channels sustain calcium entry, neutrophil migration, and superoxide production by limiting cell depolarization and acidification. *J. Exp. Med.* **207**, 129–139 (2010).
174. Okochi, Y. *et al.* The voltage-gated proton channel Hv1/VSOP inhibits neutrophil granule release. *J. Leukoc. Biol.* **99**, 7–19 (2016).
175. Okochi, Y., Umemoto, E. & Okamura, Y. Hv1/VSOP regulates neutrophil directional migration and ERK activity by tuning ROS production. *J. Leukoc. Biol.* **107**, 819–831 (2020).
176. El Chemaly, A., Nunes, P., Jimaja, W., Castelbou, C. & Demaurex, N. Hv1 proton channels differentially regulate the pH of neutrophil and macrophage phagosomes by sustaining the production of phagosomal ROS that inhibit the delivery of vacuolar ATPases. *J. Leukoc. Biol.* **95**, 827–839 (2014).
177. Yagisawa, M. *et al.* Superoxide Release and NADPH Oxidase Components in Mature Human Phagocytes: Correlation between Functional Capacity and Amount of Functional Proteins. *Biochem. Biophys. Res. Commun.* **228**, 510–516 (1996).
178. Lacy, P. *et al.* Divergence of Mechanisms Regulating Respiratory Burst in Blood and Sputum Eosinophils and Neutrophils from Atopic Subjects. *J. Immunol.* **170**, 2670–2679 (2003).
179. Zhu, X., Mose, E. & Zimmermann, N. Proton channel HVCN1 is required for effector functions of mouse eosinophils. *BMC Immunol.* **14**, 1 (2013).
180. Musset, B. *et al.* A pH-stabilizing role of voltage-gated proton channels in IgE-mediated activation of human basophils. *Proc. Natl. Acad. Sci. U. S. A.* **105**, 11020–11025 (2008).
181. Simpson, D. S. A. & Oliver, P. L. ROS Generation in Microglia: Understanding Oxidative Stress and Inflammation in Neurodegenerative Disease. *Antioxidants (Basel, Switzerland)* **9**, (2020).
182. Wu, L. J. *et al.* The voltage-gated proton channel Hv1 enhances brain damage from ischemic stroke. *Nat. Neurosci.* **15**, 565–573 (2012).
183. Kawai, T. *et al.* Unconventional role of voltage-gated proton channels (VSOP/Hv1) in regulation of microglial ROS production. *J. Neurochem.* **142**, 686–699 (2017).
184. Kawai, T. *et al.* Heterogeneity of microglial proton channel in different brain regions and its relationship with aging. *J. Neurochem.* **157**, 624–641 (2021).
185. Wang, F. *et al.* Neutralization of Hv1/HVCN1 With Antibody Enhances Microglia/Macrophages Myelin Clearance by Promoting Their Migration in the Brain. *Front. Cell. Neurosci.* **15**, 5–10 (2021).
186. Peng, J. *et al.* The voltage-gated proton channel Hv1 promotes microglia-astrocyte communication and neuropathic pain after peripheral nerve injury. *Mol. Brain* **14**, 99 (2021).
187. Capasso, M. *et al.* HVCN1 modulates BCR signal strength via regulation of BCR-dependent generation of reactive oxygen species. *Nat. Immunol.* **11**, 265–272 (2010).
188. Jones, O. T. G., Jones, S. A. & Wood, J. D. Expression of components of the superoxide generating NADPH oxidase by human leucocytes and other cells. *Protoplasma* **184**, 79–85 (1995).
189. Wienands, J., Larbolette, O. & Reth, M. Evidence for a preformed transducer complex organized by the B cell antigen receptor. *Proc. Natl. Acad. Sci.* **93**, 7865–7870 (1996).
190. Sasaki, M. *et al.* Autoimmune disorder phenotypes in Hvcn1-deficient mice. *Biochem. J.* **450**,

295–301 (2013).
191. Coe, D. *et al.* Loss of voltage-gated hydrogen channel 1 expression reveals heterogeneous metabolic adaptation to intracellular acidification by T cells. *JCI Insight* **7**, (2022).
192. Jackson, S. H., Devadas, S., Kwon, J., Pinto, L. A. & Williams, M. S. T cells express a phagocyte-type NADPH oxidase that is activated after T cell receptor stimulation. *Nat. Immunol.* **5**, 818–827 (2004).
193. Iovannisci, D., Illek, B. & Fischer, H. Function of the HVCN1 proton channel in airway epithelia and a naturally occurring mutation, M91T. *J. Gen. Physiol.* **136**, 35–46 (2010).
194. Wang, Y. *et al.* Specific expression of the human voltage-gated proton channel Hv1 in highly metastatic breast cancer cells, promotes tumor progression and metastasis. *Biochem. Biophys. Res. Commun.* **412**, 353–359 (2011).
195. Wang, Y., Wu, X., Li, Q., Zhang, S. & Li, S. J. Human Voltage-Gated Proton Channel Hv1: A New Potential Biomarker for Diagnosis and Prognosis of Colorectal Cancer. *PLoS One* **8**, e70550 (2013).
196. Wang, Y., Zhang, S. & Li, S. J. Zn2+ induces apoptosis in human highly metastatic SHG-44 glioma cells, through inhibiting activity of the voltage-gated proton channel Hv1. *Biochem. Biophys. Res. Commun.* **438**, 312–317 (2013).
197. Swietach, P., Vaughan-Jones, R. D., Harris, A. L. & Hulikova, A. The chemistry, physiology and pathology of pH in cancer. *Philos. Trans. R. Soc. B Biol. Sci.* **369**, 20130099 (2014).
198. Wang, Y., Li, S. J., Wu, X., Che, Y. & Li, Q. Clinicopathological and Biological Significance of Human Voltage-gated Proton Channel Hv1 Protein Overexpression in Breast Cancer. *J. Biol. Chem.* **287**, 13877–13888 (2012).
199. Ventura, C. *et al.* Differential expression of the long and truncated Hv1 isoforms in breast-cancer cells. *J. Cell. Physiol.* **235**, 8757–8767 (2020).
200. Haglund, S., Almer, S., Peterson, C. & Söderman, J. Gene Expression and Thiopurine Metabolite Profiling in Inflammatory Bowel Disease – Novel Clues to Drug Targets and Disease Mechanisms? *PLoS One* **8**, e56989 (2013).
201. Pollock, J. D. *et al.* Mouse model of X–linked chronic granulomatous disease, an inherited defect in phagocyte superoxide production. *Nat. Genet.* **9**, 202–209 (1995).
202. Skarnes, W. C. *et al.* A conditional knockout resource for the genome-wide study of mouse gene function. *Nature* **474**, 337–342 (2011).
203. Hasenberg, A. *et al.* Catchup: a mouse model for imaging-based tracking and modulation of neutrophil granulocytes. *Nat. Methods* **12**, 445–452 (2015).
204. Passegué, E., Wagner, E. F. & Weissman, I. L. JunB Deficiency Leads to a Myeloproliferative Disorder Arising from Hematopoietic Stem Cells. *Cell* **119**, 431–443 (2004).
205. Clausen, B. E., Burkhardt, C., Reith, W., Renkawitz, R. & Förster, I. Conditional gene targeting in macrophages and granulocytes using LysMcre mice. *Transgenic Res.* **8**, 265–77 (1999).
206. Sollberger, G., Tilley, D. O. & Zychlinsky, A. Neutrophil Extracellular Traps: The Biology of Chromatin Externalization. *Dev. Cell* **44**, 542–553 (2018).
207. Brennan-Minnella, A. M., Won, S. J. & Swanson, R. A. NADPH Oxidase-2: Linking Glucose, Acidosis, and Excitotoxicity in Stroke. *Antioxid. Redox Signal.* **22**, 161–174 (2015).
208. Patel, S. Two-pore channels open up. *Nature* **556**, 38–40 (2018).
209. Mukhopadhyay, P. *et al.* Simultaneous detection of apoptosis and mitochondrial superoxide production in live cells by flow cytometry and confocal microscopy. *Nat. Protoc.* **2**, 2295–2301 (2007).
210. Sundqvist, M. *et al.* Elevated Mitochondrial Reactive Oxygen Species and Cellular Redox Imbalance in Human NADPH-Oxidase-Deficient Phagocytes. *Front. Immunol.* **8**, (2017).
211. Santulli, G., Xie, W., Reiken, S. R. & Marks, A. R. Mitochondrial calcium overload is a key determinant in heart failure. *Proc. Natl. Acad. Sci.* **112**, 11389–11394 (2015).
212. Giorgi, C., Marchi, S. & Pinton, P. The machineries, regulation and cellular functions of mitochondrial calcium. *Nat. Rev. Mol. Cell Biol.* **19**, 713–730 (2018).
213. Vorobjeva, N. *et al.* Mitochondrial permeability transition pore is involved in oxidative burst and NETosis of human neutrophils. *Biochim. Biophys. Acta - Mol. Basis Dis.* **1866**, 165664 (2020).
214. Botelho, R. J., Tapper, H., Furuya, W., Mojdami, D. & Grinstein, S. FcγR-Mediated

Phagocytosis Stimulates Localized Pinocytosis in Human Neutrophils. *J. Immunol.* **169**, 4423–4429 (2002).
215. Thomas-Reetz, A. C. & De Camilli, P. A role for synaptic vesicles in non-neuronal cells: clues from pancreatic β cells and from chromaffin cells. *FASEB J.* **8**, 209–216 (1994).
216. DeCoursey, T. E., Cherny, V. V., Zhou, W. & Thomas, L. L. Simultaneous activation of NADPH oxidase-related proton and electron currents in human neutrophils. *Proc. Natl. Acad. Sci.* **97**, 6885–6889 (2000).
217. Reis, J. *et al.* A closer look into NADPH oxidase inhibitors: Validation and insight into their mechanism of action. *Redox Biol.* **32**, 101466 (2020).
218. Niewold, T. B., Clark, D. N., Salloum, R. & Poole, B. D. Interferon Alpha in Systemic Lupus Erythematosus. *J. Biomed. Biotechnol.* **2010**, 1–8 (2010).
219. Cash, J. L., White, G. E. & Greaves, D. R. Chapter 17. Zymosan-Induced Peritonitis as a Simple Experimental System for the Study of Inflammation. in 379–396 (2009). doi:10.1016/S0076-6879(09)05417-2.
220. Kessler, N. *et al.* Monocyte-derived macrophages aggravate pulmonary vasculitis via cGAS/STING/IFN-mediated nucleic acid sensing. *J. Exp. Med.* **219**, (2022).
221. Decout, A., Katz, J. D., Venkatraman, S. & Ablasser, A. The cGAS–STING pathway as a therapeutic target in inflammatory diseases. *Nat. Rev. Immunol.* **21**, 548–569 (2021).
222. DeCoursey, T. E., Morgan, D. & Cherny, V. V. The voltage dependence of NADPH oxidase reveals why phagocytes need proton channels. *Nature* **422**, 531–534 (2003).
223. Nguyen, G. T., Green, E. R. & Mecsas, J. Neutrophils to the ROScue: Mechanisms of NADPH oxidase activation and bacterial resistance. *Front. Cell. Infect. Microbiol.* **7**, (2017).
224. Nizer, W. S. da C., Inkovskiy, V. & Overhage, J. Surviving reactive chlorine stress: Responses of gram-negative bacteria to hypochlorous acid. *Microorganisms* **8**, 1–27 (2020).
225. Sollberger, G. *et al.* Gasdermin D plays a vital role in the generation of neutrophil extracellular traps. **6689**, (2018).
226. Martinod, K. *et al.* Neutrophil elastase-deficient mice form neutrophil extracellular traps in an experimental model of deep vein thrombosis. *J. Thromb. Haemost.* **14**, 551–558 (2016).
227. Yousefi, S., Simon, D. & Simon, H.-U. Eosinophil extracellular DNA traps: molecular mechanisms and potential roles in disease. *Curr. Opin. Immunol.* **24**, 736–739 (2012).
228. de Bont, C. M., Koopman, W. J. H., Boelens, W. C. & Pruijn, G. J. M. Stimulus-dependent chromatin dynamics, citrullination, calcium signalling and ROS production during NET formation. *Biochim. Biophys. Acta - Mol. Cell Res.* **1865**, 1621–1629 (2018).
229. Lewis, H. D. *et al.* Inhibition of PAD4 activity is sufficient to disrupt mouse and human NET formation. *Nat. Chem. Biol.* **11**, 189–191 (2015).
230. Claushuis, T. A. M. *et al.* Role of Peptidylarginine Deiminase 4 in Neutrophil Extracellular Trap Formation and Host Defense during Klebsiella pneumoniae– Induced Pneumonia-Derived Sepsis. *J. Immunol.* **201**, 1241–1252 (2018).
231. Zhou, Y. *et al.* Evidence for a direct link between PAD4-mediated citrullination and the oxidative burst in human neutrophils. *Sci. Rep.* 1–13 (2018) doi:10.1038/s41598-018-33385-z.
232. Gupta, A. K., Giaglis, S., Hasler, P. & Hahn, S. Efficient Neutrophil Extracellular Trap Induction Requires Mobilization of Both Intracellular and Extracellular Calcium Pools and Is Modulated by Cyclosporine A. *PLoS One* **9**, e97088 (2014).
233. Vorobjeva, N. V. & Chernyak, B. V. NADPH Oxidase Modulates Ca2+-Dependent Formation of Neutrophil Extracellular Traps. *Moscow Univ. Biol. Sci. Bull.* **75**, 104–109 (2020).
234. Kuwabara, W. M. T. *et al.* NADPH Oxidase-Dependent Production of Reactive Oxygen Species Induces Endoplasmatic Reticulum Stress in Neutrophil-Like HL60 Cells. *PLoS One* **10**, e0116410 (2015).
235. Kearney, P. L. *et al.* Kinetic characterization of protein arginine deiminase 4: A transcriptional corepressor implicated in the onset and progression of rheumatoid arthritis. *Biochemistry* **44**, 10570–10582 (2005).
236. Gewirtz, A. T., Seetoo, K. F. & Simons, E. R. Neutrophil degranulation and phospholipase D activation are enhanced if the NA+/H+ antiport is blocked. *J. Leukoc. Biol.* **64**, 98–103 (1998).

237. Hann, J., Bueb, J. L., Tolle, F. & Bréchard, S. Calcium signaling and regulation of neutrophil functions: Still a long way to go. *J. Leukoc. Biol.* **107**, 285–297 (2020).
238. Wang, X.-T., McCullough, K. D., Wang, X.-J., Carpenter, G. & Holbrook, N. J. Oxidative Stress-induced Phospholipase C-γ1 Activation Enhances Cell Survival. *J. Biol. Chem.* **276**, 28364–28371 (2001).
239. Banan, A., Fields, J. Z., Zhang, Y. & Keshavarzian, A. Phospholipase C-γ inhibition prevents EGF protection of intestinal cytoskeleton and barrier against oxidants. *Am. J. Physiol. Liver Physiol.* **281**, G412–G423 (2001).
240. Patel, S. & Cai, X. Evolution of acidic Ca2+ stores and their resident Ca2+-permeable channels. *Cell Calcium* **57**, 222–230 (2015).
241. Styrt, B., Schwartz, M. A. & Klempner, M. S. Calcium release associated with discharge of specific granule contents from human neutrophils. *Biochem. Biophys. Res. Commun.* **154**, 1308–1313 (1988).
242. Jin, X. *et al.* Targeting Two-Pore Channels: Current Progress and Future Challenges. *Trends Pharmacol. Sci.* **41**, 582–594 (2020).
243. Clemens, R. A. & Lowell, C. A. Store-operated calcium signaling in neutrophils. *J. Leukoc. Biol.* **98**, 497–502 (2015).
244. Gupta, A. K. *et al.* Activated endothelial cells induce neutrophil extracellular traps and are susceptible to NETosis-mediated cell death. *FEBS Lett.* **584**, 3193–3197 (2010).
245. Muñoz-Caro, T. *et al.* Eimeria bovis-triggered neutrophil extracellular trap formation is CD11b-, ERK 1/2-, p38 MAP kinase- and SOCE-dependent. *Vet. Res.* **46**, 23 (2015).
246. Demaurex, N. & Saul, S. The role of STIM proteins in neutrophil functions. *J. Physiol.* **596**, 2699–2708 (2018).
247. Najder, K. *et al.* Role of the Intracellular Sodium Homeostasis in Chemotaxis of Activated Murine Neutrophils. *Front. Immunol.* **11**, (2020).
248. Inoue, M., Enomoto, M., Yoshimura, M. & Mizowaki, T. Pharmacological inhibition of sodium-calcium exchange activates NADPH oxidase and induces infection-independent NETotic cell death. *Redox Biol.* **43**, 101983 (2021).
249. Rizzuto, R. *et al.* Close Contacts with the Endoplasmic Reticulum as Determinants of Mitochondrial Ca 2+ Responses. *Science (80-.).* **280**, 1763–1766 (1998).
250. Zhou, W. *et al.* Mitofusin 2 regulates neutrophil adhesive migration and the actin cytoskeleton. *J. Cell Sci.* **133**, (2020).
251. Ramachandra, C. J. A., Hernandez-Resendiz, S., Crespo-Avilan, G. E., Lin, Y.-H. & Hausenloy, D. J. Mitochondria in acute myocardial infarction and cardioprotection. *EBioMedicine* **57**, 102884 (2020).
252. Baev, A. Y. *et al.* Interaction of Mitochondrial Calcium and ROS in Neurodegeneration. *Cells* **11**, 706 (2022).
253. Finkel, T. *et al.* The Ins and Outs of Mitochondrial Calcium. *Circ. Res.* **116**, 1810–1819 (2015).
254. Przygodzki, T., Sokal, A. & Bryszewska, M. Calcium ionophore A23187 action on cardiac myocytes is accompanied by enhanced production of reactive oxygen species. *Biochim. Biophys. Acta - Mol. Basis Dis.* **1740**, 481–488 (2005).
255. Petersén, Å., Castilho, R. F., Hansson, O., Wieloch, T. & Brundin, P. Oxidative stress, mitochondrial permeability transition and activation of caspases in calcium ionophore A23187-induced death of cultured striatal neurons. *Brain Res.* **857**, 20–29 (2000).
256. Jou, M.-J. *et al.* Visualization of melatonin's multiple mitochondrial levels of protection against mitochondrial Ca 2+ -mediated permeability transition and beyond in rat brain astrocytes. *J. Pineal Res.* **48**, 20–38 (2010).
257. Monteith, A. J. *et al.* Mitochondrial Calcium Uniporter Affects Neutrophil Bactericidal Activity during Staphylococcus aureus Infection. *Infect. Immun.* **90**, (2022).
258. Zielonka, J. *et al.* Mitochondria-Targeted Triphenylphosphonium-Based Compounds: Syntheses, Mechanisms of Action, and Therapeutic and Diagnostic Applications. *Chem. Rev.* **117**, 10043–10120 (2017).
259. Schultz, J. & Kaminker, K. Myeloperoxidase of the leucocyte of normal human blood. I. Content and localization. *Arch. Biochem. Biophys.* **96**, 465–467 (1962).

260. Othman, A., Sekheri, M. & Filep, J. G. Roles of neutrophil granule proteins in orchestrating inflammation and immunity. *FEBS J.* **289**, 3932–3953 (2022).
261. Sengeløv, H., Kjeldsen, L. & Borregaard, N. Control of exocytosis in early neutrophil activation. *J. Immunol.* **150**, 1535–43 (1993).
262. Davis, L. C. *et al.* NAADP Activates Two-Pore Channels on T Cell Cytolytic Granules to Stimulate Exocytosis and Killing. *Curr. Biol.* **22**, 2331–2337 (2012).
263. Arlt, E. *et al.* TPC1 deficiency or blockade augments systemic anaphylaxis and mast cell activity. *Proc. Natl. Acad. Sci.* **117**, 18068–18078 (2020).
264. Breton, S. & Brown, D. Regulation of Luminal Acidification by the V-ATPase. *Physiology* **28**, 318–329 (2013).
265. Camacho, M., Machado, J. D., Montesinos, M. S., Criado, M. & Borges, R. Intragranular pH rapidly modulates exocytosis in adrenal chromaffin cells. *J. Neurochem.* **96**, 324–334 (2006).
266. Gilman-Sachs, A. *et al.* Expression and role of a2 vacuolar-ATPase (a2V) in trafficking of human neutrophil granules and exocytosis. *J. Leukoc. Biol.* **97**, 1121–1131 (2015).
267. Poëa-Guyon, S. *et al.* The V-ATPase membrane domain is a sensor of granular ph that controls the exocytotic machinery. *J. Cell Biol.* **203**, 283–298 (2013).
268. Di Giovanni, J. *et al.* V-ATPase Membrane Sector Associates with Synaptobrevin to Modulate Neurotransmitter Release. *Neuron* **67**, 268–279 (2010).
269. Hiesinger, P. R. *et al.* The v-ATPase V 0 Subunit a1 Is Required for a Late Step in Synaptic Vesicle Exocytosis in Drosophila. *Cell* **121**, 607–620 (2005).
270. Watzlawick, R., Kenngott, E. E., Liu, F. D. M., Schwab, J. M. & Hamann, A. Anti-Inflammatory Effects of IL-27 in Zymosan-Induced Peritonitis: Inhibition of Neutrophil Recruitment Partially Explained by Impaired Mobilization from Bone Marrow and Reduced Chemokine Levels. *PLoS One* **10**, e0137651 (2015).
271. Walley, K. R., Lukacs, N. W., Standiford, T. J., Strieter, R. M. & Kunkel, S. L. Elevated levels of macrophage inflammatory protein 2 in severe murine peritonitis increase neutrophil recruitment and mortality. *Infect. Immun.* **65**, 3847–3851 (1997).
272. De Filippo, K. *et al.* Mast cell and macrophage chemokines CXCL1/CXCL2 control the early stage of neutrophil recruitment during tissue inflammation. *Blood* **121**, 4930–4937 (2013).
273. Marone, G. *et al.* Physiological concentrations of zinc inhibit the release of histamine from human basophils and lung mast cells. *Agents Actions* **18**, 103–106 (1986).
274. Lämmermann, T. *et al.* Neutrophil swarms require LTB4 and integrins at sites of cell death in vivo. *Nature* **498**, 371–375 (2013).
275. Fernandez-Boyanapalli, R. *et al.* PPARγ activation normalizes resolution of acute sterile inflammation in murine chronic granulomatous disease. *Blood* **116**, 4512–4522 (2010).
276. Frangie, C. & Daher, J. Role of myeloperoxidase in inflammation and atherosclerosis. *Biomed. Reports* **16**, 53 (2022).
277. Johansson, M. W., Patarroyo, M., Oberg, F., Siegbahn, A. & Nilsson, K. Myeloperoxidase mediates cell adhesion via the alpha M beta 2 integrin (Mac-1, CD11b/CD18). *J. Cell Sci.* **110**, 1133–1139 (1997).
278. Lau, D. *et al.* Myeloperoxidase mediates neutrophil activation by association with CD11b/CD18 integrins. *Proc. Natl. Acad. Sci.* **102**, 431–436 (2005).
279. El Kebir, D., József, L., Pan, W. & Filep, J. G. Myeloperoxidase Delays Neutrophil Apoptosis Through CD11b/CD18 Integrins and Prolongs Inflammation. *Circ. Res.* **103**, 352–359 (2008).
280. Yousefi, S. *et al.* In vivo evidence for extracellular DNA trap formation. *Cell Death Dis.* **11**, 300 (2020).
281. van Timmeren, M. M., Heeringa, P. & Kallenberg, C. G. M. Infectious triggers for vasculitis. *Curr. Opin. Rheumatol.* **26**, 416–423 (2014).
282. Kettritz, R. How anti-neutrophil cytoplasmic autoantibodies activate neutrophils. *Clin. Exp. Immunol.* **169**, 220–228 (2012).
283. Kitching, A. R. *et al.* ANCA-associated vasculitis. *Nat. Rev. Dis. Prim.* **6**, 71 (2020).
284. Hewins, P., Williams, J. M., Wakelam, M. J. O. & Savage, C. O. S. Activation of Syk in Neutrophils by Antineutrophil Cytoplasm Antibodies Occurs via Fc Receptors and CD18. *J.*

Am. Soc. Nephrol. **15**, 796–808 (2004).
285. Williams, J. M. *et al.* Activation of the G i Heterotrimeric G Protein by ANCA IgG F(ab′) 2 Fragments Is Necessary but not Sufficient to Stimulate the Recruitment of Those Downstream Mediators Used by Intact ANCA IgG. *J. Am. Soc. Nephrol.* **14**, 661–669 (2003).
286. Kusunoki, Y. *et al.* Peptidylarginine Deiminase Inhibitor Suppresses Neutrophil Extracellular Trap Formation and MPO-ANCA Production. *Front. Immunol.* **7**, (2016).
287. Watad, A. *et al.* Autoimmunity in the Elderly: Insights from Basic Science and Clinics. *Gerontology* **63**, 515–523 (2017).
288. Wang, Y. *et al.* Cytoplasmic DNA sensing by KU complex in aged CD4+ T cell potentiates T cell activation and aging-related autoimmune inflammation. *Immunity* **54**, 632-647.e9 (2021).
289. Lee, S., Ko, Y. & Kim, T. J. Homeostasis and regulation of autoreactive B cells. *Cell. Mol. Immunol.* **17**, 561–569 (2020).
290. Ye, Y., Gaugler, B., Mohty, M. & Malard, F. Plasmacytoid dendritic cell biology and its role in immune-mediated diseases. *Clin. Transl. Immunol.* **9**, (2020).
291. Montes-Cobos, E. *et al.* Voltage-Gated Proton Channel Hv1 Controls TLR9 Activation in Plasmacytoid Dendritic Cells. *J. Immunol.* **205**, 3001–3010 (2020).
292. Sun, B. B. *et al.* Genomic atlas of the human plasma proteome. *Nature* **558**, 73–79 (2018).
293. Pan, Q. *et al.* Mechanistic insights into environmental and genetic risk factors for systemic lupus erythematosus. *Am. J. Transl. Res.* **11**, 1241–1254 (2019).
294. Wang, M., Ishikawa, T., Lai, Y., Nallapothula, D. & Singh, R. R. Diverse Roles of NETosis in the Pathogenesis of Lupus. *Front. Immunol.* **13**, (2022).
295. Hawkins, P. *et al.* Alpha-1 Antitrypsin Augmentation Inhibits Proteolysis of Neutrophil Membrane Voltage-Gated Proton Channel-1 in Alpha-1 Deficient Individuals. *Medicina (B. Aires).* **57**, 814 (2021).
296. Fernández, A., Pupo, A., Mena-Ulecia, K. & Gonzalez, C. Pharmacological modulation of proton channel hv1 in cancer therapy: Future perspectives. *Mol. Pharmacol.* **90**, 385–402 (2016).
297. Park, J. *et al.* Cancer cells induce metastasis-supporting neutrophil extracellular DNA traps. *Sci. Transl. Med.* **8**, (2016).
298. Demers, M. *et al.* Cancers predispose neutrophils to release extracellular DNA traps that contribute to cancer-associated thrombosis. *Proc. Natl. Acad. Sci.* **109**, 13076–13081 (2012).
299. Kanashiro, A. *et al.* The role of neutrophils in neuro-immune modulation. *Pharmacol. Res.* **151**, (2020).
300. Zenaro, E. *et al.* Neutrophils promote Alzheimer ' s disease – like pathology and cognitive decline via LFA-1 integrin. **21**, (2015).
301. Smyth, L. C. D. *et al.* Neutrophil-vascular interactions drive myeloperoxidase accumulation in the brain in Alzheimer's disease. *Acta Neuropathol. Commun.* **10**, 38 (2022).
302. Rausch, P. & Moore, T. Granule enzymes of polymorphonuclear neutrophils: A phylogenetic comparison. *Blood* **46**, 913–919 (1975).
303. Ermert, D. *et al.* Mouse Neutrophil Extracellular Traps in Microbial Infections. *J. Innate Immun.* **1**, 181–193 (2009).
304. Burn, G. L., Foti, A., Marsman, G., Patel, D. F. & Zychlinsky, A. The Neutrophil. *Immunity* **54**, 1377–1391 (2021).
305. Wang, G. *et al.* Identification of the Transgene Integration Site and Host Genome Changes in MRP8-Cre/ires-EGFP Transgenic Mice by Targeted Locus Amplification. *Front. Immunol.* **13**, (2022).

Inhibitor test: BAPTA-AM and N-acetyl cysteine

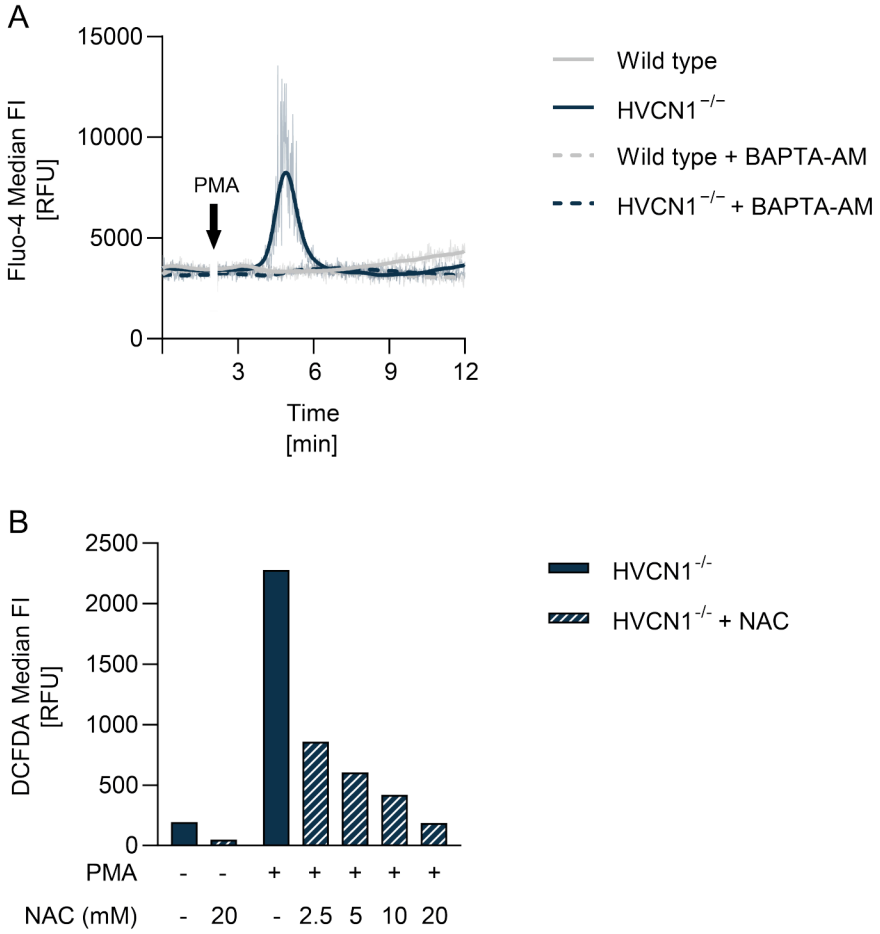

Figure A.1| Proof of inhibition for BAPTA-AM and N-acetyl cysteine.
A| The effect of BAPTA-AM was tested by its ability to block the intracellular calcium wave in HVCN1$^{-/-}$ neutrophils. To this end, neutrophils were loaded with 2 µM Fluo-4-AM and afterwards incubated for 30 min with 10 µM BAPTA-AM before measuring the intracellular calcium response to 100 nM PMA real-time. B| The effect of NAC was tested by its ability to block the intracellular ROS in HVCN1$^{-/-}$ neutrophils. To this end, neutrophils were loaded with 2.5 µM DCFDA-AM and afterwards incubated for 1 h with 10 mM NAC. Neutrophils were stimulated with 100 nM PMA, or left untreated, for 30 min. Then DCFDA median FI was determined by flow cytometry.

Cre expression and deletion efficacy Ly6G-Cre x HVCN1 floxed neutrophils

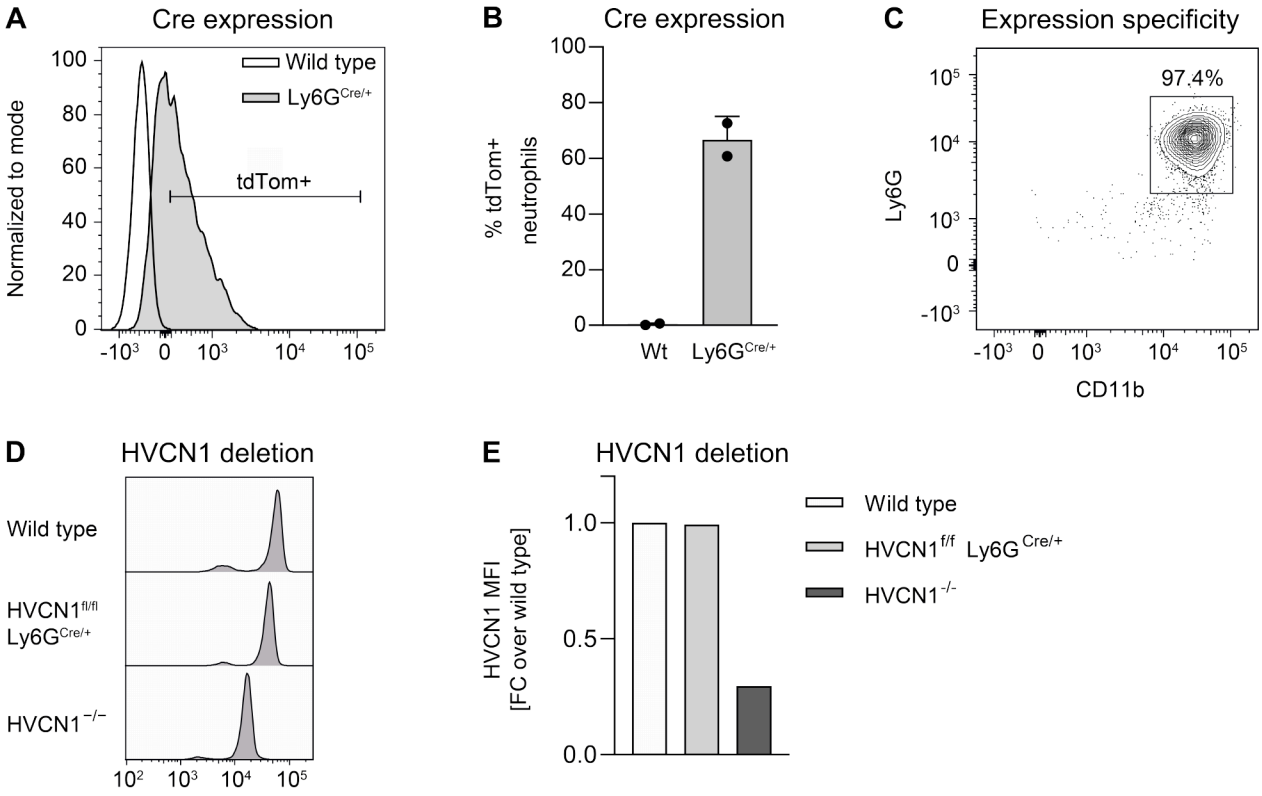

Figure A.2| Cre expression and deletion efficacy Ly6G-Cre x HVCN1 floxed neutrophils.
A| Cre expression in bone marrow neutrophils was assessed by determining tdTomato fluorescence. As the tdTomato gene is fused to the Cre gene, both proteins should be equally expressed. B| Percentage of bone marrow neutrophils positive for tdTomato as a readout for Cre expression. C| Expression specificity of the Cre-tdTomato construct. It was first gated onto all tdTomato positive cells, then checking their identity by the neutrophil markers Ly6G and CD11b. D| HVCN1 deletion in HVCN1$^{fl/fl}$; Ly6G$^{Cre/+}$ bone marrow neutrophils was assessed by flow cytometry. E| HVCN1 expression relative to HVCN1 in wild type neutrophils.

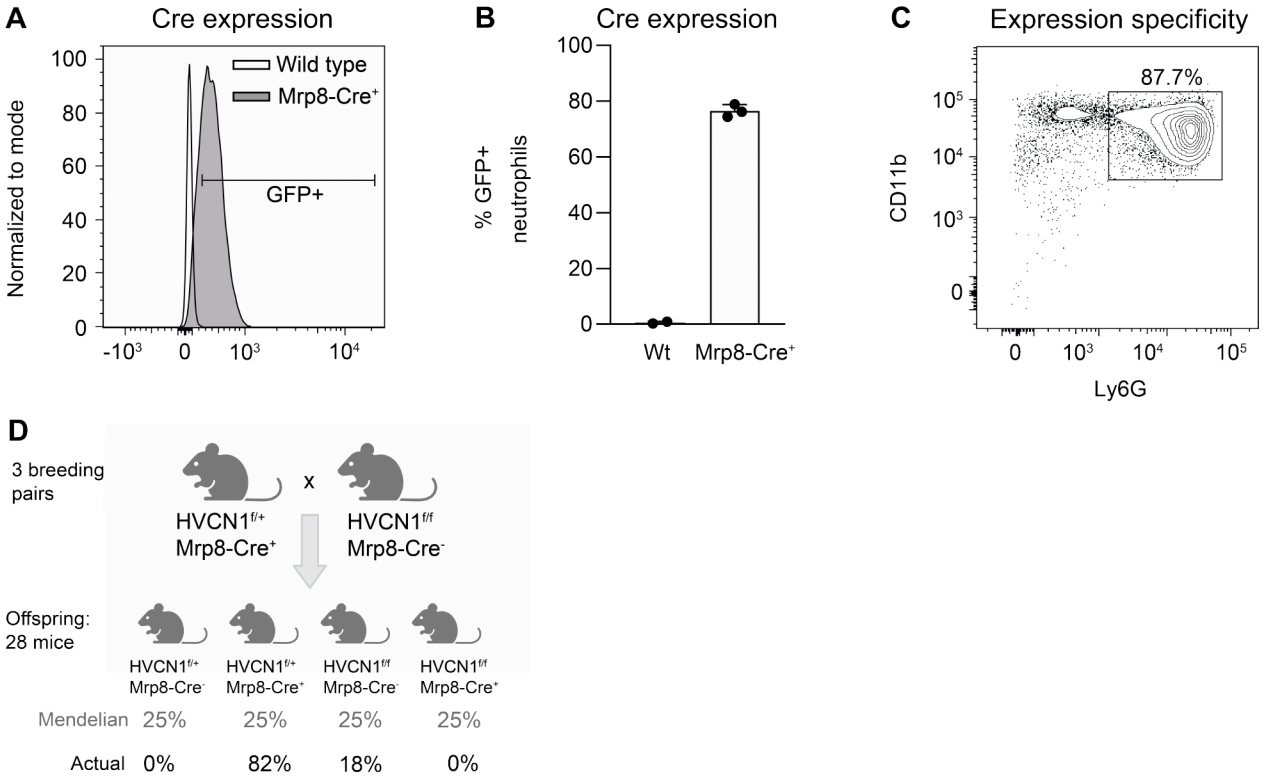

Figure A.3| Cre expression and breeding outcome MRP8-Cre x HVCN1 floxed neutrophils.
A| Cre expression in bone marrow neutrophils was assessed by determining GFP fluorescence. As the GFP gene is fused to the Cre gene, both proteins should be equally expressed. B| Percentage of bone marrow neutrophils positive for GFP as a readout for Cre expression. C| Expression specificity of the Cre-GFP construct. It was first gated onto all GFP positive cells, then checking their identity by the neutrophil markers Ly6G and CD11b. D| Outcome of the breeding that should have resulted in HVCN1$^{fl/fl}$; Mrp8-Cre^{+} offspring.

Deletion efficacy LysM-Cre x HVCN1 floxed neutrophils

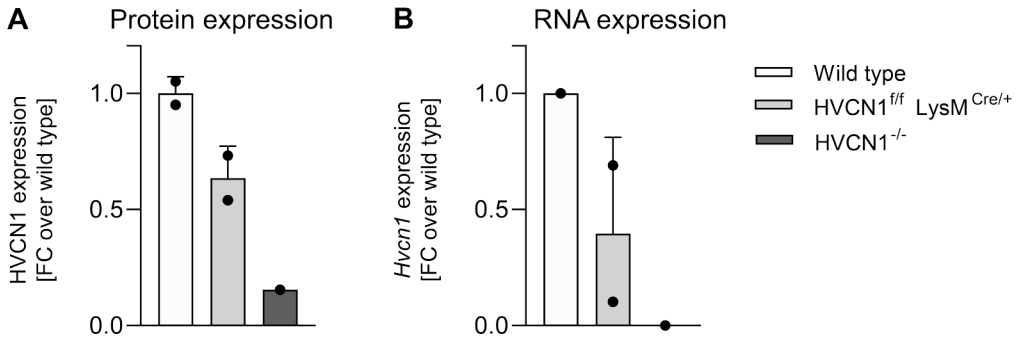

Figure A.4| Deletion efficacy LysM-Cre x HVCN1 floxed neutrophils
A| HVCN1 deletion in HVCN1$^{fl/fl}$; LysM$^{Cre/+}$ bone marrow neutrophils was assessed by flow cytometry. HVCN1 expression relative to HVCN1 in wild type neutrophils. B| Furthermore, HVCN1 expression levels were analyzed by RT-qPCR and plotted as fold change to wild type control.

FACS panel & gating – General blood panel

Antigen	Conjugate
CD45	BV711
CD11b	PE
Ly6G	BUV563
Ly6C	eF450
CXCR2	APC
CD3	BUV737
CD19	PE-Cy5
Live/Dead	Zombie Aqua

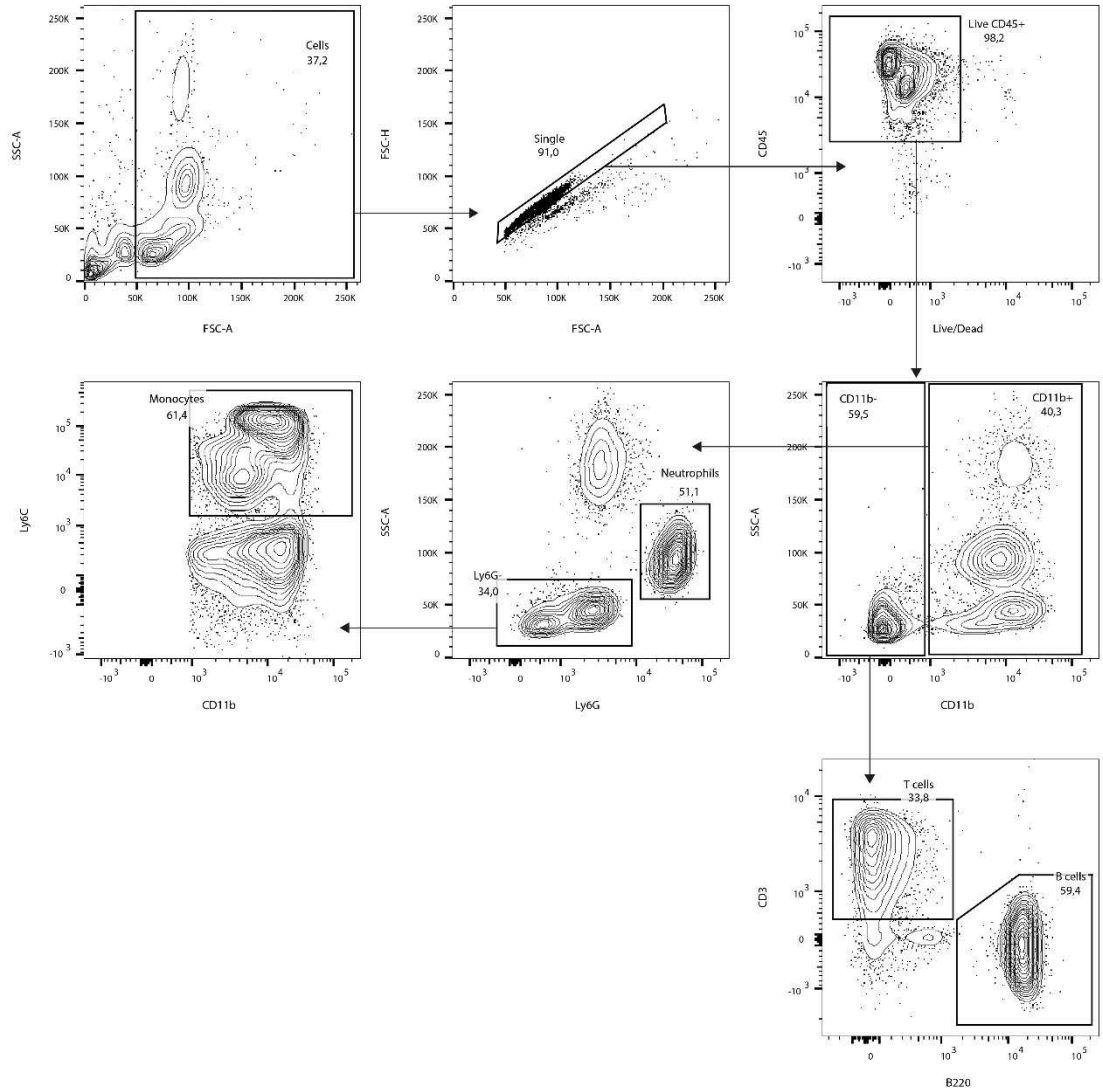

FACS panel & gating – Neutrophil progenitors

Published in Evrard et al. (2018)

Antigen	Conjugate	
B220	PE-Cy7	Lineage
CD115	PE-Cy7	
CD3e	PE-Cy7	
CD90.2	PE-Cy7	
NK1.1	PE-Cy7	
Sca1	PE-Cy7	
cKit	BV711	
CXCR2	AF647	
CXCR4	V450	
Live/Dead	Zombie Aqua	
Gr1	APC-Cy7	
Ly6G	BUV563	
CD11b	BUV395	
SiglecF	PE	

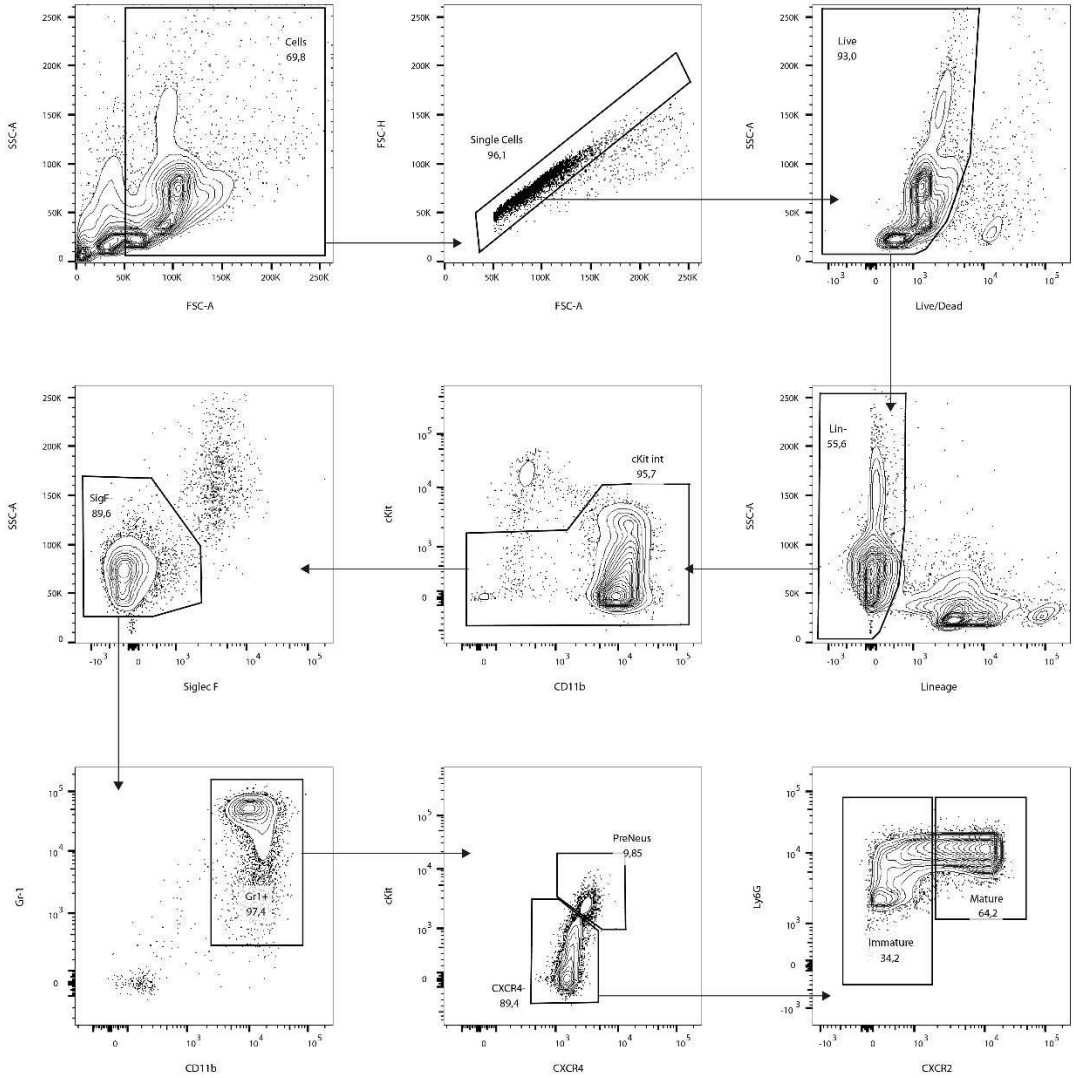

FACS panel & gating – GMPs

Antigen	Conjugate
Ter119	APC-Cy7
CD19	APC-Cy7
NK1.1	APC-Cy7
Ly6G	APC-Cy7
CD3e	APC-Cy7
B220	APC-Cy7
Live/Dead	Near-IR
cKit	PE-Cy7
Sca1	BV421
CD16/32	AF647
CD34	FITC

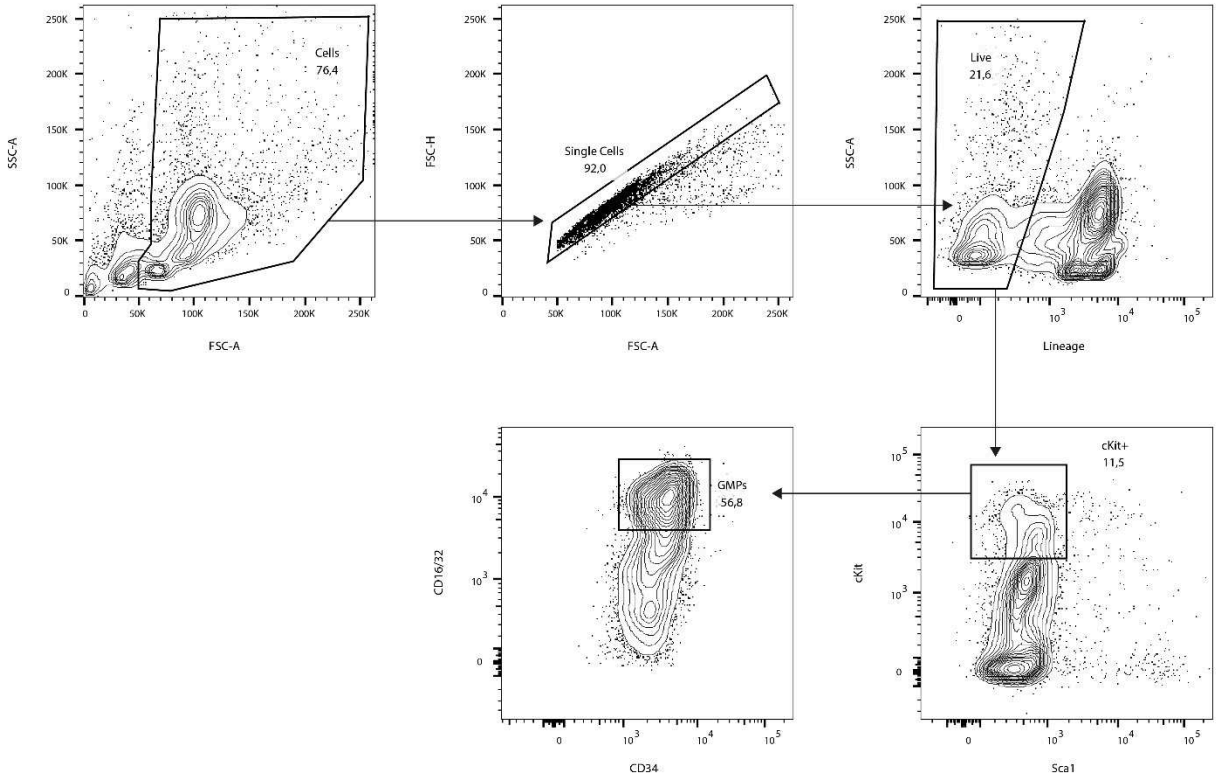

FACS panel & gating – Peritonitis (lavage)

Antigen	Conjugate
CD45	BV711
CD11b	PE
Ly6G	BUV563
CD3	APC
B220	PE-Cy7
Ly6C	PerCp-Cy5.5
gdTCR	PE
Live/Dead	Near-IR

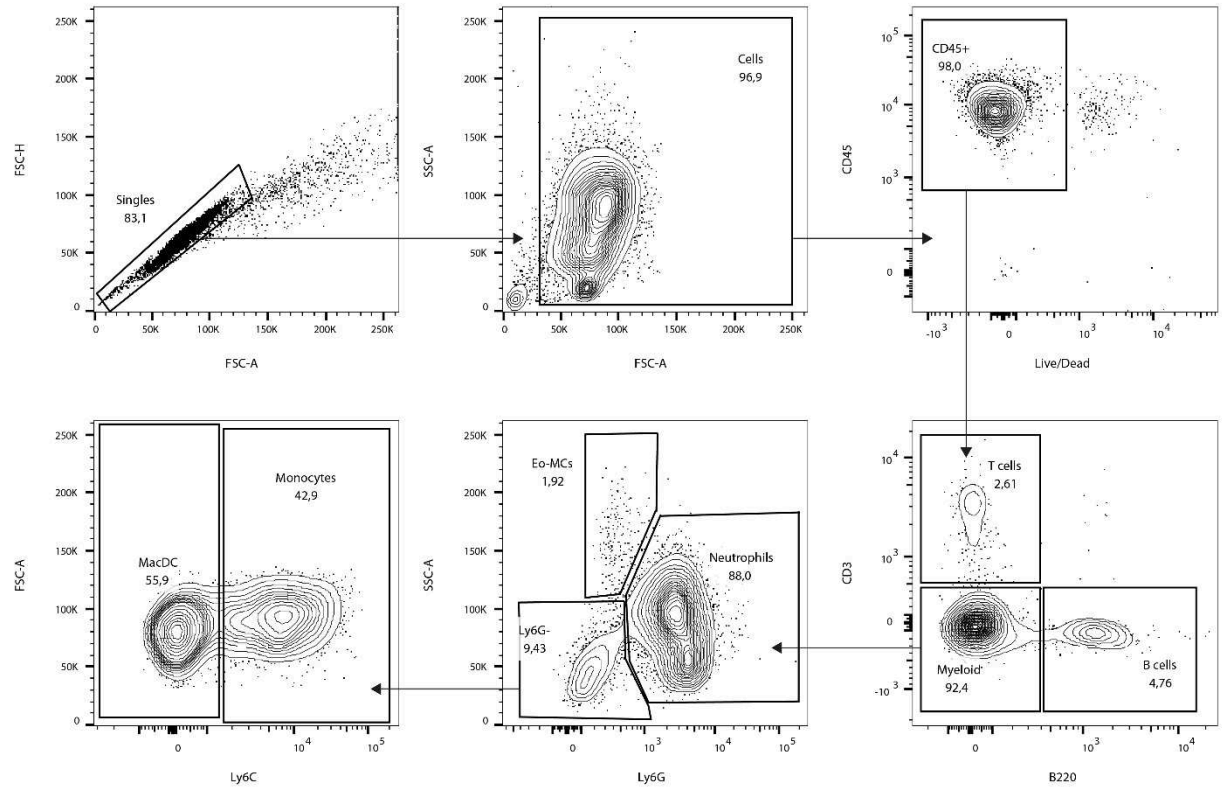

FACS panel & gating – Pulmonary ANCA vasculitis (BAL)

Antigen	Conjugate
Live/Dead	Zombie Aqua
CD11b	BUV395
CD11c	APC
CD19	PE-Cy5
CD4	FITC
CD45	BV711
CD8a	BV650
Ly6B2	AF700
Ly6G	PE-Dazzle
MHCII	BV421
NK1.1	PE-Cy7

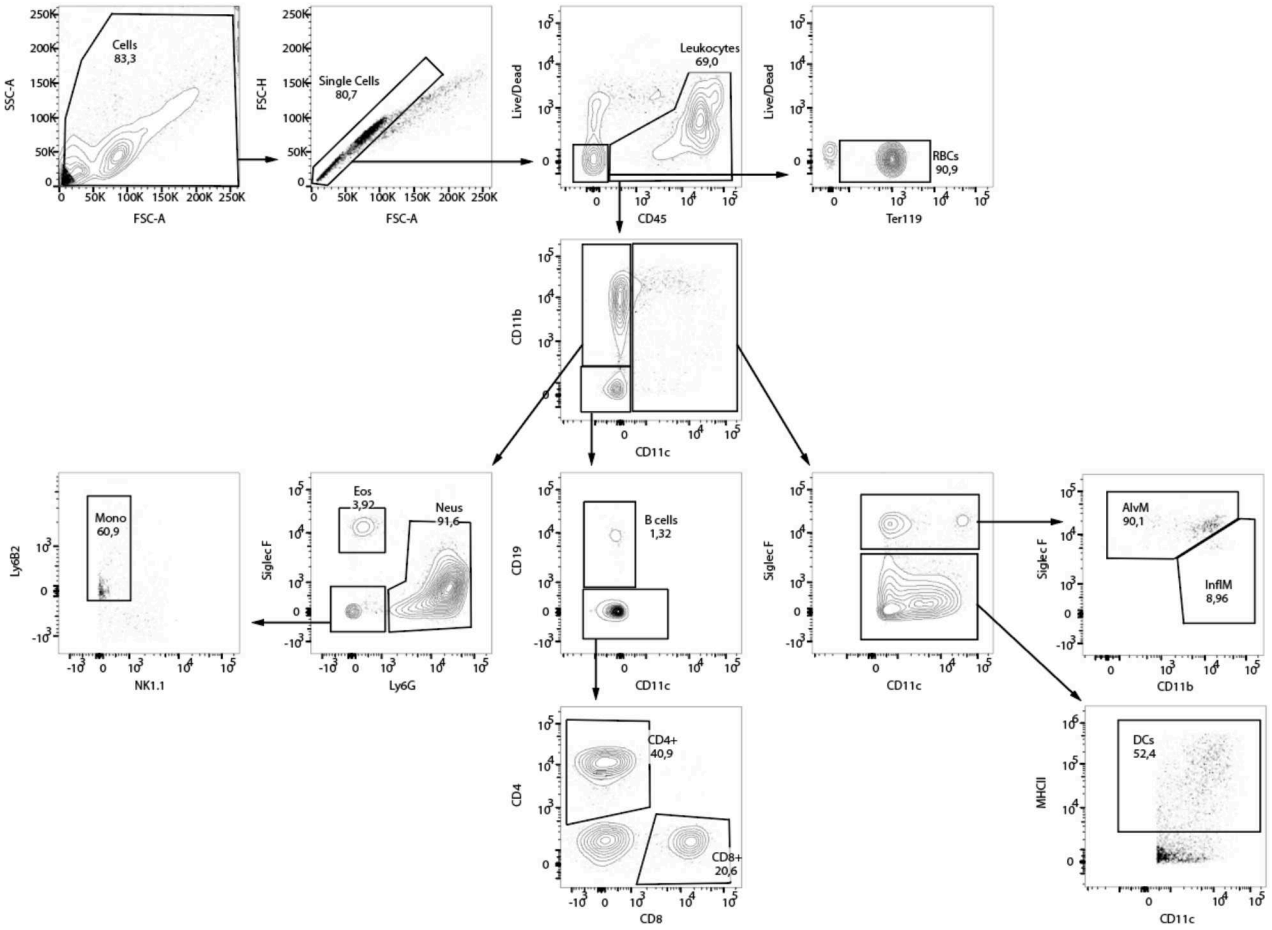

Cell Profiler Analysis – Parameters for classification

Parameter	Parameter	Parameter
ImageNumber	AreaShape_Zernike_5_5	RadialDistribution_ZernikeMagnitude_images_8_2
ObjectNumber	AreaShape_Zernike_6_0	RadialDistribution_ZernikeMagnitude_images_8_4
FileName_images	AreaShape_Zernike_6_2	RadialDistribution_ZernikeMagnitude_images_8_6
PathName_images	AreaShape_Zernike_6_4	RadialDistribution_ZernikeMagnitude_images_8_8
AreaShape_Area	AreaShape_Zernike_6_6	RadialDistribution_ZernikeMagnitude_images_9_1
AreaShape_BoundingBoxArea	AreaShape_Zernike_7_1	RadialDistribution_ZernikeMagnitude_images_9_3
AreaShape_BoundingBoxMaximum_X	AreaShape_Zernike_7_3	RadialDistribution_ZernikeMagnitude_images_9_5
AreaShape_BoundingBoxMaximum_Y	AreaShape_Zernike_7_5	RadialDistribution_ZernikeMagnitude_images_9_7
AreaShape_BoundingBoxMinimum_X	AreaShape_Zernike_7_7	RadialDistribution_ZernikeMagnitude_images_9_9
AreaShape_BoundingBoxMinimum_Y	AreaShape_Zernike_8_0	RadialDistribution_ZernikePhase_images_0_0
AreaShape_Center_X	AreaShape_Zernike_8_2	RadialDistribution_ZernikePhase_images_1_1
AreaShape_Center_Y	AreaShape_Zernike_8_4	RadialDistribution_ZernikePhase_images_2_0
AreaShape_CentralMoment_0_0	AreaShape_Zernike_8_6	RadialDistribution_ZernikePhase_images_2_2
AreaShape_CentralMoment_0_1	AreaShape_Zernike_8_8	RadialDistribution_ZernikePhase_images_3_1
AreaShape_CentralMoment_0_2	AreaShape_Zernike_9_1	RadialDistribution_ZernikePhase_images_3_3
AreaShape_CentralMoment_0_3	AreaShape_Zernike_9_3	RadialDistribution_ZernikePhase_images_4_0
AreaShape_CentralMoment_1_0	AreaShape_Zernike_9_5	RadialDistribution_ZernikePhase_images_4_2
AreaShape_CentralMoment_1_1	AreaShape_Zernike_9_7	RadialDistribution_ZernikePhase_images_4_4
AreaShape_CentralMoment_1_2	AreaShape_Zernike_9_9	RadialDistribution_ZernikePhase_images_5_1
AreaShape_CentralMoment_1_3	Granularity_10_images	RadialDistribution_ZernikePhase_images_5_3
AreaShape_CentralMoment_2_0	Granularity_11_images	RadialDistribution_ZernikePhase_images_5_5
AreaShape_CentralMoment_2_1	Granularity_12_images	RadialDistribution_ZernikePhase_images_6_0
AreaShape_CentralMoment_2_2	Granularity_13_images	RadialDistribution_ZernikePhase_images_6_2
AreaShape_CentralMoment_2_3	Granularity_14_images	RadialDistribution_ZernikePhase_images_6_4
AreaShape_Compactness	Granularity_15_images	RadialDistribution_ZernikePhase_images_6_6
AreaShape_ConvexArea	Granularity_16_images	RadialDistribution_ZernikePhase_images_7_1
AreaShape_Eccentricity	Granularity_1_images	RadialDistribution_ZernikePhase_images_7_3
AreaShape_EquivalentDiameter	Granularity_2_images	RadialDistribution_ZernikePhase_images_7_5
AreaShape_EulerNumber	Granularity_3_images	RadialDistribution_ZernikePhase_images_7_7
AreaShape_Extent	Granularity_4_images	RadialDistribution_ZernikePhase_images_8_0
AreaShape_FormFactor	Granularity_5_images	RadialDistribution_ZernikePhase_images_8_2
AreaShape_HuMoment_0	Granularity_6_images	RadialDistribution_ZernikePhase_images_8_4
AreaShape_HuMoment_1	Granularity_7_images	RadialDistribution_ZernikePhase_images_8_6
AreaShape_HuMoment_2	Granularity_8_images	RadialDistribution_ZernikePhase_images_8_8
AreaShape_HuMoment_3	Granularity_9_images	RadialDistribution_ZernikePhase_images_9_1
AreaShape_HuMoment_4	Intensity_IntegratedIntensityEdge_images	RadialDistribution_ZernikePhase_images_9_3
AreaShape_HuMoment_5	Intensity_IntegratedIntensity_images	RadialDistribution_ZernikePhase_images_9_5
AreaShape_HuMoment_6	Intensity_LowerQuartileIntensity_images	RadialDistribution_ZernikePhase_images_9_7
AreaShape_InertiaTensorEigenvalues_0	Intensity_MADIntensity_images	RadialDistribution_ZernikePhase_images_9_9
AreaShape_InertiaTensorEigenvalues_1	Intensity_MassDisplacement_images	Texture_AngularSecondMoment_images_3_00_256
AreaShape_InertiaTensor_0_0	Intensity_MaxIntensityEdge_images	Texture_AngularSecondMoment_images_3_01_256
AreaShape_InertiaTensor_0_1	Intensity_MaxIntensity_images	Texture_AngularSecondMoment_images_3_02_256
AreaShape_InertiaTensor_1_0	Intensity_MeanIntensityEdge_images	Texture_AngularSecondMoment_images_3_03_256
AreaShape_InertiaTensor_1_1	Intensity_MeanIntensity_images	Texture_Contrast_images_3_00_256
AreaShape_MajorAxisLength	Intensity_MedianIntensity_images	Texture_Contrast_images_3_01_256
AreaShape_MaxFeretDiameter	Intensity_MinIntensityEdge_images	Texture_Contrast_images_3_02_256
AreaShape_MaximumRadius	Intensity_MinIntensity_images	Texture_Contrast_images_3_03_256
AreaShape_MeanRadius	Intensity_StdIntensityEdge_images	Texture_Correlation_images_3_00_256
AreaShape_MedianRadius	Intensity_StdIntensity_images	Texture_Correlation_images_3_01_256
AreaShape_MinFeretDiameter	Intensity_UpperQuartileIntensity_images	Texture_Correlation_images_3_02_256
AreaShape_MinorAxisLength	Location_CenterMassIntensity_X_images	Texture_Correlation_images_3_03_256
AreaShape_NormalizedMoment_0_0	Location_CenterMassIntensity_Y_images	Texture_DifferenceEntropy_images_3_00_256
AreaShape_NormalizedMoment_0_1	Location_CenterMassIntensity_Z_images	Texture_DifferenceEntropy_images_3_01_256
AreaShape_NormalizedMoment_0_2	Location_Center_X	Texture_DifferenceEntropy_images_3_02_256
AreaShape_NormalizedMoment_0_3	Location_Center_Y	Texture_DifferenceEntropy_images_3_03_256
AreaShape_NormalizedMoment_1_0	Location_Center_Z	Texture_DifferenceVariance_images_3_00_256
AreaShape_NormalizedMoment_1_1	Location_MaxIntensity_X_images	Texture_DifferenceVariance_images_3_01_256
AreaShape_NormalizedMoment_1_2	Location_MaxIntensity_Y_images	Texture_DifferenceVariance_images_3_02_256
AreaShape_NormalizedMoment_1_3	Location_MaxIntensity_Z_images	Texture_DifferenceVariance_images_3_03_256
AreaShape_NormalizedMoment_2_0	Number_Object_Number	Texture_Entropy_images_3_00_256
AreaShape_NormalizedMoment_2_1	RadialDistribution_FracAtD_images_1of4	Texture_Entropy_images_3_01_256
AreaShape_NormalizedMoment_2_2	RadialDistribution_FracAtD_images_2of4	Texture_Entropy_images_3_02_256
AreaShape_NormalizedMoment_2_3	RadialDistribution_FracAtD_images_3of4	Texture_Entropy_images_3_03_256
AreaShape_NormalizedMoment_3_0	RadialDistribution_FracAtD_images_4of4	Texture_InfoMeas1_images_3_00_256
AreaShape_NormalizedMoment_3_1	RadialDistribution_MeanFrac_images_1of4	Texture_InfoMeas1_images_3_01_256
AreaShape_NormalizedMoment_3_2	RadialDistribution_MeanFrac_images_2of4	Texture_InfoMeas1_images_3_02_256
AreaShape_NormalizedMoment_3_3	RadialDistribution_MeanFrac_images_3of4	Texture_InfoMeas1_images_3_03_256
AreaShape_Orientation	RadialDistribution_MeanFrac_images_4of4	Texture_InfoMeas2_images_3_00_256
AreaShape_Perimeter	RadialDistribution_RadialCV_images_1of4	Texture_InfoMeas2_images_3_01_256
AreaShape_Solidity	RadialDistribution_RadialCV_images_2of4	Texture_InfoMeas2_images_3_02_256
AreaShape_SpatialMoment_0_0	RadialDistribution_RadialCV_images_3of4	Texture_InfoMeas2_images_3_03_256
AreaShape_SpatialMoment_0_1	RadialDistribution_RadialCV_images_4of4	Texture_InverseDifferenceMoment_images_3_00_256
AreaShape_SpatialMoment_0_2	RadialDistribution_ZernikeMagnitude_images_0_0	Texture_InverseDifferenceMoment_images_3_01_256

AreaShape_SpatialMoment_0_3	RadialDistribution_ZernikeMagnitude_images_1_1	Texture_InverseDifferenceMoment_images_3_02_256
AreaShape_SpatialMoment_1_0	RadialDistribution_ZernikeMagnitude_images_2_0	Texture_InverseDifferenceMoment_images_3_03_256
AreaShape_SpatialMoment_1_1	RadialDistribution_ZernikeMagnitude_images_2_2	Texture_SumAverage_images_3_00_256
AreaShape_SpatialMoment_1_2	RadialDistribution_ZernikeMagnitude_images_3_1	Texture_SumAverage_images_3_01_256
AreaShape_SpatialMoment_1_3	RadialDistribution_ZernikeMagnitude_images_3_3	Texture_SumAverage_images_3_02_256
AreaShape_SpatialMoment_2_0	RadialDistribution_ZernikeMagnitude_images_4_0	Texture_SumAverage_images_3_03_256
AreaShape_SpatialMoment_2_1	RadialDistribution_ZernikeMagnitude_images_4_2	Texture_SumEntropy_images_3_00_256
AreaShape_SpatialMoment_2_2	RadialDistribution_ZernikeMagnitude_images_4_4	Texture_SumEntropy_images_3_01_256
AreaShape_SpatialMoment_2_3	RadialDistribution_ZernikeMagnitude_images_5_1	Texture_SumEntropy_images_3_02_256
AreaShape_Zernike_0_0	RadialDistribution_ZernikeMagnitude_images_5_3	Texture_SumEntropy_images_3_03_256
AreaShape_Zernike_1_1	RadialDistribution_ZernikeMagnitude_images_5_5	Texture_SumVariance_images_3_00_256
AreaShape_Zernike_2_0	RadialDistribution_ZernikeMagnitude_images_6_0	Texture_SumVariance_images_3_01_256
AreaShape_Zernike_2_2	RadialDistribution_ZernikeMagnitude_images_6_2	Texture_SumVariance_images_3_02_256
AreaShape_Zernike_3_1	RadialDistribution_ZernikeMagnitude_images_6_4	Texture_SumVariance_images_3_03_256
AreaShape_Zernike_3_3	RadialDistribution_ZernikeMagnitude_images_6_6	Texture_Variance_images_3_00_256
AreaShape_Zernike_4_0	RadialDistribution_ZernikeMagnitude_images_7_1	Texture_Variance_images_3_01_256
AreaShape_Zernike_4_2	RadialDistribution_ZernikeMagnitude_images_7_3	Texture_Variance_images_3_02_256
AreaShape_Zernike_4_4	RadialDistribution_ZernikeMagnitude_images_7_5	Texture_Variance_images_3_03_256
AreaShape_Zernike_5_1	RadialDistribution_ZernikeMagnitude_images_7_7	
AreaShape_Zernike_5_3	RadialDistribution_ZernikeMagnitude_images_8_0	